The Organic Ties of Iron,

or the origin and fate of Fe-binding organic ligands

Hans A. Slagter

The Organic Ties of Iron,

or the origin and fate of Fe-binding organic ligands

Hans A. Slagter

Colophon

Work for this thesis was carried out with the great support of:

Royal Netherlands Institute for Sea Research
P.O. Box 59
1790 AB Den Burg, Texel
The Netherlands

The research reported in this thesis was made possible by a grant from the Netherlands Organisation for Scientific Research (NWO) under contract number 822.01.018 to Loes Gerringa.

Printed by: Ridderprint BV | www.ridderprint.nl

ISBN 978-94-6375-228-2

university of groningen

faculty of science and engineering

Royal Netherlands Institute for Sea Research

Netherlands Organisation for Scientific Research

rijksuniversiteit
groningen

The Organic Ties of Iron

Or the origin and fate of Fe-binding organic ligands

Proefschift

ter verkrijging van de graad van doctor aan de
Rijksuniversiteit Groningen
op gezag van de
rector magnificus prof. dr. E. Sterken
en volgens besluit van het College voor Promoties.

De openbare verdediging zal plaatsvinden op

maandag 10 december 2018 om 11.00 uur

door

Hans Arent Slagter

geboren op 29 augustus 1983
te Smallingerland

Promotores
Prof. dr. ir. H.J.W. de Baar
Prof. dr. C.P.D. Brussaard

Copromotor
Dr. L.J.A. Gerringa

Beoordelingscommissie
Prof. dr. A.G.J. Buma
Prof. dr. K.R. Timmermans
Prof. dr. E. Achterberg

Voor pa…

Table of contents

Chapter 1
Introduction

1.1. Iron and organic matter in seawater

The basic building blocks of living matter are put together by photoautotrophs. These use the energy from light to carry out various cellular metabolic processes harvesting energy from sunlight to fix inorganic carbon (C) into organic matter. This photosynthesis process brings oxygen into the atmosphere. The photoautotrophic phytoplankton (unicellular algae; including photosynthetic bacteria) form the base of food webs in the Earth's oceans. Covering 70% of the globe's surface, marine primary production is responsible for about half the oxygen generated by photosynthesis on a planetary scale (Field et al., 1998).

The process of photosynthesis may be summarized in the following equation, reflecting the relative quantities of cellular carbon (C) in relation to the major nutrients nitrogen (N) and phosphorus (P), required for organic biomass (Redfield, 1958; Redfield et al., 1963):

$$106\ C + 16\ N + 1\ P \rightarrow [C_{106}N_{16}P_1]_{organic\ biomass} + 138\ O_2 \quad (1)$$

Phytoplankton growth is when the availability of essential growth controlling variables is limited. An example of this so-called bottom-up control of primary production is the availability of inorganic nutrients. Depletion and limitation of major nutrients like nitrogen (e.g. nitrate) and phosphate are known to regulate seasonal phytoplankton production in coastal regions and open ocean, respectively (Timmermans et al., 2005; Veldhuis et al., 2005). However in about 40% of the oceans, the major nutrients nitrogen (as NO_3^-) and phosphate (as PO_4^{2-}) are abundantly available but phytoplankton growth is halted or forestalled for other reasons, these are the High Nutrient Low Chlorophyll (HNLC) regions (de Baar et al., 1995; Timmermans et al., 1998).

In order to better describe (and be more inclusive) phytoplankton stoichiometry, we must expand the above equation to include a more detailed representation of the elements involved in primary production, as here reproduced from de Baar et al. (2017):

$$106\ CO_2 + 122\ H_2O + 16\ NO_3^- + 1\ HPO_4^{2-} + (Mn, Fe, Co, Ni, Cu, Zn) + energy \rightarrow \quad (2)$$
$$[(CH_2O)_{106}(NH_3)_{16}(HPO_4)_1(Mn, Fe, Co, Ni, Cu, Zn)]_{organic\ biomass} + 138\ O_2$$

Although the trace metals manganese (Mn), iron (Fe), cobalt (Co), nickel (Ni), copper (Cu) and zinc (Zn) in the equation are present in very low concentrations in the euphotic zone (the surface ocean where there is still light to allow phytoplankton primary production), these play a nontrivial role for enzymatic activity. Primary production is dependent specifically on the trace metal Fe for many cellular processes, e.g. it is an essential component for photosynthetic pigments, DNA replication enzymes and the reduction of reactive oxygen species

(Geider and La Roche, 1994; Netz et al., 2012; Twining and Baines, 2013; Zhang, 2014; de Baar et al., 2017). The next-limiting nutrient after major nutrients N and P is Fe (de Baar et al., 1990; Martin et al., 1990; Rijkenberg et al., 2018a), often depending on seasonality (Birchill et al., 2017). Co-limitation of Fe has been found to occur as well, with light (van Leeuwe and Stefels, 1998; Timmermans et al., 2001a) or co-limitation with a major nutrient or another trace nutrient (Browning et al., 2017). This ultimately results in HNLC regions where major nutrients are abundant but a lack of Fe limits primary production.

The solubility of Fe in seawater is low, resulting in low concentrations in natural seawater, and as such it is no surprise that Fe can be the limiting factor for primary production (de Baar et al., 1990, 2017; Martin et al., 1990; Tagliabue et al., 2017). The biochemical pathways that underlie the many Fe-requiring processes have been established millions of years ago, in a primordial ocean in which conditions were very different. Given a lack of oxygen then, metals that are now trace compounds were readily available in soluble forms (de Baar and La Roche, 2003). Only when oxygen was introduced into the system on a large scale through photosynthesis did these metals begin to be oxidised into particulates that subsequently sank out of the marine system. Therefore, the current situation has developed after biological processes became entirely dependent on these, now trace-, metals.

Fe can exist in two oxidation states, Fe^{2+} and Fe^{3+}, often also referred to as Fe(II) and Fe(III). In an oxygenated modern ocean, Fe^{2+} rapidly oxidizes to Fe^{3+}, to the point where the Fe^{2+} state is negligible. The ability of Fe^{3+} to dissolve in seawater (directly or bound by inorganic oxyhydrates) is as low as 0.1 nanomoles (nM = 10^{-9} M; Liu and Millero, 2002), which essentially puts this in picomolar (pM = 10^{-12} M) ranges. As a means to reflect these low concentrations, if one were to dissolve a paperclip in 15 Olympic size swimming pools the resulting Fe concentration would be 0.213 nM, or 213 pM (de Baar, *pers. comm.*). For phytoplankton growth to occur, Fe concentrations in the nM range are required (Larry E Brand, 1991; Sunda and Huntsman, 1997; Timmermans et al., 2001a, 2001b; Maldonado et al., 2005). Sources of Fe are diverse, including terrestrial (e.g. Klunder et al., 2012a; Rijkenberg et al., 2014), hydrothermal (Tagliabue et al., 2010; Klunder et al., 2012b) and aeolian sources either through deposition of volcanic ash or dust (Korte et al., 2017; Achterberg et al., 2018; Menzel Barraqueta et al., 2018).

To retain Fe concentrations in natural seawater beyond the inorganic solubility Fe needs to be bound to a soluble substance, the so called Fe-binding organic ligands. These are part of the dissolved organic matter (DOM) pool but are

largely still uncharacterized (Gledhill and van den Berg, 1994; Rue and Bruland, 1995; Gledhill and Buck, 2012; Hassler et al., 2017).

Microorganisms, heterotrophic bacteria as well as photoautotrophic phytoplankton, exchange DOM locally through uptake and excretion processes and cell death (Figure 1, ①). Fe-binding organic ligands are argued to be formed as a result and as such are part of this diverse pool of organic substances (Figure 1, "ligands"). DOM can be directly excreted by phytoplankton, e.g. under conditions of excess light and nutrient limitation. In these cases photosynthesis continues unabated but growth is not possible, and excess organic carbon may be excreted as extracellular polymeric substances (EPS), long-chain sugar like carbohydrates produced by microorganisms for protective and/or structural functions (Passow, 2002). Specifically, capsular material from bacterial cells has been found to contribute to the DOM pool (Stoderegger and Herndl, 1998). Bacteria may also produce DOM constituents (Reinthaler et al., 2008; Jiao et al., 2010). Alternatively, dead cells may lead to the formation of DOM, transparent exopolymeric particles (TEP; Mari et al., 2005) and particulate organic debris (Figure 1, ② and ⑤). It has been speculated that marine viruses may have a fundamental role in the release of Fe-binding organic ligands. Infection of microorganisms by a lytic virus causes ultimately the infected host cell to lyse upon releasing newly produced progeny viruses. The remains of the host's cellular content, the cytosol, is released into the surrounding water (Figure 1, ⑤; Wilhelm and Suttle, 1999; Brussaard et al., 2008; Lønborg et al., 2013) and shown to increase the release of dissolved Fe (Gobler et al., 1997). Futhermore, Poorvin et al. (2011) showed that viral lysis of marine bacterium contributed to the ligand pool, and the Fe in these viral lysates seemed well bioavailable (Mioni et al., 2005; Poorvin et al., 2011). What is nevertheless still unknown is to what extent phytoplankton lysis specifically contributes to the ligand pool. Similarly unknown is the fate of Fe-binding organic ligands.

Heterotrophic bacteria subsequently modify the organic fraction through remineralisation of DOM and organic particulates to inorganic nutrients that may then be used again by phytoplankton (③ and ④). Heterotrophic bacteria are also known to excrete substances with the express purpose to bind Fe, the siderophores, discussed in more detail in the next section.

Furthermore, particulate organic matter (POM) is transferred to next trophic levels through feeding (⑥). Sloppy feeding by predators (Sarthou et al., 2008), production of fecal pellets (Laglera et al., 2017) and death tie higher trophic levels back to the particulate pool (⑦). Aggregation of particles exports POM down to the deeper seafloor (⑧). Alternatively, scavenging is a possible loss

factor for DOM, and by extension Fe-binding organic ligands, since dissolved substances are found to associate with aggregates and sinking particles.

The DOM in the oceans is formed largely in the biologically active upper ocean, the euphotic zone. DOM may also originate from terrestrial sources, entering the ocean via run-off and riverine input (Coble, 2007), although the majority of DOM flocculates and sinks out before reaching the open oceans (Sholkovitz, 1976). A group of Fe-binding organic ligands with a terrestrial origin that can contribute to the ligand pool the open ocean are the humic substances (HS). While local DOM production is greatest in areas where phytoplankton accumulates exponentially (Carlson, 2002), i.e. phytoplankton blooms, top-down growth control by grazing, viral lysis or sedimentation of algal cells may preclude bloom formation. However, in those cases DOM formation through excretion, fecal pellet production and cell death will still occur. Specific growth-limiting conditions such as trace-metal or light limitation are expected to affect ligand production and composition. For instance, siderophores have long been found to be excreted in higher concentrations in response to Fe-limitation (Wilhelm et al., 1998).

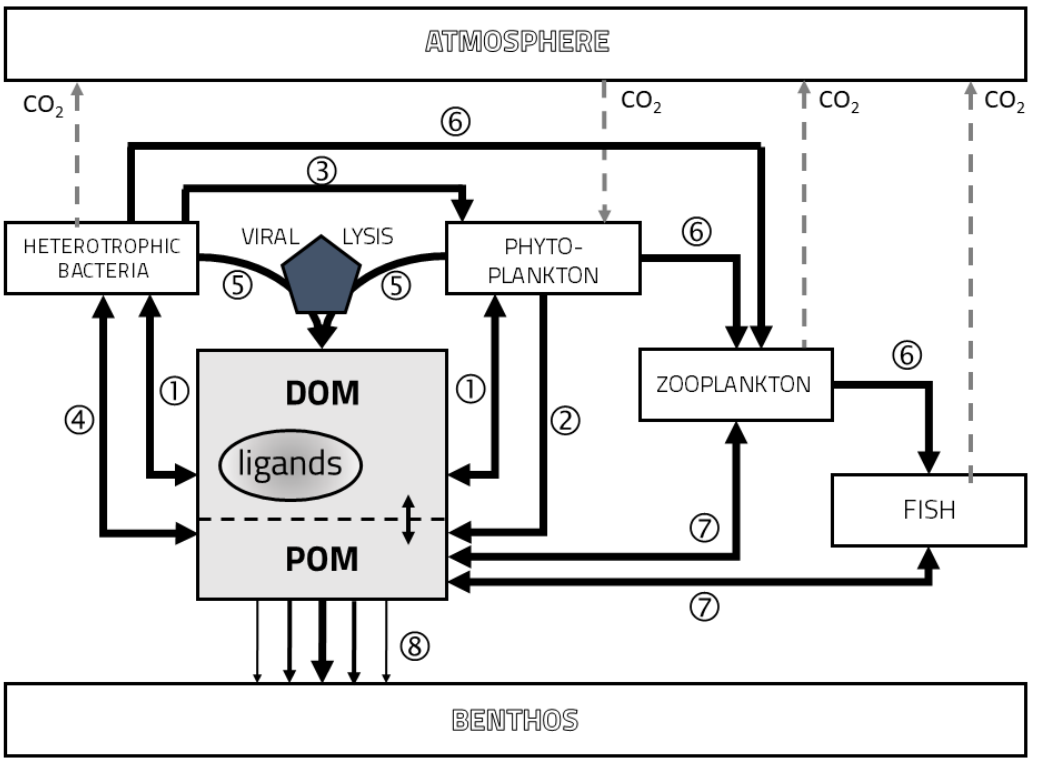

Figure 1 Roles of different trophic levels, dissolved and particle pools and interactions in the open ocean, relevant to the diverse origins and possible loss factors for Fe-binding organic ligands ("ligands" in the figure). At the centre of the diagram the pools of Dissolved Organic Matter (DOM), of which Fe-binding organic ligands are part, and Particulate Organic Matter (POM). Arrows indicate processes and their direction of influence discussed in this section (① to ⑧).

1.2. Fe-binding organic ligands

Organic ligands, i.e. the substances capable of binding the poorly soluble Fe, form a dissolved complex. The binding of Fe by ligands into an Fe-ligand complex is assumed reversible (equation 3). This by extension means that the different types of ligands form a somewhat undefined pool of binding sites that compete for Fe.

$$FeL \leftrightarrow Fe' + L' \tag{3}$$

$$K' = \frac{[FeL]}{[Fe']+[L']} \tag{4}$$

$$[L_t] = [FeL] + [L'] \tag{5}$$

From the above equations, it becomes clear that the Fe-ligand complex (FeL) is made up from free Fe (i.e. the sum of Fe and inorganically bound Fe, denoted Fe') and free organic ligands (L'). To emphasise the additional capacity to keep Fe in solution L' is henceforth described as excess organic ligands.

The conditional stability constant K' is inferred from the mass balance in equation 3 as shown in equation 4. The stability constant indicates the strength of the Fe-ligand association. It is called conditional because it is given strictly for seawater conditions, here denoted with the apostrophe. The K' value is henceforth represented by its base-10 logarithm, for the Fe-ligand complex (FeL) and with respect to Fe' (with the exception of chapter 3, where before newer insights K' was still reported with respect to Fe^{3+}), denoted $\log K'_{Fe'L}$. This value in essence represents the average binding strength of a suite of organic Fe-ligand complexes, and typical ranges may be attributed to different ligand groups or types as discussed in the next paragraph. The total ligand concentration, denoted $[L_t]$, is the sum of Fe-ligand complexes and the excess organic ligand concentrations as equation 5 states (Gledhill and van den Berg, 1994; Gerringa et al., 2007, 2014).

Fe-binding organic ligands differ in origin, occurrence and binding strength (Gledhill and Buck, 2012; Hassler et al., 2017), but their relative contribution to the ligand pool as a whole is poorly understood. The earliest characterized examples are the siderophores, first isolated in soils by Francis et al. (1949).

These are molecules purpose-produced by bacteria (Figure 2, ①) to keep Fe in the local environment in a dissolved state. Siderophores were subsequently found to play a role as an Fe carrier in marine bacteria as well (Wilhelm et al., 1998; Butler, 2005; Hopkinson et al., 2009).

Microbial processes are another important influence on the ligand pool. As described in the prior section for DOM in general, infection of phytoplankton and bacteria by lytic viruses ultimately releases the cells' cytosol into the surrounding seawater (Figure 2, ②). Additionally, heterotrophic bacteria take up and metabolize DOM and POM (Figure 1) and therefore will influence the make-up of the ligand pool through local breakdown processes, potentially removing ligands through remineralisation. EPS contribute to the ligand pool although it is still unknown to what extent (Hassler et al., 2011a, 2011b; Figure 2, ③). Humic substances (HS) are hydrophobic breakdown products with a terrestrial origin. HS are also known to contribute to the ligand pool, possibly to a large extent (Laglera et al., 2011; Figure 2, ④). HS are operationally defined by how they bind to hydrophobic resins (Buffle, 1990; Bronk, 2002). Substances structurally similar to HS but produced locally are often called humic-like substances. The local production in the water column of humic-like substances by phytoplankton and bacteria also add to the ligand pool (Norman et al., 2015; Hassler et al., 2017).

What is nonetheless unidentified about the types of Fe-binding organic ligands here discussed is their relative contribution to the ligand pool. Typical measurements of Fe-binding organic ligands are a 'black box' approach, meaning the different types of Fe-binding organic ligands in a natural sample can only be described as a combined group. This inherent non-specifity of measurements makes it very difficult to explain the role played by different substances and processes. The only means currently available to separate substances and processes is by 1) analysis via multiple methods or varying implementations which reflect separate substances differently, and 2) experimentally separating different contributing processes. My thesis embraced both approaches, while focusing on the different sources of organic ligands and their ecological impact.

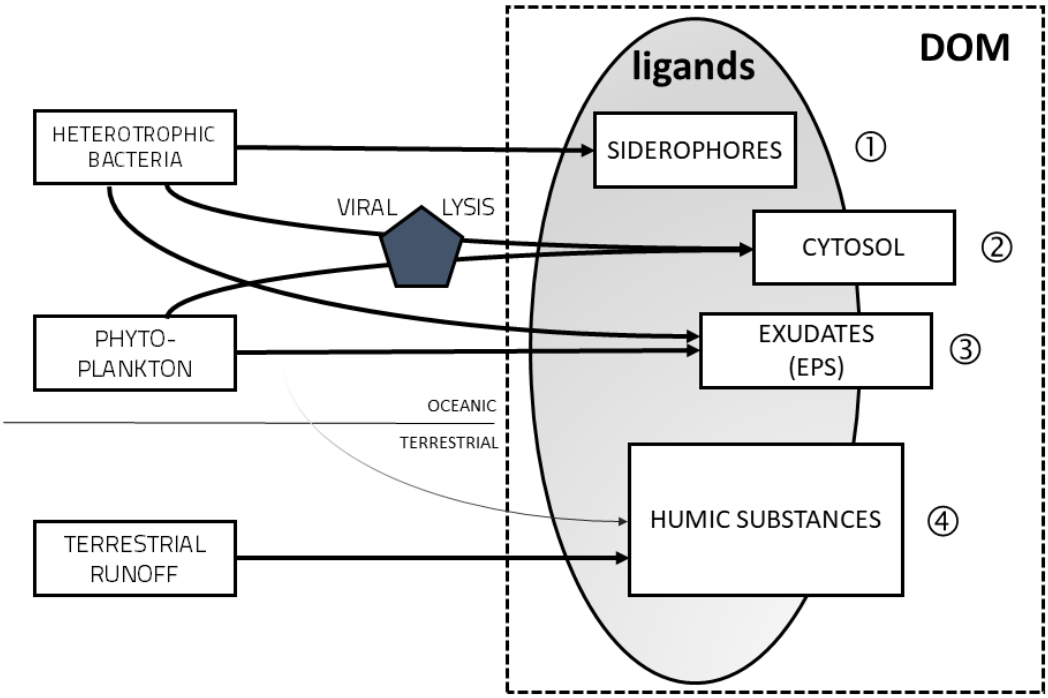

Figure 2 Different contributors to the Fe-binding organic ligand pool (referred to as ① to ④ in text) and their origins. Note the "DOM" and "ligands" sections which are also represented in Figure 1.

1.3. Thesis contents

With Fe being an essential trace nutrient for the basis of marine food webs, and its retention in seawater wholly dependent on Fe-binding organic ligands, the composition and cycling of the latter are essential to our understanding of ocean biogeochemistry. Thus far, most studies of Fe-binding organic ligands have been a 'black box' approach, with descriptors such as $[L_t]$ and $\log K'_{Fe'L}$ describing the ligand pool in its entirety, or in groups with similar binding strength. While Fe-binding organic ligands have been a long-studied subject, with total ligand concentrations and binding strengths reported for many marine regions and ecosystems, very little is known about relative contributors to the Fe-binding organic ligand pool (Gledhill and Buck, 2012; Hassler et al., 2017). The expectation is that different processes have a relative contribution to Fe speciation in the open ocean, mirroring the diversity in origins of DOM. However, what that relative contribution is, is currently unknown. Furthermore, modification of the Fe-binding organic ligand pool, e.g. loss factors, will also be an important factor in its composition. Again, these are part processes that remain veiled by study of the natural Fe-binding organic ligand pool as a whole.

This dissertation aims to generate more insight in the sources and sinks of Fe-binding organic ligands, and to that end has two objectives.

1 Identify different sources of Fe-binding organic ligands by *in-situ* study through correlations with descriptors of possible contributors and their relative importance to the Fe-binding organic ligand pool.
2 Narrow down the effect of specific microbial processes via experiments in culture in order to characterize their effect on the Fe-binding organic ligand pool, and to identify possible loss factors.

The methods most commonly used in this study are detailed in Chapter 2, explaining sampling and materials handling in trace metal clean conditions, culturing details and an overview of the electrochemical determination of Fe-binding organic ligands.

The numerous sources of Fe in the Mediterranean Sea (Gerringa et al., 2017) serve as an example for the diversity of Fe sources and complexation by ligands in Chapter 3. Here we describe how Fe-binding organic ligands support high dissolved Fe (DFe) concentrations in the surface from dust input, as well as deep patches of high DFe correlating with the occurrence of mud-volcanoes.

The relation between DFe and major nutrients under natural conditions in the Arctic Ocean is presented in Chapter 4. Under strong pressure of climate change, the Arctic Ocean is subject to rapid changes. Receding sea ice extent leads to increased light exposure and potentially increased net primary productivity in the surface water (Arrigo et al., 2008; Bhatt et al., 2014). High surface DFe (Klunder et al., 2012a; Slagter et al., 2017) is brought into the Arctic Ocean along the transpolar drift (TPD), a surface stream of sea ice and terrestrially influenced water from the Siberian shelf seas out to the north Atlantic Ocean (Gregor et al., 1998; Rudels, 2008). Even though DFe is assumed present in sufficient supply, we here show that Fe will be the next limiting factor in large parts of the Arctic Ocean when light stress is alleviated by sea ice melt.

The relatively high surface DFe indicated in Chapter 4 must be bound to Fe-binding organic ligands. The distribution of natural Fe-binding organic ligands in the Arctic Ocean is studied in detail in Chapter 5 (Slagter et al., 2017). Here the specific DOM signatures related to Fe-binding organic ligands found inside and outside of the TPD are studied. With the TPD carrying DOM with a terrestrial origin, we specifically explore the role of humic substances in the TPD's Fe-binding organic ligand pool. We illustrate the borders of the TPD flow path using multiple properties of DOM along two transects crossing the TPD.

Following this, Chapter 6 discusses specific ligands and their fate (Slagter et al., *in review*). A selection of the Arctic Ocean data from Chapter 5 was analysed

specifically for the role of humic substances, using a different application of our method of ligand analysis in comparison to the prior analyses. This approach reflects the natural Fe-binding ligands pool differently, with a stronger reflection of HS. We hope to clarify characterisation of Fe-binding organic ligands through the variations here observed in ligand properties such as L_t and $\log K'_{Fe'L}$.

Chapters 7 and 8 relate to the role of viral lysis in the formation and composition of ligands. Chapter 7 first establishes under controlled laboratory settings how Fe-limitation affects the interactions of virus and algal host (i.e., *Phaeocystis globosa* and *Micromonas pusilla*; Slagter et al., 2016). The time until the first progeny viruses are released from the algal host (latent period), the number of newly produced viruses per lysed host cell (virus burst size) and the degree of infectivity of these newly produced viruses are determined and compared to those under Fe-replete conditions. Since viral lysis may be a potential source of ligands and thus release Fe-stress, also the effect of partial alleviation of the Fe-stress on virus production was studied.

Chapter 8 gives an overview of ligand properties found in virally infected phytoplankton cultures as compared to non-infected controls (Slagter et al., *in prep*.). Special attention here is given to specific siderophores and hitherto uncharacterised siderophore-like substances, particularly upon aging of the non-infected and virally lysed cultures (to allow breakdown processes to run their course).

Finally, the thesis results and their scientific impact are summarized and discussed in Chapter 9, including a forward looking synthesis.

Chapter 2
Methods

This chapter details methods that are common to multiple chapters of this dissertation, and is modified from the peer-reviewed method sections of those chapters that have been published.

2.1. Material cleaning

Chemical preparation and bottle cleaning took place in an ISO class 7 ultra-clean (UC) laboratory environment (Interflow) with ISO class 5 workspaces. Culture handling and sampling were carried out in a 15°C climate chamber within the UC laboratory. When outside the UC environment, sample handling took place inside laminar flow hoods (ISO class 5, Interflow and AirClean systems). All material rinsing and chemical preparation was performed using ultrapure water (18.2 MΩcm, Milli-Q Element, Merck Millipore), further referred to as MQ. A Teflon® sub-boiling distillation apparatus (Savillex) was used to purify nitric acid (HNO_3) in triplicate, yielding Fe-free three-times distilled (3×D) HNO_3. A 0.3 M 3×D-HNO_3 solution was used to fill stored bottles for most purposes. A 2‰ v/v addition of ~10 M HCl (Suprapur, VWR) was used for FeL sample bottles. Labware was handled according to GEOTRACES protocols (Cuttler et al., 2010). Prior to use, general labware of high- and low-density polyethylene (HDPE and LDPE, respectively) and fluorinated ethylene propylene (FEP) was cleaned by pre-rinsing (5x) with MQ, followed by soaking in 6 M hydrochloric acid (HCl, Normapur, VWR) for a minimum of 24 h, and a final thorough (5x) MQ rinsing.Polycarbonate (PC) culture flasks (50-500 mL, VWR) and bottles (1-2 L, Nalgene) were acid cleaned with 1 M HCl (Normapur, VWR) for a minimum of 24 h, after which they were rinsed with MQ (5x). Finally, bottles were sterilized with a 10% volume of boiling MQ, i.e. the bottle with MQ was microwaved at 900 W to boiling point and left boiling for ~20 s. After vigorous shaking the hot MQ was poured out over the inverted lid. Culture vessels were then left to air-dry in a laminar flow bench for at least 2 h.

Nutrient and buffer stock solutions were cleaned by equilibration with a manganese dioxide (MnO_2) suspension and subsequent filtration after van den Berg and Kramer (1979). In short, the MnO_2 suspension was prepared by combining a 0.03 M $MnCl_2$ solution and a 0.02 M $KMnO_4$ solution, subsequent centrifugation in 50 mL tubes (VWR) at ~4000 rpm for 5 minutes using an Eppendorf 5810R centrifuge. The precipitate was resuspended in MQ and the centrifugation process was performed 3 times. Cleaning of solutions was performed twice, using a 100 µM final concentration of MnO_2 left to equilibrate in motion for ~8 hours to overnight and finally removed using 0.2 µm polycarbonate filters (Whatman, cleaned in 0.5 - 1 M HCl) in a polysulfone filter tower (Nalgene, also 1 M HCl cleaned; van den Berg, 2006).

2.2 Oceanic sampling

Samples were collected with a special ultra-clean sampling system (UCC) (Rijkenberg et al., 2015). Samples for the determination of dissolved Fe (DFe),

dissolved Fe-binding organic ligand characteristics [L_t] and log$K'_{Fe'L}$, and CDOM and HS measurements were collected through a 0.2 μm filter cartridge (Sartoban P, Sartorius) by nitrogen pressurisation (~2 bar) of the sampling bottles. All samples were taken in an ISO class 7 cleanroom environment which the UCC enters moments after arrival on deck (Rijkenberg et al., 2015).

2.3 Culturing

2.3.1. Strain information and conditions

Axenic phytoplankton cultures of the nano-eukaryotic Prymnesiophyte *Phaeocystis globosa* G(A) (culture collection of the University of Groningen, the Netherlands) and the pico-eukaryotic Prasinophyte *Micromonas pusilla* LAC38 (Marine Research Center culture collection, Göteborg University, Sweden) were maintained under trace metal clean conditions. Culture temperature was 15°C and irradiance was supplied at 90 μmol quanta m^{-2} s^{-1} under a 16:8 h light:dark cycle. Cultures were maintained semi-continuously to obtain and sustain constant and comparable physiology and growth, i.e. diluting the culture daily with new medium whereby the exact volume was determined by the maximum growth rate possible under Fe-limiting culture conditions without wash-out (Maat et al. 2014). The limiting Fe concentration determined the maximum cell abundance, which was measured before and after dilution using flow cytometry (Marie et al. 1999). Axenic viral lysate of the double-stranded DNA viruses PgV-07T (Baudoux and Brussaard 2005) infecting the host *P. globosa* G(A) and MpV-08T (Martínez Martínez et al., 2014) infecting the host *M. pusilla* LAC38 were used. Viral lysates were obtained by 10% v/v inoculation to exponentially growing phytoplankton host cultures and checked for full lysis by flow cytometry (FCM). Fe-limited viral lysates of both phytoplankton hosts were initiated by 1% v/v inoculations with Fe-replete lysates, after which a minimum of 5 subsequent 10% v/v inoculations followed before use for the experiment. This way the Fe concentration in the Fe-limited lysate was similar to the Fe concentration in the Fe-limited host culture.

2.3.2. Low-trace metal culture medium

A low Fe-containing medium (Low Trace: LT) based on natural seawater (DFe 0.2 nM, collected west of the Bay of Biscay in the Atlantic Ocean after Rijkenberg et al. 2012) was designed without metal chelators such as EDTA. Chelators as EDTA are used as metal buffers in culture media, and are added in μM to mM concentrations to ascertain that those transition metals added as micronutrients, e.g. Cu, Co, Fe, Mn, Mo, Ni, V, Zn, are kept in the dissolved phase through complexation by EDTA (Sunda and Huntsman 1995). However, these high concentrations of artificial ligands completely overrule the natural

chemistry of the metals, making the study of natural Fe binding organic ligands impossible (Gerringa et al., 2000). Therefore, an alternative medium needed to be designed. The medium was enriched with the macronutrients $NaNO_3$ (Sigma-Aldrich) and Na_2HPO_4 (Merck Millipore) to final concentrations of 128 and 8 µM, respectively. The following micronutrients were added: KBr, NaF, $CaCl_2 \cdot 2H_2O$, , $SrCl_2 \cdot 6H_2O$, $MgCl_2 \cdot 6H_2O$ and Na_2SeO_3; vitamins H, B1 and B12 and a combined Tris(hydroxymethyl)aminomethane and HCl buffer (Tris-HCl). Final concentrations are detailed in table 1. To maintain constant growth for multiple generations additional trace metals proved essential. These trace metal additions were kept to a minimum in order to avoid influencing Fe speciation, e.g. interactions between Cu and Fe (González et al. 2016). *P. globosa* received an additional trace solution containing final concentrations of 2.0 nM $ZnSO_4 \cdot 7H_2O$, 1.0 nM $CoCl_2 \cdot 6H_2O$, 4.6 nM $MnCl_2 \cdot 4H_2O$, and 0.6 nM $Na_2MoO_4 \cdot 2H_2O$. *M. pusilla* showed poor physiological condition and growth using this trace solution. Because it was impossible to maintain a steady state under these conditions, a slightly different trace solution was used, containing more comprehensive trace additions ($ZnSO_4 \cdot 7H_2O$, $CoCl_2 \cdot 6H_2O$, $CuSO_4 \cdot 5H_2O$, $NiSO_4 \cdot 6H_2O$, Na_3VO_4, K_2CrO_4, $MnCl_2 \cdot 4H_2O$, $Na_2MoO_4 \cdot 2H_2O$, and H_2SeO_3, concentrations detailed in Table 1). Fe was added from an acidified 3 µM FeCl stock solution made using a 1000 mg L^{-1} ICP stock (Fluka, Sigma-Aldrich). The Fe-limiting medium contained final concentrations of 1.0 and 3.0 nM Fe for *P. globosa* and *M. pusilla*, respectively (Chapter 7). The Fe-replete (control) medium (Chapter 7) contained 9.0 µM FeCl for both species. After the chapter 7 study, the LT medium was standardized after the modifications for *M. pusilla* (Table 1).

2.3.3. Enumeration of phytoplankton, bacteria and viruses

Phytoplankton cells in fresh samples were discriminated and counted based on Chlorophyll-a red autofluorescence using a FACSCanto flow cytometer (Becton Dickinson) equipped with a 17 mW 633 nm HeNe red laser. Viral abundances were also determined by flow cytometry using a FACSCalibur flow cytometer (Becton Dickinson) equipped with a 15 mW 488 nm argon-ion blue laser triggered on green fluorescence, following the protocol by Brussaard et al. (2010). In short, samples were diluted 200-1000-fold using a 2 M Tris-HCl buffer at pH 8 and viruses were stained using the nucleic acid-specific fluorescent dye SYBR Green I (Molecular Probes®, Life Technologies, Thermo Fisher). Raw data were analysed using Cytowin (Vaulot, 1989; Version 4.31 available at http://application.sb-roscoff.fr/Phyto/index.php), whereby PgV and MpV were easily discriminated by plotting green nucleic acid-specific fluorescence versus side scatter (A. C. Baudoux and Brussaard, 2005; Martínez Martínez et al., 2015).

Table 1 Low Trace (LT) medium constituents added to low-DFe natural seawater. See also MaCuMBA public deliverable D3.1 (www.macumbaproject.eu). All concentrations in M.

Major nutrients		**Trace nutrients**	
$NaNO_3$	1.28×10^{-4}	$FeCl_3 \cdot 6H_2O$	3.00×10^{-9}
$Na_2HPO_4 \cdot 12H_2O$	8.00×10^{-6}	H_2SeO_3	1.00×10^{-9}
H_3BO_3	3.75×10^{-6}	$CuSO_4 \cdot 5H_2O$	1.00×10^{-9}
Micronutrients		$ZnSO_4 \cdot 7H_2O$	4.00×10^{-9}
KBr	7.10×10^{-6}	$NiSO_4 \cdot 7H_2O$	1.00×10^{-9}
NaF	3.00×10^{-6}	Na_3VO_4	1.00×10^{-9}
$CaCl_2 \cdot 2H_2O$	1.79×10^{-6}	K_2CrO_4	1.00×10^{-9}
$SrCl_2 \cdot 6H_2O$	8.00×10^{-7}	$CoCl_2 \cdot 6H_2O$	5.00×10^{-9}
$MgCl_2 \cdot 6H_2O$	2.31×10^{-6}	$MnCl_2 \cdot 4H_2O$	9.00×10^{-9}
Na_2SeO_3	1.00×10^{-8}	$Na_2MoO_4 \cdot 2H_2O$	4.00×10^{-9}
Vitamins		**Buffer**	
Biotin (H)	2.03×10^{-9}	Tris-HCL	2.50×10^{-3}
Thiamin-HCL	2.96×10^{-7}		
Cyanobalamin (B12)	3.70×10^{-10}		

2.3.4. Photosynthetic capacity

Photosynthetic capacity (F_v/F_m) measurements were performed using a Chlorophyll Fluorometer with a red emitter-detector unit (Water-PAM, Waltz). Samples were kept in the dark for 30 minutes at culturing temperature, after which chlorophyll autofluorescence was measured in duplicate in the dark adapted state (F_0) and after a saturation pulse of 2.5 s (F_m). F_v is defined as the difference between F_m and F_0 (Genty et al. 1989).

2.4. Analyses related to Fe-binding organic ligands

2.4.1. Determination of DFe concentrations

Samples for DFe were collected from the Fe-binding organic ligand sample bottles at the time of voltammetric analysis and acidified with 2‰ v/v 12 M trace metal grade HCl (Seastar Chemicals). If immediate measurement of Fe-binding organic ligands was not possible the sample bottles were stored at -20

°C samples for DFe were taken at the moment of analysis after thawing. DFe concentrations (expressed in nM) were then measured using an automated Flow Injection Analysis system the same day (Klunder et al., 2011). The sample was transferred onto an iminodiacetic acid (IDA) column, binding only transition metals and serving to concentrate and desalt the retentate. The column was subsequently washed with MQ and eluted with HCl (0.4 M, Merck Suprapur). Luminol (0.6 mM, Aldrich), hydrogen peroxide (0.6 M, Merck Suprapur) and dilute ammonia (0.96 M, Merck Suprapur) are then mixed in. Fe catalyses the oxidation of luminol by hydrogen peroxide, producing blue light in correlation to the amount of catalyst present (Obata et al., 1993). The response of a photon counter is calibrated with a series of Fe standard additions (ICP standard, Fluka, Sigma-Aldrich). Samples are analysed in triplicate and reported with a standard deviation of the mean (SD). Quality control for the system was maintained by daily measurement of lab standards and regular measurement of certified reference material (Rijkenberg, Chapter 4).

2.4.2. Voltammetric determination of Fe-binding organic ligands

Total Fe-binding organic ligand concentration [L_t] and the conditional stability constant (K´) were measured with Competitive Ligand Exchange – Adsorptive Cathodic Stripping Voltammetry (CLE-AdCSV). Given that the diverse pool of organic Fe-binding organic ligands cannot be measured directly, a known ligand – the competitive ligand or added ligand (AL) – is added to the sample. As described in chapter 1, formation of Fe-ligand complexes is reversible. The diverse Fe-binding organic ligands making up the ligand pool in a sample are in competition with each other for Fe, resulting in an equilibrium over time. Therefore, the added ligand and the natural ligands in the sample need to be allowed to establish an equilibrium (Figure 1A). The sample is titrated with increasing additions of Fe. After a period of equilibration, an AdCSV scan is performed for each of these additions. During a voltammetric scan the surface active Fe-AL complex is initially deposited on a mercury (Hg) drop electrode at a (near) zero potential. This is followed by a quick potential sweep, during which the complex dissociates, which causes a current peak in nA which is representative of the amount of Fe-AL (Figure 1A, B). A titration curve resulting from these Fe additions typically changes in character after a number of additions. Initially the peak size in nA shows little to no increase with higher Fe additions. In this circumstance, the natural ligands in the sample and the AL compete for Fe. As the AL is added in excess, the titration curve changes direction once the natural ligands in the sample are saturated with Fe (Figure 1A, C).

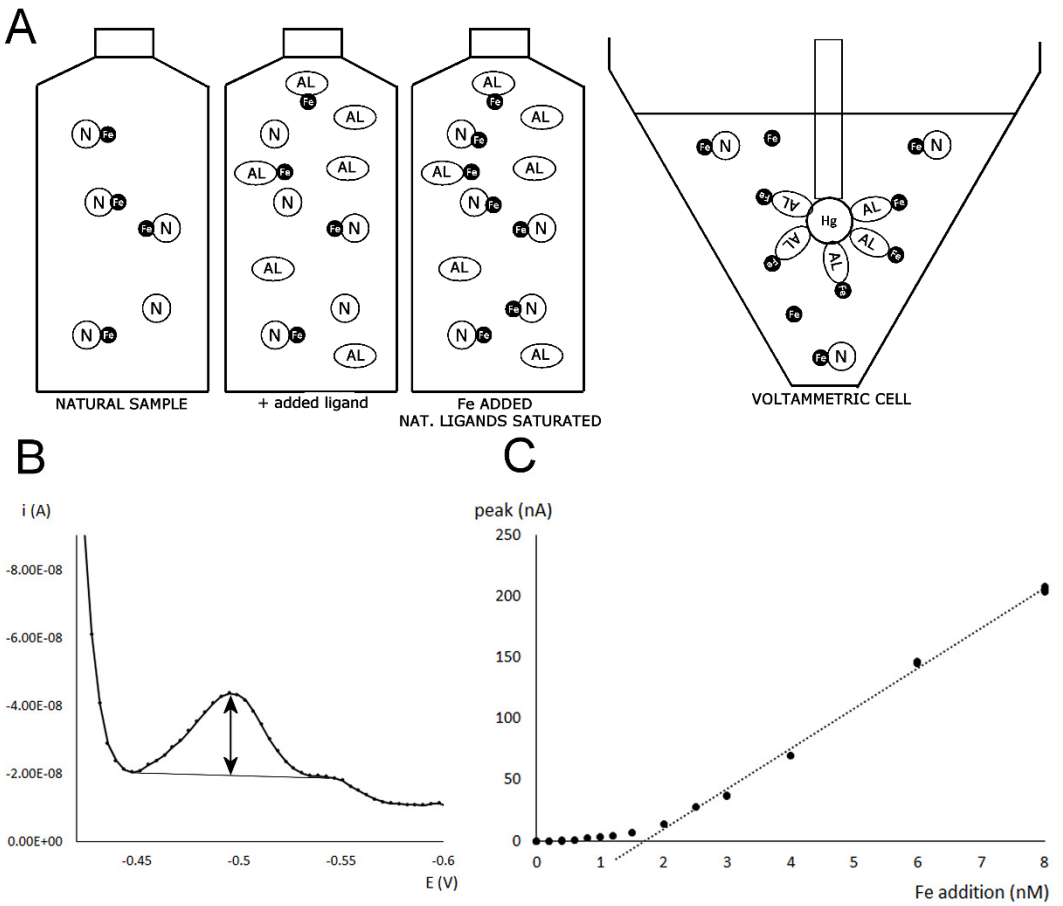

Figure 1 A) Cartoon representing Competitive Ligand Exchange Adsorptive Cathodic Stripping Voltammetry, showing 3 different stages in a titration with Fe and the principle of measurement (voltammetric cell); B) Voltammogram showing current I (A, vertical axis) vs. potential E (V, horizontal axis), in this case showing a current peak for $FeTAC_2$ at a higher Fe addition; and C) Titration plot showing current peaks of the FeAL complex, in this case for FeSA (nA, vertical axis) with increasing Fe concentration (nM, horizontal axis). The intercept of the linearization of the saturated phase with the horizontal axis gives a rough indication of natural ligand concentration.

In this dissertation two CLE-AdCSV methods are employed. One using 2-(2-Thiazolylazo)-p-cresol (TAC) after Croot and Johansson (2000), and the method using salicylaldoxime (SA; Rue and Bruland, 1995; Buck et al., 2015). For the TAC method a natural sample was left to equilibrate with the AL in the presence of a mixed boric acid - ammonia buffer (1 M, pH 8.05, Merck) and increasing standard additions of Fe(III). 30 mL PTFE cups (Savillex) were used to equilibrate 10 mL subsamples from a mix of natural sample, buffer (5 mM final concentration) and TAC (10 µM final concentration) with discrete Fe(III) additions of 0 (twice), 0.2, 0.4, 0.6, 0.8, 1.0, 1.2, 1.5, 2.0, 2.5, 3.0, 4.2, 6.0 and 8.1 (twice) nM. Equilibration lasted a minimum of 8 hours to overnight. The

resulting titration with Fe was analysed for $Fe(TAC)_2$ concentration using differential pulse voltammetry. TAC (Alfa Aesar) was dissolved in 3xD-methanol to a stock concentration of 0.02 M, Fe standards (1 and $3 \cdot 10^{-6}$ M) were prepared in MQ from a 1000 ppm ICP stock solution (Fluka) and acidified using 2xD-HNO_3. The voltammetric apparatus consisted of a 663 VA stand (Metrohm) equipped with a Hg drop multimode electrode with silanized capillary, double-junction Ag/AgCl reference electrode (KCl 3M) and glassy carbon auxiliary electrode in a polytetrafluoroethylene (PTFE) cell (all Metrohm), control hardware (μAutolab III, Metrohm Autolab B.V.) and a consumer laptop PC running Nova 1.9 (Metrohm Autolab B.V.). N_2 was used for purging and Hg drop formation. When measurements were performed at sea, interference from ship motion and vibration was minimized by suspending the VA stand in elastic bands. Any electrical interference was minimized using a consumer inline peak filter and an uninterruptible power supply with sinewave converter (Fortress 750, Best Power). Analysis was performed using a slightly altered version of the measurement procedure used by Croot and Johansson (2000): Purging for 180 seconds, no conditioning, deposition for 140 seconds at -0.4 V, a 5-second equilibration followed by a differential pulse scan from -0.4 to -0.9 V. The influence of high frequency vibrations from the ship's drivetrain was minimized by an increased scan rate of 39 mV s^{-1} (0.05 s interval and 0.004 s modulation time).

Our application of the CLE-AdCSV method using SA by Rue and Bruland (1995) and Buck et al. (2007) was modified from Abualhaija and van den Berg (2014), using the same equipment as the TAC method with the following modifications. SA was added from a stock prepared in 3xD-methanol in a final concentration of 25 μM (Abualhaija and van den Berg, 2014; Abualhaija et al., 2015). SA was added 15 minutes prior to a first analysis scan as done by Buck et al.(2007), after a minimum 1 h equilibration of the sample with buffer and discrete Fe additions in the same concentrations as above. The borate buffer for SA analyses was adjusted to a pH of 8.4 for better peak separation. The voltammetric apparatus was modified to purge with synthetic air as done by Abualhaija and van den Berg (2014) and Abualhaija et al. (2015), while still using nitrogen pressure for mercury drop formation. Analysis settings were deposition at 0 V for 240 s, followed by a differential pulse sweep from 0 to -0.7 V with a modulation time of 4 ms, an interval time of 100 ms, a step potential of 6 mV and 50 mV modulation amplitude, resulting in a 60 mV s^{-1} scan rate.

Titrations were analysed for natural ligand concentration and binding strength by a non-linear fit of the Langmuir model after Gerringa et al. (2014) using R (R Development Core Team, 2008). The conditional binding strength of the added ligand (AL) is given by the K'_{FeAL}, or $\beta'_{Fe(AL)2}$ in the case of bidentate

association. The detection window (D) is then given by the product of K'_{AL} and the free AL concentration, hence given as $D_{AL} = K'_{AL}[AL']$ in case of a single AL associating with Fe. When a the AL binds Fe in a pair D is given as $D_{AL} = \beta'_{AL}[AL']^2$. If both associations occur, $D_{AL} = (K'_{AL}[AL']) + (\beta'_{AL}[AL']^2)$. Given that AL is added in excess to the point where [AL'] does not significantly change due to formation of FeAL, [AL'] may be represented by the total [AL]. As mentioned with the definition of $\log K'_{Fe'L}$ in chapter 1, all conditional binding strengths are reported in relation to Fe'. Inorganic Fe [Fe´] is defined as the product of $[Fe^{3+}]$ and the inorganic side reaction coefficient (α_i), which depends on analysis pH as the inorganic side reactions are hydroxide complexations. For analyses at the seawater pH of 8.05, i.e. the TAC method, a value of 10^{10} was used after Liu and Millero (2002). However, as the pH for SA measurements was adjusted to 8.4, α_i needed to be recalculated. The inorganic side reaction coefficient assuming formation of FeOH and $Fe(OH)_2$ is given by equation 1:

$$\alpha_i = K_{FeOH} \times \frac{1}{[H^+]} + K_{Fe(OH)_2} \times \frac{1}{[H^+]^2} + 1 \quad (1)$$

Using $K_{FeOH} = 10^{-2.62}$ and $K_{Fe(OH)2} = 10^{-6}$ after Millero (1998), $\log\alpha_i$ for pH = 8.4 is 10.8. In chapter 3, and where the contrasting K'_{FeL} in relation for Fe^{+3} is relevant values are reported as $\log K'_{FeL,Fe3+}$ as opposed to $\log K'_{Fe'L}$. For the Langmuir fit of the TAC data a $\log\beta_{Fe'(TAC)2}$ of 12.4 was used after Croot and Johansson (2000). D is given by $D_{TAC} = \beta_{TAC}[TAC]^2 = 251.19$. For the Langmuir fit of the SA data a $\log\beta'_{Fe(SA)2}$ of 10.72 and $\log K'_{FeSA}$ of 6.52 were used, with the detection window given by $D_{SA} = (K'_{FeSA}[SA]) + (\beta'_{Fe(SA)2}[SA]^2) = 115.58$ (Abualhaija and van den Berg, 2014). As only FeSA is electroactive, this is the measured property. $FeSA_2$ is taken into account in the calculation of Fe' as $\beta'_{Fe'(SA)2}$ is part of the Langmuir fit from which $K'_{Fe'L}$ is determined. Where it was possible to resolve 2 ligand classes, the strongest class was L_1 and the weaker class designated as L_2 (Gledhill and Buck, 2012).

$[Fe^{3+}]$, [Fe'] and [L´] were determined from DFe, $[L_t]$ and K' by iterative calculations of the Fe speciation equilibrium with Newton's algorithm (Press et al., 2007), using an R implementation of the method described by Gerringa et al. (2014). In short, the following sequence is repeated 20 times:

$$x = x + \frac{1-f(x)}{f\prime(x)} \quad (2)$$

$$f(x) = \alpha_i \cdot x + \frac{K\prime\cdot[L_t]\cdot x}{1+x\cdot K'\cdot DFe} \quad (3)$$

$$f'(x) = \alpha_i + \frac{K\prime\cdot[L_t]}{1+x\cdot(K\prime\cdot DFe)} - \left(\frac{x\cdot(K\prime\cdot DFe)\cdot(K\prime\cdot[L_t])}{1+(K\prime\cdot DFe)\cdot x}\right)^2 \quad (4)$$

With initial condition $x = [Fe^{3+}] / DFe$, and the initial approximation of [Fe_{3+}] given by:

$$[Fe^{3+}] = \frac{DFe}{\alpha_i + K' \cdot [L_t]} \quad (5)$$

After the iterative process results are given as:

$$[Fe^{3+}] = x * DFe \quad (6)$$

$$[Fe'] = [Fe^{3+}] \cdot \alpha_i \quad (7)$$

$$[L'] = \frac{[L_t]}{K' \cdot [Fe^{3+}] + 1} \quad (8)$$

[L'] in equation 8 is the free ligand concentration. This represents ligands that do not bind Fe and are therefore typically referred to as excess ligands, indicating binding capacity beyond the DFe that is present. [L´] approaches 0 where [L_t] is insufficient to bind further Fe.

The ratio [L_t]/DFe reflects the surplus of Fe-binding organic ligands. Ratios >1 indicate that there is sufficient binding capacity to explain DFe, whereas a ratio between 0 and 1 would indicate a lack of binding capacity (Thuróczy et al., 2010). The reactivity of the ligands α_{FeL} is the product of K´ and [L´] (Ringbom and Still, 1972; Gledhill and Gerringa, 2017), expressed as the base-10 logarithm with respect to Fe´, further referred to as logα_{FeL}.

2.4.3. Voltammetric determination of humic substances

The concentration of humic substances (HS) was measured using cathodic stripping voltammetry (Laglera et al., 2007; Laglera and van den Berg, 2009). Samples were buffered with the same boric acid-ammonia solution (1 M, pH 8.05, Merck) as used for CLE-AdCSV using TAC, and saturated with Fe(III) by a 30 nM addition from the same $3 \cdot 10^{-6}$ M standard used for Fe additions in CLE-AdCSV. To increase the current signal of the dissociating Fe-humic complex at the electrode, $KBrO_2$ (13 µM final concentration) served as oxidizer. Standard additions of fulvic acid (Suwannee River Fulvic Acid Standard I, International Humic Substances Society (IHSS), St. Paul, USA, further referred to as SRFA) of 0.1 to 0.4 mg L^{-1} were used as a measure of equivalent quantification. Therefore [HS] is expressed in the equivalent mg L^{-1} of fulvic acid (Eq. mg/L FA) and is specific to the standard used (Sukekava et al., 2018). Analysis was performed with the same voltammetric equipment as above. The procedure employed a 180 s purge with N_2 followed by a 90 s deposition period at -0.1 V and a linear current sweep from -0.1 to -1.1 V at a scan rate of 100 mV s^{-1} (0.05 s interval).

2.5. Additional analyses

2.5.1. Spectrophotometric determination of Dissolved Organic Matter

The characterization of CDOM was performed after Stedmon et al. (2000). Absorbance spectra between 250 and 1000 nm, at 1 nm resolution, were recorded in a quartz cell with a 1 cm path length (SUPRASIL®, Hellma Analytics) using a Spectramax M2 multimode spectrophotometer (Molecular Devices). Daily measurements of MQ were used as blanks, the spectra of these were subtracted from the data as a baseline correction. A further baseline correction was performed by subtracting the mean absorbance between 450 and 500 nm in order to correct refractive index differences between seawater and the MQ blanks (H.E. Reader, pers. comm.). Extremely low values of absorbance at longer wavelengths, nearing the limit of detection, dictated the use of the 450 nm – 500nm window for that correction. The absorbance in RFU (A_λ) was converted into absorption coefficients (a_λ, m^{-1}) using path length (l, m) and ln(10) = 2.303, according to Stedmon et al. (2000):

$$a_\lambda = 2.303 \frac{A_\lambda}{l} \quad (9)$$

Spectral slopes for the intervals 275-295 nm (S_{275}) and 350-400 nm (S_{350}) were calculated by linear fitting to the ln(a) spectrum using R. Absorption values were recorded at wavelengths of 254 nm (a_{254}) and 300 nm (a_{300}) as indicators of complex organics (Helms et al., 2008).

The fluorescent fraction of DOM (FDOM) was analysed using UV fluorescence spectrophotometry (Mopper and Schultz, 1993). Emission spectra were recorded between 360 and 540 nm with an interval of 1 nm at an excitation wavelength of 250 nm using the same equipment as above. Emission at 450 nm using this excitation wavelength ($F_{250/450}$) was taken as a measure of humic-like FDOM (Coble et al., 1998; Coble, 2007). Daily measurements of a 1 mg L^{-1} quinine sulphate (QS) standard (Alpha Aesar, dissolved in MQ with 0.1 M H_2SO_4) served as an equivalent reference for expression of FDOM concentrations. FDOM measurements are thus expressed as equivalents of 1 ppb QS emission at 450 nm using 250 nm excitation, referred to as quinine sulphate units (QSU; Mopper and Schultz, 1993).

2.5.2. Nutrient analyses

Nutrient samples were analysed after Murphy and Riley (1962, phosphate), Strickland and Parsons (1972, silicate) and Grasshoff (1983, nitrate) using a TRAACS 800 auto-analyser (Technicon).

Chapter 3

Dissolved Fe and Fe-binding organic ligands in the Mediterranean Sea

Published as:
Gerringa, L.J.A., Slagter, H.A., Bown, J., van Haren, H., Laan, P., de Baar, H.J.W., Rijkenberg, M.J.A., 2017. Dissolved Fe and Fe-binding organic ligands in the Mediterranean Sea - GEOTRACES G04. Mar. Chem. 194, 100–113.

Abstract

Dissolved Fe (DFe) and Fe-binding dissolved organic ligands were analysed during two GEOTRACES cruises in the Mediterranean Sea in May and August 2013. DFe was relatively high near the surface probably due to atmospheric sources, whereas below 500–700m depth the concentrations were relatively low, < 0.4 nM, compared to typical concentrations of 0.6 nM at the same depths in the Atlantic Ocean. These relatively low concentrations are probably due to scavenging and ballasting by dust particles settling down through the water column. Especially in the Eastern Basin, and more prominent in its northern part, distinct patches with high DFe, up to 8.40 nM, were found between 200 and 3000 m depth. These patches were local, which indicates a point source and lateral transport from this source. Some of these patches coincided with sloping density lines indicating enforced along-frontal currents providing lateral transport of DFe. Sources are probably seamounts and mud volcanoes, which were found to exist at the same depths as the elevated DFe. It is conceivable that a large eddy keeps infusions of DFe isolated from mixing with other water masses. These infusions could originate from slopes or from downwards cascading materials out of canyons. Fe-binding dissolved organic ligands increase the solubility of Fe enabling high dissolved Fe concentrations, and hence longer residence time. These ligands had median total concentrations between $[L_t]$ = 0.77 and $[L_t]$ = 1.74 nEq of M Fe and conditional stability constants between $\log K'_{FeL,Fe3+}$ = 21.57 and $\log K'_{FeL,Fe3+}$ = 22.13 (N = 156). Median values of $[L_t]$ were higher in the upper 100m and its median concentration increased from west to east. The $[L_t]$ concentrations did not relate to water mass or DFe concentration. The ligands were nearly saturated with Fe where DFe was elevated near the surface and completely saturated, ratio $[L_t]$/DFe ≤ 1, in patches with high DFe at depth. The high DFe concentrations in these patches are extreme, if not even maximum, concentrations as any surplus Fe with respect to the ligands will tend to precipitate. Calculated inorganic Fe concentrations in the Mediterranean had minimum concentrations of 0.23 pM and below 100m depth median concentrations that varied between 0.68 and 1.99 pM only. This suggests that the inorganic Fe concentration is the result of a steady state between binding by organic ligands and scavenging processes. Thus scavenging will not result in lower inorganic Fe concentrations and in this way the dissolved ligand concentration determines the concentration of DFe in the Mediterranean Sea.

3.1. Introduction

The Mediterranean Sea is surrounded by land and this has a strong influence on the chemical composition of the water and mixing processes therein. It has a surface area of about 2.5 million km^2 and a mean depth of 1500 m, with typical basin depths of 3000 m, while maximum depths exceed 5000 m in its Eastern Basin. In the west, the Mediterranean is connected with the Atlantic Ocean by the Strait of Gibraltar, which is 14.3 km wide and has a sill depth of 280 m. The Western and Eastern Basins are divided by the Sicily Strait, with a sill depth of 316 m. In that region and further into the Eastern Basin, volcanic and hydrothermal activities are abundant. In the east, the Mediterranean is connected with the Black Sea via the Sea of Marmara, (average depth 490 m) and the Channel of the Bosporus (31 km long, 3 km wide, and an average midstream depth of 64 m). These narrow and shallow connections with the Atlantic Ocean and the Black Sea, in combination with high net evaporation, result in the high salinity in the Mediterranean, $38 < S < 39$. The Eastern Basin is warmest and most saline.

Near-surface upper 300 m circulation of relatively fresh Atlantic Water is counter-clockwise (cyclonic) (e.g. Millot, 1999; Millot and Taupier-Letage, 2005). This basin-scale circulation along the continents is unstable, resulting in smaller 100 km diameter spin-off meso-scale eddies. These eddies are mostly found in the southern part of the basins. They are most intense in the upper 200 m with horizontal speeds up to 1 m s^{-1}, but can reach the basin floor where they have horizontal speeds of typically 0.05 m s^{-1}. These eddies can quickly transport dissolved and particulate materials into the deep through vertical speeds of 0.01 m s^{-1}, being approximately 1000 m per day (van Haren et al., 2006). Another even faster vertical transport process occurs in the northern part of the Mediterranean, being one of the few regions outside of the polar oceans where dense water formation occurs (Voorhis and Webb, 1970; Gascard, 1973). Due to cooling and evaporation by continental winds in winter, surface waters can become denser than underlying waters so that they sink by turbulent, natural convective mixing in 0.1–1 km wide 'chimneys'. The chimneys themselves are part of sub-mesoscale eddies (Testor and Gascard, 2003), which further mix newly formed deep dense waters with overlying water masses with the aid of the Earth rotation (van Haren and Millot, 2009). In the Mediterranean, this mainly occurs in the northern part of the Western Basin and in the Adriatic Sea of the Eastern Basin. This process occurs every year reaching depths of several hundreds of meters, but roughly every 8 years it reaches all the way to the bottom. More rarely, every few decades, formation of deep dense water occurs in the Aegean Sea (Roether et al., 2007).

The influence of the surrounding continents on the chemistry of the Mediterranean is relatively large. In this study we focus on dissolved Fe (DFe). Rivers like the Nile and the Rhone are sources of dissolved and particulate matter. It is assumed that the influence of rivers as source of metals like Fe to seas and oceans is modest, since flocculation within the estuarine zone will remove the majority of these metals (Sholkovitz, 1976, 1993; Boyle et al., 1977; Dai et al., 1995; Paucot and Wollast, 1997; Tachikawa et al., 2004). However, lateral transport of DFe is known to reach very large distances of 1000 km or more in the upper 200 m (de Jong et al., 2012; Rijkenberg et al., 2012) and in the deep ocean (Fitzsimmons et al., 2014). Moreover, nepheloid layers originating from shelves can occasionally cascade down canyons and cover the whole bottom of the Western Basin (Puig et al., 2013) and groundwater discharge is important for nutrients in the oligotrophic Mediterranean (Rodellas et al., 2015; Trezzi et al., 2016). In this way, transport of fluvial materials including Fe and organic matter reach much further, here bottom nepheloid layers can generate DFe inputs from below.

Dust from the Sahara is expected to be a major source of DFe from above (Guieu et al., 1991, 1997, 2010a; Spokes and Jickells, 1995; Wagener et al., 2008, 2010) as it is for Al (Rolison et al., 2015). By using Al as crustal marker Bonnet and Guieu (2006) concluded that Saharan dust is the main source for atmospheric input of DFe in the North Western Mediterranean, but according to Heimbürger et al. (2014) dust coming from the north, i.e. Europe, can also be considerable here. Although mostly considered as a source of Fe, dust can act as a sink by scavenging and/or ballasting effects (Wagener et al., 2010). Another major source for DFe might be hydrothermal activity (Lupton et al., 2011; Nomikou et al., 2013). Two volcanic systems exist in the Mediterranean, the submarine Aeolian Arc near Sicily and the Aeolian Islands and the Aegean volcanic arc around the island of Santorini (Lupton et al., 2011; Nomikou et al., 2013).

The chemistry of DFe and notably the organic complexation of DFe is essential to keep Fe that is supplied from internal cycling, as well as from external sources, in solution by enhancing its solubility and hence increasing its residence time. The concentrations of these ligands are determining how far DFe can be transported from its fluvial (Powell and Wilson-Finelli, 2003a; Buck et al., 2007; Gerringa et al., 2007; Abualhaija et al., 2015; Bundy et al., 2015; Mahmood et al., 2015), hydrothermal (Bennett et al., 2008; Sander and Koschinsky, 2011; Hawkes et al., 2013; Kleint et al., 2016) and atmospheric (Rijkenberg et al., 2008b; Wagener et al., 2008) sources. Although the Fe-binding dissolved organic ligands are important, they are poorly defined and little is known about their sources and sinks (Hopkinson and Barbeau, 2007; Rijkenberg et al.,

2008b; Boyd et al., 2010; Gledhill and Buck, 2012). Iron-binding organic ligands are ubiquitous in the oceans and in general are more saturated with Fe in deeper waters than in surface waters. In surface waters DFe is taken up by phytoplankton, probably ligands are produced by bacteria and possibly phytoplankton, together creating a high excess ligand concentration over DFe (Gobler et al., 1997; Gledhill et al., 2004; Butler, 2005; Buck et al., 2010; Thuróczy et al., 2010; Poorvin et al., 2011; Gledhill and Buck, 2012; King et al., 2012; Bundy et al., 2016). Therefore, a high binding potential exists for Fe released either by mineralisation of organic material or from external Fe sources via lateral or horizontal transport.

There are only a few studies reporting research on Fe-binding dissolved organic ligands in the Mediterranean (van den Berg, 1995; Wagener et al., 2008). Van den Berg (1995) was one of the first to measure the Fe-binding ligands in the Western Mediterranean and concluded that 99% of DFe was organically complexed. He also found that the highest concentrations of Fe-binding organic ligands occurred in and just below the zone of maximum fluorescence, indicating an origin from phytoplankton and/or bacteria. Wagener et al. (2008) investigated the role of dissolved organic ligands in the dissolution of Fe from dust. The dissolution rate was linearly related to the concentration of Fe-binding dissolved organic ligands and to dissolved organic carbon (DOC). It is possible that dust is a source of ligands too (Saydam and Senyuva, 2002; Gerringa et al., 2006) or triggers bacterial growth and the production of ligands (Wagener et al., 2008). In this research, DFe and Fe-binding dissolved organic ligands are studied in the Dutch GEOTRACES Section GA04.

3.2. Methods and equipment

3.2.1. Sampling

GEOTRACES section GA04 in the Mediterranean consisted of two legs both on board the Dutch R/V Pelagia. A southern cruise (S), 64PE370, started 14 May 2013 departing from Lisbon (Portugal) and ended in Istanbul (Turkey) on 05 June 2013. A northern cruise (N), 64PE374, left Istanbul on 25 July 2013 and ended in Lisbon on 11 August 2013. Fig. 1 shows the cruise tracks and sampling stations.

During the southern cruise, 35S stations were sampled for DFe including 10 stations sampled for Fe-binding dissolved organic ligands. Stations 1S–4S were in the Atlantic Ocean, of which station 1S was sampled for Fe-binding dissolved organic ligands. Stations 5S–33S were sampled in the Mediterranean Sea (station 25 was not sampled). Of these stations 5S, 8S, 11S, 15S, 18S, 21S, 24S and 29S were sampled for Fe-binding dissolved organic ligands. Stations

34S–36S were sampled in the Sea of Marmara. Here station 36S was sampled for Fe-binding dis- solved organic ligands. During the northern cruise, stations 1N–19N were sampled for DFe, except for station 16N. Stations 8N, 13N and 17N were sampled for Fe-binding dissolved organic ligands.

The CTD-package consisted of a SeaBird SBE9plus underwater unit, an SBE11plusV2 deck unit, an SBE3plus temperature sensor, an SBE4 conductivity sensor, a Wetlabs C-Star transmissometer (25 cm, deep, red) and an SBE43 dissolved oxygen sensor. The sensors were freshly calibrated by Seabird. In situ calibrations of the CTD-thermometers (type SBE-3) were done with a Seabird reference-thermometer (type SBE35). For the calibration of the conductivity sensor, salinity-samples were tapped on board for analysis back home. Most of the casts were tapped for Winkler titrations in order to calibrate the dissolved oxygen sensor. The Absolute Salinity (SA in g kg^{-1}) and Conservative Temperature (CT in °C) have been computed using the GSW-software of TEOS-10 (IOC, 2010). Density was expressed as sigma-theta, the density anomaly referenced to the surface. Fluorescence was measured as the beam attenuation coefficient at 660 nm using a Chelsea Aquatracka MKIII fluorometer. The fluorometer signal was calibrated against Chlorophyll *a* and is expressed as µg Chl*a* dm^{-3}.

3.2.2. Analysis of the characteristics of Fe-binding organic ligands and DFe

Ultra-clean water sampling was performed as described in Chapter 2. During the southern cruise, samples for Fe-binding organic ligands were stored at −18 °C. Part of these were analysed on board during the northern cruise, remaining samples were analysed at the NIOZ home laboratory. Samples taken during the northern cruise were kept at 4 °C in the dark and analysed on board within two days after sampling. Competing ligand exchange adsorptive cathodic stripping voltammetry (CLE-adCSV) was performed using 2-(2-Thiazolylazo)-p-cresol (TAC) as an added measuring ligand (Croot and Johansson, 2000), as described in detail in Chapter 2. Determination of DFe via Flow injection analysis (FIA; Klunder et al., 2011; Rijkenberg et al., 2014) was also performed as described in Chapter 2. On average, the standard deviation of the DFe measurements was 3.2%, generally being <5% in samples with DFe concentrations higher than 0.1 nM. Only standard deviation (SD) of measurements near the detection limit of the system was relatively high. The average blank was determined to be at 0.033 nM during the southern cruise and 0.017 nM during the northern cruise. The blank was defined by the intercept of a low Fe sample loaded for 5, 10 and 20 s and was measured daily. The limit of detection, 0.019 nM during the southern cruise and 0.004 nM during the northern cruise, was defined as three times the SD of the mean of the daily measured blanks, loaded for 10 s. To

better understand the day-to-day variations, a duplicate sample was measured again at least 24 h after the first measurement. The relative differences between these measurements were of the order of 1–20%, while the largest differences were measured in samples with low DFe concentrations.

To correct for this day- to-day variation, a lab standard, a sample acidified for>6 months, was measured daily. The consistency of the FIA system over the course of a day was verified using a drift standard. For the long-term consistency and absolute accuracy, certified SAFe and GEOTRACES reference material (Johnson et al., 2007) were measured on a regular basis (Table 1). We did not measure a consistent DFe in the GS reference samples, like we did in the other references. We do not know the cause, we might have had a contamination in two GS bottles. FIA data is publicly available in August 2017 when the GEOTRACES Intermediate Data Product 2016 will be published at http://www.bodc.ac.uk.

Only during the northern cruise separate samples for determination of DFe (see below) were taken from the un-acidified Fe-binding dissolved organic ligand samples just before the analysis of the characteristics of the organic ligands. To be able to compare the results from both cruises, the DFe concentrations from immediately acidified samples were used for the calculation of the ligand characteristics. In 6 samples this DFe was either missing (4 samples) or so high that contamination was probable (2 samples). The sample taken at 501 m at station 1S was not analysed with FIA, DFe from measurements with inductively coupled plasma mass spectrometry (ICP-MS) was used instead giving comparable results (Middag et al., 2015). The other missing samples were from station 8N at 260 m, station 13N at 1000 and 1500 m, the contaminated samples were from station 13N at 100 and 2000 m depth. For these samples DFe was used which was measured in subsamples taken from the un-acidified 1 L bottles just before analysis of the ligand characteristics and analysed by FIA. Earlier research showed that DFe in un-acidified samples are on average 13% lower due to wall adsorption (Gerringa et al., 2015). The results of the above mentioned samples do not deviate from the general trend with depth or between stations and were thus incorporated in the results.

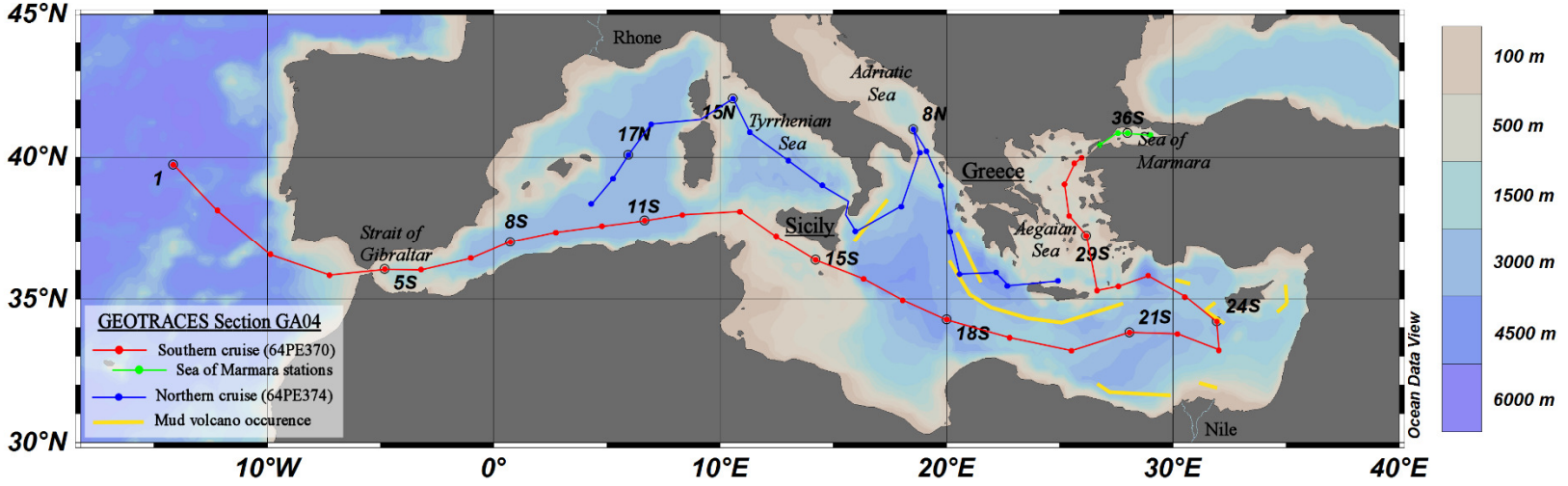

Figure 1

Cruise tracks of the Dutch GEOTRACES Section GA04 in the Mediterranean Sea. The southern cruise (S) (64PE370) is indicated with a red line and red symbols, the cruise track consists of 37 stations. The part of the southern cruise in the Sea of Marmara is indicated with a green line and green symbols. The northern cruise (N) (64PE374) is indicated with a blue line and blue symbols, it consists of 19 stations. The stations where Fe-binding dissolved organic ligands were sampled are indicated by station numbers. Geographical names used in the main text are indicated. In yellow the occurrence of mud-volcanos is indicated where these are part of the volcanic active Hellenic and Aeolian Arcs (after Mascle et al., 2014)

Table 1 *Concentrations of SAFe and GEOTRACES reference samples in nM kg^{-1}. Columns show reference ID, the Intercalibration Consensus Values (ICV) and the bottle number of GS reference samples, the values measured during the cruises 64PE370 and 64PE374 in the North Atlantic Ocean, the Mediterranean Sea and the Sea of Marmara, including the standard error, and the number of sample analyses. SAFe S is a surface, SAFe D is deep reference sample and GS is a GEOTRACES surface and GD is a GEOTRACES deep reference sample (http://www.geotraces.org/science/intercalibration).*

ID	*ICV ± SE (nM kg^{-1})*	*Bottle nr.*	*Measured ± SE (nM kg^{-1})*	*N*
SAFe S	0.093 ± 0.008	8,47,48,76	0.067 ± 0.013	7
SAFe D2	0.933 ± 0.023	29,191	0.963 ± 0.076	2
GS	0.546 ± 0.046	12	0.836 ± 0.030	3
		141	0.493 ± 0.021	2
		154	0.736 ± 0.007	2
		186	0.541	1
		55	0.473	1
GD	1.000 ± 0.100	87,238	1.088 ± 0.102	10

The ligand characteristics were calculated with two models, one assuming the presence of one ligand class and the other assuming the presence of two ligand classes (Gerringa et al., 2014) (Supplementary Table 1). We were unable to calculate the ligand characteristics for 2 ligand classes because either only one ligand group was present, or ligand characteristics of the different ligand groups did not differ enough from each other to be distinguished as separate classes. The side reaction coefficient (α_{FeL}) reflects the complexation capacity of the dissolved organic ligands to bind with Fe, which can be seen as its ability to compete for Fe with other ligands and with adsorption sites on particles. The parameter α_{FeL} is more robust to characterize the Fe-binding dissolved organic ligands than the K' and [L'] separately because the Langmuir equation does not treat K' and [L'] independently from each other. If an analytical error forces an underestimation of one, the other is automatically overestimated (Hudson et al., 2003). Moreover, in our equations, [L'] is, in contrast to [L_t], independent of DFe (Thuróczy et al., 2010). The ratio [L_t]/DFe (Supplementary Table 1) indicates the saturation of the ligands, which are saturated with Fe if the ratio ≤1, and unsaturated when >1 (Thuróczy et al., 2010).

3.3. Hydrography

Stations 1S–4S were sampled in the Atlantic Ocean before entering the Mediterranean Sea. The Mediterranean Outflow Water (MOW) is readily recognized between 500 and 1500 m by higher salinity (>36) and lower oxygen concentrations (<200 µg kg^{-1}; Figure 2A, D). In the Mediterranean, the Atlantic Water (AW) characterized by relatively low salinity is present in the surface waters (<200 m) of especially the Western Basin. AW streams counter clockwise through the basins (e.g., Millot, 1999) and becomes warmer and more saline along its course. Formed in dense water formation areas in the Eastern Basin, the Levantine Intermediate Water (LIW) between 200 and 600 m in the southern cruise transect and 100–800 m in the northern cruise transect, streams to the west and spills into the Western Basin (see also Rolison et al., 2015). It is discernible by its relatively high salinity (>38.75 in the Eastern Basin and >38.5 in the Western Basin in the southern transect; >38.8 in the northern transect) and in the northern transect also by its relatively high temperature (>14–14.5 °C) and in the Western Basin by low oxygen (Figures 2A, B, D, 3A, B, D). Below LIW, three deep water masses are distinguished, the Western Mediterranean Deep Water (WMDW), the Adriatic Mediterranean Deep Water (AdMDW) and the Aegean Mediterranean Deep Water (AeMDW). The AdMDW is less saline than the AeMDW (Figure 3A). Water masses are not only separated vertically, but also horizontally, due to their different formation areas. Horizontally, water masses are separated by fronts, as can be seen between AdDMW and AeMDW, for example in Figure 3C. Fronts occur around eddies (for example near stations 7N, 8N and 9N in Figure 3C, as further discussed in Section 3.5.2; subsection Deep high DFe patches), and near continental boundaries. Dynamically, horizontal transitions in density give rise to along-frontal currents, due to the rotation of the Earth, causing advective transport. Near continental boundaries and around eddies such currents are expected to be strongest with velocities ranging between 0.1 and 1 m s^{-1} (Millot and Taupier-Letage, 2005). They become reinforced after dense water formation events, whereby density contrasts are sharpened. This gives rise to larger along-frontal currents, following vertical convection events. The Sea of Marmara has a surface layer of about 20 m with a relatively low salinity influenced by exchange with the Black Sea (S = 21.6 in the east, S = 23 in the west; Beşiktepe et al., 1994). This layer contains high oxygen concentrations of 213–280 µg kg^{-1} and fluorescence is relatively high, 0.5–1.1 µg dm^{-3} (Figures 4A, C and D). Below a very steep pycnocline at 20 to 50 m the salinity is >38.7 and the oxygen is reduced to 10.4–18.4 µg kg^{-1} in the east and to 20–50 µg kg^{-1} in the west. The surface waters are transitional in character with a short residence time of months (Ünlülata et al., 1990; Beşiktepe et al., 1994; Rank et al., 1999). Below 50 m

salinity, temperature and oxygen concentrations are nearly homogeneous. This uniform deep water has a residence time of 6 years, which is influenced by intrusions from the Mediterranean (Ünlülata et al., 1990; Rank et al., 1999).

Figure 2 (page 41)
Southern cruise transect showing: A) Absolute Salinity (SA) in g kg^{-1}; B) Conservative Temperature (CT) in °C; C) Density as sigma-theta in kg m^{-3}; D) Oxygen in µM kg^{-3}; E) Fluorescence in µg dm^{-3}; F) Attenuation coefficient in m^{-1}. Salinity contours are given every 0.5 g kg^{-1} between 36 and 37, and every 0.1 g kg^{-1} between 37 and 39.5. Sigma-theta contours are every 0.5 kg m^{-3} between 27 and 29.5, every 0.001 kg m^{-3} between 29.1 and 29.120 and between 29.173 and 29.2 and every 0.002 kg m^{-3} between 29.2 and 29.26.

Figure 3 (page 42)
Northern cruise transect with: A) Absolute Salinity (SA) in g kg^{-1}; B) Conservative Temperature (CT) in °C; C) Density as sigma-theta in kg m^{-3}; D) Oxygen in µM kg^{-3}; E) Fluorescence in µg dm^{-3}; F) Attenuation coefficient in m^{-1}. Salinity contours are given every 0.1 g kg^{-1} between 37.5 and 39.5. Sigma-theta contours are every 0.5 kg m^{-3} between 27 and 29.5, every 0.001 kg m^{-3} between 29.1 and 29.120 and between 29.173 and 29.2 and every 0.002 kg m^{-3} between 29.2 and 29.26.

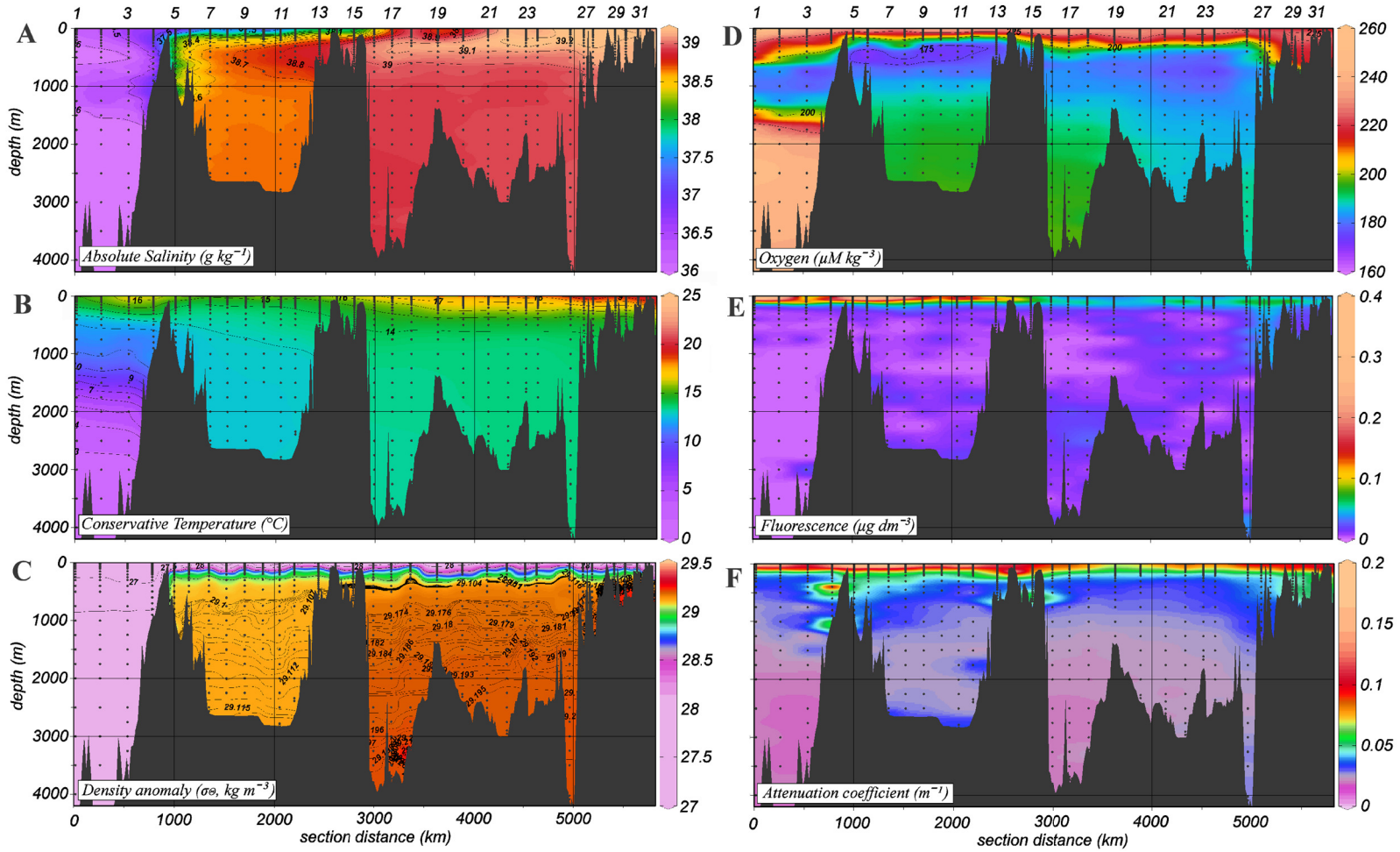
A
B
C
D
E
F
depth (m)
Absolute Salinity (g kg⁻¹)
Conservative Temperature (°C)
Density anomaly (σθ, kg m⁻³)
Oxygen (μM kg⁻³)
Fluorescence (μg dm⁻³)
Attenuation coefficient (m⁻¹)
section distance (km)

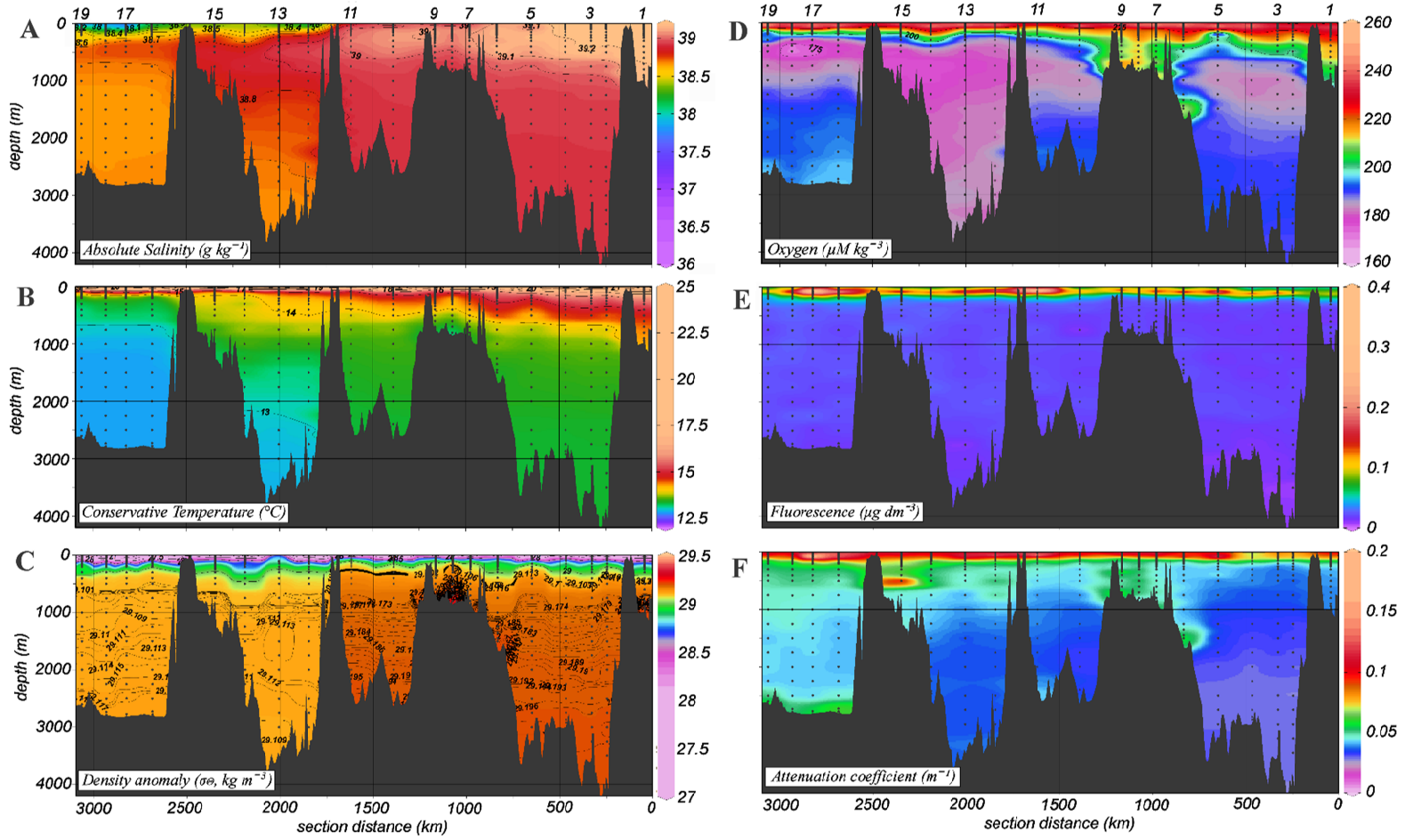
A
B
C
D
E
F
depth (m)
Absolute Salinity (g kg⁻¹)
Conservative Temperature (°C)
Density anomaly (σθ, kg m⁻³)
Oxygen (μM kg⁻³)
Fluorescence (μg dm⁻³)
Attenuation coefficient (m⁻¹)
section distance (km)
19 17 15 13 11 9 7 5 3 1
3000 2500 2000 1500 1000 500 0
0 1000 2000 3000 4000
39 38.5 38 37.5 37 36.5 36
25 22.5 20 17.5 15 12.5
29.5 29 28.5 28 27.5 27
260 240 220 200 180 160
0.4 0.3 0.2 0.1 0
0.2 0.15 0.1 0.05 0

3.4. Results

In the following paragraphs, median values are presented per depth layer (0–100 m to show the influences of dust deposition, 100–1000 m to show properties in the LIW, and 1000–2000m and >2000 m for properties of the deep water and the deepest basins, respectively) and per geographical region, the Atlantic Ocean, the Mediterranean Sea, divided in the Western Basin and the Eastern Basin, and the Sea of Marmara. Medians with interquartile ranges (IQR) were calculated instead of average because DFe and also [L_t] had maxima in deep patches, which influenced the average values and increased the standard deviations, making median values more suitable. Note that for both the Atlantic Ocean and the Sea of Marmara only one station was sampled for the Fe-binding organic ligand characteristics, and thus the number of samples (N) is rather low.

In the Atlantic Ocean DFe was low in the surface waters (stations 1S–4S) and ranged from 0.01 to 0.18 nM in the upper 100 m (Figure 5A). The DFe increased with depth to 0.69 nM at 1000 m in the MOW, and slightly decreased to 0.50 nM at depths larger than 3000m at stations 1S and 2S (Figure 6A). Closer to the Mediterranean, DFe increased to 0.71–0.99 nM around 900 m (stations 3S and 4S), also in the MOW, being well below the Camarinal sill separating the Mediterranean from the Atlantic Ocean (Figures 5A, 6A).

In the Mediterranean, the typical vertical profile of DFe was different from those in the Atlantic Ocean (Figure 6A versus B and C). In the Mediterranean, DFe was high near the surface (median DFe in upper 100 m = 1.4 nM, IQR = 0.96, N = 290, ranging from 0.20 to 15.35 nM), with highest near-surface DFe at stations in the north of the Eastern Basin (Figure 6B and C; station 27S with 15.35 nM and station 7N with 9.36 nM), decreasing to relatively low concentrations of <0.40 nM below 500–700m (Table 2A). These deep concentrations were relatively low compared to concentrations of 0.5 nM at similar depths in the Atlantic Ocean (Rijkenberg et al., 2014; Hatta et al., 2015). The lowest deep DFe of 0.09 nM in the Mediterranean was from station 18S at 3263 m. However, very high DFe of up to 8.40 nM existed in distinct patches of both transects between 200 and 3000 m (at station 6N at 1250 m; Figure 5B). These patches were mostly found in the Eastern Basin during our northern transect, (Figure 5B). The patches varied roughly between 230 and 400 km in width and between 400 and 1000 m in height.

In the Sea of Marmara, DFe was elevated in the upper 100 m as in the Mediterranean and ranged between 0.94 and 4.93 nM. DFe decreased to 0.75–0.33 nM between 100 and 1000 m and increased close to the bottom only at one station (35S) to 1.80 nM at 1110 m (Figure 6D, Table 2A).

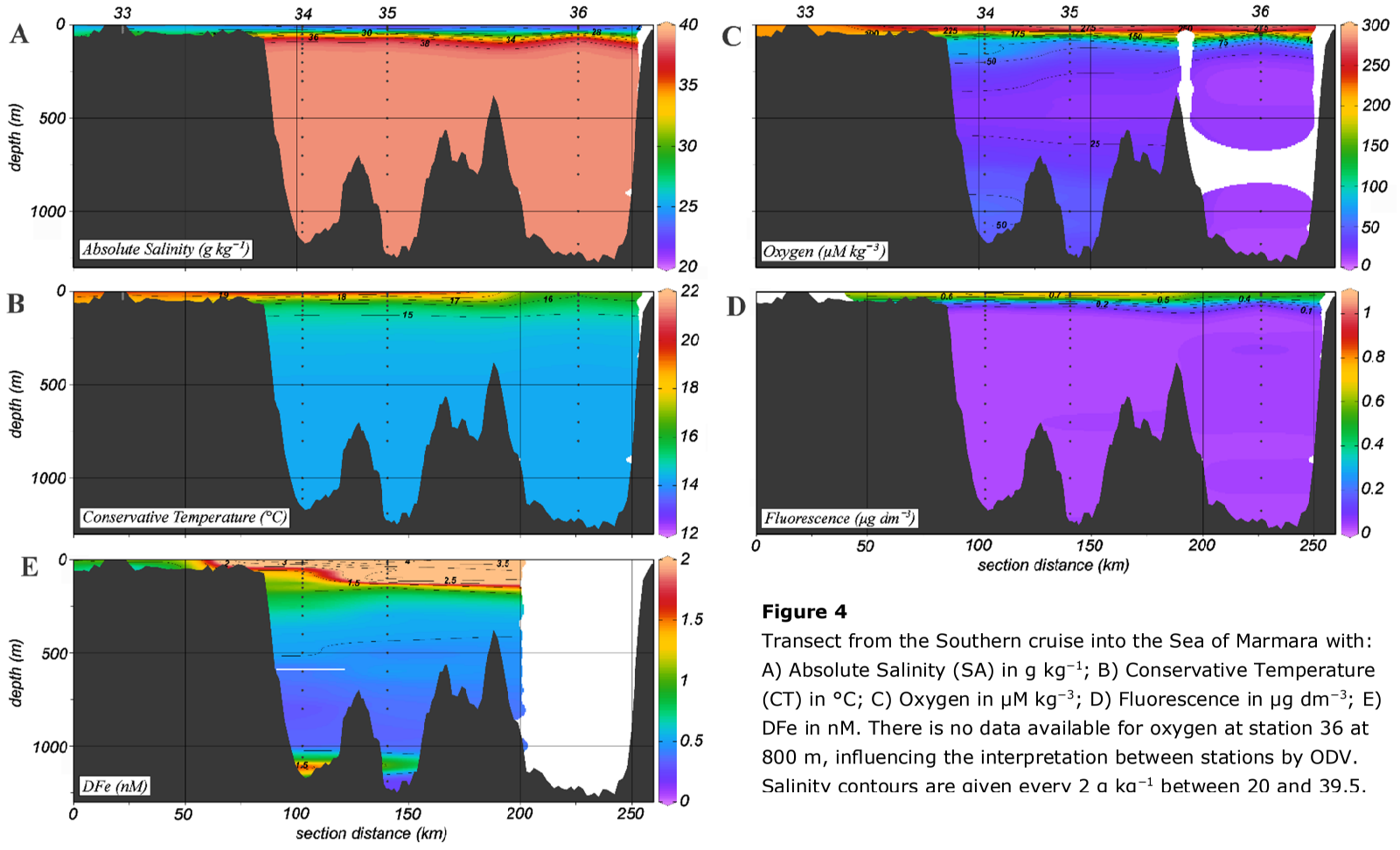

Figure 4

Transect from the Southern cruise into the Sea of Marmara with: A) Absolute Salinity (SA) in g kg^{-1}; B) Conservative Temperature (CT) in °C; C) Oxygen in µM kg^{-3}; D) Fluorescence in µg dm^{-3}; E) DFe in nM. There is no data available for oxygen at station 36 at 800 m, influencing the interpretation between stations by ODV. Salinity contours are given every 2 g kg^{-1} between 20 and 39.5.

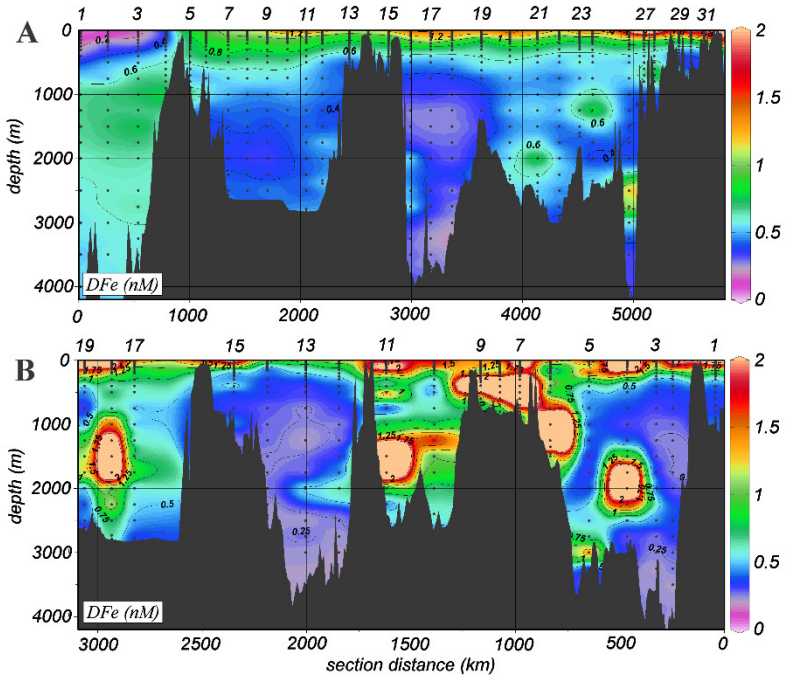

Figure 5

Southern (A) and northern (B) cruise transect showing DFe in nM. The southern transect consists of 721 data points, the northern transect consists of 421 data points. Station 25S was not sampled for DFe (see Methods and equipment). See Fig. 1 for the positions of the stations.

In the Atlantic Ocean, [L_t] varied between 0.54 and 2.01 nEq of M DFe (N = 13; Figure 7A) and had a median of 1.1 nEq of M DFe in the upper 100 m, 1.3 nEq of M DFe in the upper 1000 m and 0.8 and 1.0 nEq of M DFe in the 1000–2000 m below 2000 m, respectively (Table 2B for IQR and N per depth layer). The median $logK'_{FeL,Fe3+}$ per depth layer varied between 21.9 and 22.1 (N = 13). No trend with depth existed, but the values showed more variation in the upper 500 m and in the two samples taken just above the sediment (Supplementary Table 1). The [L_t] in the Mediterranean Sea varied between 0.23 and 5.51 nEq of M DFe (Figure 7B and C, Supplementary Table 1). $LogK'_{FeL,Fe3+}$ varied between 20.54 and 24.11. Only 17 $LogK'_{FeL,Fe3+}$ values out of 156 samples were higher than 22.5. These high values coincided with ligands that were saturated with Fe or nearly saturated as shown by the ratio [L_t]/DFe ranging between 0.6 and 2 with an average of 1.2. These high $logK'_{FeL,Fe3+}$ values are influenced by the fact that the ligands were near saturation and therefore had very few data points in the calculation, probably resulting in a correct [L_t] but not in very reliable K' by lack of degrees of freedom. This is illustrated by the high standard errors only 5 of the 17 have an upper SE smaller than 0.4 mol^{-1}. Thus we assume that actually $logK'_{FeL,Fe3+}$ varied between 20.54 and 22.5, although all values were used for calculating means and medians in the following text.

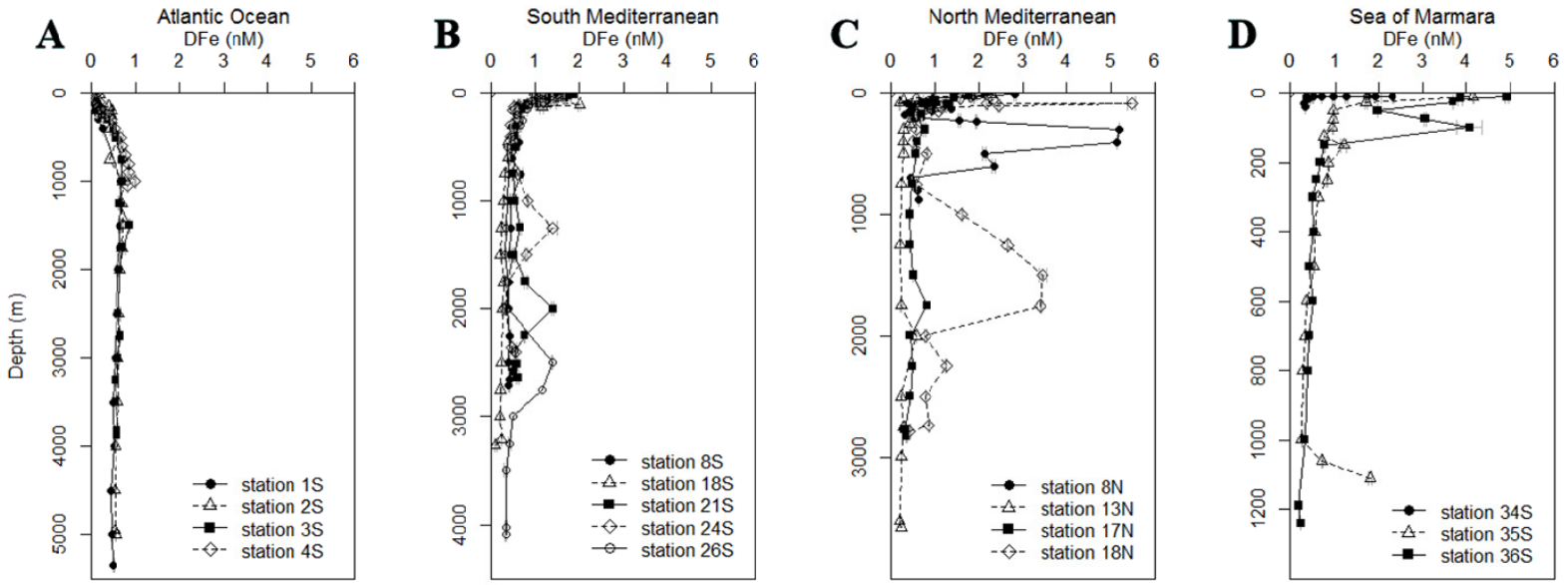

Figure 6

Dissolved Fe (DFe in nM) with standard deviations (small values falling within the size of the symbol, see Supplementary Table 1) versus depth (m) of A) stations in the Atlantic Ocean (AW); B) stations from the southern cruise (S); C) stations from the northern cruise (N); D) stations from the Sea of Marmara.

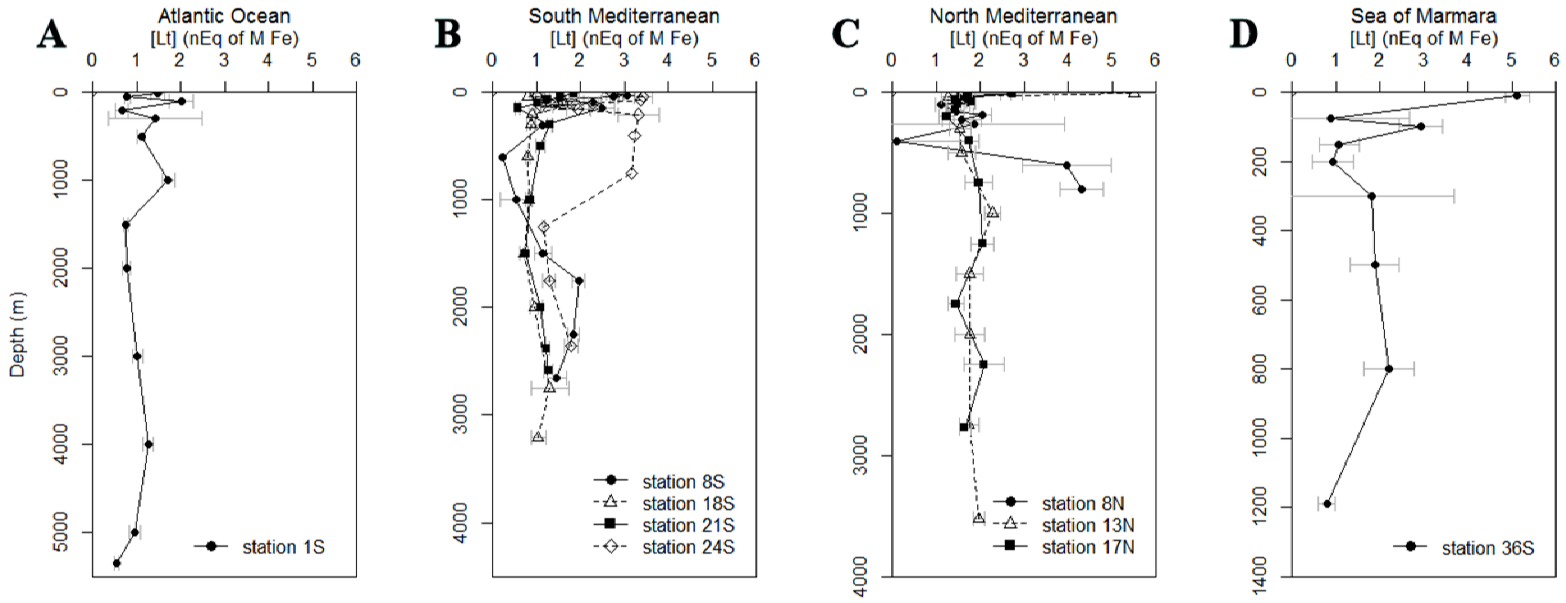

Figure 7

The concentration of Fe-binding dissolved organic ligands with standard errors ([L_t] in nEq of M Fe, small errors falling within the size of the symbol) versus depth (m) of A) stations in the Atlantic Ocean (AW); B) stations from the southern cruise (S); C) stations from the northern cruise (N); D) stations from the Sea of Marmara.

Table 2A *Median values per environment and per depth layer of DFe with the inter quartile range (IQR) of the median and the number of samples (N)*

Region	**Atlantic Ocean**			**Mediterranean Sea**			**Western Basin**			**Eastern basin**			**Sea of Marmara**		
depth layer (m)	*DFe*	*IQR*	*N*	*DFe*	*IQR*	*N*	*DFe*	*IQR*	*N*	*DFe*	*IQR*	*N*	*DFe*	*IQR*	*N*
0-100	0.04	0.04	20	1.38	0.96	290	1.15	1.03	106	1.49	0.89	184	1.27	2.09	23
100-1000	0.38	0.42	38	0.54	0.37	472	0.57	0.41	170	0.53	0.33	302	0.52	0.28	21
1000-2000	0.67	0.07	15	0.37	0.31	120	0.40	0.19	49	0.34	0.42	71	0.47	0.76	4
>2000	0.56	0.08	21	0.35	0.24	118	0.39	0.25	47	0.34	0.25	71			

Table 2B Median values per environment and per depth layer of ligand characteristics logK', [Lt], logαFeL, the calculated [Fe'] and the ratio [Lt]/DFe with the inter quartile ranges (IQR) of the median and the numbers of samples (N).

	N	$logK'_{Fe3+}$	IQR	$[L_t]$ *(nM)*	IQR	[L'] *(nM)*	IQR	$[L_t]/DFe$	IQR	$Log\alpha_{FeL,Fe3+}$	IQR	[Fe'] *(pM)*	IQR
Atlantic Ocean													
0-100	2	22.06	0.44	1.13	0.35	1.10	0.35	43.4	20.5	13.07	0.29	0.03	0.01
100-1000	4	21.71	0.44	1.27	0.58	0.95	0.86	8.0	13.7	12.73	0.53	0.52	0.54
1000-2000	3	22.04	0.34	0.77	0.49	0.19	0.48	1.3	0.7	12.37	0.16	3.44	0.80
>2000	4	21.88	0.23	0.99	0.23	0.50	0.19	2.0	0.5	12.52	0.19	1.87	0.63
whole Mediterranean													
0-100	48	21.93	0.67	1.70	1.00	0.45	1.08	1.4	1.2	12.50	1.00	3.28	26.11
100-1000	61	21.78	0.58	1.30	0.82	0.67	0.97	2.2	1.6	12.61	0.57	1.64	2.39
1000-2000	14	21.89	0.54	1.32	0.58	0.83	0.86	3.3	2.5	12.69	0.44	0.84	1.10
>2000	13	21.57	0.26	1.45	0.57	1.09	0.68	4.4	2.9	12.67	0.34	0.92	0.55
East Mediterranean													
0-100	24	21.94	0.64	1.74	1.36	0.57	1.20	1.4	1.2	12.72	0.98	1.77	14.83
100-1000	24	21.66	0.52	1.51	0.82	0.89	0.84	2.7	2.0	12.49	0.23	1.99	1.27
1000-2000	8	21.55	0.41	1.61	0.43	1.24	0.70	4.0	3.4	12.54	0.41	0.92	0.84
>2000	8	21.57	0.18	1.70	0.68	1.39	0.70	4.5	2.7	12.71	0.68	1.11	11.55
West Mediterranean													
0-100	22	21.87	0.49	1.64	0.66	0.24	0.72	1.2	0.9	12.36	1.12	5.25	48.79
100-1000	39	21.87	0.64	1.21	0.80	0.55	0.83	2.0	1.7	12.72	0.63	1.42	3.09
1000-2000	6	22.13	0.27	1.02	0.35	0.37	0.59	2.5	2.7	12.84	1.60	0.68	173.00
>2000	5	21.57	0.46	1.27	0.08	0.82	0.33	3.8	2.1	12.67	0.40	0.92	0.42
Sea of Marmara													
0-100	3	21.56	0.44	2.93	2.12	0.01	0.11	0.7	0.4	10.50	1.30	1160.0	1074.8
100-1000	5	21.20	0.31	1.81	0.81	1.33	1.12	3.7	3.1	11.82	0.86	9.24	17.72
>1000	1	21.82		0.79		0.61		4.3		12.61		0.57	

In the Sea of Marmara, high [L_t] up to 5.12 nEq of M Fe existed in the upper 100 m where fluorescence was high, in deeper water [L_t] varied between 0.79 and 2.21 nEq of M DFe; whereas $logK'_{FeL,Fe3+}$ varied between 21.97 and 20.90 with no apparent relation with depth (Figure 7D, Table 2B).

When comparing the three regions, the median DFe per depth layer increased in the Atlantic Ocean with depth and decreased with depth in the other three basins (Table 2A). The median [L_t] per depth interval generally decreased with depth in all regions. However, in the Western Mediterranean Basin it remained almost constant with depth between 1.51 and 1.74 nEq of M Fe (Supplementary Table 1 and Table 2B). The median [L_t] was lowest in the Atlantic Ocean (0.77–1.27 nEq of M Fe) and highest in the Sea of Marmara, ranging from 0.79 to 2.93 nEq of M Fe. The median values of [L_t] in the upper 0–100 m and 100–1000 m were higher in the Western compared to the Eastern Basin of the Mediterranean (Table 2B). The median values of $logK'_{FeL,Fe3+}$ decreased slightly from west to east from 21.71–22.04 in the Atlantic Ocean, 21.55–21.94 in the Western Mediterranean, 21.57–22.13 in the Eastern Mediterranean to 21.2–21.82 in the Sea of Marmara.

In the Atlantic Ocean, $logK'_{FeL,Fe3+}$ was fairly constant through the water column and ranged between 21.71 and 22.06. In the Mediterranean, both in the Western and Eastern Basins, $logK'_{FeL,Fe3+}$ decreased with depth, with an exception between 1000 and 2000 m in the Eastern Basin where a relatively high $logK'_{FeL,Fe3+}$ was found, 22.13 versus 21.87–21.57. In the Sea of Marmara, $logK'_{FeL,Fe3+}$ varied between 21.20 and 21.82 unrelated with depth. The $log\alpha_{FeL,Fe3+}$ did not vary between the Atlantic Ocean and the Mediterranean Sea but was lower in the Sea of Marmara (Table 2B). $Log\alpha_{FeL,Fe3+}$ decreased with depth in the Atlantic Ocean from 13.07 to 12.52, it varied little between 12.36 and 12.84 in the Mediterranean Sea and it increased with depth in the Sea of Marmara from 10.50 to 12.61. The ratio [L_t]/DFe decreased with depth in the Atlantic Ocean from relatively high 43.4 in the upper 100 m to values round 1 and 2 in deep waters whereas in the other regions, the ratio increased with depth. In the Mediterranean and Sea of Marmara this ratio did not vary as much and remained between 0.7 and 4.45. Excess L ([L']) decreased with depth in the Atlantic Ocean and increased with depth in the Mediterranean basins. In the Sea of Marmara [L'] and DFe vary, in the surface DFe is relatively high and [L'] is low (0.01–0.22 nEq of M Fe; Figure 4, Supplementary Table 1 and Tables 2A, B).

3.5. Discussion

3.5.1. Sources and sinks of DFe and Fe-binding dissolved organic ligands in the Atlantic Ocean and the Sea of Marmara

Atlantic Ocean

The depth-profiles of DFe at stations 1S–4S were similar to those observed by others in the Atlantic Ocean, with very low concentrations near the surface due to phytoplankton uptake and scavenging by dust, although seasonal increases in DFe are reported due to dust input (Sedwick et al., 2005, 2015; Thuróczy et al., 2010; Wagener et al., 2010; Rijkenberg et al., 2012, 2014; Hatta et al., 2015). Calculated [Fe'] are very low 0.02–0.07 in pM in the upper 100 m, lowest values obtained in the present research. Phytoplankton uptake of Fe was probably the reason for these low values. Increasing DFe concentrations with depth in the upper 500–1000 m (Figures 5A, 6A) are probably due to the release by degradation of organic matter and the DFe decrease below 1500 m at stations 1S–3S is probably due to scavenging (Bruland et al., 2014). Below 2000 m, DFe was close to 0.5 nM as also observed by Sarthou et al. (2007). Closer to the Strait of Gibraltar (Stations 3S and 4S), DFe was higher in the MOW between 500 and 2000 m. Since the salinity and the density were also higher and the oxygen concentrations were lower at these depths (Figure 2A, C, D), it is safe to conclude that the Mediterranean is the source of elevated DFe. Although they expected elevated DFe, Hatta et al. (2015) did not detect higher DFe in the MOW at their stations, in the same region as our stations. Also Thuróczy et al. (2010) did not detect elevated DFe in MOW at the position of our station 1S. However, at depths of the MOW Thuróczy et al. (2010) measured an increase in particulate Fe (PFe). Lenses of MOW, 'Meddies' or pulses of water are released into the Atlantic at different depths depending on density. These move with variable velocities and directions and are also dependent on season. In this way these hydrological features explain variability in DFe and it is thus not surprising that results are not overlapping here (Ambar et al., 2008).

The calculated values of $\log\alpha_{FeL,Fe3+}$ for both the present study and that of Thuróczy et al. (2010) compare well, with values between 12.71 and 13.25 from their study and 12.05 and 13.35 from this study. In both studies ligands got more saturated with depth until 1000–2000 m, below which $[L_t]$/DFe remained constant with depth. At our station 1S, [L'] and [Fe'] also remained constant below 1000 m. Apparently at this depth a steady state is reached for Fe between binding by organic ligands and scavenging by marine snow (Bruland et al., 2014). The $[L_t]$ is slightly higher at 1000 m in the MOW. It is thus possible that the Mediterranean is also a source of dissolved organic Fe-binding ligands for the Atlantic Ocean. (Buck et al., 2015) measured ligand characteristics East and

South of the Strait of Gibraltar. They distinguished three different ligand groups with a sum [L_t] around 2–3 nEq of M Fe, higher than the concentrations at our station 1S. However, $\log\alpha_{FeL,Fe3+}$ was between 13 and 13.5, which is close to our values of 12.05 and 13.35. This confirms that the side reaction coefficient ($\log\alpha$) is a useful parameter for comparing results of speciation data obtained with different chemical and mathematical methods (Town and Filella, 2000; Hudson et al., 2003; Gerringa et al., 2016; Gledhill and Gerringa, 2017).

Sea of Marmara

In the Sea of Marmara the elevated DFe up to 4.93 nM was not restricted to the upper 20–50 m, the layer influenced by the outflow of the Black Sea with low salinity high oxygen and high fluorescence, but it extended over 100 m. Below 100 m DFe decreased from 1.21 to 0.18 nM. Changes in DFe are not related to changes in oxygen concentration (Figure 4D, E). The sources of Fe are predominantly in the surface and determine the depth distribution in the upper 100 m. The sea is relatively polluted although not in Fe as concluded in sediment studies (Pekey, 2006). The sea is surrounded by land, with lateral supply from rivers like the polluted Dil Deresi, and from the Black Sea. The organic ligands at station 36S were weaker than in the Atlantic Ocean and in the Mediterranean Sea (see below). However, the lower conditional binding constants had comparable values between 20.74 and 22.2, obtained with the same method in the near-surface oxic layer of the Black Sea (Gerringa et al., 2016). The relatively high [L_t] between 1 and 2.8 nEq of M Fe in the Black Sea also compared rather well to the values between 0.79 and 5.12 nEq of M Fe in the Sea of Marmara confirming the role of the Black Sea as a source. Near the surface, the ligands were saturated at station 36S, [L'] is very low and the three lowest [L_t]/DFe ratios in this research are found here; thus DFe concentrations were quite extreme if not maximum concentrations in the upper 100 m. The 100 m deep layer with elevated DFe can be explained by sinking particles, predominantly dust, releasing Fe enabled by [L']. Some of the sources for Fe, most probably rivers and the Black Sea may be important for the dissolved organic Fe-binding ligands as well. The proximity of land increases the chance that humic substances are an important part of the Fe-binding ligand pool. This ligand group might be underestimated by our method, which is not very sensitive for humic substances (Laglera et al., 2011; Abualhaija et al., 2015; Bundy et al., 2015).

3.5.2. Sources and sinks in the Mediterranean

As in other seas and oceans DFe and [L_t] do not systematically vary with water masses (Thuróczy et al., 2011; Klunder et al., 2012b; Bruland et al., 2014; Rijkenberg et al., 2014; Buck et al., 2015; Gerringa et al., 2015). Even the LIW,

considered to be an important water mass in the Mediterranean, cannot be recognized in both transects of DFe (Figures 2A, 3A and 5), as was also concluded by Rolison et al. (2015) for DAl in the southern cruise. This most likely indicates the strong influence of vertical processes above the effect of horizontal processes. However in the West Atlantic Ocean, Gerringa et al. (2015) reported that [L_t] decreased along the flowpath of the NADW.

Near-surface waters

The high DFe concentration in the upper 100 m of the Mediterranean (Figures 5A, B, and 6B, C) suggests that dust is a major source of DFe, predominantly from the Sahara but also from anthropogenic sources (Guieu et al., 1991, 1997, 2010b, 2010a; Croot et al., 2004; Rijkenberg et al., 2008b; Aguilar-islas et al., 2010; Buck et al., 2010; Heimbürger et al., 2014). Guieu et al. (2010b) concluded that an increase in DFe up to 5.3 nM in the surface mixed layer in the Western Basin was due to dust input, with smaller concentrations in the Eastern Basin. In that study, the fluxes of dust and thus metals varied strongly depending to the season and weather conditions. We found the highest DFe concentrations, close to Greece and in the Adriatic Sea. Along the southern transect, Rolison et al. (2015) also measured higher surface dissolved Al (DAl) in the Eastern Basin than in the Western Basin. River input of metals is expected to be important close to the coasts, although a large fraction of DFe and other dissolved metals may be lost by flocculation upon mixing with saline waters (Sholkovitz, 1976; Boyle et al., 1977; Paucot and Wollast, 1997; Buck et al., 2007). Lateral transport of the remaining river DFe enabled by complexation (Jones et al., 2011) is most probably occurring at such a small scale that it is hard to be distinguished by us since we sampled far from the coast along the deepest part of the Mediterranean Sea. Except for stations in the Northeast (stations 26S–33S) and near the Adriatic Sea (stations 7N, 8N, 9N) where the cruise track came relatively close to the coast and rivers and lateral transport from land could play a role as source, dust is most probably the main source for the high near-surface DFe at our station locations in the Mediterranean.

The importance of dust as source of DFe depends on the amount of dust, its Fe content and on the solubility of Fe. Fe-binding organic ligands in aerosols, like oxalate or aliphatic water soluble organic carbon compounds, increase the solubility of Fe from the dust (Paris et al., 2011; Wozniak et al., 2015). The solubility in seawater depends also on the nature of the dust particles (Visser et al., 2003; Baker and Jickells, 2006; Sedwick et al., 2007; Baker and Croot, 2010; Fishwick et al., 2014). Journet et al. (2008) found that Fe solubility of clays (illite) was even larger than that of Fe-oxides in dissolution experiments. However, also the characteristics and composition of the seawater influences Fe

dissolution. Logically, it can be deduced that the solubility of Fe from dust is related to the excess ligand concentration in seawater. Indeed, Rijkenberg et al. (2008) found that the Fe-binding ligands play a key role in keeping Fe from Sahara dust in solution, as also concluded by Aguilar-Islas et al. (2010) in the Pacific and Fishwick et al. (2014) in the Sargasso Sea.

Wagener et al. (2008) found that the dissolution rates of Fe from Sahara dust were linearly related to the concentration of dissolved organic ligands in seawater. Interestingly, they discovered that excess ligands were not always successful in dissolving Fe. The dissolving capacity depended on the season and probably on the presence of freshly produced ligands by biota. Our cruises were in summer, with relatively high biological activity (van de Poll et al., 2015). Probably the presence of freshly formed ligands enabled a high solubility of Fe (Barbeau et al., 2001). Wagener et al. (2010) concluded that successive dust depositions could have different biogeochemical reactions near the surface of the Mediterranean. They found that repetitive dust depositions in mesocosms studies had opposite effects, no flux of Fe from the dust into the seawater occurred, the opposite happened, the dust particles cleaned the water column from Fe and scavenged DFe out of the water. Sarthou and Jeandel (2001) showed that near the surface in the north of the Western Basin the exchange flux of Fe from the dissolved to the particulate phase was high, but decreased considerably with depth. According to Aguilar-Islas et al. (2010) and Fishwick et al. (2014) the dissolved Fe from dust was predominantly in the colloidal fraction. The distribution over different size fractions of Fe and the Fe-binding ligands is influencing the dissolution and residence time of Fe. This is discussed elsewhere and is outside the scope of this study (Wu et al., 2001; Croot et al., 2004; Fitzsimmons et al., 2015). Thus, DFe is the resultant of dissolution and scavenging and ballasting effects of Sahara dust. The dissolution of Fe from dust depends, apart from the nature of the dust, on the nature of the ligands (Aguilar-islas et al., 2010; Wozniak et al., 2015) and on the age of the ligands (Wagener et al., 2010), as well as on the dust history of the environment.

Even if this is not as apparent as for DFe, $[L_t]$ is also higher near the surface (Figure 7B, C). Sources for Fe-binding dissolved organic ligands can be biological activity (Rue and Bruland, 1995; Barbeau et al., 2001; Gledhill et al., 2004; Gerringa et al., 2006) and in the east the Black Sea as an additional source (Gerringa et al., 2016). Due to the high DFe, the growth of phytoplankton was not limited by a lack of Fe. According to Van der Poll et al. (2015), describing the southern transect, phytoplankton was nitrate-limited in the Eastern as well as in the Western Mediterranean Sea. If there is production of siderophores it is not to relieve Fe stress, only ligands resulting from degradation and viral lysis should be formed (Poorvin et al., 2011; Slagter et al., 2016). In the Western

Basin diatoms were abundant, in the Eastern Basin Synechococcus was most abundant. In the Western Basin chlorophyll had maximum concentrations in the upper 50 m, while in the Eastern Basin its maximum was found between 100 and 130 m (van de Poll et al., 2015). No relationship could be detected between fluorescence and [L_t] in the southern transect. However, sample depths for DFe and [L_t] were not concentrated at the near-surface layer, the photic zone, hampering a detailed comparison of DFe and [L_t] versus fluorescence.

Dust is another potential source of Fe-binding ligands (Johansen et al., 2000; Saydam and Senyuva, 2002; Gerringa et al., 2006; Paris et al., 2011; Wozniak et al., 2015). Although [L_t] was relatively high in the upper 100 m, the ratio [L_t]/DFe was lowest compared to deeper waters. The ligands were not completely saturated with Fe, since the ratio was almost never below 1, as it was the case in the Sea of Marmara. The median [L_t]/DFe was 1.4 in the upper 100 m in the Western Basin and 1.15 in the Eastern Basin. The median of DFe was 0.34 nM higher in the Eastern compared to the Western Basin, whereas the median in [L_t] was only slightly, 0.1 nEq of M DFe, higher in the Eastern Basin compared to the Western Basin. Assuming that dust is the source, it is apparently not an equally important source for dissolved organic Fe-binding ligands as it is for Fe. Dust as a sink for Fe-binding ligands is as far as we know not considered, yet scavenging and ballasting of organically complexed Fe must take place since almost all DFe is complexed. We can conclude that the elevated DFe, above its inorganic solubility, near the surface of the Mediterranean Sea is possible due to the complexation by dissolved organic ligands.

Deep waters

Apart from distinct patches with elevated concentrations, which are further discussed in the next section, DFe was relatively low below 300 m along the southern transect and below 500 m along the northern transect. In most samples DFe was lower than in open oceans at similar depths. Station 18S and station 13N are good examples with deep DFe between 0.09 and 0.30 nM and 0.19 and 0.27 nM, respectively. Surface DFe inputs from Sahara dust did not impact deep waters which could be due to DFe scavenging by sinking dust itself. Wagener et al. (2010) showed that Sahara dust supply does not always increase DFe. On the contrary, they showed that through scavenging DFe can be stripped from the dissolved phase by settling dust. Due to this scavenging a direct relationship between dissolution and excess ligands is not always straightforward. It is very probable that settling dust particles scavenge Fe even though it is in its organically complexed form. Subsequently, due to the decrease of inorganic Fe (Fe') by scavenging, Fe can dissociate from the ligands, emptying the ligands over time and depth as shown by an increase in the ratio

[L_t]/DFe with depth. Such an increase in the ratio indeed happened for stations 8S and 18S (Figure 8B), but not for stations 21S and 24S which have high DFe patches at 2000 and 1250 m, respectively. Along the northern transect, an increase in the ratio was observed for stations 13N and 17N, but again not for station 8N, where high DFe patches existed (Figures 5B, 8C). The removal of Fe from the organic ligand complex has also been suggested by Thuróczy et al. (2011) for the Makarov Basin of the Arctic Ocean. The Arctic Ocean is far from being a dust impacted area, but due to the very long residence times of Deep Makarov Basin Water, scavenging was likely the reason for the decrease in DFe and the simultaneous increases in [L'] and therefore the increase of the [L_t]/DFe ratio with depth. In the present research the median of calculated concentrations of [Fe'] below 1000 m are close to 1 pM (0.7–1.7 pM). This is comparable to [Fe'] at the same depths for our station 1S in the Atlantic Ocean as well as in the North Western Atlantic Ocean (median 0.2–0.5 pM from three cruises in the Western Atlantic Ocean, Gerringa et al., 2015; Table 2B). Because [Fe'] is calculated using the ligand characteristics which depend on the analytical method (Laglera et al., 2011; Buck et al., 2012, 2016; Abualhaija et al., 2015)

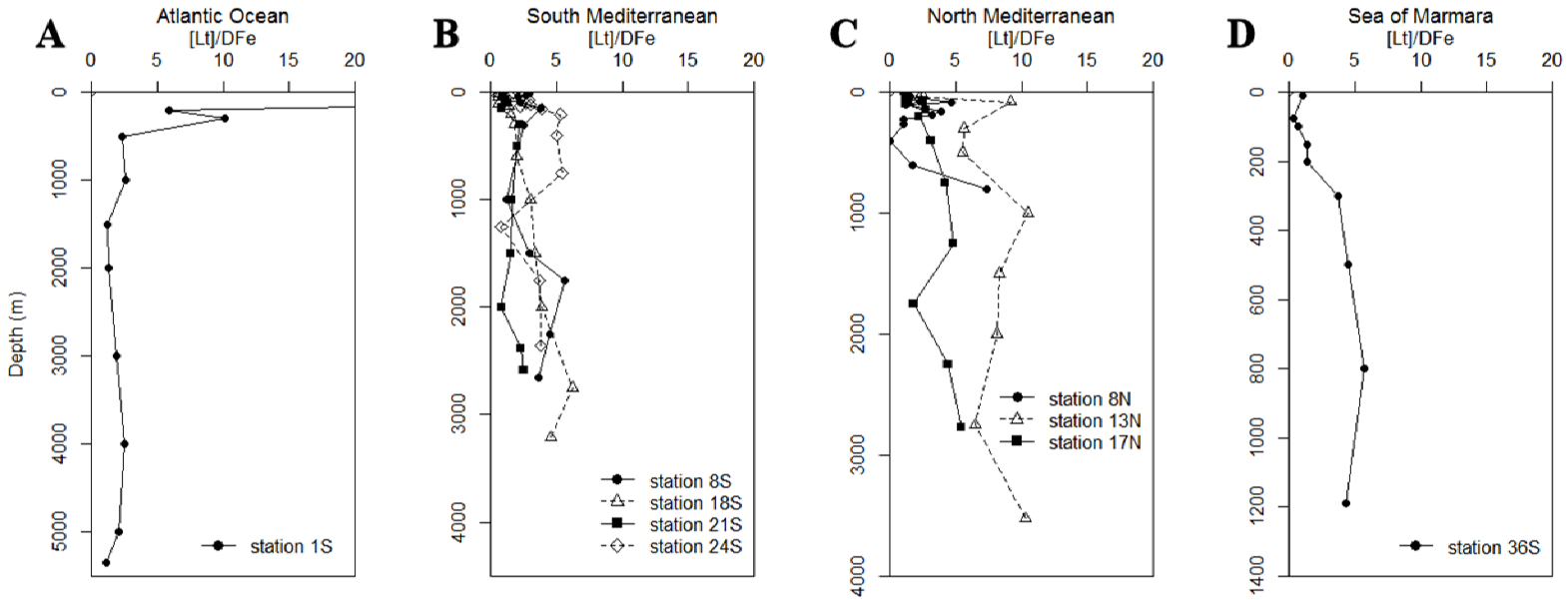

Figure 8

The ratio of Fe-binding dissolved organic ligands ([L_t] in nEq of M Fe) and dissolved Fe (DFe in nM) versus depth (m) of: A) stations in the Atlantic Ocean (AW); B) stations from the southern cruise (S); C) stations from the northern cruise (N); D) stations from the Sea of Marmara. Three values off scale in panel A vary between 22.94 and 63.91, see Supplementary Table 1 for the values.

and on how the parameters were calculated (Luis M Laglera et al., 2013; Gerringa et al., 2014; Pižeta et al., 2015; Buck et al., 2016) we only compare our data with data collected using the same methods. The methods in this research were also applied in the Western Atlantic, Gerringa et al. (2015) concluded that [Fe'] between 0.2 and 1 pM represent an equilibrium or steady state concentration between complexation by organic ligands and scavenging. Only where ligands were saturated with Fe, near hydrothermal vents where DFe was relatively high, [Fe'] were higher. In the present research median values in the deep (> 1000 m) Atlantic Ocean and Mediterranean Sea vary between 0.52 and 3.44 pM and 0.68 and 1.99 pM, respectively and are never below 0.23 pM (Supplementary Table 1). As α_{FeL} is given by $K'_{FeL,Fe3+} \times [L']$, or alternatively [FeL] / [Fe'], the values of $\log\alpha_{FeL,Fe3+}$ should show the same small but reversed range by a factor 3 since high α results in low [Fe']. Median values of $\log\alpha_{FeL,Fe3+}$ (values expressed with respect to Fe3+) of 12.49–12.84 existed at depths > 100 m in Mediterranean waters, slightly higher than in the Western Atlantic Ocean with $\log\alpha_{FeL,Fe3+}$ = 13.1 (Table 2B, Supplementary Table 1). Both the relatively small variation in [Fe'] and in $\log\alpha_{FeL,Fe3+}$ outside the deep high Fe patches indicate an equilibrium or steady state for Fe' that exist between the organic ligands and scavenging particles. At a lower [Fe'], Fe is so firmly bound that scavenging is hardly possible.

Deep high DFe patches

The high DFe patches could be ascribed to Fe supply by (I) lateral transport from land and shelves, (II) vertical transport from the sediment and (III) vertical and lateral transport from hydrothermal vents. These processes might be reflected by elevated particle densities. Particle densities can be related to the attenuation coefficient. The attenuation coefficient is high in the surface probably due to phytoplankton (Figures 2E, F, 3E, F). Evidence of particles elsewhere is scarce. Along the southern transect only near the Straits of Gibraltar and Sicily, elevated attenuation coefficients coincide with slightly elevated DFe (stations 5S and 6S near 1000 m depth and stations 11S and 12S at 2000 and 2500 m depth, respectively).

Along the northern transect more deep patches with higher DFe were found (Figure 5B). The attenuation coefficient is slightly higher near the bottom in the Western Basin, at station 15N, not coinciding with elevated DFe. It is also higher near the sills, especially near stations 7N, 8N and 9N (no data for station 6N exists) at the entrance of the Adriatic. The patches of elevated DFe at stations 7N, 8N and 9N are located at the southern end of the Adriatic Sea. At these stations, especially the most northern station 8N, the attenuation coefficient and oxygen are also elevated (Figure 3D, F) and temperature is lower (Figure 3B).

Elevated oxygen, higher than elsewhere in the Mediterranean, occurred also near the bottom at station 6N in the direction of the Aegean Sea at 1500 m. This is unexpected since the Adriatic Sea is known to suffer from anoxic periods (Koron et al., 2015). Elevated oxygen points to recent contact with the atmosphere and thus recently formed deep water. The attenuation coefficient is high and the temperature (<13.5 °C) and salinity are low. Indeed this cold water can be identified as AdMDW originating from the shallow northern Adriatic where it formed in winter (Pollak, 1951). The DFe is elevated over almost the whole water column of stations 7N, 8N and 9N except for the deep samples 100–200 m above the sediment, apparently AdMDW contains less DFe. The elevated DFe in the layer just above the AdMDW is advected by strong currents as evidenced by the large horizontal density gradients (Figure 3C). At station 8N, the ligand characteristics were analysed and the ligands were saturated at 160 and 600 m depth. In between these depths and below 600 m the $[L_t]$/DFe ratio was between 1.5 and 3.9, thus enabling this high solubility in almost all depths with calculated [Fe'] between 0.3 and 1 pM. At 160 and 600m depth, the calculated [Fe'] is 231 and 316 pM above the solubility of Fe, this DFe is expected to be labile and either complexed to relatively weak dissolved organic ligands outside the detection window of our method, or present as inorganic colloids. If we assume that particles above the sediment are the source, dissolved organic ligands enable Fe to stay in the dissolved phase and explain that DFe diffused away from the source (Thuróczy et al., 2011; Klunder et al., 2012b).

Highest deep DFe exists at mid depth, 0.81 nM at station 17N, 3.42 nM at station 18N and 1.35 nM at station 19N at 1750, 1750 and 1500 m, respectively. Samples from station 17N have been analysed for organic ligands. At 1750 m depth the $[L_t]$/DFe ratio is 1.5, and thus ligands were not saturated, enabling the high DFe of 0.81 nM. These three stations are relatively far from islands and coasts. There is no information about hydrothermal activity here that could explain this elevated DFe. Density contours below 1000 m bend downward from stations 17N and 19N to station 18N. This suggests a deep mesoscale eddy, which is the prominent feature in the mid-southern part of the Western Basin (Millot and Taupier-Letage, 2005; Schroeder et al., 2008). Apparently, DFe is transported by such an eddy. At these stations the densest water with relatively strong stratification is found below 2400 m, while the beam attenuation coefficient is only increasing in the lower 150 m above the bottom. Thus there is no indication that enhanced DFe results from deep-water formation. From our results we cannot distinguish the possible sources of DFe here.

The stations 1N–9N, 11N, 12N and 15N are closer to land and thus lateral transport from shelves and islands can be the source of DFe here. Still more than one specific source of DFe must exist to explain the multiple deep elevated

DFe patches. These are mainly found between 1000 and 2500 m (Figures 5B, 6B, C). The depth differences indicate that not one source but at least three different sources for the three different depths are involved. From such sources the enhanced DFe spreads relatively slowly through the basins. The spreading is partially diffusive, as suggested from the form of the DFe profiles around the depths where maximum DFe is found, a gradual decrease above and below the maximum DFe. This diffusive spreading across density stratification is likely dominated by turbulence, enforced by internal wave breaking, in the vicinity of topography (van Haren et al., 2014). Horizontally, the spreading is via boundary currents near topography and eddies further in the interior. Such eddies are observed (Figures 2C, 3C) in the upper 500 m nearly everywhere, but especially strong in the Adriatic Sea. These eddies can explain transport of DFe to the high DFe patches, at station 6N (1000–1500 m), stations 7N, 8N and 9N (400–800 m) stations 17N–19N (800–2500 m), and at stations 23S, 24S (1000–1500 m), 27S and 28S (near 700 m). However, density profiles do not indicate lateral transport for explaining the high DFe patches at station 4N (1500–2200 m), although between stations 4N and 5N there is a horizontal gradient, and also not at stations 10N–11N (1000–2000 m). In the Southern transect lateral transport is not supported around station 21S (near 2000 m). Therefore, either the source here is nearby or transport is in a perpendicular direction to the E-W transect. Horizontal spreading indicates deep sources, and immediately hydrothermal vents come to mind since they are known deep sources deemed to be very important (Bennett et al., 2008; Tagliabue et al., 2010; Klunder et al., 2012b; Rijkenberg et al., 2014; Hatta et al., 2015). Although there are two well-known volcanic active arcs, the Hellenic Arc in the Aegean Sea and the Aeolian Arc in the Tyrrhenian Sea near Sicily, the thus far known hydrothermal activity is restricted to very shallow depths of maximum 100 m (Beaulieu et al., 2015).

Station 26S, 4100 m deep, is situated at the Rhodes depression which is 4500 m deep, nearby the Anaximander mountains of approximately 1200 m deep, also known for its mud-volcanos (Figure 1). Although, as far as we know no references exist indicating mud-volcanos as a source of DFe, mud-volcanos exist in the Mediterranean Sea at depths that coincide with the presently observed high DFe patches. For instance the Anaximander Mountains are associated with faults allowing over-pressured fluids to be erupted at the seafloor and the Amsterdam mud-volcano (at 35°19.91’N, 30°16.12’E) at 2028 m is the most active (Lazar et al., 2012). The Texel mud-volcano is located near our station 24S, at 1600 m depth (Zitter, 2004) the Kula and San Remo mud-volcanos are at 1650 m and close to our station 26S. The Milano mud-volcano is at 1900 m at 34 N, 24.8 E (Bonini and Mazzarini, 2010). The Chefren mud-volcano at 2900

m (approximately south of station 21S, but not close to this station, at 32.6° N and 28,1° E) has been identified as a potential Fe source as its porewaters have very high Fe (II) concentrations (up to 1 mM; Omoregie et al., 2008). Also Southeast of Sicily near our station 11N mud-volcanos were discovered (Figure 1; Mascle et al., 2014).

It is conceivable that deep Fe sources can be formed by nepheloid layers, land, or due to steep topography and the sides of canyons, while most probably also mud-volcanos play a role.

3.6. Conclusions

The Mediterranean Sea and the Sea of Marmara have high DFe in the upper 100 m probably due to dissolution from dust. In almost all samples [L_t] was larger than DFe thus enabling the high DFe concentrations.

In the Sea of Marmara, vertical processes determined the DFe concentrations, which were elevated not only in the surface 20 m but well below the strong picnocline (22 to 38 g kg^{-1}).

Concentrations of DFe in the deep Mediterranean were either relatively low compared to the Atlantic Ocean, or relatively high in distinct patches. Deep DFe concentrations in the Mediterranean Sea were most likely low as a result of scavenging by sinking dust. This suggestion is the most probable explanation for our results and is supported by results from mesocosm experiments (Wagener et al., 2010).

The presence of distinct patches in deep waters with elevated DFe can only be explained by a combination of physical processes and sources at specific locations and depths. The outlines of the deep high DFe patches indicate lateral transport by, for example, mesoscale eddies from deep sources. These sources are probably diverse, and can be mud-volcanos, land and deep-sea mountains. Although no previous data is known about mud-volcanos as source of Fe and no supporting data such as an increase in particle density was observed, mud-volcanos were located at coinciding depths where high DFe patches were found. In most cases in these patches the [L_t] was higher than DFe, explaining that these high dissolved concentrations can exist and be maintained for longer time.

Calculated [Fe’] in deep waters were not below 0.23 pM. Apparently this is a steady state concentration due to competition between the Fe-binding dissolved organic ligands and scavenging particles. Lower [Fe’] does exist but only in the top 100 m in the Atlantic Ocean, at our station 1S, indicating that a phytoplankton bloom can lead to lower [Fe’].

Chapter 4

Dissolved Fe in the Deep and Upper Arctic Ocean with a Focus on Fe Limitation in the Nansen Basin

Published as

Rijkenberg, M.J.A., Slagter, H.A., Rutgers van der Loeff, M., van Ooijen, J., Gerringa, L.J.A., 2018. Dissolved Fe in the Deep and Upper Arctic Ocean With a Focus on Fe Limitation in the Nansen Basin. Front. Mar. Sci. 5, 1–14.

Abstract

Global warming resulting from the release of anthropogenic carbon dioxide is rapidly changing the Arctic Ocean. Over the last decade sea ice declined in extent and thickness. As a result, improved light availability has increased Arctic net primary production, including in under-ice phytoplankton blooms. During the GEOTRACES cruise PS94 in the summer of 2015 we measured dissolved iron (DFe), nitrate and phosphate throughout the central part of the Eurasian Arctic. In the deeper waters concentrations of DFe were higher, which we relate to resuspension on the continental slope in the Nansen Basin and hydrothermal activity at the Gakkel Ridge. The main source of DFe in the surface was the Trans Polar Drift (TPD), resulting in concentrations up to 4.42 nM. Nevertheless, using nutrient ratios we show that a large under-ice bloom in the Nansen basin was limited by Fe. Fe limitation potentially prevented up to 54% of the available nitrate and nitrite from being used for primary production. In the Barents Sea, Fe is expected to be the first nutrient to be depleted as well. Changes in the Arctic biogeochemical cycle of Fe due to retreating ice may therefore have large consequences for primary production, the Arctic ecosystem and the subsequent drawdown of carbon dioxide.

4.1. Introduction

The Arctic Ocean is the most rapidly changing region of our planet due to recent global warming (IPCC, 2013); yet the central Arctic belongs to the least studied parts of the Earth. Over the last decade, Arctic sea ice has been observed to decline in extent (Stroeve et al., 2012; IPCC, 2014; Serreze et al., 2016) and thickness (Haas et al., 2008; Serreze and Stroeve, 2015) and changed from multi-year sea ice into more first-year sea ice (Maslanik et al., 2011). The largest decrease occurred between 2007 and 2008 resulting in the export of a large part of the remaining thick ice through Fram Strait (Kwok et al., 2009). The Arctic sea ice reached a record minimum extent of 3.41 million km^2 on September 16, 2012 (National Snow and Ice Data Center, 2012) with the fourth lowest minimum on September 11, 2015 (National Snow and Ice Data Center, 2015).

Increased light penetration and nutrient availability during spring from earlier ice breakup enhances primary production in the Arctic Ocean and its adjacent shelf seas (Bhatt et al., 2014). The assumption has been for a long time that primary productivity is negligible in waters beneath ice because of insufficient light (Arrigo and Van Dijken, 2011). However, large under-ice blooms have been observed in the Barents Sea, Beaufort Sea, Canadian Arctic Archipelago, Chukchi Sea and also in the Nansen basin (Strass and Nöthig, 1996; Fortier et al., 2002; Mundy et al., 2009; Arrigo and Van Dijken, 2011; Ulfsbo et al., 2014) suggesting that under-ice blooms are widespread. Most studies expect nitrate to be the next limiting factor to determine primary productivity (Nishino et al., 2011; Vancoppenolle et al., 2013; Fernández-Méndez et al., 2015; Tremblay et al., 2015). However, in the Eurasian basin surface nitrate concentrations are significant and even persist in summer (Codispoti et al., 2013). Light limitation and/or grazing pressure have been suggested to prevent the full use of surface nitrate here (Olli et al., 2007; Bluhm et al., 2015).

Another consequence of global warming is the increase in river discharge (Peterson et al., 2002, 2006) which, combined with net loss of the Greenland ice-cap and melting of sea ice, can contribute to freshening of surface waters and increased stratification. However, the accumulation and distribution of this fresh water is strongly influenced by the Arctic circulation (Rabe et al., 2014). River discharge in the shelf-surrounded Arctic Ocean is a source of nutrients. These nutrients, including dissolved Fe (DFe) complexed by humic organic ligands (Laglera and van den Berg, 2009; Slagter et al., 2017), are transported in the upper 50m through the Arctic Ocean by the transpolar drift (TPD) from the Eurasian rivers over the central Arctic to Fram Strait (Gordienko and

Laktionov, 1969; Gregor et al., 1998). The TPD track varies annually depending on the Arctic Oscillation index (Macdonald et al., 2005).

These climate-induced changes will change the biogeochemical cycling and therefore the distribution of many trace elements and isotopes. Of these Fe has proven to be the most important trace element as its low concentrations limit primary production in 30–40% of the global surface ocean and therefore regulates ocean processes such as marine ecosystem dynamics and carbon cycling (de Baar et al., 2005; Boyd et al., 2007). We do not directly expect Fe limitation in the Arctic Ocean because of the above-mentioned input and transport of DFe, confirmed by Klunder et al. (2012a). However, the results of the present investigation proved otherwise. Arctic Ocean waters form an important part of the global thermohaline circulation (Aagaard et al., 1985; Rudels, 2015; Carmack et al., 2016). Changes in the Arctic biogeochemical cycle of Fe will not only affect the Arctic ecosystem but will affect also the chemical composition of for example the North Atlantic Deep Water. Gerringa et al. (2015) assumed that the Arctic is a source of Fe-binding dissolved organic ligands, since these decreased with distance from Fram Strait.

The deep water composition of DFe depends on the input of Atlantic water (200–900 m) with more elevated DFe in the Nansen Basin, and on slope processes with downwards convection of Fe released from resuspended sediments (Klunder et al., 2012b). A major source in the Nansen Basin is the hydrothermal activity at the Gakkel Ridge (Edmonds et al., 2003; Baker et al., 2004). These three processes are not expected to be rapidly affected by climate change. Scavenging, however, might be prone to changes due to a higher biological activity in the euphotic zone, influencing the flux of sinking particles. According to Klunder et al. (2012b) the reason why DFe in the deep Makarov Basin is so low, is that sources affecting the Nansen Basin are absent.

To investigate if climate change could affect the biogeochemical cycle of Fe in the Arctic Ocean we measured dissolved Fe, nitrate and phosphate throughout the central part of the Eurasian Arctic during the TransArcII expedition between August 15th and October 17th 2015 (FS Polarstern, PS94; Figure 1). We compared the DFe with earlier work of Klunder et al. (2012a,b) on surface and deep concentrations measured in 2007. We found a different hydrothermal source of Fe than discussed by Klunder et al. (2012b).Using nutrient ratios we showed that a large under-ice bloom in the Nansen basin was limited by Fe.

4.2. Methods and equipment

4.2.1. Sampling

A total of 28 stations were sampled for DFe during the GEOTRACES TransARC II cruise (PS94) on the German icebreaker RV Polarstern between 17 August and 14 October 2015 (Figure 1). Two CTD systems were used, a standard rosette sampling system equipped with a fluorometer for Chl a fluorescence and an "ultraclean CTD" sampling system; both were equipped with a SEABIRD 911 CTD. The temperature and salinity data from the standard sampling system were used for their higher spatial resolution (Rabe et al., 2016). The standard system also employed an uncalibrated fluorometer for CDOM measurement in

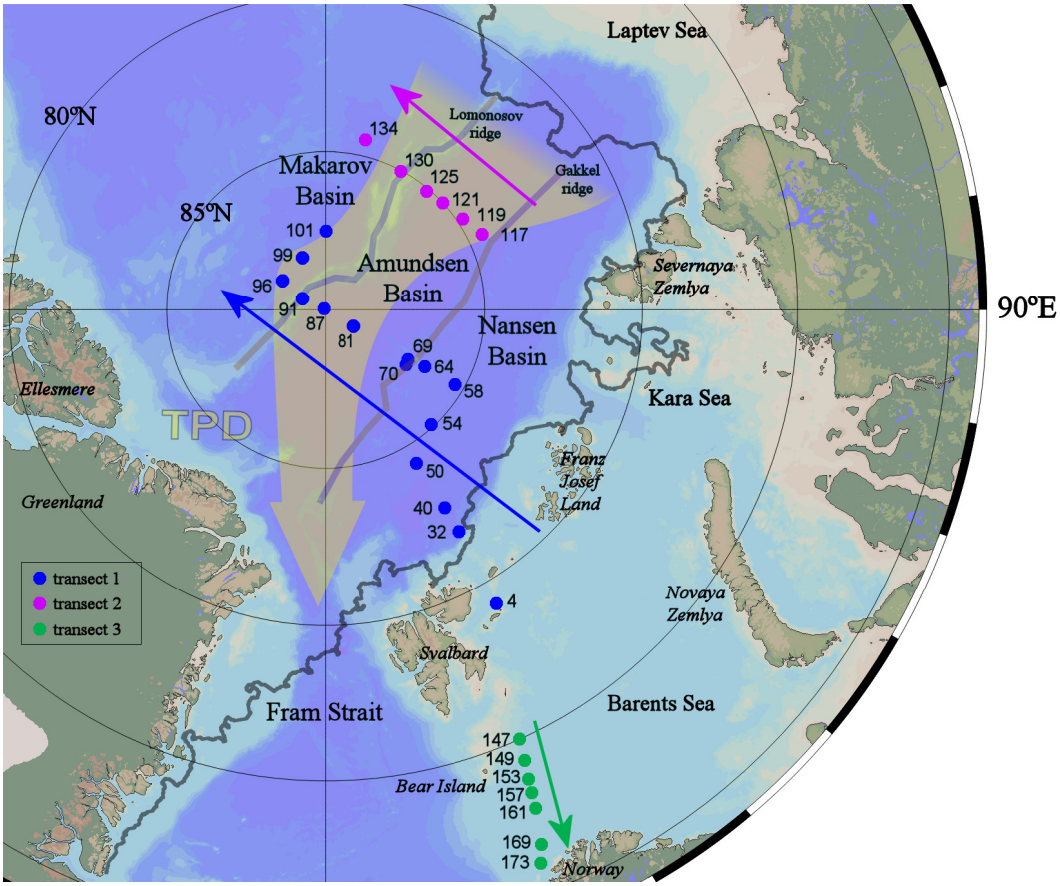

Figure 1: Station map of the ultraclean casts sampled during the TransARC II cruise (PS94) on the German icebreaker RV Polarstern in the summer of 2015.The direction of the Transpolar Drift is indicated with the broad grey-yellow arrow (Chapter 5). Stations numbers are given in three transects, 1-3, the arrows give the direction in which transects are presented in figures 2, 5-9. The grey line indicates the sea ice edge at the time of sampling station 32 (23 August 2015, NSIDC database, 2015). Map and all section plots following were generated using Ocean Data View 4 (Schlitzer, 2016).

arbitrary units (a.u.; BackScat, Dr. Haardt). Samples for DFe and nutrients were taken using 24 ultra-trace-metal clean polypropylene samplers of 24 L each mounted on an all titanium frame with a SEABIRD 911 CTD system and deployed on a 11 mm Dyneema cable without internal signal transduction cables. We used the SBE 17plus V2 Searam in a titanium housing to provide power, save the CTD data and close the sampling bottles at pre-programmed depths. After deployment, the complete "ultraclean CTD" was immediately placed in an ISO Class 6 clean room container, where samples for dissolved metals were filtered directly from the polypropylene samplers over < 0.2µm Sartobran 300 cartridges (Sartorius) under pressure of filtered N2 (0.7 bar) applied via the top-connector of the polypropylene sampler (de Baar et al., 2008; Rijkenberg et al., 2015). Filters were rinsed with approximately 700 mL seawater before use.

4.2.2. Calibration and detection limits

A five-point calibration in low iron containing seawater and blank determination were made daily. The blank was determined as the intercept of the signals of increasing preconcentration times (5, 10, 15 s) of the seawater used for the calibration. The analytical blank was on average 0.007 ± 0.004 nM DFe (N = 32) and the average detection limit (defined as 3σ of the blank pre-concentrated for 5 s) was 0.012 ± 0.007 nM DFe (N = 32). The Fe added by the Seastar acid (maximum ~0.4 pM) was ignored. Table 2 shows the measured DFe concentrations in SAFe and GEOTRACES reference samples and their consensus values. For the SAFeS1 consensus value our measurements, although low, fall within the uncertainty values (Johnson et al., 2007).

Table 1 Detection limits, precision and accuracy in µM of the nutrients. The precision in one run is calculated to check whether small differences in one run are significant. The accuracy of the measurements of Si in the reference material seems high, but the concentration is high.

	PO_4	Si	NO_2	NO_3
Detection limits	0.003	0.03	0.008	0.04
Precision Cocktail (in one run) n=12	0.002	0.06	0.002	0.02
Precision Cocktail (between runs) n=79	0.005	0.06	0.004	0.05
Precision Ref Mat. n=60	0.006	0.08	0.007	0.04
Accuracy Ref Mat. n=60	0.007	0.56	0.015	0.05

4.2.3. Fe Calculations*

In order to investigate whether Fe can reach growth-limiting values we define,

$$Fe^* = [DFe] - (Fe{:}GLnut) \times [GLnut]$$

where (Fe:GLnut) is the average biological uptake ratio of Fe over the growth-limiting macronutrient (GLnut).Which of the macronutrients is expected to be growth limiting can be determined from N/P plots. Surface waters in many samples outside the TPD are depleted in N, or N will be the first macronutrient to deplete when extrapolating the N/P slope. Therefore, the ratio Fe:GLnut will be the uptake ratio of Fe:N (RFe:N).

As we don't have any information about the Fe:nutrient ratios of the Arctic phytoplankton communities we used two extreme scenarios based on phosphate uptake ratios (RFe:P) from the literature assuming the Arctic phytoplankton community to have Fe:nutrient ratios in between. Using the two extreme scenarios, one with less strict limitation assumptions (RFe:P = 0.47 $mmol \cdot mol^{-1}$) and one with strict limitation assumptions (RFe:P = 0.18 $mmol \cdot mol^{-1}$), we show the minimum and maximum potential extent of Fe-limitation in the Nansen Basin. The less strict assumption (maximum extent Fe*) is hereafter indicated as scenario 1, the strict with scenario 2. The RFe:P of 0.47 $mmol \cdot mol^{-1}$ of scenario 1 was used in studies in Antarctic waters by Blain et al. (2008) and Lannuzel et al. (2011) after Parekh et al. (2005). The RFe:P of 0.18 $mmol.mol^{-1}$ of scenario 2 was recalculated based on the Redfield ratio (106C:16N:1P), using the average Fe:Cratio of 0.17 $\mu mol \cdot mol^{-1}$ in Fe limited Southern Ocean species according to (Strzepek et al., 2011), which is close to the 0.18 $\mu mol \cdot mol^{-1}$ obtained from Fe:AOU relationships by (Sunda, 1997). As N is the limiting macronutrient we have converted the reported RFe:P to RFe:N using 14.14, being the slope of the N/P plot at depths below 100 m in the Nansen Basin. A cut-off of 100 m was chosen since this is the maximum depth for primary production due to light limitation.

4.2.4. Calculation Percentage Unused Nitrogen due to Fe-Limitation

To calculate the percentage unused nitrogen due to Fe-limitation we integrated the sum of nitrate and nitrite concentrations over the upper 100m along our transect in the Nansen basin (PS94, Station 40, 50, 54, and 58) and subtracted the nitrogen used when all DFe would be fully used using the RFe:N of scenario 1 and 2 (Table 3). To express this as a percentage we used two estimates of the background nitrogen inventory in absence of a bloom. For the first estimate we integrated the sum of nitrate and nitrite concentrations over the upper 100 m of the Stations 255-1, 258-1, 260-2, 261-1 as measured during ARKXXII/2 (Klunder et al., 2012a). For the second estimate we integrated the sum of

nitrate and nitrite concentrations over 100–200 m in the Nansen Basin (PS94, Station 40, 50, 54, and 58).

Table 2 The values of SAFe and GEOTRACES reference samples for DFe measured on board using flow injection analysis based on luminol chemiluminescence during cruise PS94 in the Arctic Ocean. Also included are the SAFe and GEOTRACES intercalibration consensus values (http://www.geotraces.org/science/intercalibration). GS is a GEOTRACES surface reference sample and GD is a GEOTRACES deep reference sample.

reference sample	bottle#	element	measured value	n
			nmol kg^{-1}	
SAFe S	358	Fe	0.056 ± 0.004	3
GS	126	Fe	0.560 ± 0.044	10
GD	127	Fe	0.947 ± 0.041	9
SAFe D2	42	Fe	0.890 ± 0.046	7
SAFe D2	151	Fe	0.895 ± 0.021	6
SAFe D1	185	Fe	0.610 ± 0.082	10
Intercalibration consensus values as per May 2013:				
			reference value	
SAFe S		Fe	0.093 ± 0.008	
GS		Fe	0.546 ± 0.046	
GD		Fe	1.000 ± 0.100	
SAFe D2		Fe	0.933 ± 0.023	
SAFe D1		Fe	0.670 ± 0.040	

Table 3 The unused nitrogen due to Fe-limitation calculated for the different RFe:N in mmol mol^{-1} as used in scenario 1 and 2 as percentage of two different estimates of background of the sum of nitrate and nitrite

	RFe:N	background nitrate + nitrite	unused nitrogen *(%)*
Scenario 1	0.033239	nitrate + nitrite in 2007 (0-100m)	54
Scenario 2	0.01273	nitrate + nitrite in 2007 (0-100m)	8
Scenario 1	0.033239	nitrate + nitrite in 2015 (100-200m)	37
Scenario 2	0.01273	nitrate + nitrite in 2015 (100-200m)	5

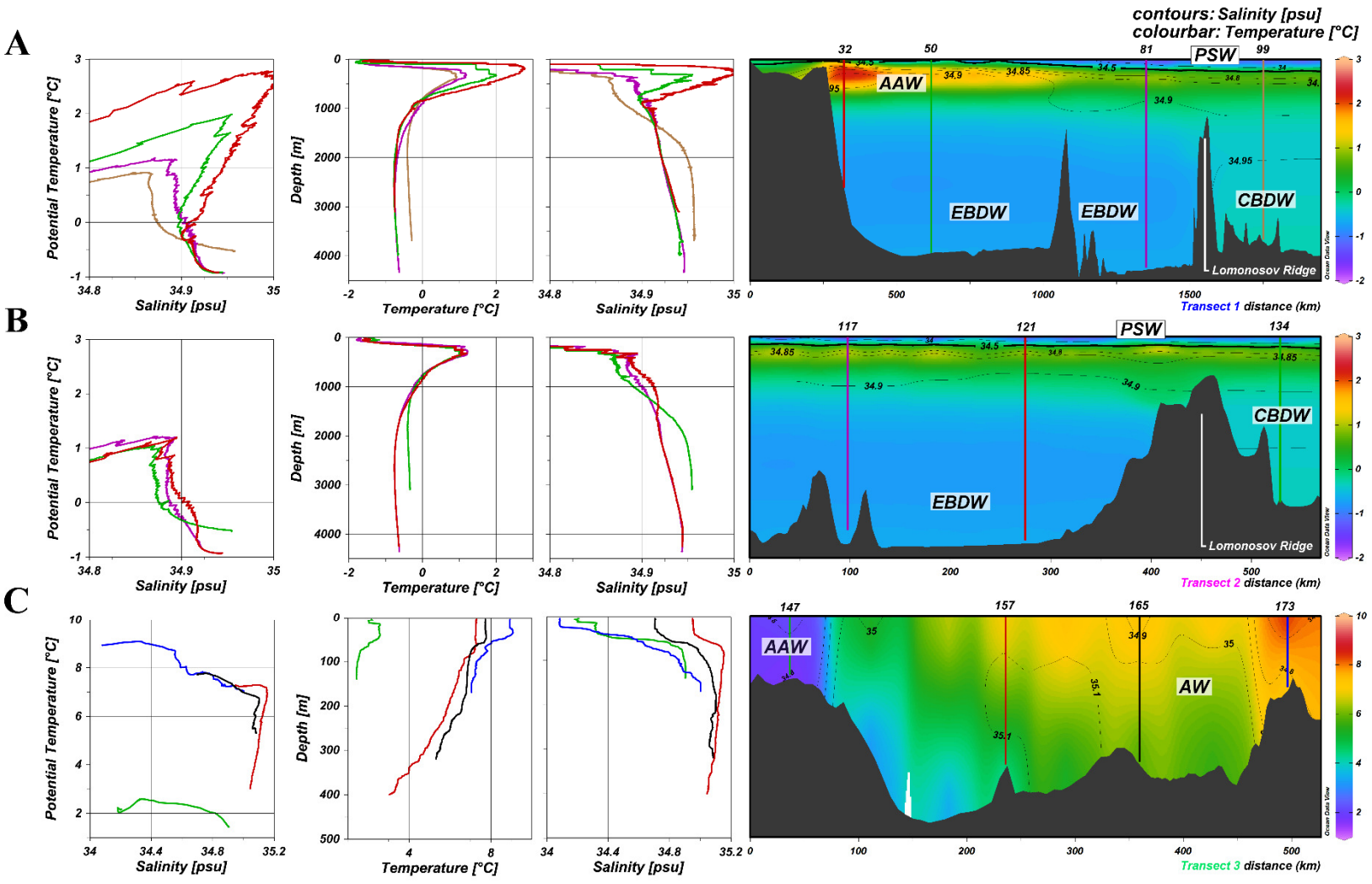
A
B
C
contours: Salinity [psu]
colourbar: Temperature [°C]
Potential Temperature [°C]
Salinity [psu]
Depth [m]
Temperature [°C]
AAW
PSW
EBDW
CBDW
AW
Lomonosov Ridge
Transect 1 distance (km)
Transect 2 distance (km)
Transect 3 distance (km)
Ocean Data View

Figure 2 (page 70)
TS profiles and section plots of Transects 1-3. At the left side property-property plots show potential temperature versus salinity (T-S, left) followed by depth profiles of potential temperature (middle) and salinity (right) for those stations indicated in the section plots of temperature (colourbar) and salinity (contours) of the transects (far right). Station numbers are indicated above the transects. Polar Surface Water (PSW), Eurasian Basin Deep Water (EBDW), Canadian Basin Deep Water (CBDW) Atlantic Water (AW) and Arctic Atlantic Water (AAW) are indicated in the temperature sections. T-S plots are scaled to detail small-scale variations to help characterize water masses after (Rudels, 2008, 2012). Salinities of 34.5 are indicated in a thicker contour denoting the PSW border (Rudels, 2008). Note the difference in scale for the transect 3 colour bar.

4.3. Results

4.3.1. Hydrography

The hydrography of the Transects I and II is described in detail by Slagter et al. (2017; Chapter 5) using definitions by (Rudels, 2008, 2012) and is repeated here briefly (Figures 2A,B). The Polar Surface Water (PSW) influenced by sea ice melt and river water is characterized by potential temperatures <0 °C and salinities <34.5. In the Central Arctic the PSW flows into the direction of Fram Strait in the TPD (Gordienko and Laktionov, 1969; Gregor et al., 1998; Macdonald et al., 2005). Atlantic Water enters the Arctic Ocean via Fram Strait and is then called Arctic Atlantic Water (AAW), becoming colder and fresher on its flow path along the continental slopes of the Nansen and Amundsen Basins. This water mass between 200 m and 900 m has potential temperatures >0 °C and higher salinities than the PSW and, in the Eurasian Basin, the underlying deep water. The Lomonosov Ridge (sill depth approximately 2,000 m) separates the Eurasian Basin Deep Water (EBDW) in the Nansen and Amundsen Basin with potential temperatures down to −1 °C from the warmer and saltier Canadian Basin Deep Water (CBDW, Figure 2).

One branch of the Atlantic water enters the Arctic Ocean via the Barents Sea (Figure 2C) resulting in high potential temperatures and salinities (Rudels, 2012). The potential temperature decreases northward from Stations 173 to the AAW at Station 147, close to Bear Island. However, at the stations close to the Norwegian Coast the salinity in the upper 100m is lower than at similar depths in the central Barents Sea, pointing to river input.

N was the limiting macronutrient in all surface waters during PS94 (Figure 3).

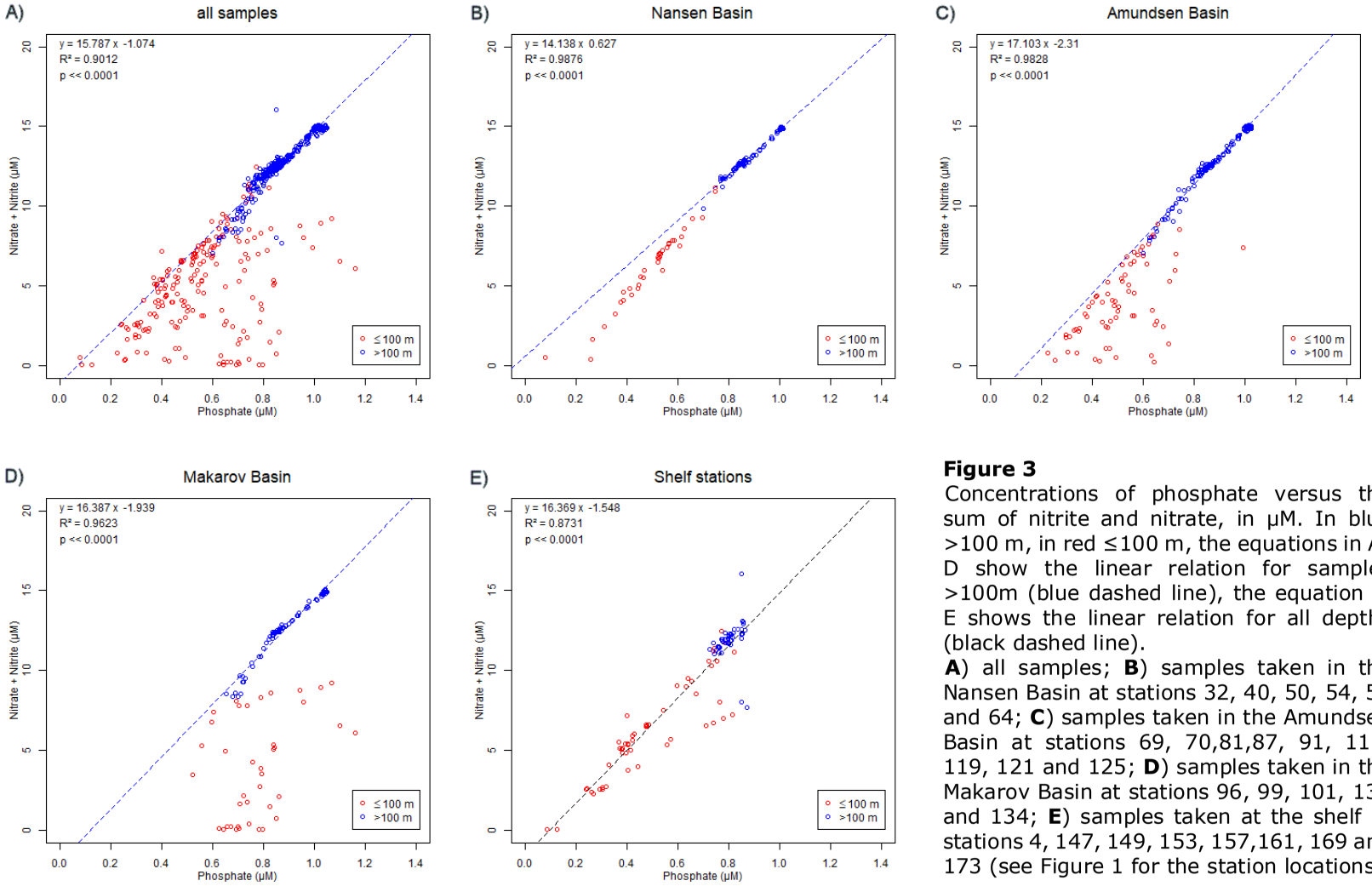

Figure 3
Concentrations of phosphate versus the sum of nitrite and nitrate, in µM. In blue >100 m, in red ≤100 m, the equations in A-D show the linear relation for samples >100m (blue dashed line), the equation in E shows the linear relation for all depths (black dashed line).
A) all samples; **B**) samples taken in the Nansen Basin at stations 32, 40, 50, 54, 58 and 64; **C**) samples taken in the Amundsen Basin at stations 69, 70,81,87, 91, 117, 119, 121 and 125; **D**) samples taken in the Makarov Basin at stations 96, 99, 101, 130 and 134; **E**) samples taken at the shelf at stations 4, 147, 149, 153, 157,161, 169 and 173 (see Figure 1 for the station locations).

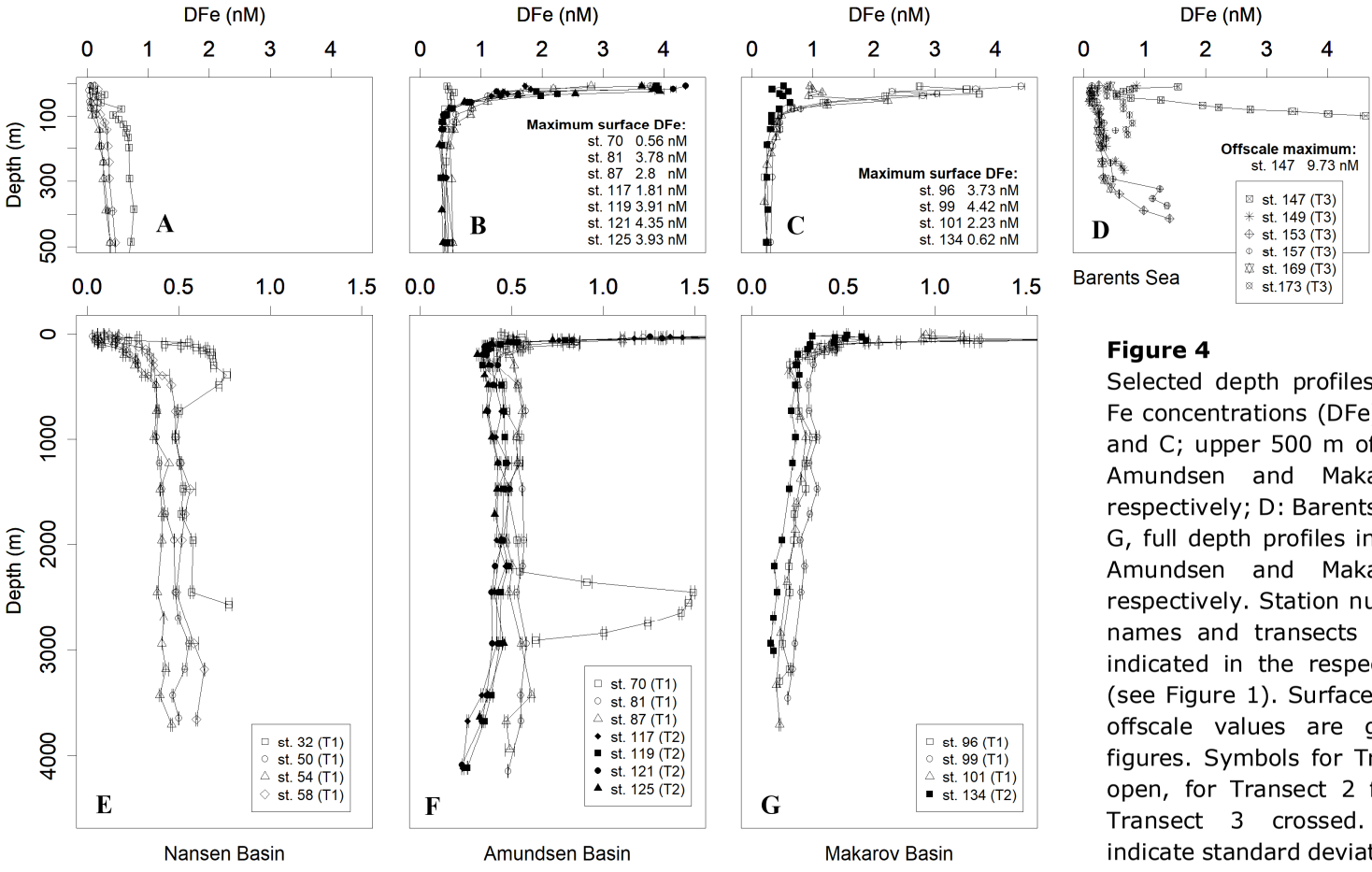

Figure 4

Selected depth profiles of dissolved Fe concentrations (DFe) in nM. A, B, and C; upper 500 m of the Nansen, Amundsen and Makarov Basins, respectively; D: Barents Sea, E,F and G, full depth profiles in the Nansen, Amundsen and Makarov Basins, respectively. Station numbers, basin names and transects numbers are indicated in the respective legends (see Figure 1). Surface maxima and offscale values are given in the figures. Symbols for Transect 1 are open, for Transect 2 filled and for Transect 3 crossed. Error bars indicate standard deviations (N= 2 or 3). Most error bars fall inside of the symbols.

4.3.2. DFe

In the upper 100 m of the Nansen Basin DFe concentrations were extremely low and ranged between 0.03 and 0.21 nM (Stations 32, 40, 50, 54, 58, 64; Figures 4A, 5A). At Station 32 in the transition between the Nansen Basin and the Barents Shelf, DFe concentrations were low in the surface but ranged between 0.48 and 0.77 nM at depths below 100 m. These DFe concentrations were higher than those found at similar depths at the more northerly stations in the central Nansen Basin (Stations 40–58, 0.34, and 0.5 nM). This reflects both the inflow of Atlantic water in the upper 1,000 m and the effect of sediment resuspension at depths below 2,600 m, confirming findings by Klunder et al. (2012b) (Figures 4E, 5B). At the Gakkel Ridge (Station 70) a hydrothermal vent (Edmonds et al., 2003; Baker et al., 2004) resulted in deep DFe concentrations between 0.91 and 1.50 nM at depths between 2,300 m and 2,850 m (Figures 4E, 5B).

In the Amundsen and Makarov Basins, DFe in the upper 100 m was high within the boundaries of the TPD, defined in Chapter 5 as in-situ CDOM fluorescence ≥0.5 a.u. (0.5–4.42 nM, Stations 81–101; Figures 4B,C, 6A). Silicate and phosphate were also high in the TPD whereas nitrate was only slightly elevated compared to the same depths outside the TPD (Chapter 5). Station 117 at the rim of the TPD had lower DFe concentrations of 0.51–1.81 nM, whereas at Station 134 outside the TPD, DFe was even lower with 0.32–0.62 nM at depths <100 m (Figures 4B, C, 6A). In the Amundsen Basin the deep DFe concentrations remain between 0.5 and 0.6 nM at Stations 81–87 in Transect 1, but are lower between 0.32 and 0.45 nM at Stations 117–125 in Transect 2 in the more Eastern part of the Amundsen Basin (Figures 4F, 5B, 6B). In the Makarov Basin the deep DFe concentrations are even lower (0.10–0.36 nM at Stations 91–101, Figures 4G, 5B and Station 134, Figures 4G, 6B).

The DFe concentrations in the Barents Sea (Transect 3, Figures 4D, 7) are higher than in the central Arctic. Concentrations in the surface vary from 1.54 nM at Station 147 to 0.09–0.24 nM at Stations 149–161 and 0.4 nM at Station 169–172. The deep concentrations vary even more, from9.73 nM at Station 147 to 0.47–1.41 nM at the other stations.

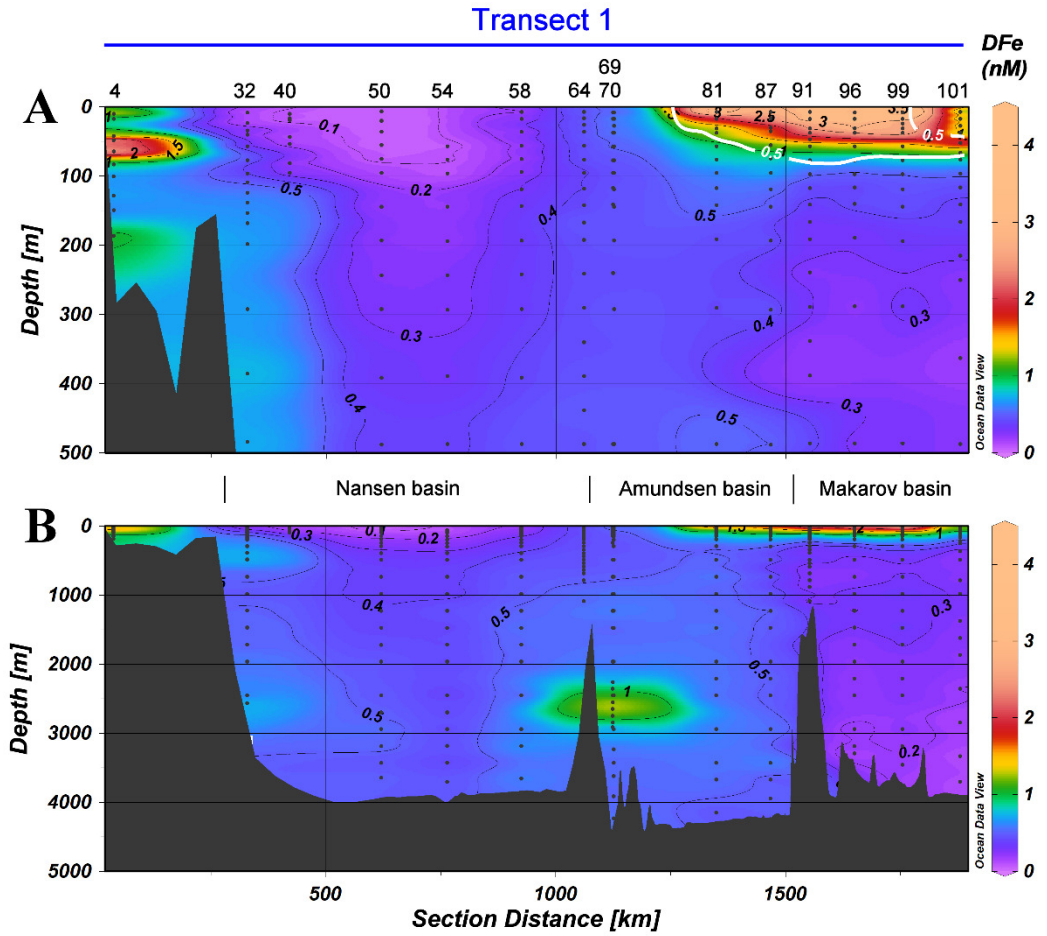

Figure 5 DFe in nM in Transect 1, with **A**) the top 500m and **B**) the full depth. Station numbers and basin names are given (see Figure 1). The white contours indicate the border of the TransPolar Drift as defined in Chapter 5, which was operationally defined as in-situ CDOM fluorescence ≥0.5 a.u. during the same cruise. Black contours indicate DFe and have an equidistance of 0.1 nM for the range 0≤DFe≤0.5 nM and of 0.5 nM for the range 0.5<DFe≤4.5 nM.

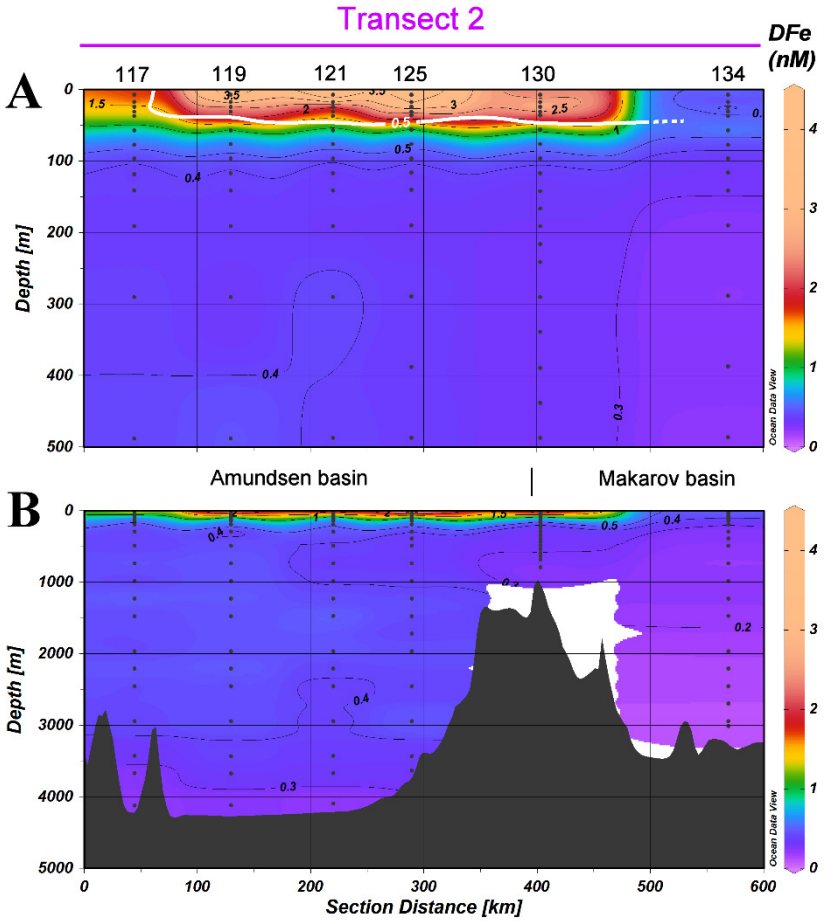

Figure 6 DFe in nM in Transect 2, with A the top 500m and B the full depth. Station numbers and basin names are given (see Figure 1). The white contours indicate the border of the TransPolar Drift as defined in Chapter 5, which was operationally defined as in-situ CDOM fluorescence ≥0.5 a.u. during the same cruise. Black contours indicate DFe and have an equidistance of 0.1 nM for the range 0≤DFe≤0.5 nM and of 0.5 nM for the range 0.5<DFe≤4.5 nM.

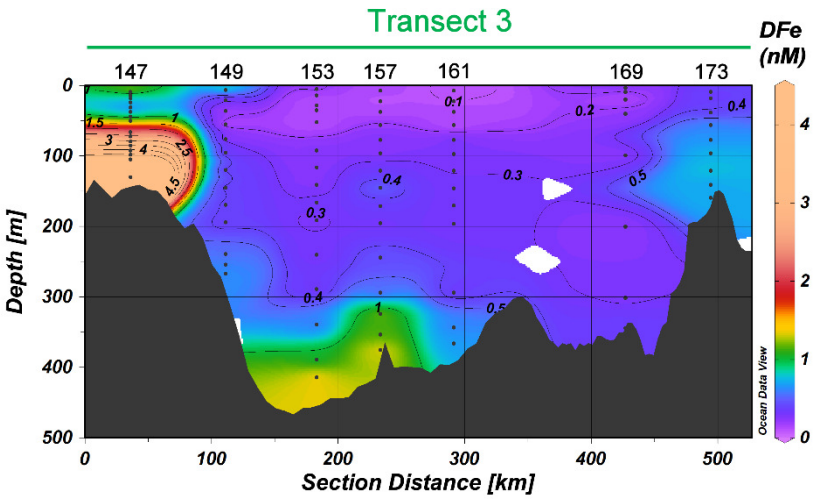

Figure 7 DFe in nM in Transect 3. Station numbers are given (see Figure 1). Black contours indicate DFe and have an equidistance of 0.1 nM for the range 0≤DFe≤0.5 nM and of 0.5 nM for the range 0.5<DFe≤4.5 nM.

4.4. Discussion

4.4.1. Deep Basins

Sources of DFe to the deep Arctic are shelf seas, sediments and hydrothermal vents. (Klunder et al., 2012b) concluded that Atlantic water transported through Fram Strait carried DFe into the Nansen Basin (Figure 2). This was also the source of the enhanced DFe at Station 32 between approximately 75 m and 750 m (Figures 4A, E, 5), where elevated DFe concentrations coincided with an increase in the potential temperature and salinity. At our Station 32 below 2,000 m DFe was also elevated suggesting local sediment resuspension at the slope as a source of DFe (Figures 4E, 5; Middag et al., 2011; Klunder et al., 2012b).

In general, with the exception of Station 70, we see that DFe concentrations stayed constant or changed slightly between 1,000 m and the bottom throughout the central Nansen and Amundsen basins (Figure 4). Deep DFe concentrations were similar or slightly lower than deep DFe concentrations in the North Atlantic and the North pacific (Moore and Braucher, 2008; Klunder et al., 2012b; Rijkenberg et al., 2014). It is possible that a higher scavenging rate indicated by stronger ^{230}Th scavenging as observed during this same expedition (Valk et al. *submitted*) explains the lower deep DFe concentrations. In the Makarov basin, DFe concentrations decreased below 100 m toward the bottom (Transect 1 & 2, Figure 4G). The overall low DFe concentrations decreasing toward the bottom are probably due to the absence of Fe sources in the Makarov

Basin (Thuróczy et al., 2011; Klunder et al., 2012b). However, not only DFe decreased with depth in the Makarov Basin, also the saturation state of the Fe-binding organic ligands decreased with depth in contrast to the Eurasian Basins (Thuróczy et al., 2011; Slagter et al., 2017). This needs additional explanation and indicates that scavenging might play a role here. Fitzsimmons et al. (2017) showed the important role the dissolved organic ligands play in the exchange between different dissolved and particulate Fe species in a hydrothermal plume in the S-E Pacific. They describe reversible scavenging processes between dissolved species, colloids and particles, where the driving factor is the presence of empty sites of the organic ligands. Scholten et al. (1995) found that the scavenging residence time of ^{230}Th was shorter in the Eurasian Basins than in the Makarov Basin. During the same expedition of the present study, Valk (pers. comm.) found even higher ^{230}Th residence times in the Makarov Basin than Scholten et al. (1995). However, the residence time of water in the deep Canadian Basins is longer (~300 years) compared to the Eurasian Basins (~200 years; Tanhua et al., 2009). According to Gerringa et al. (2015) the residence time of Fe-binding organic ligands in the North Atlantic Deep Water is 2.5–4 times that of DFe. So perhaps a longer exposure to less scavenging had a net removal result for organically complexed dissolved Fe, which has not necessarily been recorded in the ^{230}Th signal. Our results again show how important it is to understand and quantify the scavenging of DFe. (Tagliabue et al., 2016) raises poorly constrained scavenging rates as key priority for improving the modelling of iron in global ocean biogeochemistry models.

Hydrothermal input was found near the Gakkel Ridge with elevated DFe in the Amundsen Basin (Figures 4F, 5), as was also observed by Middag et al. (2011) and Klunder et al. (2012b). The position of the hydrothermal vent at the Gakkel Ridge in 2007 during ARKXXII/2 was 85°39’N, 84°50’E. We found hydrothermal activity in a more western direction at station 70 at 86°57’N and 55°49’E, one of the many vent positions of the Gakkel Ridge (Edmonds et al., 2003; Baker et al., 2004).

Klunder et al. (2012b) reported average concentrations for the Nansen, Amundsen and Makarov Basins >250 m depth of 0.70 ± 0.25, 0.47 ± 0.11, and 0.39 ± 0.19 nM, respectively, for the 2007 expedition. Averages from the same depth for our 2015 study were 0.47 ± 0.10, 0.51 ± 0.21, 0.24 ± 0.06 nM, respectively. These data compare well although our data were lower in general. Apparently Klunder et al. (2012b) sampled in more hydrothermally influenced areas in the Nansen Basin, than we did in the Amundsen Basin, as shown by higher average concentrations and standard deviations.

4.4.2. Surface and Shelf

Sources of DFe to the surface Arctic Ocean are sea ice melt, atmospheric inputs, lateral input from land with rivers as the main contributor, Atlantic inflow and mixing with deep water.

Sea ice melt is found to be important in the Gulf of Alaska and the Bering Sea (Aguilar-Islas et al., 2008, 2016) which feeds the coastal blooms alleviating Fe limitation; but we did not find distinct proof of the importance of sea ice melt as an Fe source in the Arctic during our cruise. However, Lam et al. (2006) concluded that melting sea ice provided substantial DFe to the water column. The additional DFe input from melting sea ice is thought to become important for biological uptake for under ice and ice edge blooms. Most of our stations in Transects 1 and 2 had sea ice cover (Stations 32-134 were ice covered, Figure 1), and DFe concentrations were low outside the TPD (Figures 4A–C, 5). Apparently microbial utilization hid any contribution from melting sea ice at these locations.

Although the potential influence of dust input is acknowledged not much is known from dust input in the Arctic Ocean (Bullard, 2017). In Transect 3 we did see increased DFe in the surface at Station 147 (Figures 4D, 7). Although this might be due to dust input, as DFe concentrations were high throughout the depth profile, lateral transport from Svalbard, Bear Island (North of Station 147) or sediment resuspension may be more likely explanations. The CTD transmission data (not shown) was slightly lower at stations in the Barents Sea (4.35–4.55 a.u.) compared to the deep open Arctic (4.62– 4.63 a.u.). In the Barents Sea the transmission became lower in the 100 m toward the bottom, with a corresponding increase in DFe (Figures 4D, 7) except at Station 169 and 173, where no transmission data was available (Station 173) and DFe did hardly increase near the bottom (both 169 and 173).

According to literature (Lam et al., 2006; Brown et al., 2012) lateral transport from the coast, shelves and land-fast-glaciers, with or without further transport by mesoscale eddies, is feeding the blooms over nearby Canadian Basin. In the present study the major driver of such lateral transport is the TPD (Gordienko and Laktionov, 1969; Gregor et al., 1998; Macdonald et al., 2005). The TPD is the major surface current over the Arctic Ocean transporting sea ice and river water from the Arctic shelf seas toward Fram Strait. Its influence on the distribution of Fe is distinct (Klunder et al., 2012a; Slagter et al., 2017). According to Klunder et al. (2012a) ice melt resulted in a relatively small increase in DFe relative to the effect of the TPD. Outside the TPD, in the Nansen Basin (Stations 32, 40, 50, 54, 58, and 64), surface concentrations of DFe were very low and coinciding with under ice bloom (Figures 5, 8).

To investigate if Fe could become a limiting factor for this under ice bloom preventing the full use of the macronutrients, as described in the method section (Fe^* <0), we calculated Fe^* for both the Klunder data as well as our own (Parekh et al., 2005; Blain et al., 2008; Lannuzel et al., 2011). Nitrogen is generally considered to be the limiting macro nutrient in the Arctic Ocean (Nishino et al., 2011; Vancoppenolle et al., 2013; Fernández-Méndez et al., 2015; Tremblay et al., 2015) and was the limiting macronutrient during PS94 (Figures 3A–E). Using the data of Klunder et al. (2012a), potentially Fe-limiting waters were only found at depths below 300 m in the Makarov basin. These Fe^* values <0 coincide with low DFe explained by scavenging of DFe by particles (Thuróczy et al., 2011; Klunder et al., 2012b). However, in the present study we do find Fe limitation in the Nansen Basin (Transect 1). All results showed Fe^* <0 in the surface of the Nansen Basin. The extent of potential Fe limitation (Fe^* <0) depends on the assumptions (Figure 9). It is unknown what the biological uptake ratio and its variation is in the Arctic Ocean. Twining et al. (2015) showed that RFe:P varied significantly between phytoplankton species in the North Atlantic Ocean. We show that Fe-limitation exists in the Nansen Basin under any known RFe:P (Figure 9A). However in Transect 2 and 3 only phytoplankton with higher Fe requirements will become Fe limited. Our stringent RFe:P has lower Fe requirements as obtained via N:P found for phytoplankton in the Canadian Basin representative for those shelf seas by Mills (personal communication by Mills referring to Tremblay et al., 2008; Bergeron and Tremblay, 2014; Mills et al., 2015), using that N:P ratio the area of Fe^* <0 occurrence would be larger.

Along Transect 3 DFe is also low (i.e., 0.08 nM at Station 169 at 10–25 m depth) and the macronutrient concentrations between Stations 153 and 169 are not depleted. The N:P slope for depths >100 m is inconclusive here. Extrapolating the N:P slope for all depths (Figure 3E), nitrogen would be the first to be depleted, but phosphorous would also be low. Like Transects 1 and 2 we used nitrogen as macronutrient to calculate Fe^*, and indeed Fe^* <0 also occurs here, though only in scenario 1 (Figure 9).

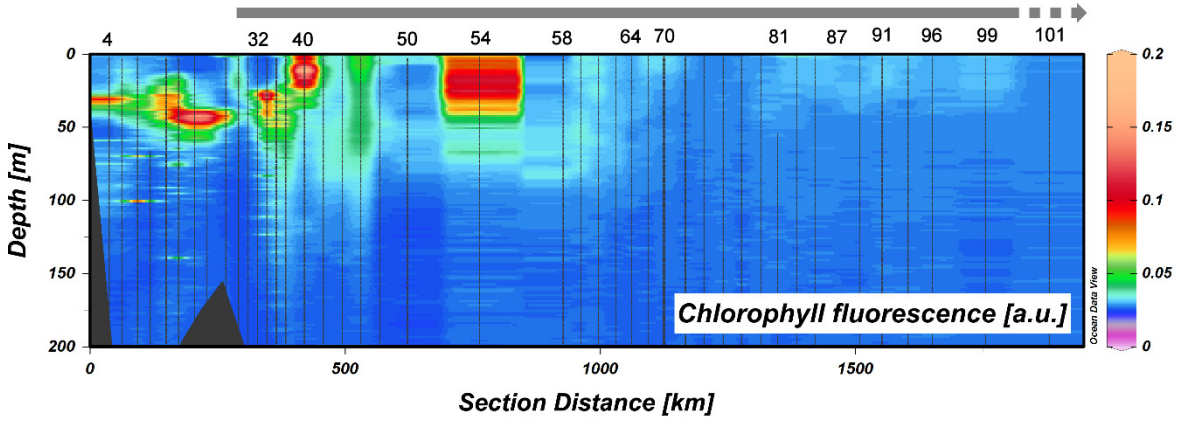

Figure 8
Chlorophyll a fluorescence in arbitrary units in the upper 200 m of Transect 1. Station numbers are given and the thick grey line at the top indicates sea ice cover (see Figure 1).

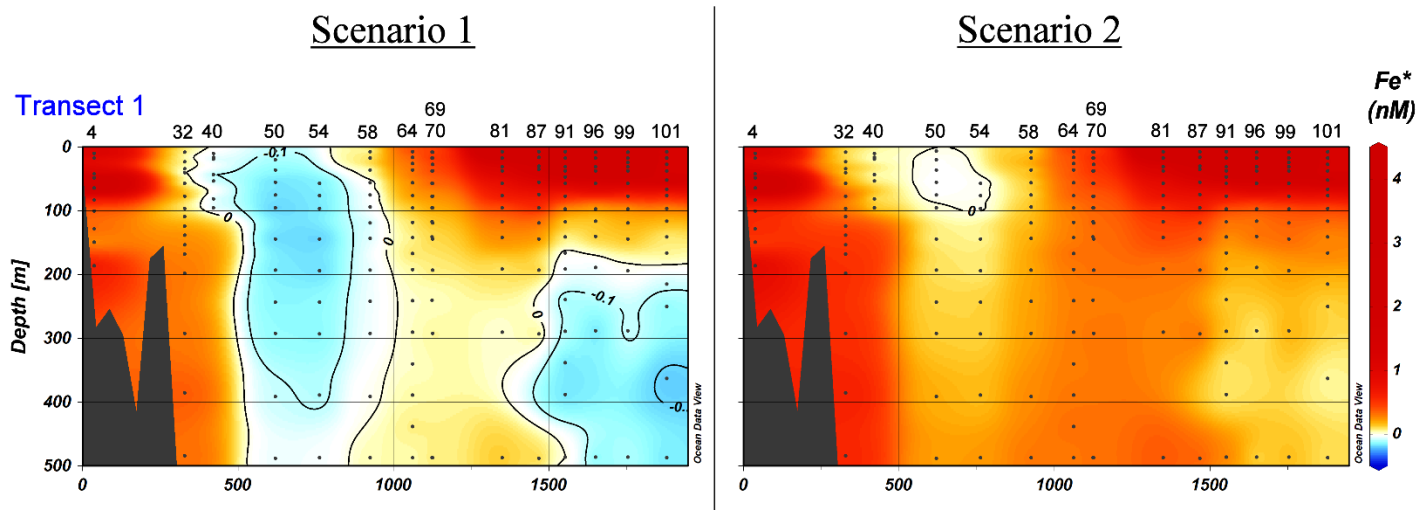

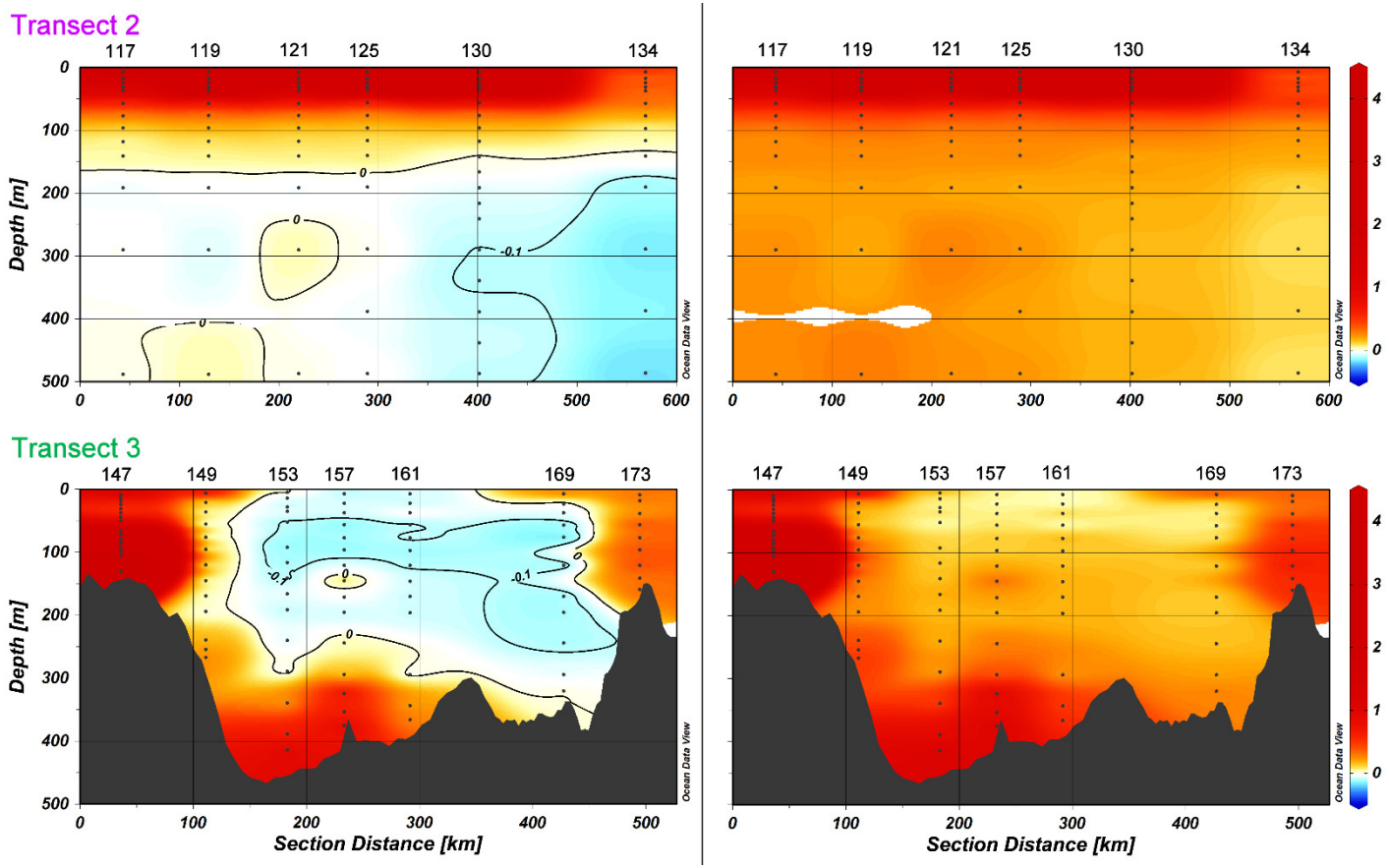

Figure 9 Fe* in nM in the upper 500 m and full depth of Transects 1 (page 81), 2 and 3 (page 82) according to two scenarios. Scenario 1 (A) and scenario 2 (B). The black contour indicates where F*≤0, with an equidistance of -0.1 nM. Station numbers and basin names are given (see Figure 1).

The increase of light by melting of the sea ice and the subsequent increase of primary production, and as a consequence a larger consumption of available nutrients, has been discussed by others predominantly in the Pacific part of the Arctic Ocean (Arrigo et al., 2008; Tremblay and Gagnon, 2009; Vancoppenolle et al., 2013; Bhatt et al., 2014). Nitrogen limitation has been anticipated to occur (Vancoppenolle et al., 2013; Bluhm et al., 2015). However, the possibility of Fe limitation has not yet had any attention, although Taylor et al. (2013) found co-limitation by light, nitrate, and iron in culture experiments in the Beaufort Sea. In the Eurasian Basin Codispoti et al. (2013) and Bhatt et al. (2014) both mention light and grazing as the reason why macronutrients are not removed, in contrast to our results. Empirically based extrapolations presented by Arrigo and Van Dijken (2011) show that when the Arctic sea ice cover during summer minimum falls to zero, total annual primary production could reach ~730 TgC $year^{-1}$ (a ~48% increase over the 1998–2009 average). In a warming Arctic Ocean, ice cover decreases releasing primary producers from light limitation. We here show that Fe may become the next limiting factor. In the Nansen Basin, depending on the RFe:N scenario and the estimate of the background concentration of nitrate + nitrite, between 5 to 54% of available nitrate + nitrite would remain unused for the production of biomass due to Fe limitation (Table 3).

The TPD, driven by Atlantic and Pacific inflow to the shelf seas with an estimated transition time across the Arctic Ocean of 3 years (Gregor et al., 1998), forms an important distribution pathway for DFe from the rivers and the shelves to the surface of the Eurasian Central Arctic. The TPD track and relative contributions of the different shelf seas is known to vary with the Arctic Oscillation index (Macdonald et al., 2005). Surface concentrations of DFe inside the TPD are expected to be dictated by a strong riverine influence (Bauch et al., 2011; Klunder et al., 2012a; Roeske et al., 2012; Rutgers van der Loeff et al., 2012; Chapter 5). One major impact of climate change is the thaw of permafrost soil (Stedmon et al., 2011; Schuur et al., 2015) resulting in an increase in DOM released into the Arctic Ocean (Vonk et al., 2012, 2013). These rivers also transport Fe containing particles and colloids into the Arctic Ocean contributing to an increase in DFe (Hirst et al., 2017). Chapter 5 shows that transport of DFe with the TPD through the Arctic Ocean is facilitated by complexation with humic substances as part of DOM. We could therefore expect that the TPD will become more important in the distribution of DFe throughout the Arctic Ocean and via Fram Strait to the Atlantic Ocean.

4.5. Conclusions

This study identified sediment resuspension along the continental slope and hydrothermal venting at the Gakkel Ridge as sources of DFe to the deep Nansen and Amundsen basins, respectively, confirming the findings of (Klunder et al., 2012b). The longer residence time of the deep water together with the absence of sources of DFe to the deep Makarov basin results in concentrations of DFe decreasing toward the bottom due to the net removal of DFe by scavenging. Scavenging of Fe and other trace elements is the most important sink warranting further research.

The most important source of DFe to the surface of the Arctic Ocean is the TPD, transporting river water with high concentrations of Fe complexed by organic ligands (Chapter 5) from the Arctic shelf seas toward Fram Strait. As an effect of climate change, the increase of DOM entering the Arctic Ocean with the rivers may allow more Fe to be organically complexed in the dissolved phase and transported by the TPD. Climate change resulting in sea ice melt and therefore increasing light availability will increase DFe uptake by increasing primary production. In the present study we found Fe to be limiting in the Nansen Basin. Depending on the Fe requirements of the Arctic microbial community Fe has the potential to also limit primary production in the Barents Sea. So depending on how climate change will affect the role of the TPD in the provision of DFe to the surface of the Arctic Ocean Fe limitation may either be alleviated or exacerbated in a future Arctic Ocean.

Chapter 5

Organic Fe speciation in the Eurasian Basins of the Arctic Ocean and its relation to terrestrial DOM

Published as:
Slagter, H.A., Reader, H.E., Rijkenberg, M.J.A., Rutgers van der Loeff, M., de Baar, H.J.W., Gerringa, L.J.A., 2017. Organic Fe speciation in the Eurasian Basins of the Arctic Ocean and its relation to terrestrial DOM. Mar. Chem. 197, 11–25.

Abstract

The bio-essential trace metal iron (Fe) has poor inorganic solubility in seawater, and therefore dissolution is dependent on organic complexation. The Arctic Ocean is subject to strong terrestrial influences which contribute to organic solubility of Fe, particularly in the surface. These influences are subject to rapid changes in the catchments of the main contributing rivers. Here we report concentrations and binding strengths of Fe-binding organic ligands in relation to spectral properties of Dissolved Organic Matter (DOM) and concentrations of humic substances. Full-depth profiles of Fe and Fe-binding organic ligands were measured for 11 stations, good agreement to previous studies was found with ligand concentrations between 0.9 and 2.2 Equivalent nM of Fe (Eq. nM Fe) at depths > 200 m. We found nutrient-like profiles of Fe in the Atlantic-influenced Nansen basin, surface enrichment in the surface over the Amundsen and Makarov basins and scavenging effects in the deep Makarov basin. A highly detailed surface transect consisting of two sections crossing the surface flow from the Siberian continental shelf to the Fram Strait, the TransPolar Drift (TPD), clearly indicates the flow path of the riverine contribution to Fe and Fe-binding organic ligands with concentrations of 0.7 to 4.4 nM and 1.6 to 4.1 Eq. nM Fe, respectively. This is on average 4.5 times higher in DFe and 1.7 times higher in Fe-binding organic ligands than outside the TPD flow path. Conditional binding strengths of ligands in the entire dataset were remarkably similar at $11.45 \leq \mathrm{LogK'_{Fe'L}} \leq 12.63$. Increased organic Fe-binding organic ligand concentrations were evident in the Arctic Ocean surface. To better identify the organic substances responsible for Fe complexation in the Arctic Ocean, diverse analytical approaches and a standard other than Suwannee River Fulvic Acid are recommended.

5.1. Introduction

Iron is an essential trace element for marine primary production. It is an essential component for phytoplankton photosynthesis (Geider and La Roche, 1994) and eukaryotic DNA replication (Netz et al., 2012; Zhang, 2014). Fe concentrations in the oceans are low, and in many areas even limiting phytoplankton growth (de Baar et al., 1990; Martin et al., 1990). Poor solubility of Fe in seawater limits inorganic Fe concentrations, depending on temperature, with lower temperatures increasing Fe solubility only in the picomolar range at seawater pH of 8.05. At room temperature the solubility of freshly precipitated Fe is ~0.08 nM, and for aged oxides it is even lower ~0.01 nM (Millero, 1998; Liu and Millero, 2002). Dissolved Fe concentrations higher than the inorganic solubility must be facilitated by complexation with a dissolved organic ligand (Gledhill and van den Berg, 1994; Rue and Bruland, 1995). These organic ligands are diverse in nature, and relative contributions to this ligand pool are poorly understood (Gledhill and Buck, 2012; Hassler et al., 2017). Known constituents are specific Fe-binding ligands purpose-produced by bacteria called siderophores (Butler, 2005; Mawji et al., 2011). Other constituents include polysaccharide exudates (exopolysaccharides, or EPS) from bacteria and phytoplankton (Hassler et al., 2011b, 2011a), the release of cytosol contents due to viral lysis (Poorvin et al., 2011) and humic substances of terrestrial origin (Laglera et al., 2011). While the highest concentrations of Fe-binding organic ligands sometimes correlate with biological activity (Rue and Bruland, 1995; Gerringa et al., 2006, 2016), this is often not the case as described by Gerringa et al. (2015), which would then indicate non-biological or more indirect contributors to the diverse organic Fe-binding organic ligand pool.

The Arctic Ocean is a shelf-surrounded ocean and the surface waters are strongly terrestrially-influenced as described in detail by Rudels (2012). Typically the world oceans have a low source area to basin ratio (Raiswell and Anderson, 2005), whereas the abundant Arctic shelf seas subject the Arctic Ocean to very high fluvial discharge (Stedmon et al., 2011). The introduction of river water to the Polar Surface Water (PSW) from the Siberian shelf areas is the largest terrestrial input to Eurasian Basins. This influence can be measured by a number of biogeochemical tracers of terrestrial and/or meteoric input into the Arctic Ocean. Examples are $\delta^{18}O$ in conjunction with nutrients indicating the separate inputs meteoric water and sea ice melt (Klunder et al., 2012a; Bauch et al., 2016), with the recent addition of Neodymium and other rare earth elements serving to better separate these properties in terms of the influence of the major water masses (Laukert et al., 2017). Additionally, elevated dissolved Fe (Klunder et al., 2012a) and dissolved Mn (Middag et al., 2011)

indicate river water and the ^{228}Ra isotope indicates continental shelf influence (Rutgers van der Loeff et al., 1995). These tracers show surface transport along the TransPolar Drift (TPD). The TPD moves sea ice and surface water from the Siberian great rivers across the Arctic Ocean, and eventually into the northern Atlantic Ocean through Fram Strait (Gordienko and Laktionov, 1969; Gregor et al., 1998). The TPD track varies yearly dependent on the Arctic Oscillation index (Macdonald et al., 2005).

The Arctic is subject to rapid changes as a consequence of climate change (IPCC, 2014), such as the increase in river runoff (Peterson et al., 2002) and the widespread loss of permafrost (Stedmon et al., 2011; Schuur et al., 2013, 2015). Thawing permafrost has strong effects on the biogeochemistry of major rivers such as the Lena and Kolyma which flow out into the Laptev and East Siberian seas, as the thawing permafrost causes a rapid increase in organic discharge (Frey and McClelland, 2009; Vonk et al., 2012). The consequences of this discharge on DOM composition, in the shelf seas as well as in the Arctic Ocean through surface transport, are still largely unknown. The path of the TPD crosses two of three basins beyond the Siberian continental plane – the Amundsen and Makarov, separated by the Lomonosov ridge. The Nansen Basin, separated from the Amundsen basin by the Gakkel ridge, is largely uninfluenced by the TPD (Fig. 1).

Chromophoric Dissolved Organic Matter (CDOM) absorption properties can be used as tracers for riverine input (Stedmon et al., 2011) and the pool contains Fe-binding organic ligands in the form of humic substances (Laglera et al., 2007, 2011; Laglera and van den Berg, 2009). CDOM can be defined as an ocean colour property both in terms of UV-visible absorbance and UV fluorescence (Coble, 2007). With the input of humic substances, the Arctic is an area where the prime contributor to the Fe-binding organic ligand pool may be terrestrial in origin.

As techniques for the determination of Fe-binding organic ligands are essentially indirect and still non-specific with the exception of specific siderophores (E Mawji et al., 2008), characterisation in natural waters is largely unknown. Characterisation of Fe-binding organic ligands starts with the relative contributions of different constituents to this diverse pool. In the Arctic Ocean the relative contribution of terrestrial sources is expected to be large as well as an important source for the Atlantic Ocean. Prior work in the Arctic Ocean was performed during the International Polar Year 2007 (Thuróczy et al., 2011). That study measured Fe-binding organic ligands with full depth profiles in the Nansen, Amundsen and Makarov Basins. Lower conditional binding strengths and excess ligand concentrations were found in the deep Makarov and

Amundsen Basins compared to the Nansen Basin. Some surface increase of dissolved Fe-binding organic ligands was observed at stations near the TPD influence area. However, spatial resolution in this study was aimed at full depth profile comparisons between the different basins and coastal seas rather than elucidation of surface water influence. Moreover, while intersection with the TPD influence area was indicated for the Amundsen and Makarov profiles (Klunder et al., 2012a), the number of profiles sampled for ligands did not provide high lateral surface detail. In order to study the terrestrial influences in more detail, we show dissolved Fe-binding organic ligand concentrations and characteristics along two detailed transects traversing the TPD taken during the TransArcII expedition between August 15th and October 17th 2015 (FS Polarstern, PS94; Fig. 1). Additionally, spectral properties were measured to ascertain the role of CDOM, and humic substance representative concentrations were measured by way of standard additions of Fulvic acid (FA). These properties allow a first step in characterizing relative contributions to the dissolved Fe-binding organic ligand pool in the terrestrially dominated surface of the Arctic Ocean.

5.2. Methods

5.2.1. Sampling

Two sections in the central Arctic Ocean cross the TPD (Figure 1), encompassing 29 rosette (ROS) stations and 13 ultra-clean (UCC) stations. Furthermore, a third section is defined from the Norwegian coast passing Svalbard into the Nansen Basin, encompassing 16 ROS stations and 6 UCC stations. The UCC system employed here differed from the one described previously (Rijkenberg et al., 2015; chapter 2 and others) in that the sample bottles were constructed of polypropylene and a polyethylene cable was used (Dyneema, DSM). The standard rosette sampling system was equipped with an *in-situ* fluorometer for CDOM spectral ranges (BackScat, Dr. Haardt). ROS casts typically preceded UCC casts and CDOM fluorescence served to target UCC bottle closure at CDOM-relevant depths. Both the UCC and rosette frame employed a set of Conductivity Temperature Depth (CTD) sensors for the calculation of practical salinity, potential temperature and sampling depths.Full depth profiles for [L_t] and all CDOM spectral properties were sampled at UCC stations 32, 50, 69, 81, 87, 96, 99, 101, 117, 125 and 134. Other UCC stations were limited to 200 m depth and humic substances were measured down to 150 m. Maps and section plots are generated using Ocean Data View 4 (Schlitzer, 2016). Stations 32 to 134 were under full ice cover, while stations 4 and 153 to 173 were in open water (Schauer, 2016). Nutrient samples were taken from both systems

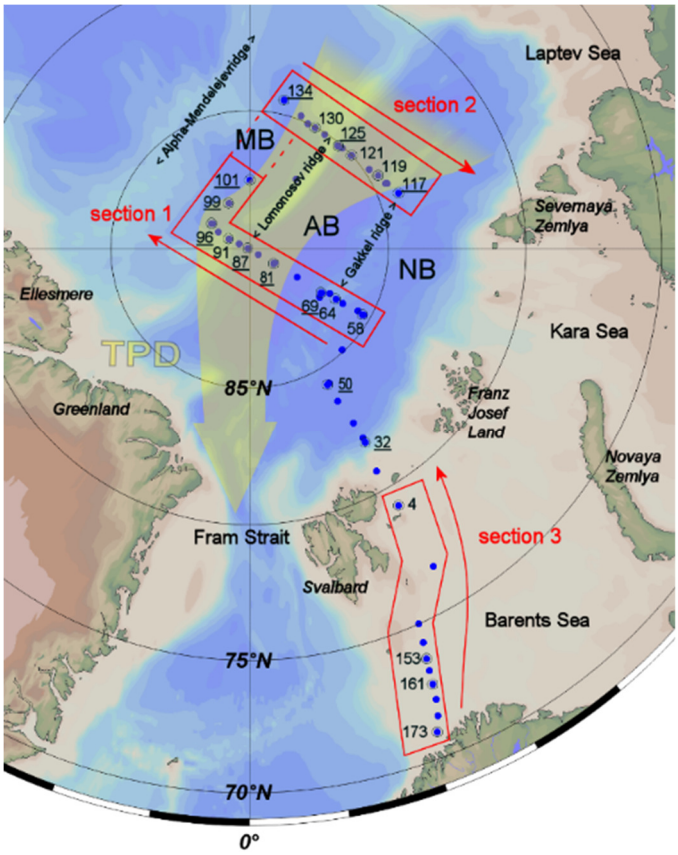

Figure 1

Map of the study area. Stations are indicated in blue dots, stations with numbers are UCC stations, and where these are underlined basin-deep profiles were sampled. Red lines indicate the different sections with arrows indicating the direction they are plotted and/or discussed. Section 1 and 2 are combined into a single surface transect, shown in 1 section plot (figure 2, 5, 6). Also indicated are the Nansen Basin (NB), Amundsen Basin (AB) and Makarov Basin (MB). The broad blue arrow indicates the approximate flow path of the TPD, with boundaries based on our measurements. Map and section plots following were generated using Ocean Data View 4 (Schlitzer, 2016).

5.3. Results

5.3.1. Hydrography and nutrients

Figure 2 shows temperature and salinity data with emphasis on the deep parts of the study area. Polar Surface Water (PSW), discussed in more detail in the next paragraph, is characterized by salinities under 34.5 and temperatures <0 °C. Atlantic Water enters the Arctic Ocean from Fram Strait along the Eurasian shelf seas. This becomes Arctic Atlantic Water (AAW) in the upper layer between 200 and 900 m, characterized by the highest potential temperatures of >0 °C (Rudels, 2008). Below the AAW, low temperature Polar Deep Water (PDW) is found, characterized by potential temperatures <0 °C and salinities > 34.9. A distinction is made between Eurasian Basin Deep Water (EBDW) in the Nansen and Amundsen Basins where potential temperatures down to -1 °C are found, and Canadian Basin Deep Water (CBDW) characterized by a higher potential temperature maximum of -0.5 °C (Rudels, 2008, 2012), which is also found in the Makarov basin (Fig. 2). An intermediate layer with temperatures of -0.5-0 °C identified by Rudels (2010) is not differentiated from PDW in this study.

The surface of the Arctic Ocean is subject to sea ice melt and terrestrial runoff, giving the PSW relatively low salinities and temperatures. Sections 1 and 2 are connected and presented as one transect (Figs. 1, 3). All stations in this transect were under full sea-ice cover. This transect is limited to 200 m depth and will be further referred to as the surface transect. Temperature in the upper 100 m was relatively constant (mean -1.54 °C, SD = 0.21, N=278) with a small protrusion of warmer water between Station 81 and 121 in the middle of the surface transect ($\Delta T \approx 0.25$ °C; Fig. 3a, contours). Between 100 and 200 m temperature changed with depth from -1.25 to ~0 °C (mean -0.04 °C, SD = 0.93, N=123), marking the transition to the upper boundary of AAW. For Stations 58 to 64 of Section 1 the warmer layer occurred further upward in the water column, nearer to 100 m depth and with a mean temperature of 1.58 °C between 200 and 400m depth. This area correlates with the inflow of Atlantic water (Fig. 2). Rudels (2010) describes a Polar Mixed Layer (PML), which is limited to the upper 50 m and has salinities <34 PSU. We will use this PML depth of 50 m as a constraint to report mixed layer values inside our surface transect. Surface hydrography is discussed in terms of density anomaly (σ_θ), for which salinity is the dominating factor in the PSW (Fig. 3a). A decrease of σ_θ (<25 kg m^{-3}) was observed in the surface transect above 50 m between Stations 81 and 119, pressing the halocline downward. This part of the surface transect encompasses our samples over half the Amundsen Basin and all our samples over the Makarov Basin. Outside this area (Stations 58 to 76 and 115 to 119), σ_θ was 26.8 kg·m^{-3} with values up to 27.7 kg·m^{-3} (depth <50 m (PML), SD = 0.6 kg·m^{-3}, N = 63). In contrast, in the low-σ_θ region σ_θ was 24.3 kg·m^{-3} with values as low as 21.8 kg·m^{-3} (<50 m, SD = 1.5 kg·m^{-3}, N = 98).

Elevated phosphate concentrations extended from ≥100 m depth to the PML in the low-σ_θ region (Fig. 3b, colours). Phosphate concentrations in the low-σ_θ region were 0.65 µM (<50 m, stations as above, SD = 0.16 µM, N=117) against a mean background of 0.38 µM (<50 m, stations outside the low-σ_θ region as above, SD = 0.08 µM, N = 58). The surface minimum phosphate concentration between Stations 58 to 76 of 0.38 µM connected to a subsurface minimum of similar values, with higher concentrations of 0.65 µM at Stations 81 and 85 above that at 25 m (Fig. 3b). Nitrate concentrations show a similar deepening minimum towards station 87 (Fig. 3b, contours). However, surface concentrations stayed ≤2.5 µM above 25 m in the low-σ_θ region. Horizontally along our surface transect nitrate concentrations mostly increase evenly with depth to ≥7.5 µM from 100 m depth downwards, only disturbed by the subduction between Stations 76 and 87 (Fig. 3b). Average silicate concentrations were higher in the low-σ_θ region at 11.13 µM (depth <50 m,

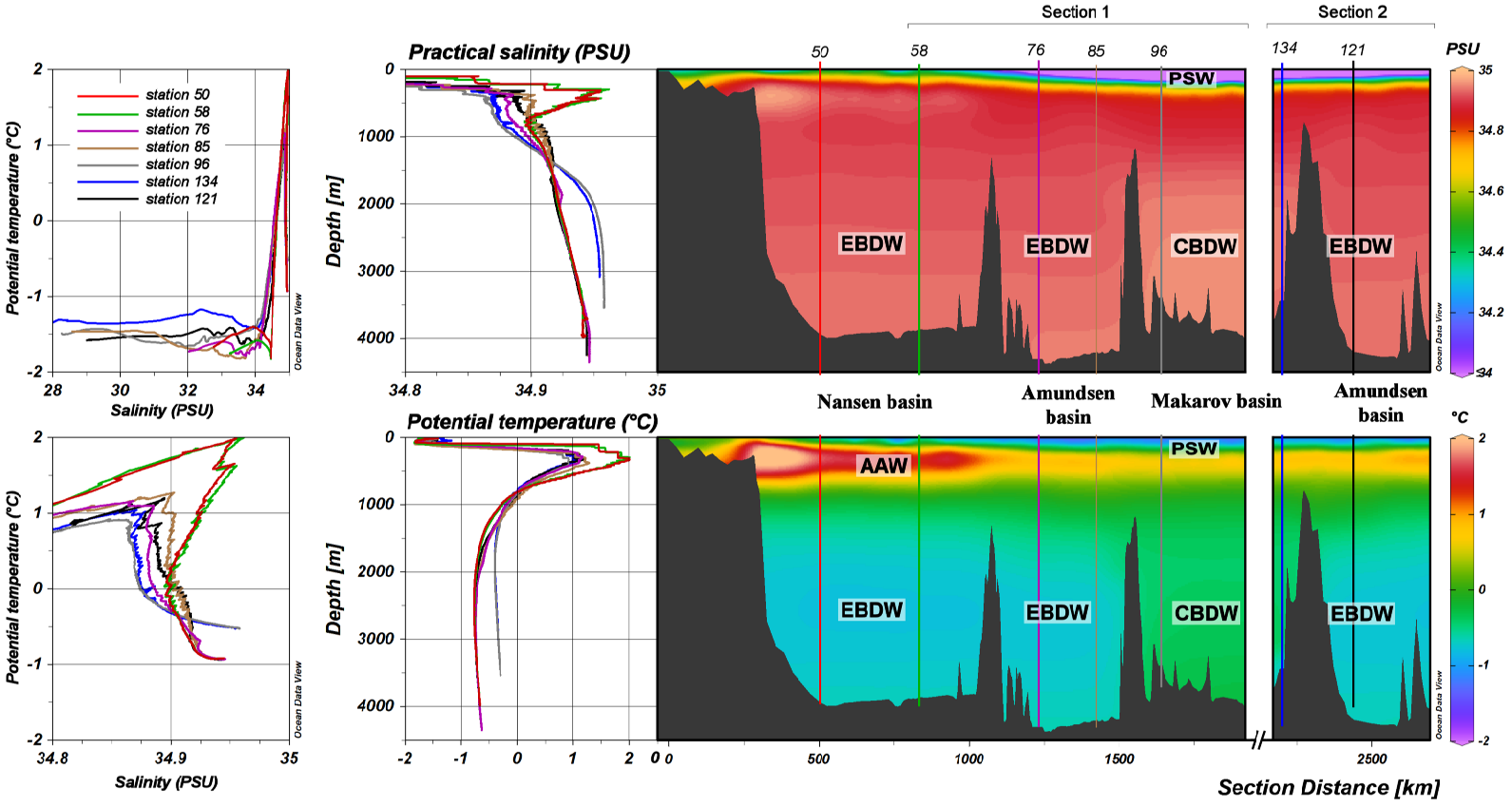

Figure 2

TS profiles and section plots of the deep parts of the study area, from the shelf at Station 4 to the end of Section 2 at Station 134. The left side property-property plots show the relation between potential temperature and salinity (T-S, left), as well as depth profiles attached to the section plots (middle), for Stations 40, 58, 76, 85, 96, 134 and 121. Of the T-S plots on the left, the top shows the entire salinity range and the bottom plot details small-scale salinity variations to help characterize water masses after Rudels (2010, 2012). Polar Surface Water (PSW), Eurasian Basin Deep Water (EBDW), Canadian Basin Deep Water (CBDW) and Arctic Atlantic Water (AAW) are indicated in the practical salinity and

stations as above, SD = 3.42 µM, N = 117), outside of the low-σ_θ region concentrations were 2.85 µM (<50 m, SD = 1.35 µM, N = 58; Fig. 3c). Given the nutrient and salinity-derived density character of the low- σ_θ region, a strong influence from the Chukchi Sea with a Pacific origin is indicated here (Cooper et al., 1997).

A surface increase of CDOM fluorescence data from the *in-situ* sensor on the rosette sampler was observed between Stations 81 and 101 in section 1 and between Stations 118 and 132 in section 2 (Fig. 3d). Measurements by this sensor were 0.59 arbitrary units (a.u.) at these stations (<50 m, SD = 0.07 a.u., N = 53) against a background of 0.36 a.u. (<50 m, SD = 0.07 a.u., N = 42). Based on this known tracer for the terrestrial influence that defines the TPD (Amon et al., 2003; Coble, 2007), the TPD influence area during our study was operationally constrained as those records where *in-situ* CDOM fluorescence was 0.5 a.u. or higher. At Station 134 there were no measurements due to a break in rosette sampler deployment. Based on the strong agreement with CDOM absorption coefficients (See paragraph 5.3.3) this station was judged as outside the TPD.

5.3.2. Deep water properties of DFe and Fe-binding organic ligands

Below 200 m in the Nansen Basin the DFe profiles showed a subsurface maximum near the continental shelf (0.76 nM at 385 m, Station 32), and otherwise settled at a more or less constant value of 0.50 nM at depth (>200 m, SD = 0.14 nM, N = 13). A deep maximum was observed near the continental shelf (0.77 nM at 2556 m, Station 32). In the Amundsen Basin there was surface enrichment of DFe with a subsurface minimum reached at <200 m depth. Deep values were constant at 0.53 nM (>200 m, SD = 0.04 nM, N = 34) for the Section 1 stations in the Amundsen Basin (64, 69, 81 and 87) and 0.39 nM (>200 m, SD = 0.06 nM, N = 12) for the Section 2 stations (117 and 125), the latter had bottom minima of 0.23 nM at 4119 m and 0.32 nM at 3633 m, respectively. In the Makarov Basin the surface characteristics of DFe were similar to Amundsen Basin. However, here there was a small decrease of concentrations with depth from subsurface minima of 0.20-0.31 nM (Station 101 at 363 m, Station 99 at 486 m) to deep minima of 0.10-0.19 nM (Station 134 at 2939 m, Station 99 at 3453 m).

In the Nansen Basin below 200 m depth [L_t] was relatively constant with an average of 1.28 Eq. nM Fe (>200 m, SD = 0.16 Eq. nM Fe, N = 12), with the exception of a local deep high concentration of 2.22 Eq. nM Fe at 2940 m (Station 50, Fig. 4). [L_t] in the Amundsen Basin was 1.33 Eq. nM Fe on average at >200 m depth (SD = 0.25 Eq. nM Fe, N = 29).

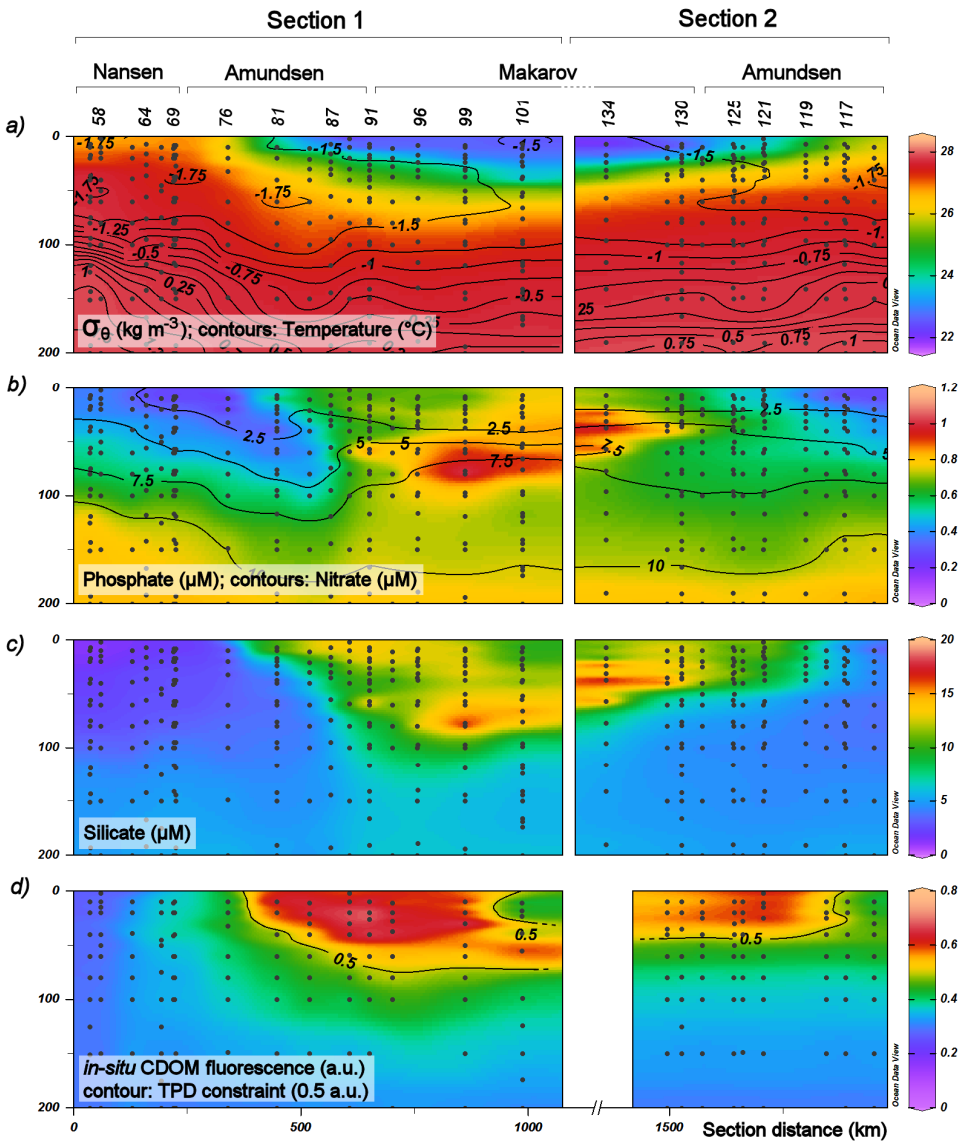

Figure 3 Hydrographical, nutrient and in-situ CDOM fluorescence properties for the upper 200 m of the water column along sections 1 (Stations 58 to 101) and 2 (Stations 117 to 134). a) potential density σθ expressed in kg m^{-3} (colour scale) and potential temperature in degrees Celsius (contours), b) phosphate concentration in µM (colour scale) and nitrate concentration in µM (contours), c) silicate concentration in µM, and d) In situ CDOM fluorescence measurements as registered for discrete bottle closure depths in arbitrary units, the contour indicates the 0.5 a.u. constraining value used to discriminate between records inside and outside the TPD. Stations and corresponding sections are indicated above the image.

Notable elevated concentrations were found at 1962 m at Station 87 (2.02 Eq. nM Fe) and at 980 m at Station 81 (1.83 Eq. nM Fe). Maxima at ~1000 m occurred at Stations 81, 101 and 117 in the Amundsen Basin. In the Makarov Basin [L_t] depth profiles were similar to those in the Amundsen Basin, but with gradual increases with depth from 1000 m onwards at Stations 96, 101 and 134. [L_t]/DFe ratios at >200 m depth (Fig. 5) settled at a low value of 2-3 in the Nansen basin with a minimum approaching 1 in the upper AAW layer at station 32 (Nansen basin) and gradually declined to another minimum at 2500 m depth. At Station 50 a deeper occurrence of higher ratios towards the surface also coincides with the AAW layer. In the Amundsen Basin the [L_t]/DFe ratios were consistently varying around 3 with no discernible trend, with variation dictated by changes in [L_t]. In contrast to the Nansen and Amundsen basins, [L_t]/DFe ratios in the Makarov Basin (Stations 96, 99, 101 and 134) increased with depth. Deep maxima here were 7.1 (Station 96, 3292 m), 4.9 (Station 99, 3453 m), 9.4 (Station 101, 3702 m) and 11.8 (Station 134, 3010 m).

Table 1 summarizes DFe and Fe-binding organic ligand data for all profiles at full depth stations in the Arctic Ocean. The most pronounced variability in DFe, [L_t], [L'], and ratio [L_t]/DFe was observed in the surface (≤ 200 m depth). In most cases the most extreme values and highest standard deviations were found in this layer, which is described in a higher spatial resolution in the next section. The AAW layer did not substantially differ from the PDW or entire >200 m depth layers in terms of DFe and Fe-binding organic ligand properties, therefore this layer is not separately shown in Table 1. The Nansen and Amundsen basins did not differ significantly below 200 m depth, with respectively a mean DFe of 0.50 and 0.48 nM (SD = 0.13 and 0.09 nM), a mean [L_t] of 1.35 and 1.37 Eq. nM Fe (SD = 0.30 and 0.28 Eq. nM Fe) and a mean [L'] of 0.85 and 0.89 Eq. nM Fe (SD = 0.31 and 0.25 Eq. nM Fe). The mean [L_t]/DFe ratio was 2.9 for both Nansen and Amundsen basins (SD = 0.9 and 0.6). Mean DFe in the Makarov basin differed significantly from the Nansen and Amundsen basins at 0.23 nM (SD = 0.07). Mean [L_t] and [L'] were only slightly and not significantly lower than in the Nansen and Amundsen basins at 1.20 Eq. nM Fe (SD = 0.21) and 0.96 Eq. nM Fe (SD = 0.23), respectively. As a result the mean [L_t]/DFe ratio was also different at 5.5 (SD = 2.4). Logα_{FeL} was slightly but not significantly higher in the Makarov Basin compared to the Nansen and Amundsen basins at 3.07±0.32 versus 2.95±0.22 and 2.83±0.20, respectively (Table 1). Mean Log$K'_{Fe'L,}$ values are near uniform across the entire >200 m dataset at 11.99 mol^{-1} (SD = 0.26, N = 63, range 11.50 ≤ Log$K'_{Fe'L}$ ≤ 12.62 mol^{-1}).

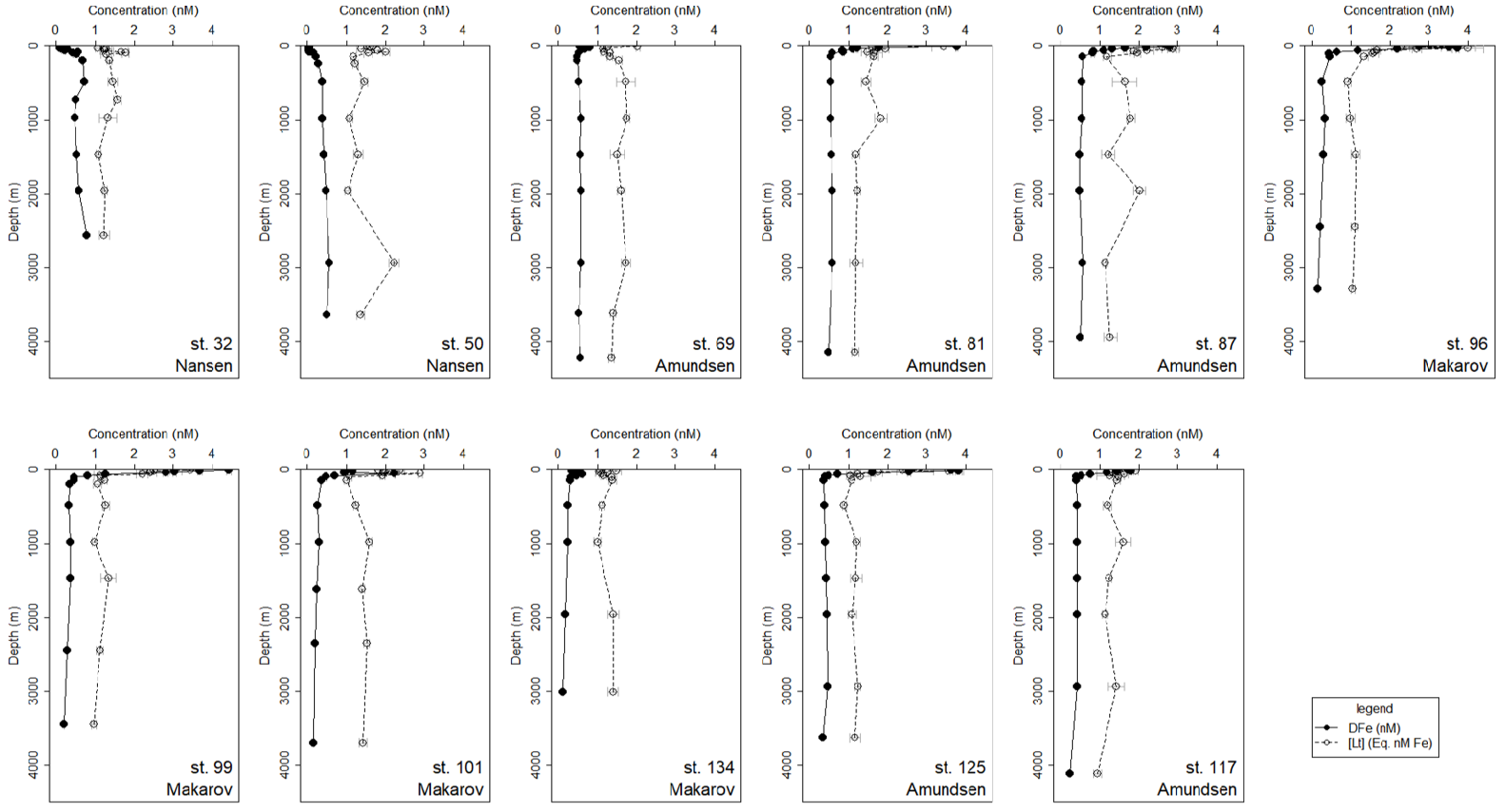

Figure 4

Depth profiles of dissolved Fe concentrations (DFe) in nM (solid lines with filled circles) and Fe binding organic ligand concentrations ($[L_t]$) in equivalent nM of Fe (dashed lines with open diamonds). Station numbers are indicated as well as the basins these reside in. Error bars indicate standard deviations for multiple measurements (N = 2 or 3) for DFe and the standard error of the Langmuir fit for $[L_t]$. Where error bars are not visible these fall inside of the symbols.

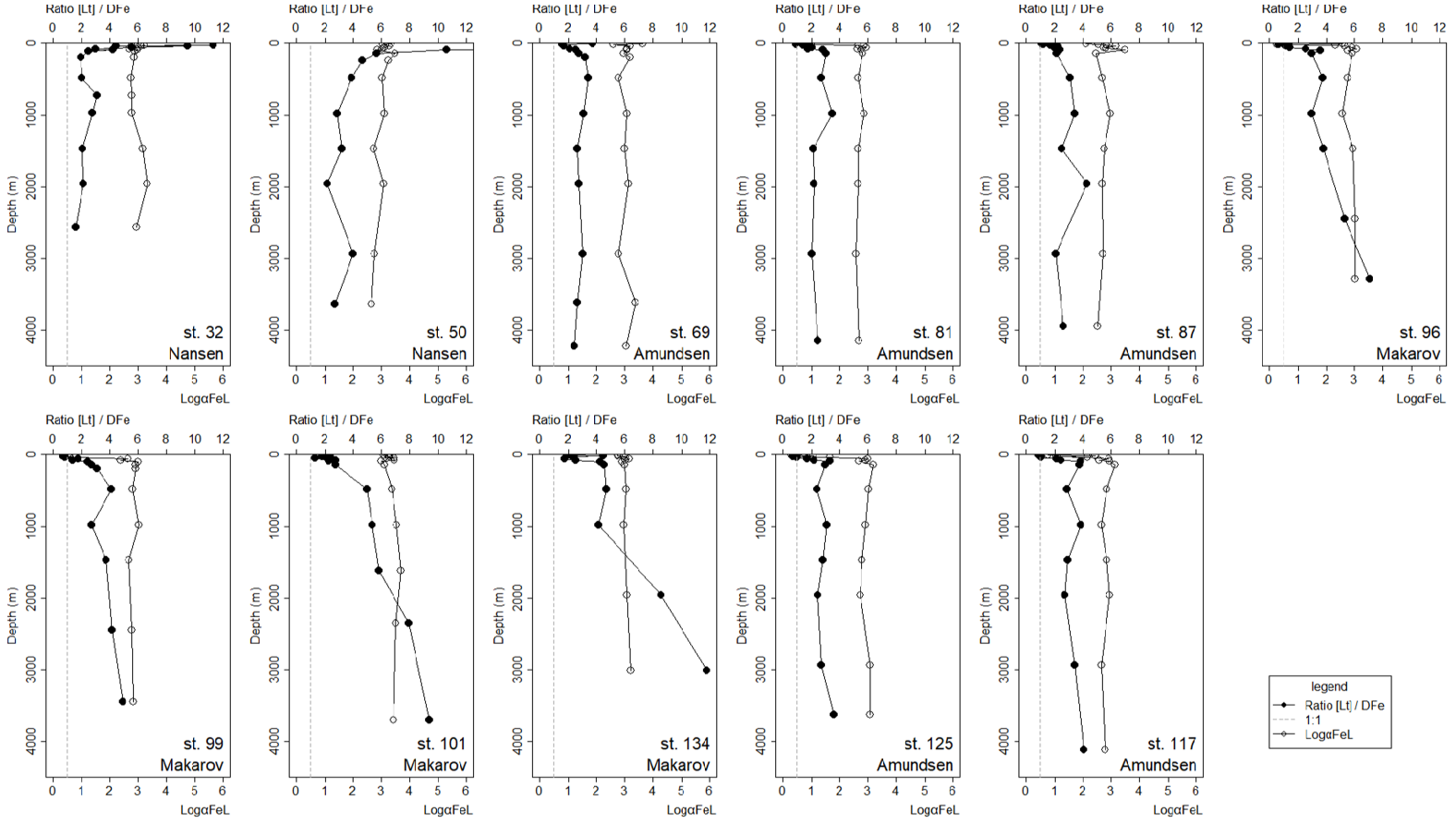

Figure 5

Depth profiles of the ratio between [L_t] and DFe (top axis, filled circles) as well as $Log\alpha_{Fe'L}$ (bottom axis, open circles) for the same stations as in Figure 4. The dashed line indicates a ratio of 1.

Table 1 Mean values with standard deviations, number of records and extreme values for Fe speciation at full depth stations in the Arctic Ocean (St. 32, 50, 69, 81, 87, 96, 99, 101, 117, 125 and 134).

		DFe	$[L_t]$	$LogK'_{Fe'}$	$Log\alpha_{FeL}$	[L']	$[L_t]$ / DFe
		(nM)	*(Eq. nM Fe)*	*(mol^{-1})*		*(Eq. nM Fe)*	*(ratio)*
Surface	*Average*	0.99	1.75	12.03	2.60	0.75	4.6
(≤ 200 m)	*SD*	1.01	0.68	0.26	0.84	0.47	8.9
	N	116	87	87	87	87	87
	min	0.03	1.00	11.45	0.26	<0.01	0.6
	max	4.42	4.01	12.63	3.64	1.95	53.5
Deep Nansen Basin	*Average*	0.50	1.35	12.04	2.95	0.85	2.9
(> 200 m)	*SD*	0.13	0.30	0.31	0.22	0.31	0.9
St. 32 & 50	*N*	27	13	13	13	13	13
	min	0.26	1.04	11.54	2.64	0.46	1.6
	max	0.77	2.22	12.50	3.32	1.66	4.7
Deep Amundsen Basin	*Average*	0.48	1.37	11.90	2.83	0.89	2.9
(> 200 m)	*SD*	0.09	0.28	0.22	0.20	0.25	0.6
St. 69, 81, 87 117 & 125	*N*	66	31	31	31	31	31
	min	0.23	0.89	11.50	2.52	0.52	2.0
	max	0.63	2.02	12.42	3.36	1.55	4.3
Deep Makarov Basin	*Average*	0.23	1.20	12.10	3.07	0.96	5.5
(> 200 m)	*SD*	0.07	0.21	0.25	0.32	0.23	2.4
St. 96, 99, 101 & 134	*N*	52	19	19	19	19	19
	min	0.10	0.92	11.67	2.56	0.62	2.7
	max	0.36	1.58	12.62	3.69	1.32	11.8

Table 2 2-ligand determination for full depth profiles in Sections 1 and 2 (Stations 32, 50, 69, 81, 87, 96, 99, 101, 117, 125 and 134).

		$[L_t]$ 1	**$LogK'_{Fe'L}$ 1**	**$Loga_{Fe'L}$1**	**[L'] 1**	**$[L_t]$ 2**	**$LogK'_{Fe'L}$ 2**	**$Loga_{Fe'L}$ 2**	**[L'] 2**
		(Eq. nM Fe)	*(mol^{-1})*		*(Eq. nM Fe)*	*(Eq. nM Fe)*	*(mol^{-1})*		*(Eq. nM Fe)*
All	*Average*	0.62	13.14	3.41	0.29	1.28	11.16	2.23	1.23
> 200 m	*SD*	0.20	0.61	0.81	0.21	0.49	0.17	0.22	0.48
	N	27	27	27	27	27	27	27	27
	Min	0.16	12.30	1.77	<0.01	0.70	10.61	1.59	0.67
	max	0.95	14.59	5.09	0.79	2.70	11.38	2.64	2.60
Nansen Basin	*Average*	0.64	12.85	3.18	0.25	1.13	11.19	2.21	1.08
St. 32 & 50	*SD*	0.18	0.37	0.30	0.14	0.25	0.12	0.22	0.24
	N	5	5	5	5	5	5	5	5
	min	0.46	12.30	2.81	0.09	0.71	11.06	1.90	0.69
	max	0.88	13.34	3.50	0.40	1.38	11.34	2.47	1.34
Amundsen Basin	*Average*	0.62	13.05	3.29	0.21	1.34	11.18	2.26	1.28
St. 69, 81, 87 117	*SD*	0.16	0.57	0.67	0.11	0.48	0.11	0.14	0.47
& 125	*N*	12	12	12	12	12	12	12	12
	min	0.41	12.44	2.47	0.04	0.70	11.01	2.06	0.67
	max	0.91	14.59	4.98	0.36	2.34	11.36	2.52	2.32
Makarov Basin	*Average*	0.61	13.38	3.68	0.41	1.28	11.14	2.20	1.26
St. 96, 99, 101 &	*SD*	0.26	0.69	1.10	0.27	0.61	0.24	0.31	0.59
134	*N*	10	10	10	10	10	10	10	10
	min	0.16	12.54	1.77	<0.01	0.73	10.61	1.59	0.73
	max	0.95	14.39	5.09	0.79	2.70	11.38	2.64	2.60

Determination of a second ligand class was possible for 27 measurements out of 63 samples at depths >200 m (Table 2). Where these were found the L_1 class had a mean concentration of 0.62 Eq. nM Fe ($0.16 \leq [L_1] \leq 0.95$, SD = 0.20 Eq. nM Fe) and the L_2 class had a mean concentration of 1.28 Eq. nM Fe ($0.70 \leq [L_2] \leq 2.70$, SD = 0.49 Eq. nM Fe). $LogK'_{Fe'L}$ for the L_1 class was a mean 13.14 mol^{-1}, $LogK'_{Fe'L}$ for the L_2 class was a mean 11.16 mol^{-1} (SD = 0.61 and 0.17 mol^{-1}, respectively). These concentrations and corresponding $LogK'_{Fe'L}$ values did not differ significantly between basins.

5.3.3. Surface properties of DFe, Fe-binding organic ligands, CDOM and humic substances

In the Nansen Basin, DFe was very low in the upper 200 m, at 0.21 nM (SD = 0.20, N = 18, Stations 32, 40 and 50), with a minimum of 0.03 nM at 20 m depth over the middle of the basin (Station 50) and a maximum of 0.69 nM at 198 m near the shelf (Station 32). Horizontal variation of Fe speciation and CDOM properties was large and similar between all properties in the surface transect (Fig. 6). In strong agreement with the *in-situ* CDOM fluorescence (Fig. 3d) and our TPD definition of ≥0.5 a.u., DFe (Fig. 6a) in Section 1 increased sharply between Stations 81 and 99 with the highest concentrations in the upper 10-40 m (e.g. 4.42 nM at 8 m depth, Station 99) against an average background of 0.58±0.38 nM (outside the TPD). Similarly, DFe was high between Stations 119 and 130 inside the TPD in Section 2 (e.g. 4.35 nM at 7 m depth, Station 121).

Between Stations 81 and 99 $[L_t]$ (Fig. 6b) also increased, with the highest concentration of 4.13 Eq. nM Fe at 39.9 m depth (Station 91). $[L_t]$ also increased to a lesser extent between Stations 119 and 130, with the highest concentration in the area corresponding with TPD constraints of 3.55 Eq. nM Fe at 16.7 m depth at station 125. Additionally, at 95.6 m depth at Station 119 an $[L_t]$ of 3.91 Eq. nM Fe (SE = 0.185 Eq. nM Fe) is recorded outside the TPD constraints. Similarly, a singular high $[L_t]$ of 2.44 Eq. nM Fe (SE = 0.323 Eq. nM Fe) is found at 141.3 m depth at Station 91. The outside-TPD background $[L_t]$ using the same constraints is 1.51 Eq. nM Fe (SD = 0.48 Eq. nM Fe, N = 74; Table 3). In the Nansen Basin $[L_t]$/DFe ratios (Fig. 5, Fig. 6c) at the surface (<200 m depth) are high, whereas surface $[L_t]$/DFe ratios in the Amundsen and Makarov Basins are low, in cases between 0 and 1 in the PML in the surface transect. Ratios of $[L_t]$/DFe shown in Fig. 6c are very low inside the TPD, with values between 0 and 1, especially in Section 2 between Stations 117 and 130. The outliers reported for $[L_t]$ results in high ratios (7.9 at 141.3 m, Station 91; 8.9 at 95.6 m, Station 119) which are also higher than the outside-TPD background of 2.7 (SD = 1.4, N = 74; Table 3). The average $Log\alpha_{FeL}$ inside the TPD was notably

lower at 1.66 against 2.89 outside the TPD. However, variability of $Log\alpha_{FeL}$ inside the TPD was high leading to a large SD of 1.17 (N = 35), lowering significance of the difference with values outside the TPD (SD = 0.53, N= 74; Table 3).

$LogK'_{Fe'L}$ in the surface transect reprises the uniformity observed in deep water at 12.08 mol^{-1} (SD=0.30, N=109, range 11.40 ≤ $LogK'_{Fe'L}$ ≤ 12.91 mol^{-1}). Two ligand classes could be determined for 32 out of 86 samples at ≤ 200 m depth (Table 4). However, the ability to resolve two ligand classes was highly biased towards samples outside the TPD where 30 samples could be resolved, as opposed to only 2 samples inside the TPD. The mean L_1 class concentration outside the TPD was 0.69 Eq. nM Fe (0.30 ≤ [L_1] ≤ 1.28, SD = 0.27), the mean L_2 class concentration was 1.34 Eq. nM Fe (0.61 ≤ [L_2] ≤ 3.23, SD = 0.56). For the same records $LogK'_{Fe'L}$ were 13.26 mol^{-1} (SD = 0.71) and 11.20 mol^{-1} (SD = 0.17), respectively. Inside the TPD at station 87 L_1 and L_2 concentrations were 1.58 and 2.76 Eq. nM Fe with $LogK'_{Fe'L}$ of 13.30 and 11.60, respectively (16 m depth). At Station 101 L_1 and L_2 concentrations were 2.29 and 1.26 Eq. nM Fe with $LogK'_{Fe'L}$ of 13.60 and 11.76, respectively. Depth for the Station 101 measurement was 52 m, corresponding to maxima in DFe, [L_t] and CDOM at that station.

Absorption coefficients were higher in the upper 100 m for both a_{254} (Fig. 6d, colours) and a_{300} (Fig. 6d, contours) with highest values in agreement with *in-situ* CDOM fluorescence (5.81±1.45 m^{-1} and 2.33±0.65 m^{-1}, respectively; Table 3). Spectral slopes were slightly steeper outside of the TPD with a mean slope ratio of 0.97±0.33 inside the TPD and 1.15±0.63 outside the TPD. FDOM measurements were in agreement with a_{254} and a_{300} with $F_{250/450}$ giving high values of up to 4.08 QSU (17 m depth, Station 91) within TPD constraints against a low and relatively uniform background of 0.67 QSU (deep values, SD = 0.04 QSU, N = 65, range of 0.54 to 0.74).

Humic substance concentration [HS] profiles for the top 150 m (Fig. 7) had elevated concentrations in the upper 100 m. Concentrations were higher at Stations 87, 99, 119 and 125, which fall within TPD constraints. [HS] up to 0.32 Eq. $mg \cdot L^{-1}$ FA (Station 99, 17.2 m) were found at these stations. In contrast, concentrations outside the TPD (Stations 101, 117 and 134) were 0.07 Eq. $mg \cdot L^{-1}$ FA at average (<100 m depth, SD=0.03 $mg \cdot L^{-1}$, N=21). Overall, concentrations inside the TPD were higher with a mean of 0.14 Eq. $mg \cdot L^{-1}$ FA against a 0.06 Eq. $mg \cdot L^{-1}$ FA background (Table 3). In all cases, deeper values approached zero near 150 m depth.

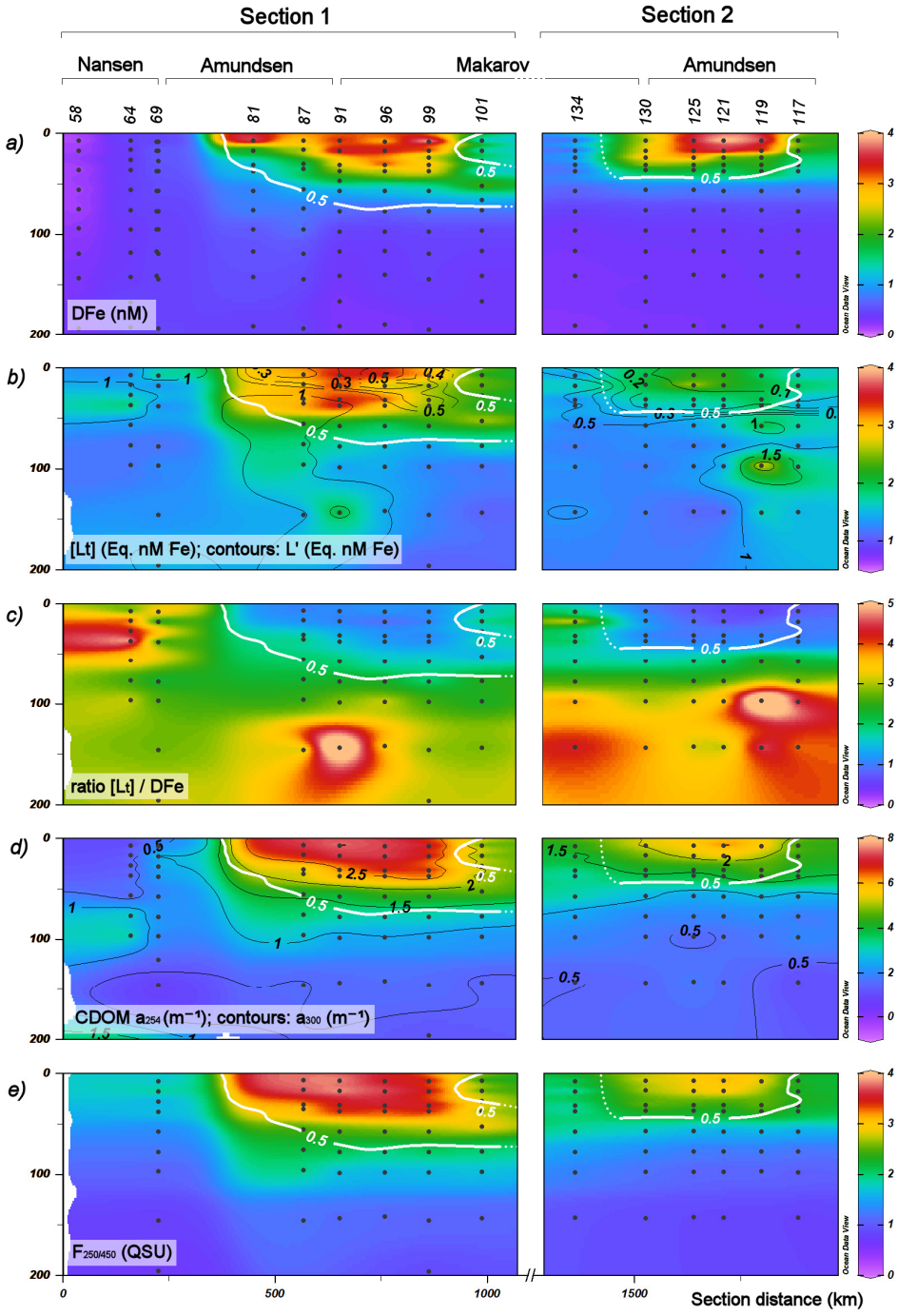

Figure 6 DFe, [L_t], and CDOM properties for the upper 200 m of the water column along Sections 1 and 2. a) DFe in nM, b) [L_t] (colour scale) and [L'] (contours) in equivalent nM of Fe, c) the ratio between [L_t] and DFe, d) CDOM representative absorption coefficients at 254 nm (colour scale) and 300 nm (contours) and e) CDOM fluorescence at 450nm. A white contour indicates the constraining value for the TPD of in-situ CDOM fluorescence (0.5 a.u.).

Table 3 *Mean values with standard deviations, number of records and extreme values for Fe speciation and CDOM spectral properties inside and outside the TPD within the surface transect (Stations 58, 64, 69, 81, 87, 91, 96, 99, 101, 117, 119, 121, 125, 130 and 134, all ≤200 m). Records inside the TPD are selected on the basis of in-situ CDOM fluorescence.*

		DFe *(nM)*	**[L_t]** *(Eq. nM Fe)*	**Log$K'_{Fe'L}$** *(mol^{-1})*	**Log$\alpha_{Fe'L}$** *(mol^{-1})*	**[L']** *(Eq. nM Fe)*	**[L_t]/DFe ratio**	**HS** *(Eq. mg/L FA)*	**$F_{250/450}$** *(QSU)*	**a_{254}** *(nm^{-1})*	**a_{300}** *(nm^{-1})*	**$S_{275-295}$** *(nm^{-1})*
Inside TPD	*Average*	2.63	2.60	11.97	1.66	0.42	1.2	0.18	3.17	5.81	2.33	0.026
	SD	1.07	0.78	0.32	1.17	0.52	0.5	0.07	0.59	1.45	0.65	0.002
	N	42	35	35	35	35	35	18	35	35	35	35
	Min	0.73	1.60	11.40	-0.08	<0.01	0.5	0.07	2.17	3.16	1.09	0.020
	Max	4.42	4.13	12.65	3.45	1.78	2.3	0.32	4.08	7.83	3.26	0.032
Outside TPD	*Average*	0.58	1.51	12.13	2.89	0.82	2.7	0.06	1.56	2.51	0.92	0.035
	SD	0.38	0.48	0.28	0.53	0.51	1.4	0.03	0.51	1.13	0.51	0.023
	N	128	74	74	74	74	74	38	69	76	76	76
	Min	0.12	0.84	11.43	0.76	<0.01	0.9	0.01	0.72	0.52	-0.01	0.011
	Max	2.25	3.91	12.91	4.12	3.47	8.9	0.17	2.83	5.39	2.19	0.160

Table 4 *2-ligand determination for surface transect samples in Sections 1 and 2 (Stations 58, 64, 69, 81, 87, 91, 96, 99, 101, 117, 119, 121, 125, 130 and 134, all ≤200 m). Two samples were resolved for 2 ligand classes inside the TPD; averages, standard deviations, minimum- and maximum values are given for the 30 samples which were resolved outside of the TPD.*

		$[L_t]$ 1	**$LogK'_{Fe'L}$ 1**	**$Loga_{Fe'L}$ 1**	**[L'] 1**	**$[L_t]$ 2**	**$LogK'_{Fe'L}$ 2**	**$Loga_{Fe'L}$ 2**	**[L'] 2**
		(Eq. nM Fe)	*(mol^{-1})*		*(Eq. nM Fe)*	*(Eq. nM Fe)*	*(mol^{-1})*		*(Eq. nM Fe)*
Inside TPD	st101 b20	2.29	13.60	3.94	0.22	1.26	11.76	2.81	1.11
	st87 b23	1.58	13.30	3.25	0.09	2.76	11.60	2.92	2.07
Outside TPD	*Average*	0.69	13.26	3.24	0.22	1.34	11.20	2.27	1.24
	SD	0.27	0.71	0.83	0.18	0.56	0.17	0.27	0.56
	N	30	30	30	30	30	30	30	30
	min	0.30	12.33	1.97	<0.01	0.61	10.88	1.81	0.57
	max	1.29	15.56	6.25	0.69	3.23	11.51	2.88	3.08

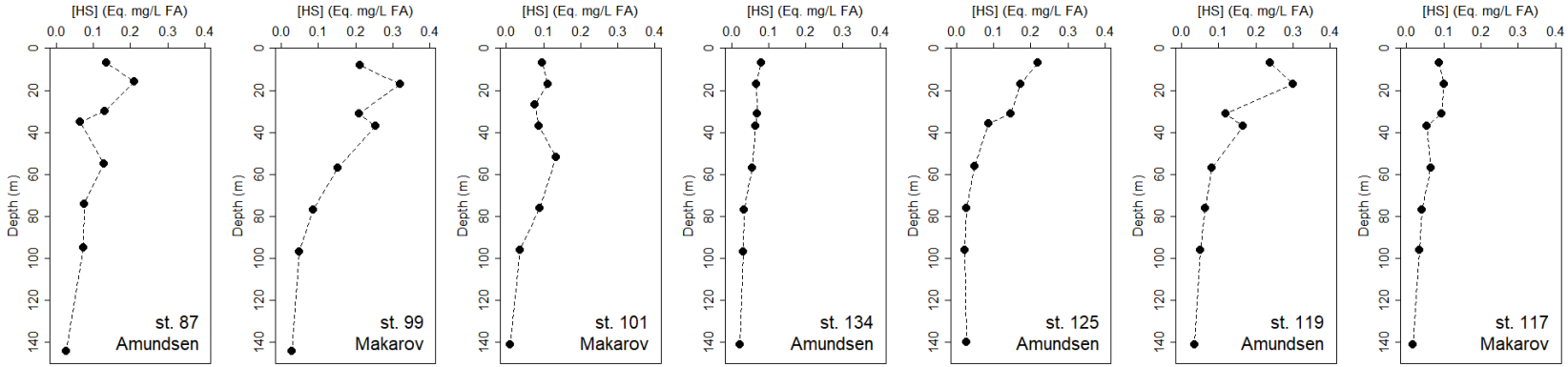

Figure 7

Depth profiles of humic substances of stations in Sections 1 and 2 of the upper 150 m expressed in equivalent mg · L^{-1} of FA. Stations and basins where these were sampled are indicated.

5.3.4. Barents Sea properties of DFe and Fe-binding organic ligands

DFe in the Barents Sea (Fig. 8a) was depleted at the surface and increased with depth, to a maximum concentration of 1.41 nM (414 m depth, Station 153). This is higher than most deep maxima in the other sections but lower than maxima observed at the surface in the TPD. An exception is Station 4 near Svalbard, which had a subsurface high DFe of 3.21 nM at 48 m. Mean [L_t] concentration across the section is 1.43 Eq. nM Fe (SD=0.34, N=28; Fig. 8b). The profile at Station 4 again stands out with a subsurface maximum (2.15 Eq. nM Fe at 48 m) and a decrease in concentrations at greater depths. This was also the only station where the ratio [L_t]/DFe (Fig. 8c) was lower than 1 at this same depth (0.7 at 48 m). Otherwise, ratios are >1 with values for stations 4 and 173 relatively lower compared to stations 153 and 161. Finally, $LogK'_{Fe'L}$ values are very constant along this section as well, similar to sections 1 and 2 with a mean 12.13 mol^{-1} (SD = 0.28 mol^{-1}, N = 20, 11.66 ≤ $LogK'_{Fe'L}$ ≤ 12.95 mol^{-1}).

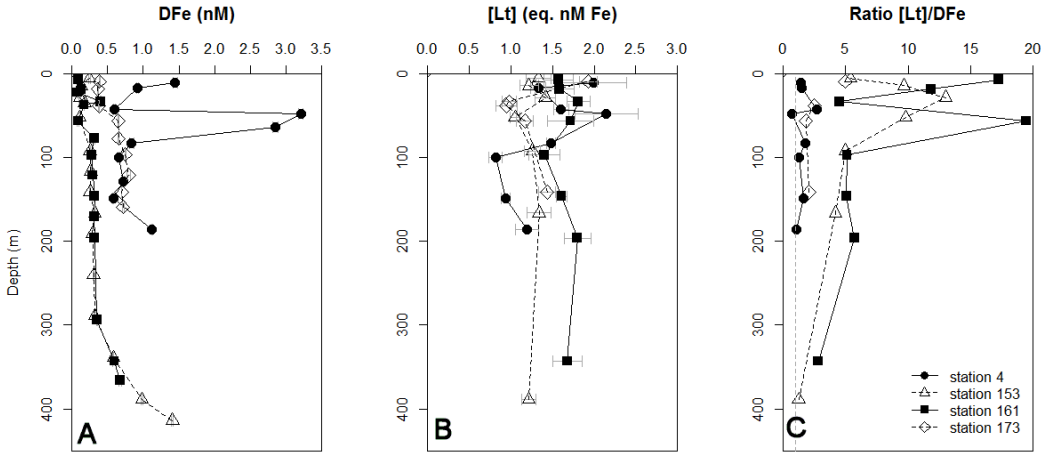

Figure 8 Depth profiles of DFe and organic ligand characteristics of Stations 4, 153, 161 and 173 along Section 3 in the Barents Sea. **A**) DFe in nM, **B**) [Lt] in Eq. nM Fe and **C**) the ratio between [Lt] and DFe. The dashed line indicates a ratio of 1.

5.4. Discussion

5.4.1. Deep water properties of Fe-binding organic ligands

The DFe depth profiles (Fig. 4) of the Nansen basin stations have a traditional nutrient-like profile. Station 32 is the only station showing a subsurface maximum coupled with surface depletion, as well as an increase towards the sea floor. This subsurface maximum coincided with the strongest AAW influence observed over the Nansen basin (Fig. 2) and was only observed near the continental shelf. Klunder et al. (2012b) observed high DFe values at 400 m, 1000 m and near the bottom over the Barents Sea slope at stations with approximately the same location as our Station 32. While our data had a less variable character, our vertical resolution was lower. The occurrence of a maximum at that study's slope station at 400 m was explained by melt water influence while the 1000 m and bottom maxima were connected to a slope influence. Our data for Station 32 shows a maximum from 200 to 500 m. However, attenuation data representing turbidity (not shown) does not show an increase coinciding with increased DFe at our Station 32. It is possible that our sampling location was less acutely at the slope, limiting slope resuspension effects. With the data available to us the distinction cannot be made if the Station 32 DFe increases were due to an Atlantic influence, meltwater or slope resuspension influence.

Overall, DFe at depths over 200 m was not influenced significantly by location and, where DFe was enriched in the upper 200 m, did not differ beyond standard deviations between deep water masses. Only in the Makarov basin did DFe gradually decrease with depth (Fig. 4), which has earlier been attributed to scavenging (Thuróczy et al., 2011; Klunder et al., 2012b). Klunder et al. (2012b) conclude the lower deep DFe concentrations in the Makarov Basin may be attributed to the scavenging removal in the Makarov Basin being particularly more effective due to a longer water mass residence time than in the other basins, allowing for a longer exposure to the scavenging process and due to a lower input from hydrothermal sources. This in turn was coupled with a lower ligand binding strength found in the Makarov and Amundsen Basins (Thuroczy et al., 2011). However, in the present study we could not replicate such a clear difference between $LogK'_{Fe'L}$ in the Nansen, Amundsen and Makarov basins, with mean values of 12.08, 11.93 and 12.11, respectively (>1000 m depth; SD's of 0.39, 0.22 and 0.31 for N of 7, 21 and 8, respectively, Table 1). On the contrary, the $LogK'_{Fe'L}$ values were very similar across the dataset. $[L_t]$ showed little variability at depths over 200 m, with average concentrations of 1.35, 1.37 and 1.20 Eq. nM Fe in the Nansen, Amundsen and Makarov basins, respectively (SD = 0.30, 0.28 and 0.21 Eq. nM Fe, N = 13, 31 and 19).

For those samples where two ligand classes could be resolved, L_1 and L_2 did not significantly differ between basins. Although the determination could not be made in all samples, the spread and deviations between L_1 and L_2 as well as their corresponding $LogK'_{Fe'L}$ values were very small, indicating the good quality of the data. One notable difference between basins was a slight increase in $[L_t]$ with depth in the Makarov basin stations (96, 99, 101 and 134; Fig. 4). This was more pronounced in the ratio $[L_t]$/DFe (Fig. 5) as first described by (Thuróczy et al., 2011). This, coupled with a higher particulate Fe concentration at depth in that study, further confirmed the aforementioned stronger effect of scavenging in the Makarov Basin. In the present study, surface (<200 m depth) $[L_t]$ was clearly enriched, further discussed in greater spatial resolution in the next section. Surface ratios of $[L_t]$/DFe between 0 and 1 suggest that further Fe input would tend to precipitate, possibly adding to a higher scavenging influence lower in the water column. A strong surface influence of humic substances, which would increase the $[L_t]$/DFe ratio, would preclude such surface precipitation as an explanation, though a higher particle load might explain increased scavenging. However, attenuation data from rosette sampler sensors in the Makarov Basin do not support increased particle loads. While humic substances have in some cases been reported at depth (Laglera and van den Berg, 2009), persistence lower in the water column or flocculation of these high-MW substances and / or possible contributions to the scavenging effects are not known. Additionally, the presence of a similar riverine surface influence over part of the Amundsen basin did not lead to increased scavenging effects at depth at those stations. $Log\alpha_{FeL}$ also did not change significantly with depth in the Makarov basin, indicating that the reactivity of the ligands present there did not change with depth. Our findings confirm that DFe input and water mass differences in the deep Makarov basin drive Fe speciation there (Thuróczy et al., 2011; Klunder et al., 2012b), as there were no indications of fluxes in Fe binding organic ligands.

5.4.2. Surface properties of DFe, Fe-binding organic ligands, CDOM and humic substances

The TPD influence area was constrained using *in-situ* CDOM fluorescence data. While this sensor was uncalibrated, its agreement with other CDOM spectral properties was excellent. As the sensor was on the rosette sampler, typically preceding UCC casts, it was initially used to target UCC sampling for Fe-binding ligand and CDOM. Additionally, any calibration performed would depend on a standard that may not be representative of the study area, as further discussed later in this section, yielding a similarly arbitrary relation. Average DFe inside the TPD was significantly higher at 2.63 nM (SD = 1.07 nM, N = 42) against an average background outside the TPD of 0.58 nM (SD = 0.38 nM, N = 127, Table

3). In concert, average [L_t] inside the TPD was higher than outside with hardly any overlap in standard deviations at 2.60 Eq. nM Fe (SD = 0.78 Eq. nM Fe, N = 35) and 1.51 Eq. nM Fe (SD = 0.48 Eq. nM Fe, N = 74). Note that the average [L_t] inside the TPD was actually slightly lower than DFe. Where this was the case in specific records, assuming that DFe beyond the inorganic solubility of Fe in seawater (Liu and Millero, 2002) must be bound to organic ligands (Gledhill and van den Berg, 1994), DFe being higher than [L_t] indicates that more ligands are present in these locations than measured with the TAC method and the analytical window used in this study. The [L_t]/DFe ratio, where this is between 0 and 1, also indicates insufficient Fe binding capability to explain DFe (Fig. 6c). Average [L_t]/DFe ratios inside the TPD are 1.2 (SD = 0.5, N = 35) with a minimum ratio of 0.5 (Table 3). The [L_t]/DFe ratio outside the TPD is much higher with an average value of 2.7 (SD = 1.4, N = 74), indicating a surplus of ligands detected with the TAC method. Further differences between ligands inside and outside the TPD are shown by low [L´] (Fig. 6b). Low [L´] indicates ligand saturation, which coincided with highest DFe and [L_t] in the surface transect. Log$K'_{Fe'L}$ values are similar inside and outside the TPD (11.97±0.32 mol^{-1} and 12.13±0.28 mol^{-1}, respectively; Table 3). This suggests all ligands are of similar strength, though measured within the confines of the binding strengths our competitive exchange ligand TAC will establish an equilibrium with.

Two ligand classes could only be resolved for samples outside the TPD barring two exceptions (Table 4). The corresponding Log$K'_{Fe'L}$ values did not significantly differ from those found for the two ligand classes found in >200 m samples, much like in the case of the single ligand class determination. The inability to detect two ligand classes in samples inside the TPD is not surprising given that ligands inside the TPD are near saturation, as determined from the [L_t]/DFe ratio nearing 1 and low [L´]. In such a case a stronger ligand class would be entirely saturated and therefore undetectable through titration with TAC at the detection window used in this study. The observed lack of significant difference in Log$K'_{Fe'L}$ inside and outside the TPD therefore may also be attributed to measurements using TAC only showing part of the riverine input effect on speciation. To what extent an alternate added ligand might alleviate this must be attempted, perhaps only a combination of analytical methods provides a full understanding in this study area. The high variability of Log$\alpha_{Fe'L}$ inside the TPD is also explained by the highly saturated state of ligands there. As $\alpha_{Fe'L}$ is the product of [L´] and $K'_{Fe'L}$, when [L´] nears 0 the value of Log$\alpha_{Fe'L}$ is no longer representative of the true reactivity of the ligands. While less precise at saturation, Log$\alpha_{Fe'L}$ may be more descriptive of the situation as the ratio [L_t]/DFe simply approaches 1 and [L'] approaches 0 asymptotically, while

$Log\alpha_{Fe'L}$ amplifies the differences and adds information on the probability of Fe binding (Gledhill and Gerringa, 2017)

According to Laglera et al. (2011) the method we use to determine the ligand characteristics applying TAC as competing ligand is not capable of measuring the entire contribution of humic substances to the ligand pool. The many weaker binding sites in a humic substance may not fall within the typically employed detection windows for TAC. While applying a lower analytical window for TAC increased the detectability of weaker ligands (Gerringa et al., 2007), fulvic acid additions could not be detected, confirming at least part of Laglera's conclusions. According to Laglera et al. (2011), TAC itself interacts with humic substances, suppressing Fe-TAC complexation. Indeed, adding the IHSS FA standard to a sample did not significantly change $[L_t]$ and $LogK'_{Fe'L}$ determinations (unpublished results; addition of 0.1 mg/L FA to Station 134 sample from 2695 m depth).

From earlier studies using TAC, riverine influence on the ligand pool was found in a number of occasions (e.g. Gerringa et al., 2007; Batchelli et al., 2010), including the influence of Arctic outflow water on surface Fe speciation in the Western Atlantic ocean (Gerringa et al., 2015) but this riverine input of ligands is probably underestimated given that part of the humic influence is missing. Other studies concentrating on the effect of humic substances in particular apply other methods such as 2,3-dihydroxynaphtalene (DHN) and salicylaldoxime (SA) (Laglera and van den Berg, 2009; Abualhaija et al., 2015; Mahmood et al., 2015). Prior intercomparisons between the TAC and SA methods showed that agreement within similar detection windows could be dependent on the sample matrix. A study in the North Pacific comparing methods concluded that methods using TAC and SA gave more or less comparable results but still recommended further research (Buck et al., 2012). A comparison study in the north Atlantic showed an excellent agreement between the methods using SA and TAC when the 1 ligand model was applied to the data. However, when applying the 2 ligand model to the two datasets different results were obtained, with the SA method resulting in the discrimination of 2 ligands where the TAC method could not (Buck et al., 2016). While an increased Fe-binding organic ligand concentration inside the TPD is indicated in the present study, the exact effect on speciation might be underestimated by the analytical method employed here.

CDOM spectral properties a_{254} and a_{300} represent CDOM concentrations, and therefore the organic substance load also including humic substances (Helms et al., 2008). $F_{250/450}$ is typically reported as humic-like substances (Coble, 2007). All these properties have very good agreement with our *in-situ* CDOM fluorescence discriminator for the TPD (Fig. 3d; Fig. 6, white contours). As a result significantly higher average values were recorded inside the TPD for all

three terms (Table 3). The spectral slope at an interval of 275-295 nm ($S_{275-295}$) showed more uniformly low slopes inside the TPD compared to outside the TPD (0.026 vs. 0.035 nm^{-1}, SD = 0.002 and 0.023 nm^{-1}, respectively) which, coupled with high absorbance at both 254 and 300 nm, indicate a higher CDOM concentration of samples inside the TPD (Helms et al., 2008). However, higher-wavelength intervals fall outside of our instrument's sensitivity, with $S_{350-400}$ at or below the limit of detection for many samples (N = 62 for $S_{350-400}$ vs. N= 76 for $S_{275-295}$ for outside-TPD samples), creating a bias in the dataset for samples with higher absorbance, and therefore, slope ratios yielded little further information. In most oceanic samples, slope ratios are driven by the UV slope ($S_{275-295}$; Helms et al., 2008) and given the restrictions of our equipment our discussion is focused on these properties.

Measurements of [HS] inside the TPD yielded a higher average of 0.18 Eq. mg/L FA (SD = 0.07 Eq. mg/L FA, N = 18) against an average 0.06 Eq. mg/L FA outside the TPD (SD = 0.03 Eq. mg/L FA, N = 38). From the [HS] profiles (Fig. 7) it is visually apparent that inside-TPD stations (87, 99, 119 and 125) had well-defined surface enrichment. In prior studies measuring riverine-sourced humic substances it was shown that humic substance concentrations explained 100% of Fe-binding organic ligands measured (Laglera and van den Berg, 2009; Abualhaija et al., 2015). According to Laglera and van den Berg (2009) 1 mg L^{-1} Suwannee River FA should offer an Fe binding capacity of 16.7±2.0 nM under controlled purified circumstances using UV digested seawater. By extension, the 0.18 Eq. mg/L FA found in the present study would account for an Fe binding capacity of around 3.0±0.4 nM. Inside the TPD, [L_t] was shy of that at 2.60±0.78 nM (Table 3). However, while it is evident from literature and our own findings that the TAC method cannot measure all humic substance influence, the [L_t] we found did not differ from the humic contribution we measured outside of standard deviation. Furthermore, [L_t] increase from deep to surface is more pronounced in Section 1 than it is in Section 2 (Fig. 6b). With a DFe increase of similar proportion in either section (Fig. 6a), this leads to a stronger effect of low (between 0 and 1) ratios of [L_t] and DFe, indicating a lack of ligands to explain DFe concentrations in Section 2. This may indicate a stronger underestimation of ligands in Section 2 than in Section 1, and an overestimation when compared to [HS] in Section 1. The differences between Sections 1 and 2 are not surprising as the TPD has a transition time of 3 years (Gregor et al., 1998) and the TPD flow path varies yearly with the arctic oscillation (Macdonald et al., 2005). Therefore local samples from the TPD are subject to changes in conditions over time in the source catchments, sea ice melt and coverage and shelf sea interaction. Additionally, possible modification

of the surface water influence over time may take place, e.g. by microbial action, local DOM production, deposition by ice rafted sediments, etc.

Many of these processes may be presumed involved in the local CDOM pool and contributing to the ligand pool regardless of transition time. Ice rafted sediments have been indicated to carry trace elements (Hölemann et al., 1999) and presumably Fe-binding organic ligands. Occasionally we found areas of strong discolouration by ice rafted sediments during the PS94 expedition (2 sampling locations pending analysis, cruise report: Schauer, 2016), but this remained a local phenomenon. Biota may also have been present to release DOM. However, given that all stations in sections 1 and 2 were under full ice cover at the time of sampling, contemporaneous microbial activity may be presumed to be minimal. EPS carried by the TPD from the ostensibly more active source areas may be a factor, given that recalcitrant fractions are known to be present (Hofmann et al., 2009). However the relative contribution thereof cannot be ascertained as EPS are methodically indistinguishable from HS using the method here employed (Hassler et al., 2011b).

It must be noted that [HS] are measured in equivalent [FA] using the IHSS Suwannee River standard. This is a humic substance originating in the Okefenokee Swamp in GA, USA, depositing in the blackwater Suwannee River which ultimately flows out in the Gulf of Mexico. This FA standard may not necessarily represent humic substances present in the Arctic Ocean, which for our study area originate from broad Arctic shelves, sea ice, and rivers with catchments characterised by permafrost soil which is under pressure of climate change (Schuur et al., 2015). How measurement of humic substances from this area would differ electrochemically is currently unknown as there is no representative standard available for this type of catchment. However, changes in riverine discharge as a result of changing conditions, both quantitatively and qualitatively, have been described (Peterson et al., 2002; Vonk et al., 2012, 2013). Finally, particle load from rivers is also high, potentially transporting particle- or colloid-bound Fe into the Arctic Ocean interior (Hirst et al., 2017). Particles and colloids may contribute to the dissolved Fe pool via exchange with ligand-bound DFe, as is also found to be the case in the Southern Ocean (von der Heyden et al., 2012). The exchangeability of particle- or colloid-bound DFe in the Arctic Ocean is not certain, given the unknown extent to which these are refractory (Thuróczy et al., 2011). If there is a large fraction of irreversibly bound DFe, $[L_t]$ will be overestimated (Gledhill and Buck, 2012; Gerringa et al., 2014). Particle-bound DFe may be a source of exchangeable DFe and of binding sites, procedurally put outside of the methodological size cut-off due to filtration.

CDOM (a_{254}, a_{300}; Fig. 6d) and FDOM ($F_{250/450}$, Fig. 6e) spectral properties also showed higher values in Section 1, while [HS] profiles suggest that surface

concentration increases were similar at stations inside the TPD in either transect (Stations 87 and 99 in Section 1, Stations 119 and 125 in Section 2; Fig. 7). This suggests that the CDOM spectral properties measured here are also limited in their ability to elucidate the relative contribution of humic substances. The most specific humic-like descriptors for CDOM are reported to be slope ratios (Helms et al., 2008) and comprehensive analysis of Excitation Emission Matrix fluorescence spectroscopy (EEM) (Walker et al., 2009). Comprehensive analysis of absorption spectra also shows promise in deriving source information from DOM (Reader et al., 2015), but has not yet been applied in this region. More detailed exploration of CDOM spectral properties using EEMs in concert with absorption spectra and using a more sensitive instrument may improve upon these comparisons, allowing for the use of multivariate analysis to explore of humic-like substances (Reader et al., unpublished data).

In order to further explore the relation between ligand characteristics on the one hand and CDOM spectral properties and [HS] on the other, pairwise Spearman rank-order correlations were performed on the surface transect data (≤200 m depth, Stations 58 to 101 and 117 to 134). These are summarized in Table 5 where these are reported for DFe, [L_t] and their ratio and [L´]. [HS] have a strong correlation with DFe. However, while a reasonable correlation with [L_t] exists, it is less pronounced. This may be explained by the specific FA standard for [HS] used, which may not represent local humic substances. Additionally, the inherent non-specificity of CLE-AdCSV methods and the competitive ligand TAC's reported inability to measure all humic substances (Laglera et al., 2011) may limit to what extent [L_t] is explained by [HS]. Similarly, correlations between DFe and $F_{250/450}$, a_{254} and a_{300} are strong and those for [L_t] and [L´] are less pronounced. Correlations of these humic indicators with the ratio [L_t]/DFe is higher again, indicating that the fact we measure insufficient ligands to explain DFe inside the TPD has good agreement with [HS]. Spectral slope correlations between $S_{275\text{-}295}$ and [L_t], [L´] and the ratio [Lt]/DFe in a similar fashion as above were less pronounced. However, correlations for S_{350} (not shown) could not be resolved, and therefore nor could the slope ratio. As the variability of $LogK´_{Fe'L}$ is very low across the dataset, no correlation statistics were calculated for it.

CDOM spectral properties are not available for the Barents Sea transect. [L_t] and the ratio [L_t]/DFe differ from measurements in the surface Arctic Ocean. DFe is depleted at the surface here, while [L_t] has a well-mixed character to depths beyond 200 m. The ratio [L_t]/DFe is low but not saturated at nearshore Stations 4 and 173, while it is high at the surface with a decline with depth in the central Barents Sea stations (153 and 161). This shows us that the riverine influence inside the TPD is different to that of this shelf sea in terms of Fe-

binding organic ligands. The Barents Sea is characterized by a large influence of Atlantic water and the continental shelf, and lacks the influence of large rivers and organic loads from such catchments (Rudels, 2012).

Finally, we may estimate the TPD flow path by way of the tracers we have measured, particularly DFe, CDOM spectral properties a_{254}, a_{300} and $F_{250/450}$, and to a lesser extent [L_t], [L´] and the ratio [L_t]/DFe. While [HS] confirms this information, the horizontal resolution for these measurements is insufficient to directly indicate the TPD flow path. Hydrographical data supports the fundamentally different character of the surface water, particularly in terms of density. However, with the data at hand a distinction in ice melt and river water cannot be made based on our data, but other data collected during the cruise will help elucidate this distinction. In synthesis, we can surmise that Stations 81 to 99 in Section 1 and Stations 119 to 130 in Section 2 are part of the TPD. While Stations 101 and 117 fall outside of our initial constraint of the TPD using the *in-situ* CDOM fluorescence, some influence of the TPD is apparent here and therefore the border of the flow path is not sharply defined. The indication of the TPD flow path in Fig. 1 is based on the preceding.

Table 5 Spearman rank order correlations of Fe speciation properties with [HS] and CDOM spectral properties in the surface transect. All p-values <0.001

	[HS]	**F_{450}**	**a_{254}**	**a_{300}**	**$S_{275-295}$**
DFe	0.90	0.93	0.90	0.87	-0.52
[L_t]	0.69	0.74	0.69	0.66	-0.36
[L']	-0.47	-0.50	-0.53	-0.54	0.36
Ratio [L_t]/DFe	-0.79	-0.83	-0.82	-0.80	0.49

5.5. Conclusions

$LogK'_{Fe'L}$ was very constant across the entire dataset, indicating a single group of ligands or very consistent mix of ligands in terms of binding strength. Two ligand groups could be resolved for part of the dataset, and where these could be resolved the $LogK'_{Fe'L}$ values were again very consistent across basins. Scavenging seemed relatively important in the deeper Makarov basin, and low Fe in deep Makarov is most probably driven by DFe sources alone, confirming earlier findings. In the surface Arctic Ocean Fe-binding organic ligands correlated significantly with CDOM, including humic proxies, which in turn tie this to the TPD. A lack of ligands to explain DFe indicated by $[L_t]$/DFe ratios < 1 was unexpected, but agree with an underestimation by the TAC method in detecting humic influences or DFe contributors beyond the scope of our measurements. While average ligand concentrations measured inside the TPD agree with [HS] found within standard deviations, similar $logK'_{Fe'L}$ were found inside and outside of the TPD. A differing response in relation to the distance from the TPD source area of Sections 1 and 2 suggests that modification during surface transport across the Arctic Ocean surface and / or seasonal differences are present. Elucidating the role of humics specifically, beyond the correlation indicated in this study, requires a different approach in CLE-AdCSV. Different methods have their respective roles in a detailed analysis of Fe-binding organic ligands. Such measurements may then be coupled with high resolution direct measurement of humic substances, which call for a more representative expression standard for the catchments around the influential mediterranean Arctic. Detailed examination of CDOM pools and their characteristics, along with other tracers, may enhance our understanding of riverine influences further.

The TPD flow path was well-discernible from our measurements of known tracers such as CDOM spectral properties and DFe, sustained by $[L_t]$. DFe and $[L_t]$ inside the TPD flow path were high. The TPD and therefore the Arctic major rivers are a source of Fe-binding organic ligands. River output of CDOM is already known to be under the influence of climate change, possibly changing Fe speciation throughout the Arctic Ocean surface. As the Arctic Ocean flows out into the Atlantic Ocean through the Fram strait, the effect of climatic change in Arctic river catchments and sea ice dynamics may reach well beyond the Arctic Circle.

Chapter 6

Fe-binding Organic Ligands in the Humic-Rich TransPolar Drift in the Surface Arctic Ocean using Multiple Voltammetric Methods

This chapter is at the time of printing in review with the *Journal of Geophysical Research: Oceans* as:
Slagter, H.A., Laglera, L.M., Sukekava, C., Gerringa, L.J.A.; Fe-binding Organic Ligands in the Humic-Rich TransPolar Drift in the Surface Arctic Ocean using Multiple Voltammetric Methods.

Abstract

Samples inside and outside of the Arctic Ocean's transpolar drift (TPD) have been analysed for Fe-binding organic ligands with Competitive Ligand Exchange Adsorptive Stripping Voltammetry (CLE-AdCSV) using salicylaldoxime (SA). This analysis is compared to prior analysis with CLE-AdCSV using 2-(2-thiazolylazo)-p-cresol (TAC). The TPD's strong terrestrial influence is used to compare the performance of both CLE-AdCSV methods in representing the nature of the natural organic ligands. These measurements are compared against direct voltammetric determination of humic substances (HS) and spectral properties of dissolved organic matter. The relations between the two CLE-AdCSV derived organic ligand concentrations and HS in the TPD have a comparable slope, though with an offset of 40% towards higher values for the SA method. These higher organic ligand concentrations, most probably due to HS, explain the high dissolved Fe concentrations transported over the Arctic Ocean by the TPD.

Outside the core of the TPD in the surface Arctic Ocean HS occur as well but at lower concentrations. Here HS still relate to dissolved Fe concentrations and to organic ligand concentrations obtained with SA, whereas organic ligand concentrations obtained with TAC remain constant. Moreover with decreasing HS the offset between the methods using TAC and SA decrease to smaller values. We hypothesize that the method using TAC either detects HS only at higher concentrations or detects only HS of a specific composition. On the other hand, the SA method might overestimate organic ligand concentrations as the offset with the TAC method remains where HS are not detected.

Ultimately, multiple approaches will be required to elucidate origin and nature of Fe-binding organic ligands in the marine environment.

6.1. Introduction

Fe is an essential trace metal for marine primary production (Geider and La Roche, 1994; Netz et al., 2012; Zhang, 2014). Fe solubility in seawater is governed by the presence of organic ligands to bind Fe, as inorganic solubility is lower than the minimum required concentrations for primary productivity (Timmermans et al., 2001a, 2001b; Strzepek et al., 2011; Boyd et al., 2012; Wilhelm et al., 2013). Fe-binding organic ligands form a poorly characterized pool as part of Dissolved Organic Matter (DOM; Gledhill and Buck, 2012; Hassler et al., 2017). Some very specific contributors such as siderophores are now becoming better characterized, though the relative contribution of these is in picomolar ranges and are a minor fraction of DFe and the Fe-binding organic ligand concentrations (Gledhill et al., 2004; Velasquez et al., 2011, 2016; Boiteau et al., 2016; Bundy et al., 2018). Given the inherently indirect nature of Fe-binding organic ligand measurements, the relative contribution of different groups of Fe-binding organic ligands is as of yet unknown. However, relative contributions by groups like humic substances (HS; Laglera and van den Berg, 2009) and exopolymeric substances (EPS; Hassler et al., 2011) may be considerable, given that there is no single contributor to the ligand pool indicated that explains Fe-binding ligand concentrations up to the nanomolar range as of yet.

The surface of the Arctic Ocean is strongly affected by terrestrial DOM as it is a shelf-surrounded ocean subject to terrestrial influences with a very high source area to basin ratio as defined by Raiswell and Anderson (2005). Runoff from the many rivers contains complex organic material, which for a large part is deposited in the Arctic shelf seas. The input of terrestrial HS is thought to be a major influence in the context of Fe-binding organic ligands. HS are persistent and heterogenic complex organic degradation products, ubiquitous particularly in coastal areas (Buffle, 1990) and long known to bind trace metals (Buffle, 1988). In fact, HS have been shown to account for an important part of the Fe-binding capacity in seawater (Laglera and van den Berg, 2009; Abualhaija et al., 2015; Dulaquais et al., 2018). HS are a complex black box with components that are typically operationally defined. Humic acids are hydrophobic at low pH and therefore separated from fulvic acid by precipitation after acidification (Buffle, 1988; Bronk, 2002), these form the oldest or most recalcitrant fraction of HS. A distinction is also made between terrestrial HS and marine humic or humic-like substances, produced in-situ by marine microbial activity as opposed to transported in from a terrestrial source (Bronk, 2002; Nakayama et al., 2011). However, this distinction is hypothetical and cannot be supported by analytical means. Low salinity waters in the surface Arctic Ocean carry important

DOM concentrations of terrestrial nature whereas marine humics could contribute significantly to higher salinity waters.

Here we study a selection of samples from the ice covered Arctic Ocean and one of the open shelf seas. The surface of the Arctic Ocean is of particular interest due to the relatively well-constrained Transpolar Drift (TPD) surface current. It is well established that the TPD transports riverine-based water and ice from the shelf seas across the Arctic Ocean, eventually out to the Atlantic Ocean through the Fram Strait (Gordienko and Laktionov, 1969; Gregor et al., 1998). The flow path of the TPD varies yearly with the arctic oscillation index (Macdonald et al., 2005) and has been constrained in the context of DOM and Fe biogeochemistry (Rijkenberg et al., 2018, Chapter 4; Slagter et al., 2017, Chapter 5). Given its susceptibility to rapid climate change (IPCC, 2014), the Arctic Ocean is a particularly important region to study the biogeochemistry of terrestrial matter. Rapid and widespread loss of permafrost (Schuur et al., 2015) in the river catchments is indicated to cause increases in the deposition of terrestrial organic matter in the Arctic shelf seas (Vonk et al., 2013) and effects on the larger Arctic Ocean are as of yet largely unknown. In the present study samples were collected during the 2015 PS94 TransArcII expedition inside the TPD and therefore subject to the terrestrial influence from major Arctic rivers; outside the TPD and in the Barents Sea, majorly under influence of the shelf and Atlantic inflow (Rudels, 2012). Early *in-situ* measurements of HS and CDOM establish that the TPD carries HS, though they were also detected in nontrivial concentrations outside of the TPD flow path (Chapter 5), which is unsurprising as HS and/or marine humics are ubiquitous also in non-coastal waters (Obernosterer and Herndl, 2000).

The definition of HS is essentially operational based on column retention with alkaline elution (Buffle, 1990). These analytical techniques are very time consuming and hard to apply in seawater. Spectral properties of DOM (Chromophoric DOM or CDOM and Fluorescent DOM or FDOM) are indicative of many subgroups, including HS (Coble, 2007). Measurements of HS and their relative contribution to the Fe-binding organic ligand pool are not straightforward. Direct voltammetric measurement of HS is possible, with HS indicated by standard addition of a representative reference material (Laglera et al., 2007; Quentel and Filella, 2008; Laglera and van den Berg, 2009).

Measurement of Fe-binding organic ligands using Competitive Ligand Exchange – Adsorptive Cathodic Stripping Voltammetry (CLE-AdCSV) is a technique proven to resolve the presence of most major ligands in the ocean (Gledhill and van den Berg, 1994; Rue and Bruland, 1995; Croot and Johansson, 2000; van den Berg, 2006). However, elucidation of the contribution of HS meets with mixed results. Voltammetric determination of Fe-binding organic ligands

measures the concentration and binding strength integrally for the Fe-binding organic ligand pool as a whole, and these are at best divided into several groups by binding strength. The method using 2-(2-thiazolylazo)-p-cresol (TAC) as a competing ligand (Croot and Johansson, 2000) has been shown not to reflect humic influences (Laglera et al., 2011). In contrast, recent work using salicylaldoxime (SA) as competing ligand has been shown to indicate HS (Laglera et al., 2011; Abualhaija and van den Berg, 2014; Mahmood et al., 2015).

In Chapter 5 we reported a strong relation between Fe-binding organic ligand measurements using TAC and the presence of the TPD as well as humic representative CDOM and FDOM measurements. The present study expands on this by re-analysing select samples from that study using SA as a competing ligand in CLE-AdCSV and additional measurements of HS. Comparing these results with those of TAC we provide an explanation to the values of ligand concentration below dissolved iron concentrations found in Chapter 5 and hope to further unveil the relative contribution of HS in the Fe-binding organic ligand pool in the Arctic Ocean in the TPD and in the coastal Barents Sea.

6.2. Materials and Methods

Specific samples collected during the 2015 PS94 TransArcII expedition on board FS Polarstern were analysed during the cruise with the TAC method (Chapter 5) and a subset of samples stored at -20 °C and re-analysed using CLE-AdCSV with SA. Re-analysis of samples with the SA method was performed for stations 69, 99, 101, 125 and 153 (Figure 1). Stations 69 and 125 are full depth profiles in the open Arctic Ocean (3500 and 4200 m, respectively); station 153 is a full depth profile over the Barents Sea shelf (400 m); and stations 99 and 101 have been sampled for the top 200 m. The SA method of analysis was applied according to Rue and Bruland (1995) following the adaptations by Buck et al. (2015).

A subset of frozen samples was analysed after cruise in the laboratories of the University of the Balearic Islands (UIB lab) with a voltammetric system identical to the system used on board. In this case the original voltammetric method (Laglera et al., 2007) was slightly modified to ensure the saturation with iron of the HS binding groups of both the sample and the reference standard (Sukekava et al., 2018). In the presence of 20 nM $KBrO_3$ and 5 mM POPSO buffer (from a mixed solution cleaned with MnO_2 as in Laglera et al., 2013) the sample was saturated with iron (20-60 nM depending on the DFe concentration) and was continually measured until the voltammetric signal decreased to a constant value. This decrease is caused by the total precipitation of iron in excess of the binding capacity of the HS. This process was described in Laglera and van den

Berg (2009). Calibration was attained via additions of 0.2 mg SRFA L^{-1}, dissolved in ultrapure water and in this case carefully saturated with iron before use. HS were therefore expressed as mg SRFA L^{-1}. The datasets for [HS] from both labs (on board and UIB lab) showed good correlation and could therefore safely be combined into one (Sukekava et al., 2018), and are from here on reported after conversion to $[L_t]_{FA}$ for most purposes. A complexing capacity of 14.6±0.7 mg SRFA L^{-1} (Sukekava et al., 2018). was used to convert HS concentrations into HS derived ligand concentrations ($[L_t]_{HS}$).The complexing capacity was obtained by titration with iron of the SRFA standard dissolved in UV digested seawater as suggested in Laglera and van den Berg (2009).

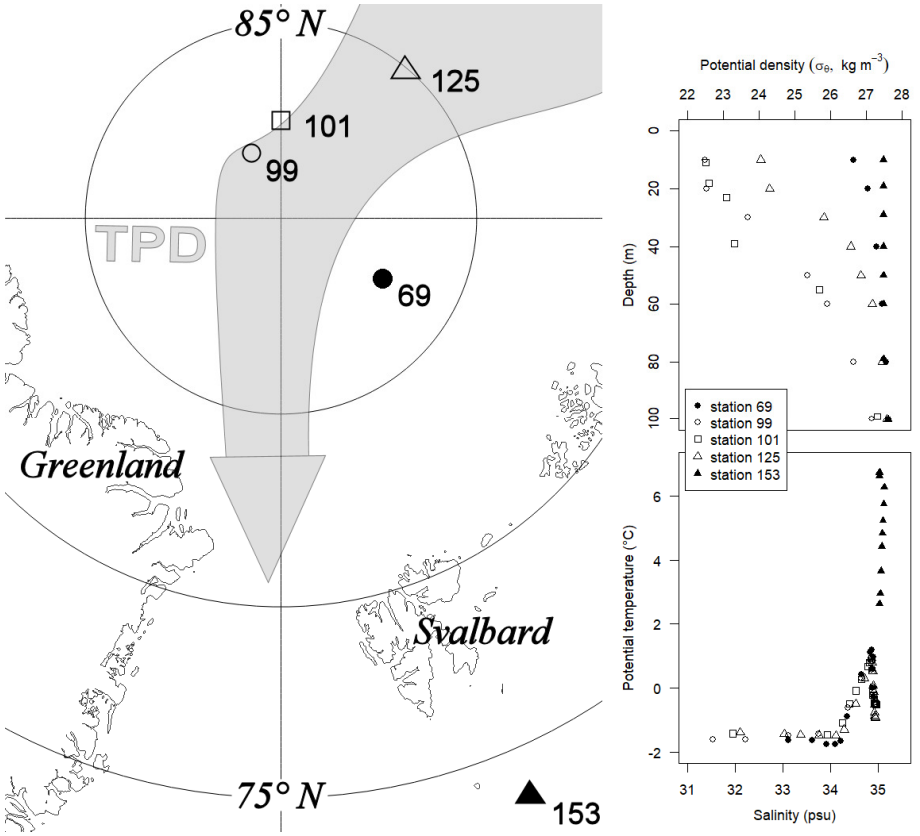

Figure 1 Map of the study area showing the selected stations 69, 99, 101, 125 and 153. The expected flow path of the TPD after Slagter et al. (2017, Chapter 5) is shown by the grey arrow. Potential density (top right) is shown for the upper 100 m indicating the TPD influence. A potential temperature-salinity (Θ-S) plot of the selected stations is shown to the lower right.

6.3. Results

6.3.1. Overall oceanographic characteristics

The TPD influence area in the Arctic Ocean surface coincides with a low density anomaly resulting from low surface salinity within the upper 100 m. Specifically, surface samples from Stations 99, 101 and 125 inside the TPD, as defined in Chapter 5 by in-situ CDOM fluorescence ≥ 0.5 a.u. (Rabe et al., 2016), show this low surface salinity and density (Figure 1, open symbols), down to 28 psu and 23 kg m^{-3}, respectively. Station 69, outside the TPD, has a higher surface salinity and density of 33.5 psu and 27 kg m^{-3}, respectively. Station 153 in the Barents Sea has a salinity of >35 psu and relatively constant density between 27.5 and 28 kg m^{-3} with a higher potential temperature (3-7 °C, Figure 1). From the three stations in the TPD, station 101 is bordering closely rather than inside.

6.3.2. Arctic Fe speciation

All SA measurements show higher $[L_t]$ than the TAC measurements (Figure 2 second row vs. first row, Excess L in Figure 3B). Specifically, $[L_t]_{TAC}$ is an average 60% of $[L_t]_{SA}$ across all samples that have data for both methods(SD = 12.9%, N = 47). At depths beyond 150 m $[L_t]_{SA}$ approaches the $[L_t]_{TAC}$ more closely. The difference is most pronounced for measurements inside the TPD. $[L_t]_{TAC}$ inside the TPD was in some cases lower than DFe (Stations 99 and 125, Figure 2, top row), with more occurrences in the complete TAC dataset (Chapter 5). This was not the case for $[L_t]_{SA}$, which was higher than DFe in all samples measured. Overall, $[L_t]_{TAC}$ was 2.46±0.63 Eq. nM Fe inside the TPD and 1.36±0.33 eq. nM Fe outside the TPD; $[L_t]_{SA}$ was 4.19±0.74 and 2.33±0.58 Eq. nM Fe, respectively (Table 1). In contrast to TAC data, most SA analyses could also be resolved for 2 ligand groups inside the TPD. When comparing the sum of SA-derived $[L_1]$ and $[L_2]$ from the 2 ligand model ($\Sigma_{L1,L2;SA}$) to $[L_t]_{SA}$ from the model assuming the existence of 1 ligand, there is very good agreement (Figure 2, second row). Additionally, the SA-derived $[L_1]$ has a good agreement with $[L_t]_{TAC}$ (Pearson's product-moment correlation score of 0.82 ($p<0.001$; N=12). For those samples where 2 ligand groups could be resolved for the TAC method, $\Sigma_{L1,L2;TAC}$ is higher than $[L_t]_{TAC}$. High surface $[L_t]_{HS}$ (Figure 2, bottom row) was especially pronounced in the two unequivocal TPD stations (99 and 125) with $[L_t]_{HS}$ over 4 Eq. nM Fe in the upper 50 m, coinciding with high values of parameters describing CDOM. $[L_t]_{HS}$ was elevated to a lesser extent in the surface in the TPD-bordering station 101 and station 69 outside the TPD, and no elevated concentrations were observed for station 153 in the Barents Sea. The difference between measurements of $[L_t]$ using TAC and SA ($[L_t]_{SA}$ - $[L_t]_{TAC}$) are referred to as δLt. δLt was consistently >0 with a value inside the TPD of 1.73±0.56 Eq. nM Fe whereas outside the TPD and over the continental shelf

outside the TPD flow path δLt is lower, but still considerable at 0.92±0.44 and 0.81±0.43 Eq. nM Fe, (Table 1, ranges given are standard deviations).

$LogK'_{Fe'L}$ is similar for either method and remarkably stable (table 1). Measurements using TAC have a $logK'_{Fe'L}$ of 12.01±0.39 mol^{-1} inside the TPD, and 12.13±0.23 mol^{-1} outside the TPD. Measurements using SA have a $logK'_{Fe'L}$ of 11.75±0.35 mol^{-1} inside the TPD and 11.60±0.27 mol^{-1} outside the TPD. In the Barents Sea $logK'_{Fe'L}$ using TAC is similar to the other subsets at 12.14±0.17 mol^{-1}, whereas here the SA method results in a lower $logK'_{Fe'L}$ of 11.17±0.20 mol^{-1} which has very little SD overlap. Figure 3 shows the relation between the TAC and SA methods in terms of $log\alpha_{Fe'L}$, and excess L. $Log\alpha_{Fe'L}$ is less prone to bias and therefore a good parameter for comparison (Gledhill and Gerringa, 2017). For the SA method $log\alpha_{Fe'L}$ is invariably near 3, for the TAC method $log\alpha_{Fe'L}$ is near 3 outside the TPD, inside the TPD values decrease to below 1 (Table 1, Figure 3A). Since $logK'_{Fe'L}$ does not significantly change inside the TPD, the low $log\alpha_{Fe'L}$ values for the TAC method are tied to the excess ligand concentration. Saturation of the measured ligands is indicated with excess ligands near zero and thus $logK'_{Fe'L}$ values that are difficult to calculate. This is caused by a lack of data points with large standard deviations, thus resulting in $log\alpha_{Fe'L}$ values that are imprecise (Gerringa et al., 2014). Measurements using the TAC method give consistently lower excess ligand concentrations for all depths, including sporadic occurrence of near-zero values (Figure 3B; Table 1).

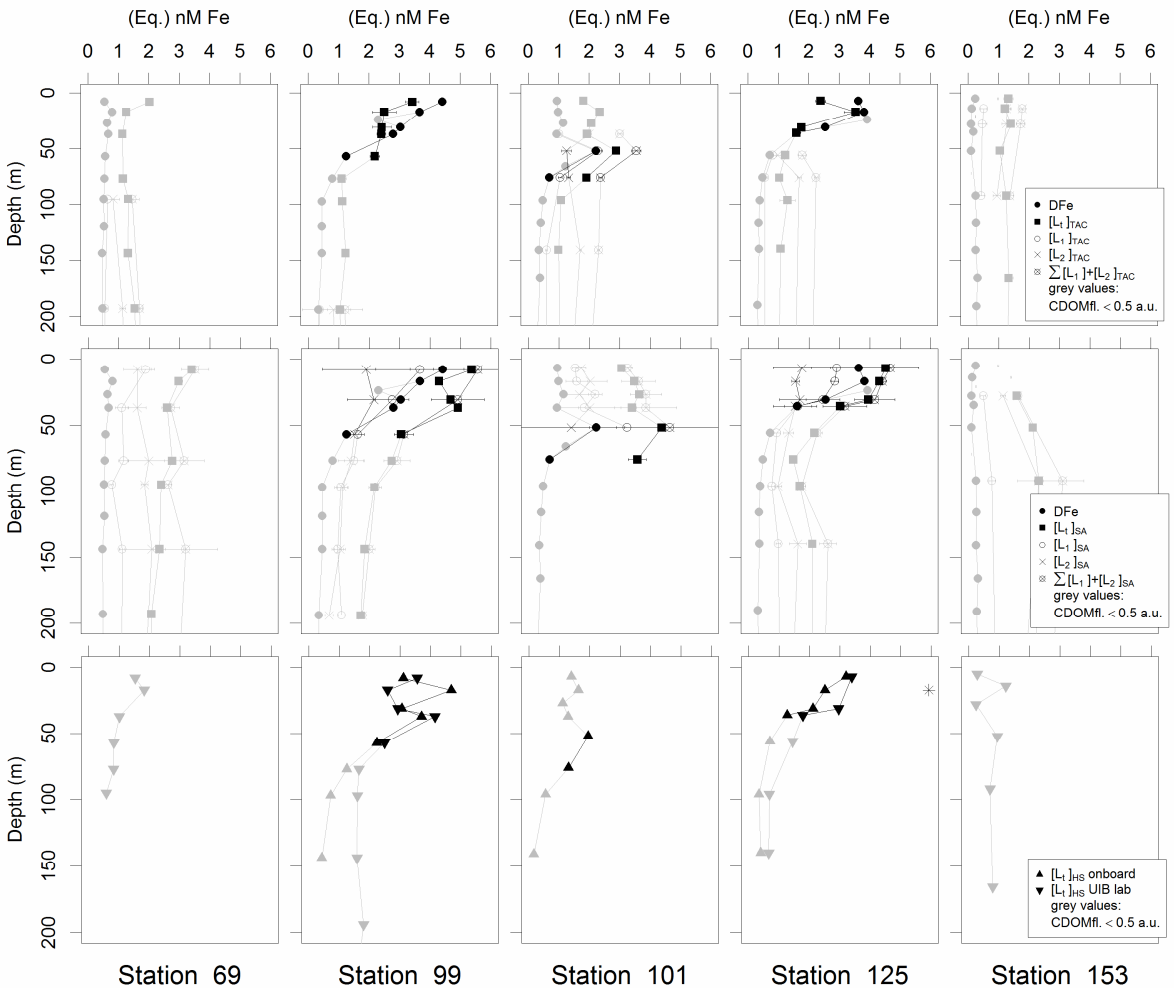

Figure 2 DFe and ligand concentrations for determinations using two models one allowing 1 ligand ($[L_t]$), and one allowing two ligands ($[L_1]$ and $[L_2]$) to exist. Per station results obtained using TAC are in the top row, and those using SA are in the middle row. The bottom row shows equivalent ligand concentrations derived from SRFA complexing capacity for HS measurements in two labs. Samples outside the TPD (grey symbols) and inside the TPD (black symbols) are determined by the CDOM fluorescence (CDOMfl.) ≤ 0.5 a.u. boundary for all graphs.

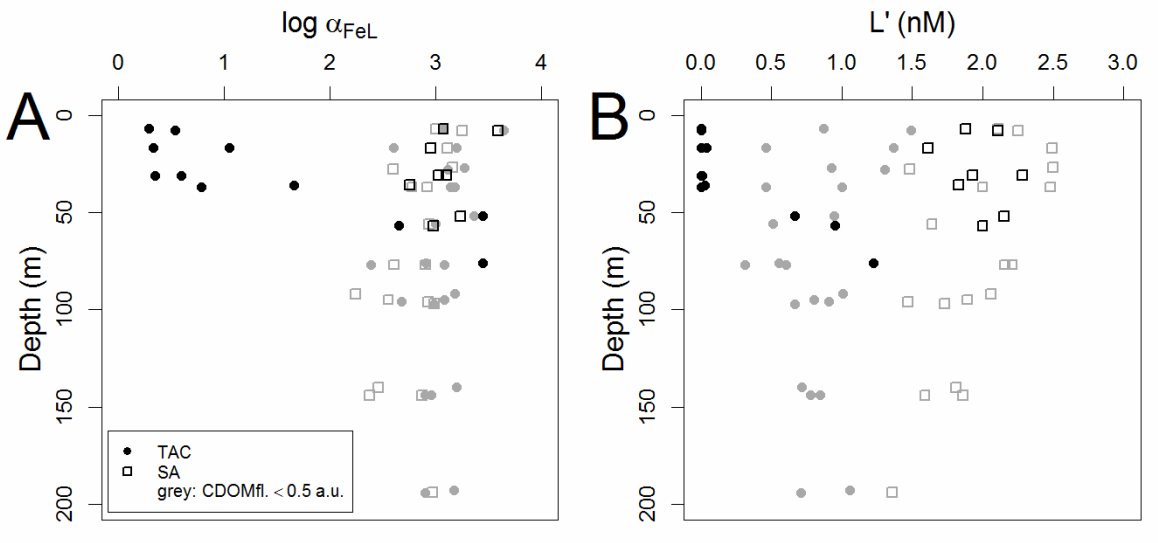

Figure 3 Log$\alpha_{Fe'L}$ (**A**, dimensionless) and Excess L (**B**, [L´] in Eq. nM Fe) for 1-ligand class determination by depth using TAC (closed circles) and SA (open squares). Samples outside the TPD (grey symbols) and inside the TPD (black symbols) are determined by the CDOMfl. ≤ 0.5 a.u. boundary for all graphs.

Table 1 DFe and Fe-binding organic ligand characteristics using a 1-ligand-class model for calculation using both the TAC and SA method of CLE-AdCSV for samples from stations 69-125 separated by TPD presence based on CDOMfl. ≤ 0.5 a.u. and for samples from station 153 in the Barents Sea separately. Properties include the ligand concentration [L_t] and the absolute difference in L_t between CLE-AdCSV methods (δL_t) as well as relative to $[L_t]_{SA}$; the relative complexation capacity attributed to HS determined directly through standard addition with SRFA ($[L_t]_{HS}$); the conditional binding constant relative to Fe´ ($\log K'_{Fe'L}$), the excess ligand concentration (L´), and the reactivity relative to Fe´ ($\log\alpha_{Fe'L}$).

		DFe	**$[L_t]_{TAC}$**	**$[L_t]_{SA}$**	**δL_t**	**$[L_t]_{TAC}$ /$[L_t]_{SA}$**	**$[L_t]_{HS}$**	**$\log K'_{Fe'L}$ (TAC)**	**$\log K'_{Fe'L}$ (SA)**	**L'_{TAC}**	**L'_{SA}**	**$\log\alpha_{Fe'L}$ (TAC)**	**$\log\alpha_{Fe'L}$ (SA)**
		nM		*Eq. nM Fe*		*%*	*Eq. nM Fe*	*mol^{-1}*	*mol^{-1}*		*Eq. nM Fe*		
Inside TPD	*mean*	2.70	2.46	4.19	1.73	59%	2.83	12.01	11.75	0.27	2.05	1.38	3.05
CDOMfl. ≥ 0.5 a.u.	*SD*	1.17	0.63	0.74	0.56	11%	0.97	0.39	0.35	0.46	0.40	1.24	0.33
St. 99, 101 and 125	*N*	11	11	11	11	11	11	11	11	11	11	11	11
	min	0.69	1.6	3.03	0.76	45%	1.3	11.45	10.89	0	1.41	0.29	2.35
	max	4.42	3.55	5.37	2.51	82%	4.22	12.63	12.27	1.23	2.88	3.45	3.59
Outside TPD	*mean*	0.50	1.36	2.33	0.92	62%	1.04	12.13	11.6	0.86	1.77	3.04	2.84
CDOMfl. < 0.5 a.u.	*SD*	0.22	0.33	0.58	0.44	13%	0.5	0.23	0.27	0.27	0.40	0.27	0.28
St. 69, 99, 101 and	*N*	44	44	32	32	32	19	44	32	44	32	44	32
125	*min*	0.15	0.89	1.48	0.13	41%	0.16	11.67	11.11	0.31	1.16	2.39	2.38
	max	1.15	2.36	3.65	1.71	93%	1.83	12.62	12.35	1.49	2.5	3.69	3.65
Barents Sea	*mean*	0.31	1.26	2.04	0.81	62%	0.70	12.14	11.17	0.95	1.67	3.07	2.38
Station 153	*SD*	0.31	0.12	0.31	0.43	18%	0.38	0.16	0.20	0.34	0.44	0.24	0.18
	N	7	7	4	4	4	6	7	4	7	4	7	4
	min	0.11	1.05	1.59	0.18	50%	0.24	11.95	10.93	0.23	1.15	2.61	2.23
	max	0.98	1.41	2.32	1.07	89%	1.22	12.39	11.43	1.31	2.06	3.37	2.6

While 2 ligand groups could be resolved for few of the TAC-derived measurements, especially in the surface, yielding few records for comparison, the $LogK'_{Fe'L}$ values for the L_1 class agree well for the TAC and SA methods (Figure S1, second column of graphs). This agreement is dependent on α_i, as using $LogK'_{FeL,Fe3+}$ results in better agreement for the L_2 class (data not shown). Such correlations based on $logK'_{FeL,Fe3+}$ are an artefact of the pH used in analysis through α_i. As our TAC measurements are performed at pH=8.05 and our SA measurements are performed at pH=8.40, $logK'_{FeL,Fe3+}$ is not a suitable comparison (Gledhill and Buck, 2012). Over the entire dataset $logK_1'_{Fe'L(SA)}$ and $logK_1'_{Fe'L(TAC)}$ do not differ significantly, with values of 13.88±0.65 (N = 41) and 13.49±0.58 mol^{-1} (N = 26) respectively. The weaker L_2 class is found to be significantly stronger in the case of TAC measurements, with an average $logK_2'_{Fe'L,(SA)}$ of 10.43±0.21 mol^{-1} and an average $logK_2'_{Fe'L(TAC)}$ of 11.19±0.21 mol^{-1}. This difference in particular would have been veiled had K′ been reported in relation to Fe^{3+} here, since the difference between the values is ~0.8. $Log\alpha_{Fe'L}$ (Figure S1, third column, page 138) is higher towards the surface for the SA-derived L_1 fraction. Over the Barents Sea shelf (station 153), values are very similar regardless of the CLE-AdCSV method employed.

6.3.3. Method intercomparison

When comparing $[L_t]$ between the TAC and SA methods directly, the initial view is a reasonable agreement with consistently higher values for $[L_t]_{SA}$ as noted in the prior paragraphs. All points are below the 1:1 line in favour of $[L_t]_{SA}$ (Figure 4). When we separate the data using CDOMfl. ≤ 0.5 a.u. boundary, dividing samples inside and outside the TPD, the CLE-AdCSV methods show distinct relations with one outlier, the uppermost sample of station 69 (10 m depth; triangle in Figure 4). The relationship between $[L_t]_{TAC}$ and $[L_t]_{SA}$ at station 101 indicates that this station is in the TPD influence zone (crosses in Figure 4). Samples inside the TPD correlate with a slope of 0.56 ($[L_t]_{TAC}$:$[L_t]_{SA}$), whereas outside the TPD there is no correlation, with $[L_t]_{TAC}$ unchanging while $[L_t]_{SA}$ varies between samples.

$LogK'_{Fe'L}$ for the measurements using SA were lower than those for the measurements using TAC, but otherwise shared in a remarkable consistency observed earlier for this dataset (Chapter 5). The only exception herein is the Barents Sea station, where the difference between TAC- and SA-derived $logK'_{Fe'L}$ was slightly higher due to lower $logK'_{Fe'L}$ for measurements using SA. $Log\alpha_{Fe'L}$ for the SA analyses does not significantly differ inside and outside the TPD. In contrast, $log\alpha_{Fe'L}$ for TAC analyses is significantly lower inside the TPD.

Increments in DFe, $[L_t]_{TAC}$ and $[L_t]_{SA}$ crossing into the TPD influence were compared to increments in [HS] based on the same boundary. Resulting is an

increment ratio between ΔDFe, $\Delta[L_t]_{TAC}$ and $\Delta[L_t]_{SA}$ over Δ[HS] (Table 2). For instance, the increment ratio for DFe may be defined as:

$$\frac{\Delta DFe}{\Delta[HS]} = \frac{\overline{DFe_{inside\ TPD}} - \overline{DFe_{outside\ TPD}}}{\overline{[HS]_{inside\ TPD}} - [HS]_{outside\ TPD}} \quad (1)$$

The $\Delta[L_t]/\Delta[HS]$ ratio is lower for TAC measurements than for SA measurements, 8.4 Eq. nM Fe mg^{-1} and 12.2 Eq nM Fe mg^{-1}, respectively. The ΔDFe/Δ[HS] ratio is higher at 17.4 nM mg^{-1}. The lower ratio $\Delta[L_t]_{TAC}/\Delta[HS]$ indicates a lack of representation of Δ[HS] in $[L_t]_{TAC}$. However, as it is 68% of $\Delta[L_t]_{SA}/\Delta[HS]$ as opposed to near-zero, some contribution to [HS] is detected by TAC. The ΔDFe/Δ[HS] and $\Delta[L_t]_{SA}/\Delta[HS]$ ratios resemble more the binding capacity of 14.6±0.7 nM mg^{-1} found for the SRFA standard and the value of 16.7 nM mg^{-1} as found by Laglera and van den Berg (2009).

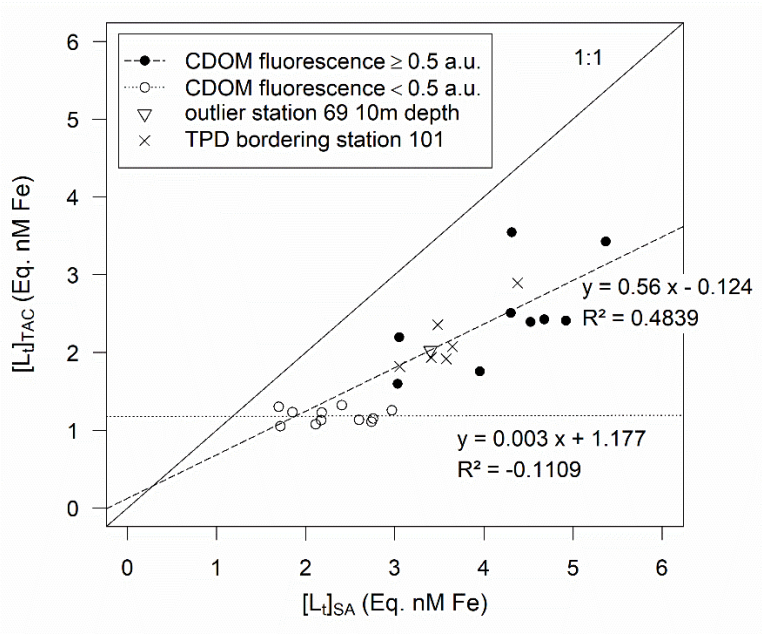

Figure 4 The ligand concentrations $[L_t]$ in Eq. nM Fe as measured using CLE-AdCSV with TAC (vertical) and SA (horizontal), samples are subdivided on the basis of their presence inside the TPD (filled symbols, CDOMfl. ≥ 0.5 a.u.) and outside the TPD (open symbols, CDOMfl. < 0.5 a.u.). One value does not conform to the split (triangle symbol), which is objectively outside the TPD influence area, this value is not included in the regressions. Functions and R^2 values describe the linear regressions of the subsets inside and outside the TPD. Station 101, indicated by crosses, is considered inside the TPD.

Table 2 Average concentrations with standard deviations of DFe, [L_t] (using two CLE-AdCSV methods) and [HS] inside and outside the TPD based on CDOM fluorescence. The increments (Δ) across the CDOM fluorescence boundary (0.5 a.u.) of the averages are calculated for each property, and increments divided by Δ[HS] for DFe and [L_t] per mg SRFA across the TPD border.

	DFe	**$[L_t]_{TAC}$**	**$[L_t]_{SA}$**	**[HS]**
	nM	*Eq. nM Fe*	*Eq. nM Fe*	*Eq. mg L^{-1}*
inside TPD	2.70±1.17	2.46±0.63	4.19±0.73	0.18±0.07
outside TPD	0.50±0.22	1.40±0.42	2.64±0.65	0.05±0.03
Δ (increment)	**2.20**	**1.06**	**1.55**	**0.13**
Δ[HS]$^{-1}$	**17.4**	**8.4**	**12.2**	**1**

The $[L_t]_{HS}$ and DFe have a distinct relation inside the TPD, near the 1:1 line (Figure 5A). Comparing $[L_t]_{HS}$ to TAC- and SA-derived [L_t] inside the TPD (Figure 5B), both relate almost similarly though with an offset between the two comparisons (intercepts of -0.40 and 0.88 Eq. nM Fe for linear regressions of $[L_t]_{TAC}$:$[L_t]_{HS}$ and $[L_t]_{SA}$:$[L_t]_{HS}$ in Figure 5B, respectively). While $[L_t]_{TAC}$ correlates with $[L_t]_{HS}$ in a near 1:1 ratio (slope is 0.99), $[L_t]_{SA}$ has a consistently higher value while maintaining a smaller slope (0.89). Outside the TPD $[L_t]_{TAC}$ is constant over low but variable $[L_t]_{HS}$, whereas $[L_t]_{SA}$ and $[L_t]_{HS}$ outside the TPD co-vary similarly to their relation inside the TPD (grey values in Figure 5B). The lack of $[L_t]_{TAC}$ correlation with $[L_t]_{HS}$ outside the TPD corresponds to a poorer correlation of $[L_t]_{HS}$ with DFe outside of the TPD (Figure 5A). Comparison between $[L_t]_{HS}$ and δL_t shows no clear correlation inside and outside of the TPD,. Pearson product-moment correlation proved to be highly significant for $[L_t]_{HS}$ with DFe, with the strongest r values for samples inside the TPD. Similar relations between r values are seen for $[L_t]_{HS}$ vs. $[L_t]_{SA}$ and $[L_t]_{TAC}$, though with lower significance levels and no formal significance for the latter for samples outside of the TPD (Table 3). In contrast, the relation between $[L_t]_{HS}$ and δL_t was only significant for samples outside of the TPD, though there is a relation closer to a 1:1 ratio for the entire dataset (Table 3, Figure 5C). Paradoxically to the ratios of increment above and the occurrence of ligand saturation for measurements using TAC, the correlation score for the $[L_t]_{HS}$-$[L_t]_{TAC}$ relation inside the TPD is very similar to the $[L_t]_{HS}$-$[L_t]_{SA}$ relation.

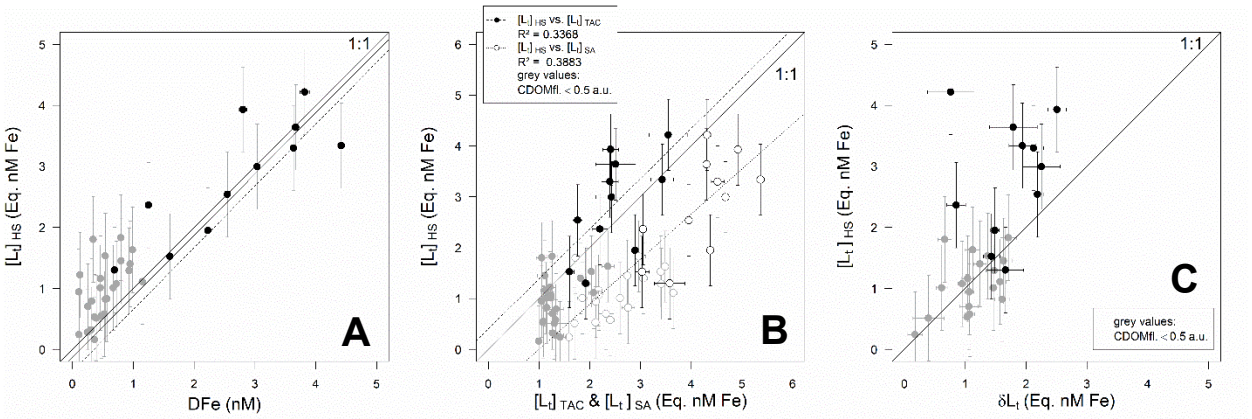

Figure 5 **A**) Comparison of $[L_t]_{HS}$ and DFe. The error bars along the vertical axis are derived from the uncertainty of 0.7 nM mg^{-1} in the conversion factor from [HS] to $[L_t]_{HS}$. R^2 values indicate the quality of fit of linear regressions, of which those for all data and data inside the TPD (CDOMfl. ≥ 0.5 a.u.) are plotted. **B**) Comparison of $[L_t]_{HS}$ with $[L_t]$ derived from CLE-AdCSV with SA (open symbols) and TAC (closed symbols). Only measurements inside the TPD (CDOMfl. ≥ 0.5 a.u.) were considered for the linear regressions. **C**) Comparison of $[L_t]_{HS}$ with the difference between CLE-AdCSV-derived $[L_t]$ values (δLt) inside the TPD (black) and outside the TPD (grey). Grey values represent values outside of the TPD (CDOMfl. < 0.5 a.u.).

Table 3 Pearson product-moment correlation scores (r) for relations between $[L_t]_{HS}$ and DFe, $[L_t]$ by two CLE-AdCSV methods. Correlation significance levels are p<0.005***, p<0.01** and p<0.05*. Lower- and upper limits of 95% confidence intervals for correlations scores are reported in the last two columns.

relation	r	p-value		95% conf. LL	95% conf. UL
$[L_t]_{HS}$ vs. DFe inside TPD	**0.83**	**0.001**	***	**0.46**	**0.96**
$[L_t]_{HS}$ vs. DFe outside TPD	**0.55**	**0.004**	***	**0.20**	**0.78**
$[L_t]_{HS}$ vs. $[L_t]_{TAC}$ inside TPD	0.63	0.036	*	0.06	0.89
$[L_t]_{HS}$ vs. $[L_t]_{TAC}$ outside TPD	0.38	0.063		*0*	0.67
$[L_t]_{HS}$ vs. $[L_t]_{SA}$ inside TPD	0.67	0.024	*	0.12	0.91
$[L_t]_{HS}$ vs. $[L_t]_{SA}$ outside TPD	0.52	0.022	*	0.09	0.79
$[L_t]_{HS}$ vs. δL_t inside TPD	0.17	>> 0.05		*0*	0.70
$[L_t]_{HS}$ vs. δL_t outside TPD	0.49	0.031	*	0.05	0.77

6.4. Discussion

6.4.1. Arctic Fe speciation

Stations inside the TPD influence area show an increase in DFe and Fe-binding organic ligands along with HS representative properties such as [HS] and CDOM fluorescence. When measured using the TAC method these higher concentrations have been found to correlate significantly to known descriptors of riverine influences and HS in particular (Chapter 5). At stations 99 and 125 the $[L_t]_{TAC}$ was lower than DFe for 4 and 3 samples inside the TPD, respectively (Figure 2), suggesting that there are insufficient ligands to bind Fe and thus explain DFe. In contrast, $[L_t]_{SA}$ is higher than DFe in all samples, explaining the high Fe solubility in the TPD. The good correlation between HS and DFe indicates that HS is responsible for this high solubility.

The difference between $[L_t]_{TAC}$ and $[L_t]_{SA}$ is more pronounced inside the TPD but still present outside the TPD. There is a remarkably similar $LogK'_{Fe'L}$ inside and outside of the TPD. Mahmood et al. (2015) found an average range of $10.60 \leq logK'_{Fe'L} \leq 12.74$ mol^{-1} and a correlation between $[L_t]$ and HS in the Liverpool Bay area (Irish Sea). Abualhaija et al. (2015) found similar values in the same area ($11.1 \leq logK'_{Fe'L} \leq 11.3$ mol^{-1}). Measurements by Batchelli et al. (2010) in the Thurso Bay area (Atlantic Ocean) put $logK'_{Fe'L}$ between 11.8 and 12.0 mol^{-1} whereas the dataset used for the Mediterranean HS by Gerringa et al. (2017) gave $11.57 \leq logK'_{Fe'L} \leq 12.13$ mol^{-1}. In the present study $logK'_{Fe'L}$ values fell within those found in the quoted studies, but lacking a significant difference between samples inside and outside the TPD (Table 1), whereas the differences in $[L_t]$ and [HS] were profound.

The TAC-derived $logK'_{Fe'L}$ in the Barents Sea was the same as the samples in the open Arctic Ocean. In contrast, the SA-derived $logK'_{Fe'L}$ was lower in the Barents Sea than in the open Arctic Ocean stations and the only significantly lower $logK'_{Fe'L}$ in comparison to TAC.

Results for 2 ligand classes where these could be resolved, closest to the surface primarily from measurements using SA (Figure S1), show two distinct classes based on K´, with across methods a strong L_1 class ranging $12.56 \leq logK'_{Fe'L} \leq 14.53$ mol^{-1} taking standard deviations into account, and a weaker L_2 class ranging $10.22 \leq logK'_{Fe'L} \leq 11.37$ mol^{-1}. Generally, there is a maximum spread of 1 to 2 orders of magnitude of $\alpha_{Fe'L}$ each side of D_{AL} considered to be an acceptable spread for CLE-AdCSV measurements (Apte et al., 1988; van den Berg et al., 1990; Gerringa et al., 2014). Between L_1 and L_2 for measurements using SA, this range is close to 4 orders of magnitude, though this is something that is not unique to the present study (Gledhill and Buck, 2012). In the present

study, the upper end of the $\log K'_{Fe'L}$ interval for the L_1 class may be outside of the detection window of SA and thus the large K' range may potentially be an artefact. The above ranges for L_2 have been connected to estuarine outflow and HS (Gledhill and Buck, 2012; Bundy et al., 2015). $\Sigma_{L1,L2;SA}$ agreed very well with $[L_t]_{SA}$. Therefore, the concentrations of Fe-binding organic ligands are probably good, but K´ may be imprecise. Moreover, due to the formation of $FeSA_2$ which is not electroactive (Abualhaija and van den Berg, 2014) the sensitivity was low at low Fe concentrations making higher K´ values more difficult to determine. In the few surface samples where 2 ligand groups could be resolved using TAC, K´ is inside the detection window. There was a marked difference between $\Sigma_{L1,L2;TAC}$ and $[L_t]_{TAC}$, with the sum of the separate ligand groups being higher (Figure 2, top row). $\Sigma_{L1,L2;TAC}$ may explain the presence of the high DFe in the uppermost samples where these concentrations are not explained by $[L_t]_{TAC}$. However, the disagreement between $[L_t]_{TAC}$ and $\Sigma_{L1,L2;TAC}$ also indicates a troublesome fit of the 2-ligand Langmuir model, hampering data quality in this respect. Ostensibly, there is an issue measuring HS using TAC, as oversaturation of ligands is not likely to persist if it occurs and L_t and $\Sigma_{L1,L2}$ need to agree. These issues do not occur for measurements using SA. TAC not reflecting all HS is the most probable explanation, as revisited in the next section.

6.4.2. Method intercomparison

Overall $[L_t]_{TAC}$ and $[L_t]_{SA}$, while both reflecting increased Fe-binding organic ligands in the TPD, are fairly different to each other. With the conversion factor of 14.6±0.7 nM mg^{-1} for [HS], allowing expression of Eq. nM Fe mg^{-1} (Sukekava et al., 2018), we add $[L_t]_{FA}$ as a third measure of Fe-binding organic ligands. However, we must remember that these are methodically constrained to be Fe-binding fulvic acids in practice. In comparing the ratios of DFe and $[L_t]$ over [HS], as well as the ratios of increment going into the TPD (Table 2, Figure 5), we find reasonable agreement with the above conversion factor in accounting for the presence of Fe in the Arctic Ocean. The conversion factor is lower than the [DFe]/[HS] increment ratio of 17.4 nM mg^{-1} (Table 2), and close to the 16.7 nM mg^{-1} as estimated by Laglera and van den Berg (2009).

The increment ratio of 12.2 for $[L_t]_{SA}$ (Table 2) is near the complexing capacity of 14.6±0.7 nM mg^{-1} found for the SRFA standard and the DFe/HS ratio of 13±2.5 nM Fe mg $SRFA^{-1}$ found in Mediterranean seawater by Dulaquais et al. (2018) using a similar SRFA standard but a different analytical method (Pernet-Coudrier et al., 2013). The much lower ratio for the TAC method coincides with an underestimation relative to SA of the TPD Fe-binding ligand pool which is so strongly influenced by HS. However a very significant increase of 61 % (SD = 12.9, N = 47) of the $[L_t]_{SA}$ is still observed in $[L_t]_{TAC}$ with a strong correlation

with the TPD influence, as well as a positive increment ratio with [HS] of 68% the values for DFe and $[L_t]_{SA}$.

It may well be that the SRFA standard is too specific to describe fulvic acids as a group but it is the best we have presently as extensively explained by Sukekava et al. (2018). Furthermore, the Arctic today is subject to rapid loss of permafrost, releasing many complex organics into the rivers (Frey and McClelland, 2009), a signal already proven to reach well into the shelf seas (Vonk et al., 2012), adding to the (C)DOM pool transported by the TPD. The binding capacity of HS can very well have spatial and temporal differences that are currently not taken into account. Without the availability of HS standards that are specific for seawater, results need to be viewed in context of the standard used.

A near 1:1 ratio as found for $[L_t]_{HS}$ vs. $[L_t]_{TAC}$ inside the TPD (Figure 5B) can be interpreted as an indication that all Fe-binding organic ligands inside the TPD are HS, whereas Fe-binding organic ligands outside the TPD are of a different origin. These can be resulting from sea ice melt or of a marine origin, even marine humics. $[L_t]_{HS}$ vs. $[L_t]_{SA}$ gives an almost similar slope (0.89), but there is a strong offset compared to $[L_t]_{HS}$ vs. $[L_t]_{TAC}$ (Figure 5B). This indicates that using SA, Fe-binding organic ligands present outside the TPD are measured which are not measured using TAC. $[L_t]_{TAC}$ does not vary with $[L_t]_{SA}$ outside the TPD (Figure 4), more or less constant $[L_t]_{TAC}$ is also observed in relation to $[L_t]_{HS}$ (Figure 5B). This further indicates measurements with TAC do not represent all HS. Values for $[L_t]_{HS} > \delta L_t$ especially inside the TPD (Table 1, Figure 5C) could indicate that not all unrepresented HS are accounted for by measurements using SA as well. However, given the range of conversion factors reported (Laglera and van den Berg, 2009; Sukekava et al., 2018), this relation may depend on the conversion factor used. Additionally, δL_t combines two CLE-AdCSV measurements each with their own issues. The poor correlation between $[L_t]_{HS}$ and δL_t may further illustrate this (Table 3).

Given the limited resolution provided by the remarkably stable K´ values for either method, further characterization with CLE-AdCSV based measurements proves difficult. Correlation of $[L_t]_{HS}$ and $[L_t]_{TAC}$ is not significant outside the TPD, and the other correlation scores of $[L_t]_{HS}$ and CLE-AdCSV-derived $[L_t]$ are of poor significance (Table 3). There is no significant correlation or poor correlation between $[L_t]_{HS}$ and δL_t inside and outside of the TPD (Figure 5C) as shown by the constant ratio $[L_t]_{TAC}/[L_t]_{SA}$ irrespective of the TPD (Table 1). This suggests that the difference between the methods is not caused by the presence of HS in the TPD alone, and is indicative of a systemic difference between the CLE-AdCSV methods.

It has been shown that HS are resolved by the SA method of CLE-AdCSV (Abualhaija and van den Berg, 2014; Mahmood et al., 2015). Earlier work indicated that CLE-AdCSV using SA would be more suitable to detect weaker binding HS, whereas TAC is the stronger added ligand and therefore less able to establish a competitive equilibrium with HS (Laglera et al., 2011; Gledhill and Buck, 2012). Direct addition of the SRFA standard to a TAC-analysed sample did not result in any change in $[L_t]_{TAC}$ (Laglera et al., 2011; Chapter 5). TAC itself may interact with HS, which limits formation of the $FeTAC_2$ complex and obfuscates its competition with Fe-binding organic ligands in the sample (Laglera et al., 2011). Furthermore, where a stark difference is observed across the TPD influence, $logK'_{Fe'L}$ does not reflect this (Table 1). However, this is true for both TAC and SA methods in this study. From the present data it cannot be concluded whether TAC misses a specific ligand group or that a threshold value exist below TAC cannot detect HS because of an interference between TAC and HS as suggested by Laglera et al. (2011). Attributing the greater Fe-binding organic ligand concentrations found by the SA method to the ability of resolving the iron binding properties of HS alone is proven wrong here, as the representation of the Fe-binding organic ligand pool by either method is more nuanced. For one, increases in $[L_t]_{TAC}$ are observed in the humic-rich Arctic surface samples. While lower than $[L_t]_{SA}$, the increase in $[L_t]_{TAC}$ strongly correlates with HS descriptors (Chapter 5) and direct voltammetric measurements of HS with SRFA as a humic representative standard (Dulaquais et al., 2018; this study). While ligand saturation is found using the TAC method, suggesting part of the ligand pool is not measured, we do show that TAC sees at least part of the HS. TAC has been used successfully to relate HS to Fe-binding organic ligand concentrations on several occasions (Batchelli et al., 2010; Slagter et al., 2017; Dulaquais et al., 2018). However, this work calls into question if the entire contribution of HS to the complexing capacities reported was accounted for in those previous works. Uncertainties are exacerbated by the fact that $FeSA_2$ has been described as non-electroactive (Abualhaija and van den Berg, 2014). The equilibration time of 15 minutes is further influencing the results.

6.5. Conclusions

Analyses with SA as a competitive ligand were performed on select samples coinciding with analyses using TAC in Chapter 5. Additionally measurements of [HS] were performed as well. $[L_t]_{SA}$ was higher overall, but especially inside the TPD and explained the existence of high DFe above the solubility product of inorganic Fe-oxy(hydr)oxides. Still both CLE-AdCSV methods clearly show correlation with this TPD influence, which in turn is well-described by HS

properties including a representative $[L_t]_{HS}$ derived from the binding capacity of the SRFA standard used.

Both CLE-AdCSV methods have a ratio near 1 with $[L_t]_{HS}$, with an offset to higher concentrations for $[L_t]_{SA}$. While an $[L_t]_{HS}/[L_t]_{TAC}$ ratio near 1 could be seen as suggestive of domination of the Fe-binding organic ligand pool by HS, the occurrence of ligand saturation in TAC measurements, which is thermodynamically improbable, indicates that part of the (humic) ligand pool remains veiled using the TAC method. The offset between both methods does remain outside the TPD, but decreases. Here $[L_t]_{SA}$ decrease with $[L_t]_{HS}$, whereas $[L_t]_{TAC}$ does not, possibly due to a different origin of the (humic) ligands. Additionally, our results and the lack of response of CLE-AdCSV using TAC to addition of the SRFA standard in prior work further confirms that TAC cannot resolve part of HS.

Differences in $[L_t]$ using either method and correlations to HS are not reflected in K´, making it very difficult to recognize the contribution of HS by ligand class. Analysis using SA can be resolved for 2 ligand groups for more samples, again especially for surface samples. In these cases $logK_{1}{}'_{Fe'L(SA)}$ agrees reasonably with $logK_{1}{}'_{Fe'L(TAC)}$, and therefore presumably describe the same ligand group. $LogK_{2}{}'_{Fe'L(SA)}$ is weaker than $logK_{2}{}'_{Fe'L(TAC)}$, indicating a disparity in the ligands.

The HS carried across the Arctic Ocean surface by the TPD is responsible for the transport of DFe. Issues with TAC's ability to resolve certain HS lead to TAC only reflecting 61% of $[L_t]_{SA}$. Issues with SA equilibration may lead to an overestimation of $[L_t]$. In conclusion, comparison between methods brings a more complex relation to light, and suggests that method intercalibration in the presence of a variety of model ligands, multiple methods and detection windows may be required to properly ascertain the overall organic Fe-binding organic ligand pool in natural seawater samples. Especially in an area subject to complex changing terrestrial influences such as the Arctic Ocean.

Figure S1 (page 138)
Graphs representing from left to right: total ligand concentration ($[L_t]$), conditional binding strength ($logK'_{Fe'L}$), reactivity ($log\alpha_{Fe'L}$) and excess ligands (L'), for stations 69, 99,101,125 and 153 (rows of graphs). Shown are the top 200 m of the water column, with off scale plot lines indicating the next deeper value beyond. Closed symbols represent measurements with TAC, open symbols represent measurements with SA.

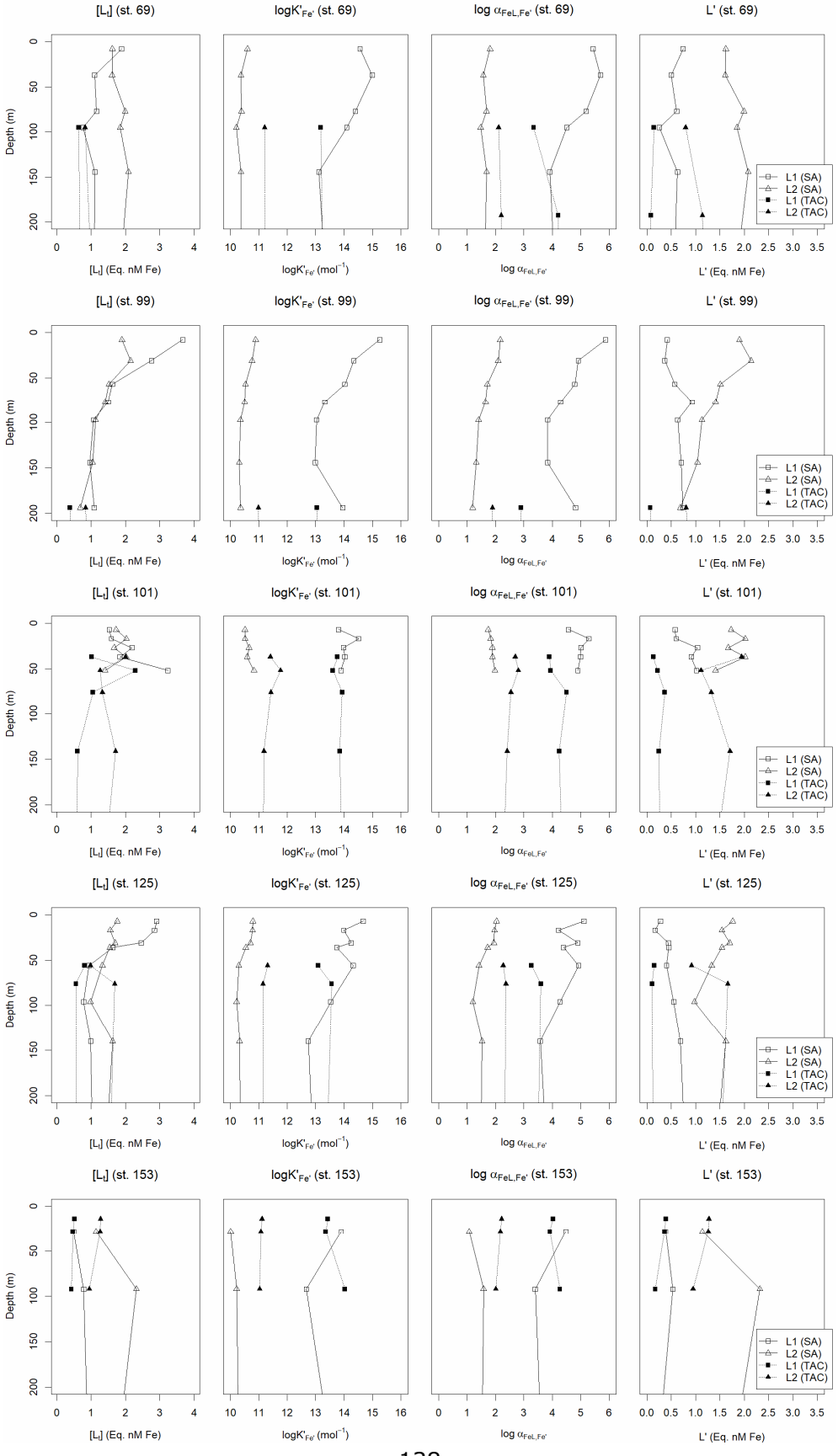
[Lₗ] (st. 69)
logK'Fe' (st. 69)
log αFeL,Fe' (st. 69)
L' (st. 69)
[Lₗ] (st. 99)
logK'Fe' (st. 99)
log αFeL,Fe' (st. 99)
L' (st. 99)
[Lₗ] (st. 101)
logK'Fe' (st. 101)
log αFeL,Fe' (st. 101)
L' (st. 101)
[Lₗ] (st. 125)
logK'Fe' (st. 125)
log αFeL,Fe' (st. 125)
L' (st. 125)
[Lₗ] (st. 153)
logK'Fe' (st. 153)
log αFeL,Fe' (st. 153)
L' (st. 153)
Depth (m)
[Lₗ] (Eq. nM Fe)
logK'Fe' (mol⁻¹)
log αFeL,Fe'
L' (Eq. nM Fe)
L1 (SA)
L2 (SA)
L1 (TAC)
L2 (TAC)

Chapter 7

Phytoplankton virus production negatively affected by iron limitation

Published as:
Slagter, H.A., Gerringa, L.J.A., Brussaard, C.P.D., 2016. Phytoplankton Virus Production Negatively Affected by Iron Limitation. Front. Mar. Sci. 3, 1–11.

Abstract

Fe-limited monocultures of the ubiquitous algae Micromonas pusilla and Phaeocystis globosa were infected with their respective viruses (MpV and PgV) to ascertain the effect of Fe-limitation on phytoplankton host-virus dynamics. The effect of the viral shunt on Fe concentrations and bioavailability is starting to gain attention, since not only is Fe released through lysis, but also its solubility is increased by the simultaneous release of Fe-binding dissolved organic ligands. However, the effect of Fe-limitation on the process of viral lysis itself is poorly understood. In this study fine adjustment of a seawater-based culture medium including the use of ultra-clean trace metal conditions and protocols allowed for Fe-limited growth at nanomolar amounts as opposed to micromolar amounts typically employed in culturing. Viral lysates derived from Fe-limited and Fe-replete (for comparison) hosts were cross-inoculated in hosts of both Fe treatments, to judge the quality of the resulting lysate as well as the effect of Fe introduction after initial infection. For both phytoplankton host-virus systems, the virus burst size reduced strongly under Fe stress, i.e. on average 28 ±1% of replete. Moreover, the MpV virus progeny showed highly reduced infectivity of 30±7%, whereas PgV infectivity was not affected. A small addition of Fe to Fe-limited cultures coming from the Fe-replete lysate counteracted the negative effect of Fe-limitation on phytoplankton virus production to some extent (but still half of replete), implying that the physiological history of the host at the moment of infection was an important underlying factor. These results indicate that Fe-limitation has the strong potential to reduce the loss of phytoplankton due to virus infection, thereby affecting the extent of Fe-cycling through the viral shunt. To what extent this affects the contribution of viral lysis-induced organic ligand release needs further study.

7.1. Introduction

Phytoplankton form the base of most marine pelagic food webs and are important in sequestering atmospheric carbon dioxide (CO_2) through photosynthesis. The production of phytoplankton is controlled by physicochemical variables (bottom-up) as well as by biological factors (top-down). Main bottom-up controls of phytoplankton are light and nutrient availability (Behrenfeld et al., 2006). The latter can be subdivided into major (nitrate, phosphate and silicate) and micro-nutrients (e.g. iron) (de Baar et al. 1990; Martin et al. 1990). Top-down factors, e.g. grazing and viral infection, influence the organic matter flux differently (Wilhelm and Suttle, 1999; Weitz and Wilhelm, 2012). While grazing transfers photosynthetically fixed carbon and organic nutrients up the food chain (Calbet and Landry, 2004), viral lysis results in the release of the hosts' cellular content into the surrounding water (Gobler et al., 1997; Wilhelm and Suttle, 1999). Thereupon, the flow of nutrients through the microbial food web is stimulated by bacterial recycling of the dissolved and dead particulate matter (Suttle 2005; Brussaard et al. 2005; Brussaard and Martínez 2008). Virally-induced mortality of various different natural phytoplankton groups was found to be at least an equally important loss factor as microzooplankton grazing (Baudoux et al., 2007; Mojica et al., 2016).

In order to understand and predict changes in phytoplankton community composition, it is important to elucidate how bottom-up and top-down factors interact and affect phytoplankton population dynamics. Several studies using phytoplankton host-virus culture systems showed that major nutrient availability influences viral production (Maat and Brussaard 2016 and see review by Mojica and Brussaard 2014). For example, phosphorus (P) limitation of the virally infected phytoplankton host results in a prolonged latent period, i.e. the time between infection and the initial release of progeny viruses from the host cell, for the infecting viruses (Maat et al., 2014). Moreover, P-stress resulted in reduced viral burst size, i.e. the number of newly formed viruses released per lysed host cell (Bratbak et al., 1998; Maat et al., 2014). These studies proposed shortage of phosphorus as a viral production substrate as well as possible host energy deficiency as reasons for the lower and delayed viral particle yield. There is, however, virtually nothing is known on the effect of micronutrient limitation on phytoplankton host-virus interactions.

Furthermore, as iron (Fe) solubility in seawater is low (Millero, 1998; Liu and Millero, 2002), marine phytoplankton depend on Fe-binding ligands to increase solubility and therefore bioavailability (Gledhill and van den Berg, 1994; Rue and Bruland, 1995). The redox state of Fe is an important factor in Fe bioavailability. The oxidized Fe(III) state is the more stable and thus prevalent

state in marine conditions, while the reduced Fe(II) state is the more bioavailable (Breitbarth et al., 2010; Shaked and Lis, 2012). Release of reactive oxygen species during phytoplankton growth has been shown to contribute to bioavailability of Fe by facilitating reduction of Fe(III) (Kustka et al., 2005; Garg et al., 2007). Furthermore, organic exudates have been connected to lowered Fe(II) oxidation rates experimentally (González et al., 2014). Part of the Fe-binding ligand pool is thought to be of marine biological origin. Strong Fe-binding organic ligands called siderophores are purposefully produced by bacteria (Butler, 2005; Mawji et al., 2011). Humic acids and polysaccharide excretions are other recognized Fe chelators with a biological origin (Laglera et al. 2011; Hassler et al. 2011). The highest Fe-binding ligand concentrations generally correlate with biological activity (Rue and Bruland, 1995; Gerringa et al., 2006; Ibisanmi et al., 2011). Viral lysis, releasing organic substances in seawater, may well be an important contributor to the ligand pool (Gobler et al. 1997; Poorvin et al. 2004; Poorvin et al. 2011). In these studies by Poorvin and others, it was found that bacterial and cyanobacterial lysates provided organically bound Fe in a form more bioavailable than supplied inorganic, ethylenediaminetetraacetic acid (EDTA) bound or desferrioxamine B (DFB) bound Fe. In comparison to the studied bacteria's self-produced siderophores, lysates were also found to contain more bioavailable Fe.

Fe-limitation negatively affects phytoplankton physiology and growth (Behrenfeld et al. 1996; de Baar et al. 1990; Martin et al. 1990; Timmermans, Gerringa, et al. 2001). Besides energetic consequences of Fe-limitation in terms of the cell's ability to harvest light energy (Geider and La Roche, 1994), Fe is also found to be an essential micronutrient for DNA replication (Netz et al., 2012; Zhang, 2014). As parasites viruses are dependent on the metabolism of their host for the production of their progeny. We hypothesize that viral production depends on the degree of Fe-stress of the host. Viral lysis in turn affects the production of Fe-binding organic ligands and thus the solubility of the limiting Fe. Thus far, in terms of impact on Fe cycling, studies focussed solely on the release of Fe or Fe-binding organic ligands upon viral lysis and not on the virus growth cycle (Gobler et al. 1997; Poorvin et al. 2004; Poorvin et al. 2011). Here we examine virus production characteristics under Fe-limitation for two key ecologically relevant phytoplankton hosts: the nanoeukaryotic bloom-forming Prymnesiophyte *Phaeocystis globosa* and the picoeukaryotic Prasinophyte *Micromonas pusilla*. *Phaeocystis* is a globally occurring, bloom-forming genus (Vaulot et al., 1994), with *P. globosa* ecologically relevant in temperate marine waters (Schoemann et al., 2005). Viruses have been found to drive *P. globosa* bloom decline (Brussaard, 2004a; Brussaard et al., 2005; Baudoux et al., 2006). *M. pusilla* is a common species that is distributed globally

(Not et al., 2004, 2005; Vaulot et al., 2008). It has been speculated that viral control of this species is continuous (Cottrell et al., 1995). As model species for diverse regions and ecological niches, these species were chosen in this study to offer a broad insight in the response to Fe-limitation of phytoplankton host-virus systems in world oceans subject to changing conditions. Limiting concentrations were of ecological relevance to represent a natural context.

7.2. Methods

7.2.1. Experimental design and sampling

Steady state exponentially growing phytoplankton cultures were subdivided per treatment (Fe-limited and Fe-replete) in 6 replicate 500 mL culture flasks. Two days later the viral infection experiment started 3 h into the light period. For each treatment, 2 replicate cultures received viruses produced on Fe-limited host culture (VL), 2 replicates received viruses produced on Fe-replete host culture (VR), and 2 replicates did not receive viruses and served as non-infected controls (C). Fe-limited lysates were added not only to the respective Fe-limited host cultures, but also to the Fe-replete host in order to test for the reduced infectivity we observed under Fe-limitation (see Results). For this reason and to still guarantee a one-step infection cycle we aimed to add 20-25 viruses per algal cell for *P. globosa*. Given lower yields for *M. pusilla,* we endeavoured to add at least 5-10 viruses per algal cell, while still maintaining a ~10% v/v addition. Similarly, Fe-replete lysate was also added to Fe-limited host cultures. This caused a Fe-spike of about 0.9 µM (10% v/v of Fe-replete medium containing lysate), which allows testing whether a spike of Fe influences virus proliferation.

At steady state, i.e. after at least 8 volume changes and consistent phytoplankton counts ($2.1\pm0.4 \times 10^6$ and $2.1\pm0.7 \times 10^6$ for *P. globosa* and *M. pusilla*, respectively), samples were collected for dissolved macronutrients (nitrogen and phosphorus) and Fe, as well as pigment composition. Nutrient samples (5 mL after washing of filter and tube) were 0.2 µm filtered (25 mm diameter Acrodisk, Pall) and frozen at -20°C until analysis. GF/C filtered (1.2 µm nominal pore size, 25 mm diameter, Whatman) algal pigment samples of 50 mL were frozen at -80°C until analysis. The number of infective phytoplankton viruses was determined using the most probable number (MPN) endpoint dilution assay according to Suttle (1993). In short, 10-fold dilution series were set up in 5 replicate tubes using a dilute Fe-replete phytoplankton culture at a density of $\sim10^6$ cells mL^{-1}. A row of uninfected control tubes was added to each analysis. Cell lysis was regularly scored by eye and the final score after 14 days post-infection was used to calculate the number of infectious viruses. Dividing this number of infectious by the total number of PgV or MpV provided the %

infectious viruses. MPN data was analysed using the University of British Columbia Computer Science department's Assay Analyser software program (Passmore et al., 2000).

The moment viruses were added, cultures were maintained in-batch. We examined the effect of frequent handling by taking along a control subculture per Fe-limited treatment that was only gently mixed once a day. Samples for phytoplankton and virus abundance as well as photosynthetic capacity (F_v/F_m) were taken every 4 h until full lysis of the cultures (48 h for *P. globosa* and 96 h for *M. pusilla*). Phytoplankton abundance and F_v/F_m were determined directly upon sampling, while viral abundance samples were fixed with glutaraldehyde (EM-grade, 0.5% final concentration), flash frozen in liquid nitrogen and stored at -80°C (Brussaard et al., 2010).

7.2.2. Additional analyses

High Performance Liquid Chromatography (HPLC) pigment analysis was performed on steady state phytoplankton samples after Zapata et al. (2000). Concentrations of dissolved inorganic macronutrients nitrate and orthophosphate were verified as per chapter 2 and were non-limiting at all times (> 128 µM nitrate and > 8 µM phosphate). Verification of the dissolved Fe concentration was done using flow injection analysis after Klunder et al. (2011), also detailed in chapter 2. The detection limit of this method was 0.01 nM.

7.3. Results & Discussion

7.3.1. Steady state

Exponential growth rate (μ_{max}) for both Fe-limited and Fe-replete *P. globosa* and Fe-replete *M. pusilla* was 0.99 ±0.11 d^{-1}. *M. pusilla* showed, however, reduced growth under Fe-limitation (0.63 ±0.07 d^{-1}). Initial difficulties encountered with consistent semi-continuous culturing of *M. pusilla* required us to increase the Fe concentration to 3 nM as compared to the 1 nM for *P. globosa.* Still, the lower steady state μ_{max} found for *M. pusilla* under Fe-limitation suggests a less efficient Fe-uptake or utilization of *M. pusilla* as compared to *P. globosa*. However, the photosynthetic capacity (F_v/F_m) of the Fe-limited *M. pusilla* remained high around 0.6. Thus the smaller-sized *M. pusilla* requires more Fe to grow, albeit at a lower μ_{max}, while it is capable of retaining F_v/F_m at a value similar to Fe-replete conditions. Reduced F_v/F_m and growth rate under Fe-limitation has been reported for a small diatom species (Timmermans et al., 2001a); however, both variables were reduced for the same species and not one or the other as found in present study. Our result do not support the earlier reports that small phytoplankton (diatoms and cyanobacteria) are growing better under Fe-limitation than larger phytoplankton (Price et al. 1994; Timmermans, Gerringa,

et al. 2001; Timmermans et al. 2004). Whether the differences are due to species-specific or phytoplankton group related responses is currently unclear.

The cellular Chlorophyll-a concentration at steady state was lower under Fe-limitation compared to the Fe-replete control cultures for both algal species (Tables 1 and 2). For *M. pusilla* the reduction was larger, i.e. Chlorophyll-a concentration was only 40% of Fe-replete concentration, compared to 63% for *P. globosa*. In the Fe-limited *P. globosa* cultures, cellular Chlorophyll-c concentration was reduced (to a similar extent; Table 1), whereas for *M. pusilla* the Chlorophyll-b concentration also decreased compared to Fe-replete (Table 2). Furthermore, Fe-limitation led to a different distribution of light-harvesting xanthophylls in *P. globosa* (Table 1). Cellular 19'-hexafucoxanthin concentration was found 5-fold higher in the Fe-limited cultures as compared to Fe-replete *P. globosa* (4.8×10^{-12} g cell^{-1}), while 19'-butanoyloxyfucoxanthin and fucoxanthin concentrations were 0 and 89% of Fe-replete, respectively. The photoprotective xanthophyll derivatives in Fe-limited *P. globosa* are increased relative to Chlorophyll-a, i.e. the diadinoxanthin concentration over Chlorophyll-a is 162% of Fe-replete (0.58 and 0.57×10^{-11} g x cell $^{-1}$, respectively) and the diatoxanthin concentration is 181% of Fe-replete (0.08 and 0.07×10^{-11} g x cell^{-1}, respectively). Fe-limited *M. pusilla* cultures (Table 2) had lower cellular Chlorophyll-b and light-harvesting xanthophyll concentrations. Relative to the Chlorophyll-a concentration, photoprotective xanthophyll derivatives antheraxanthin, zeaxanthin and lutein were present in higher amounts. Only violaxanthin remains lower both in absolute and relative terms.

Overall, the pigment analysis shows that for both phytoplankton species the photosystem shifted towards a more photoprotective character under Fe-limited conditions. The lower concentrations of chlorophyll and most light-harvesting xanthophylls furthermore indicated that the Fe-limited cells suffered a lower light-harvesting capacity. Fe is essential for all life and earlier studies showed that Fe-deficiency can lead to anemia in mammals, the dysfunction of Fe-dependent enzymes in yeast, the reduction of the amount of electron-transferring complexes and induction of chlorosis in plants, and a decrease in Fe-intensive light harvesting pigment synthesis and increased photoprotective pigments in phytoplankton (Geider et al., 1993; Mengel, 1994; van Leeuwe and Stefels, 2007; van de Poll et al., 2009; Zhang, 2014). In line with the fact that the Fe concentrations in the Fe-limited cultures were always below the limit of detection, these results confirm that both phytoplankton cultures were indeed Fe-limited, despite that *M. pusilla* showed healthy F_v/F_m. The more pronounced shift to photoprotective pigment production relative to light-harvesting Chlorophyll-a in *M. pusilla* compared to *P. globosa* is in agreement with the strong decline in steady state *M. pusilla* cell abundance with Fe-limitation while

F_v/F_m was unaffected. However, *M. pusilla* was unable to grow at 1 nM Fe while *P. globosa* grew well. Our results imply that *P. globosa was* more affected energetically by Fe-limitation, while *M. pusilla* suffered instead in overall cellular production.

Table 1 Steady state phytoplankton pigment composition in non-infected Fe-limited (first column) and Fe-replete (second column) *P. globosa* cultures. Concentrations of pigments are expressed in 10^{-11} g $cell^{-1}$. The third column shows the ratio of Fe-limited over Fe-replete cultures, serving to indicate relative shifts in pigment composition. Chlorophylls ([1]), light harvesting xanthophyll derivatives ([2]) and photoprotective xanthophyll derivatives ([3]) are grouped together.

Pigments	***Treatment***		
	limited	*replete*	***ratio***
Chlorophyll a [1]	1.31	2.08	0.63
Chlorophyll c2 [1]	0.31	0.37	0.86
Chlorophyll c3 [1]	0.23	0.48	0.47
19'-hexafucoxanthin [2]	0.48	0.09	5.16
19'-butanoyloxyfucoxanthin [2]	0.00	0.20	0.00
Fucoxanthin [2]	1.13	2.01	0.56
Diadinoxanthin [3]	0.58	0.57	1.02
Diatoxanthin [3]	0.08	0.07	1.07

Table 2 Steady state phytoplankton pigment composition in non-infected Fe-limited (first column) and Fe-replete (second column) *M. pusilla* cultures. Concentrations of pigments are expressed in 10^{-11} g cell^{-1}. The third column shows the ratio of Fe-limited over Fe-replete cultures, serving to indicate relative shifts in pigment composition. Chlorophylls ([1]), light harvesting xanthophyll derivatives ([2]) and photoprotective xanthophyll derivatives ([3]) are grouped together.

Pigments	***Treatment***		
	limited	*replete*	***Ratio***
Chlorophyll a [1]	2.70	6.78	0.40
Chlorophyll b [1]	2.06	4.50	0.46
Neoxanthin [2]	0.44	0.88	0.50
Prasinoxanthin [2]	0.71	1.52	0.47
Antheraxanthin [3]	0.27	0.12	2.33
Zeaxanthin [3]	0.17	0.10	1.75
Lutein [3]	0.13	0.29	0.44
Violaxanthin [3]	0.29	1.14	0.25

7.3.2. Viral infection characteristics

Infection of both phytoplankton species resulted in one-step infection cycles with full lysis of the cultures whereas the non-infected controls grew or maintained constant cell number (Figures 1A,B and 2A,B). Cell growth in the non-infected Fe-replete cultures reflects the synchronized cell division during the dark period (Brussaard et al., 1999). In the Fe-limited cultures growth of *P. globosa* halted, which was due to stress from the frequent sampling, since the Fe-limited subcultures that were sampled only once a day did show some growth (data not shown). The F_v/F_m of the uninfected Fe-replete phytoplankton cultures remained constant (Figures 1C,D and 2C,D), whereby the small variations observed in the Fe-replete *P. globosa* cultures relate to the light:dark cycle (Figure 1D). The Fe-limited non-infected control cultures showed a decline in F_v/F_m over time as a result of the Fe deprivation, but to a lesser extent than the infected cultures.

When infected with the corresponding Fe-treatment virus (i.e. Fe-limited host with VL and Fe-replete host with VR), Fe-limitation resulted for the infected *P. globosa* in slightly delayed (about 4h) and slower cell lysis than for the Fe-replete cultures (full lysis occurring about a day later; Figures 1A,B). F_v/F_m showed similar differences in temporal dynamics between the Fe-limited and Fe-replete infected cultures upon infection with these viruses (Figures 1C,D). At large, the infected *M. pusilla* cultures showed similar results (Figure 2). The

alterations in host physiological condition in the Fe-limited cultures resulted for both phytoplankton species in slower release of virus progeny and reduced virus yield when infected with VL as compared to Fe-replete cultures (Figures 1E,F and 2E,F). The latent period, e.g. the time period to extracellular release of newly produced viruses, was however unaffected by Fe-limitation of the host. Experiments with the same strain of *M. pusilla* did show prolonged latent periods when under phosphorus (P) and nitrogen (N) limitation (Maat et al., 2014; Maat and Brussaard, 2016). These were suggested to be due to reduced substrate and host energy availability resulting from impaired photophysiology under major nutrient limitation. In our study Chlorophyll-a concentration was comparably reduced but F_v/F_m of Fe-limited steady state *M. pusilla* was not impaired. Then again, F_v/F_m of *P.globosa* cells prior to infection was reduced compared to Fe-replete, still not prolonging the latent period. We cannot be sure of the exact underlying mechanism from the here presented data, but the proliferation of DNA viruses is directly dependent on Fe due to the essential role Fe plays in the catalytic centre of ribonucleotide reductase, produced early in infection to support dNTPs production needed for viral DNA synthesis (Romeo et al., 2001). As such, it can be speculated that not the time to produce a virus is affected but instead the number of viruses that can be produced before cell lysis occurs. The burst size of MpV and PgV indeed decreased strongly under Fe-limitation, i.e., to 24 and 29% of the burst size produced under Fe-replete conditions (20 and 196 viruses lysed host cell^{-1}; Table 3). In comparison to *P. globosa,* the reduced growth rate of Fe-limited steady state *M. pusilla* did not significantly affect the extent of reduction in virus burst size. Nonetheless, *M. pusilla* required a higher cellular Fe concentration. This implies that Fe-limited *P. globosa*, able to grow at the lower Fe concentration, displays a more efficient virus proliferation (despite the low F_v/F_m at the start of infection).

Noteworthy, the higher Fe concentration needed to allow for sustainable growth of *M. pusilla* under Fe-limitation did not prevent the loss of infectivity of the virus progeny. Infectivity of the Fe-limited MpV lysate was reduced to 30±7%, while in contrast PgV did not show decreased infectivity for Fe-limited hosts. Our results signify that a stronger Fe-stress experienced by the Fe-limited *M. pusilla* (expressed in reduced growth rate) is more likely responsible for the production of impaired virus progeny than a changed photosynthetic capacity (F_v/F_m 0.2 for *P. globosa* compared to 0.6 for *M. pusilla*). The fact that total virus abundance, as measured after staining with a nucleic acid dye, was higher than the infective abundance indicates that (i) virus particles and (ii) viral nucleic acids were produced. Still, impaired capsid proteins or host receptors may explain a loss of infectivity. Alternatively, processes known to be Fe-intensive are DNA replication and repair (Netz et al., 2012; Zhang, 2014). Failure of DNA

repair could indeed explain the result of reduced percentage infective viruses. Future research should not only focus on the causal aspects per se but also study what causes the dissimilarities in loss of infectivity between the algal viruses since different responses will directly regulate community composition. Furthermore, future studies should screen if and how other marine taxa and different viruses are affected by virus proliferation under Fe-limitation. For example, non-marine tailed bacteriophages have been found to contain iron ions in the tail proteins that can utilize the siderophore-bound iron receptors on the host cell membrane for attachment of the phage and subsequent infection of the bacterial host (Bartual et al., 2010). It is likely that similar interactions also exists for marine bacteriophages (Bonnain et al., 2016). Still open questions are whether such phages will obtain fewer iron ions in their tail under Fe-deprivation, and if this will negatively affect their infectivity. Furthermore, the recently proposed 'Ferrojan Horse Hypothesis' by Bonnain and colleagues (2016) posits that introduction of phage-attached Fe may aid the host. More study is needed to test this theory and its potential interference with siderophore-specific uptake mechanisms and effect on Fe cycling.

For all Fe-replete cultures (i.e. high Fe concentration and consequently high F_v/F_m of around 0.6) and the Fe-limited *M. pusilla* the lysis dynamics and decline in F_v/F_m for the VR- and VL-infected cultures were largely comparable (Figure 1D and 2D). However, the Fe-treatment history of the virus (VL or VR) did matter in combination with Fe-limited *P. globosa* cells, i.e. infection with VR did delay the decline in F_v/F_m with more than a day (Figure 1C). Infection with a VR lysate is analogous to a relief in Fe-limitation at the time of infection. When the Fe-limited *P. globosa* cultures were infected with a VR lysate, they were effectively spiked with an Fe increase of ~10% relative to Fe-replete conditions (0.9 µM). The 100- to 300-fold increase of Fe with the addition of an Fe-replete lysate (0.9 µM vs. 1-3 nM) takes the culture Fe concentration well out of limitation ranges which are generally considered to be in nano- to picomolar ranges (de Baar et al. 1990; Martin et al. 1990; Brand 1991). The concentration increase in our experiment is comparatively drastic to assure lifting of Fe-limitation to levels nearer normal replete cultures. This cross-inoculation provides insight in the potential effects of sudden introduction of Fe, e.g. with (seasonal) dust deposition or terrestrial runoff. The effect of this spike with Fe was apparently enough to prevent instant loss of photosynthetic capacity in the Fe-limited *P. globosa* cells. For both phytoplankton species, the improved physiological condition upon infection of Fe-limited host with VR virus resulted in enhanced viral production compared to Fe-limited infected with VL virus (by 1.6 and 2.3-fold for PgV and MpV, respectively; Table 3). The effect on burst size is thus stronger for the more Fe-sensitive *M. pusilla*, indicating that *M.*

pusilla is more capable of mobilizing the Fe added for viral production. Utilization of the limiting macronutrient P when added post infection was also found to stimulate virus production of *M. pusilla* (Maat et al., 2016). Although our results indicate that an infected host is capable of mobilizing the limiting Fe for viral production upon addition post infection, it did not lead to a complete recovery of virus production as compared to Fe-replete conditions (around 50% of the replete treatment; Table 2).

Table 3 Burst sizes (number of virus progeny per lysed host cell) of PgV-07T and MpV-08T infecting Fe-replete and Fe-limited *P. globosa* (Pg) and *M. pusilla* (Mp), respectively. Viruses were derived from a Fe-replete host (VR) or a Fe-limited host (VL). Burst sizes for Fe-limited cultures are also expressed as a percentage of the corresponding infections in Fe-replete cultures.

Treatment	*Burst size*	*% of replete*
Pg replete + VR	671 ± 62	
Pg replete + VL	679 ± 5	
Pg limited + VL	196 ± 35	29 ± 0.2
Pg limited + VR	308 ± 4	46 ± 2.3
Mp replete + VR	84 ± 14	
Mp replete + VL	83 ± 6	
Mp limited + VL	20 ± 0	24 ± 5.2
Mp limited + VR	46 ± 2	54 ± 0.5

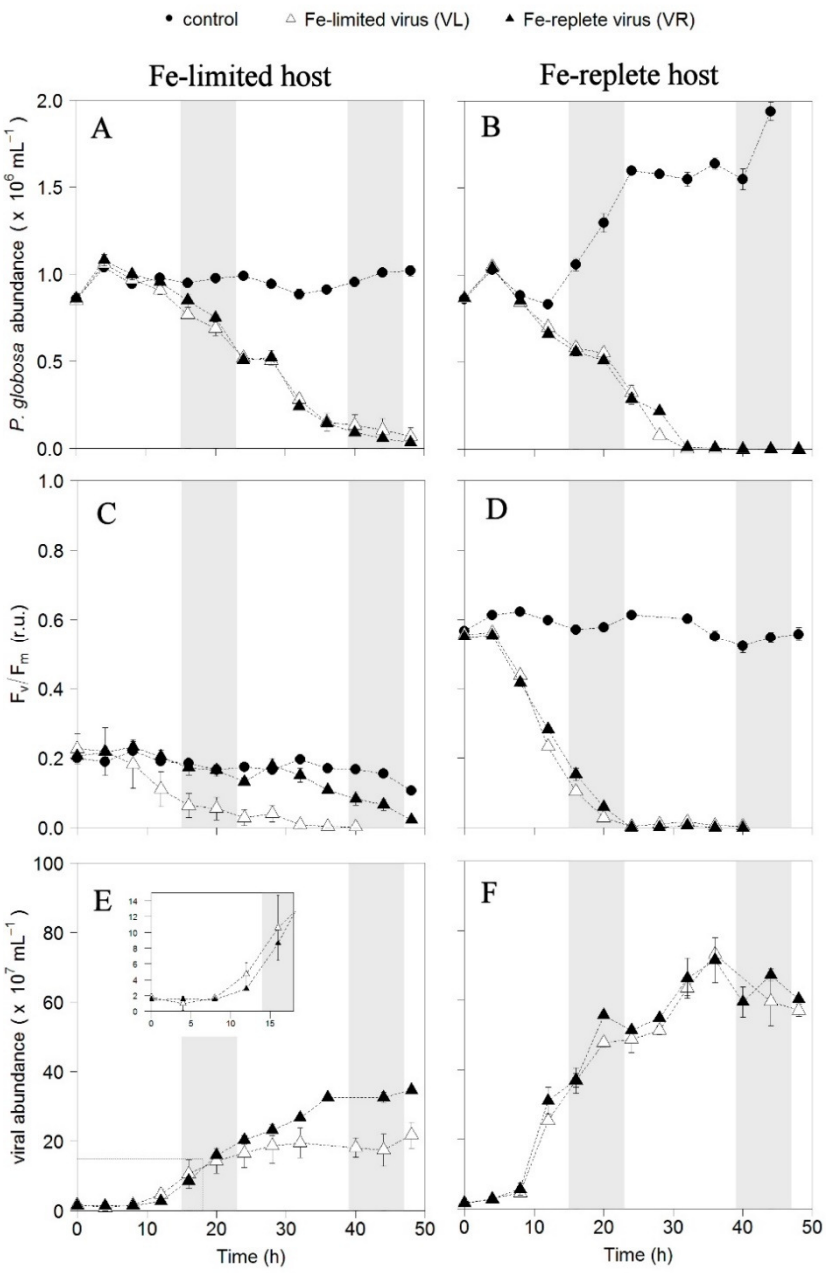

Figure 1 Temporal dynamics of *P. globosa* viral infections: host cell abundance over time (h) in Fe-limited (A) and Fe-replete cultures (B); photosynthetic capacity (F_v/F_m) over time (h) of Fe-limited (C) and Fe-replete cultures (D); viral abundance in Fe-limited (E) and Fe-replete (F) cultures. Circles represent non-infected controls, black triangles represent infections with Fe-replete host derived viruses (VR) and white triangles represent infections with Fe-limited host derived viruses (VL). Error bars indicate deviation of replicates (N=2) and fall within symbols when not visible. Shaded areas indicate dark periods. Inlay in (E) magnifies the first 20 hours post-infection.

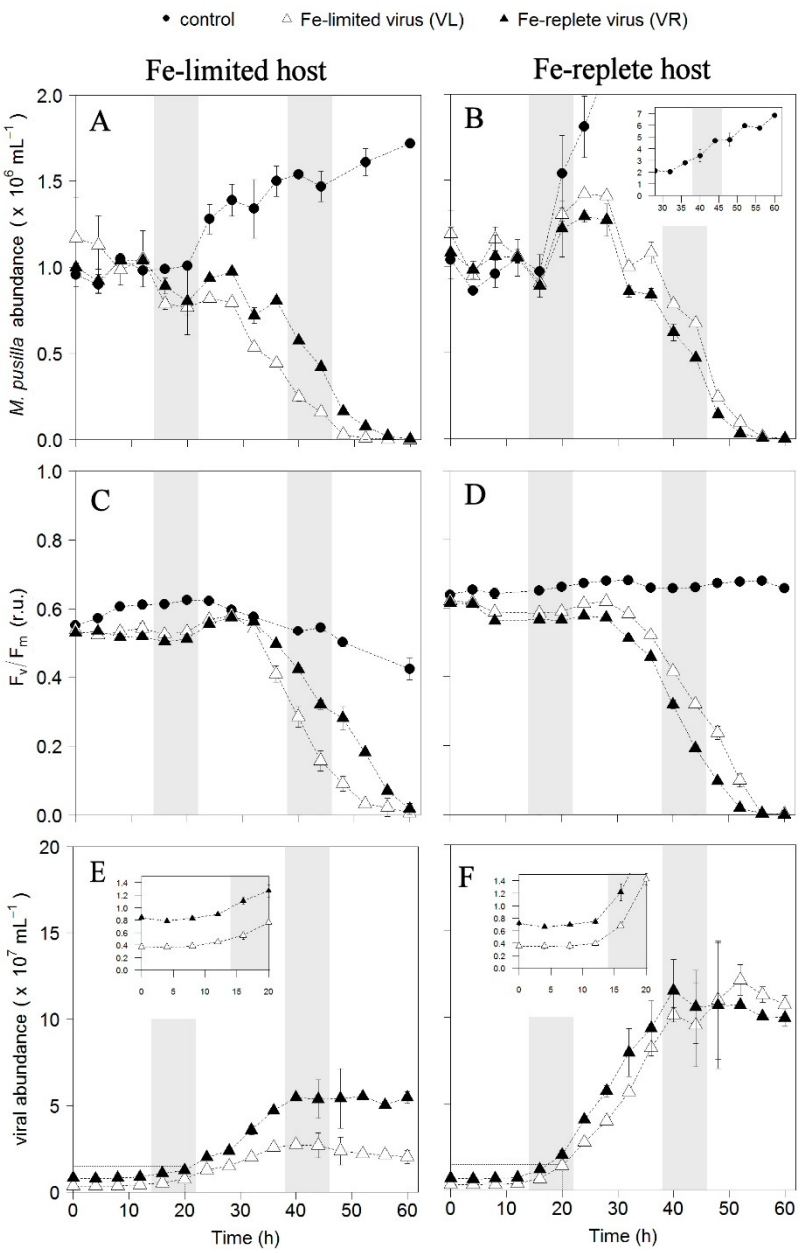

Figure 2 Temporal dynamics of *M. pusilla* viral infections: host cell abundance over time (h) in Fe-limited (A) and Fe-replete cultures (B); photosynthetic capacity (F_v/F_m) over time (h) of Fe-limited (C) and Fe-replete cultures (D); viral abundance in Fe-limited (E) and Fe-replete (F) cultures. Circles represent non-infected controls, black triangles represent infections with Fe-replete host derived viruses (VR) and white triangles represent infections with Fe-limited host derived viruses (VL). Error bars indicate deviation of replicates (N=2) and fall within symbols when not visible. Shaded areas indicate dark periods. Inlay in (B) shows off scale host control growth, inlays in (E and F) magnify the first 20 hours post-infection.

In conclusion, viral infection of both phytoplankton species is distinctly influenced by Fe-limitation. The differences in sensitivity of the host to Fe-limitation subsequently affected the progeny virus growth properties. *Phaeocystis* and *Micromonas* occur in Fe-limited and Fe-replete conditions alike (Not et al. 2004, 2005; Schoemann et al., 2005). Viral lysis has been shown to be an important mortality term for *P. globosa* under natural conditions, and also *M. pusilla* is readily infected (Cottrell et al., 1995; Brussaard, 2004a; Brussaard et al., 2005; Baudoux et al., 2006; Martínez Martínez et al., 2015). Virus burst sizes became strongly reduced (on average by 70%) under Fe-limiting relative to Fe-replete conditions. Although addition of Fe at the time of infection was utilized by the infected Fe-limited host to increase virus production, it was not to the level found under Fe-replete conditions. Thus Fe-limitation irrevocably interfered with viral productivity. Additionally, Fe-limited *M. pusilla* demonstrated an evident effect on the quality of the viruses produced as only 30% were infective. The lowered virus infectivity and/or virus yield impair viral control of the specific host species under Fe-limitation. However, at the same time, reduced viral lysis may affect the productivity of remaining non-infected cells and of other phytoplankton species, because viral lysis is considered a driver of Fe cycling by releasing ligand-bound dissolved Fe-species back into the dissolved organic matter pool (Gobler et al. 1997; Poorvin et al. 2004; Poorvin et al. 2011). What relative contributions different ligands have, and in how far their release is facilitated or impaired by viral lysis requires further study. Further experimental and *in-situ* study of phytoplankton host-virus dynamics under Fe-limitation is essential to elucidate the level of response specificity, but also the effects on the viral shunt in terms of nutrient cycling in general as well as Fe speciation.

Chapter 8

Effects of viral lysis and dark-induced senescence of phytoplankton on Fe-binding organic ligand production and composition

Abstract

Low-Fe adapted cultures of *Micromonas pusilla* and *Phaeocystis globosa* infected by their specific viruses (PgV-07T and MpV-08T) showed highest ligand concentrations only for the infected *P. globosa*. Conditional ligand binding strength was also higher for *P. globos*a, but more so for the control than the infected cultures. An inventory of siderophore-like substances yielded as of yet unknown Gallium (Ga) complexes in all treatments, i.e. controls, infected and 30 day dark-induced senesced phytoplankton. These complexes possibly represent siderophore-like substances. We found changes in the composition of these siderophore-like substances due to bacterial presence, in cases irrespective of the phytoplankton host and treatment. Ga-complex signature types unique to samples post senescence period suggest that heterotrophic bacteria are a possible source of specific Fe-binding organic ligands. Loss of Ga-complex signature types detected before the senescence period suggests that dissolved Fe-binding organic ligands within this group are subject to bacterial uptake and modification in addition to ligand production. An overall loss in Ga-complex ion counts would suggest these processes are a loss factor of Fe-binding organic ligands over time. Ultimately, both viral lysis and senescence of phytoplankton and viral lysis thereof act on the Fe-binding organic ligand pool as both sources and loss factors.

8.1. Introduction

Marine phytoplankton form the base of most marine foodwebs and play a key role in sequestration of atmospheric carbon. Phytoplankton production is regulated by growth-relevant environmental variables, so called bottom-up control factors. Amongst these, the trace metal iron (Fe) has been shown to limit phytoplankton growth in vast oceanic regions (de Baar et al., 1990; Martin et al., 1990). Fe is an essential nutrient for enzymes involved in DNA replication, electron transport in photosynthesis and cellular respiration, , the reduction of reactive oxygen and the nitrogen cycle (Geider and La Roche, 1994; Hogle et al., 2014; Zhang, 2014; de Baar et al., 2017). However, organic Fe-binding ligands are required to keep Fe in the bioavailable dissolved state beyond inorganic solubility (Liu and Millero, 2002). The vast majority of dissolved Fe is bound to organic ligands, yet the identity of these ligands is still largely unknown (Gledhill and Buck, 2012; Hassler et al., 2017).

Fe-binding organic ligands in marine systems may originate from terrestrial sources as humic substances (Laglera and van den Berg, 2009), but may also be produced locally in biologically active regions (Rue and Bruland, 1995; Gerringa et al., 2006). Viral lysis of a unicellular host releases the cytosol directly into the surrounding seawater, delivering carbon and nutrients in bioavailable forms. Subsequent bacterial remineralisation mobilizes these nutrients in the microbial food web (Brussaard et al., 2005; Suttle, 2005). Viral lysis of phytoplankton has been shown to increase the release of dissolved iron (Gobler et al., 1997). What is as nevertheless still unknown is to what extent phytoplankton lysis specifically contributes to the ligand pool. Poorvin et al. (2011) showed that viral lysis of marine bacteria contributed to the ligand pool, and the Fe in these viral lysates seemed well bioavailable (Mioni et al., 2005; Poorvin et al., 2011).

The Fe-binding ligand pool is modified by bacterial activity not only via microbial consumption of virally-released ligands, but also of ligands from exudates such as exopolymeric substances (EPS; Hassler et al., 2011b, 2011a) and those associated with terrestrial produced organic matter (Laglera and van den Berg, 2009). Alternatively, bacteria produce ligands via production of siderophores (Butler, 2005; Hassler et al., 2017). Siderophores are a long-studied subject, with the first examples isolated from soils by Francis et al. (1949), before their relevance in marine systems became apparent following the iron hypothesis (Martin and Fitzwater, 1988). Since then siderophores have been purposefully produced as metal chelators, i.e. for medical purposes, and have been studied in their role as Fe mobilizers for (cyano-)bacteria (Wilhelm and Trick, 1994; Butler, 2005; Hopkinson et al., 2009) and their possible utilization as Fe sources

for phytoplankton directly (Soria-Dengg et al., 2001). Enzymes tied to high-affinity Fe-uptake systems and siderophore-specific genes have been detected in phytoplankton species before (Wilhelm et al., 2006). *In situ* studies of siderophore production have shown that specific siderophores drive bioavailability of Fe (Velasquez et al., 2011, 2016). However, siderophore characterization is incomplete and relative contribution to the dissolved organic Fe-binding ligand pool is unknown. Modification of the Fe-binding organic ligand pool has been indicated indirectly via multiple avenues (Rijkenberg et al., 2008a; Boyd et al., 2010). The growth of heterotrophic bacteria supported by the processes described above is expected to be a loss factor to Fe-binding organic ligands.

Here we investigate the role of viral lysis of two cosmopolitan phytoplankton species, *Micromonas pusilla* and *Phaeocystis globosa*, in dissolved organic Fe-binding ligand production and composition. Furthermore, the influence of bacterial breakdown of the virally lysed phytoplankton cells as well as dark-induced senescence of the non-infected phytoplankton during a 4 week period.

8.2. Method

8.2.1. Model systems

Phytoplankton species used were the picoeukaryotic prasinophyte *Micromonas pusilla* (LAC38, Marine Research Center culture collection, Göteborg University, Sweden) and the nanoeukaryotic Prymnesiophyte *Phaeocystis globosa* (G(A); culture collection of the University of Groningen, the Netherlands). Monospecific cultures of each were cultured in a low-trace metal (LT) medium containing no added complexing agents after Slagter et al. (2016). The double stranded DNA algal viruses MpV-08T infecting *M. pusilla*(Martinez Martinez et al., 2015) and PgV-07T infecting *P. globosa* (Baudoux and Brussaard, 2005) were maintained by regular transfer (10% v/v) of the lysates to new exponentially growing algal cultures (in LT medium).

8.2.2. Experimental design, sampling and abundance analysis

Prior to the infection experiment, phytoplankton cultures were scaled up to 2 L in PC vessels (Nalgene). Following, phytoplankton were transferred to 10 L PC carboys (Nalgene). The exponentially growing phytoplankton were each split into two batches that served as non-infected controls and two batches that were inoculated with the specific virus (10% v/v). Experiments started with an average host abundance of 7.1×10^5 mL^{-1} (SD=1.0, N=4) for *P. globosa* and 1.4×10^6 mL^{-1} (SD=0.1, N=4) for *M. pusilla*. Samples for flow cytometric enumeration of phytoplankton, bacteria and viruses, and samples for photosynthetic capacity (F_v/F_m) were taken at regularly until 96 h post infection

(p.i.). Phytoplankton abundances were directly determined using a FACSCanto flow cytometer (Becton Dickinson) equipped with a 12 mW HeNe laser (633 nm) with the trigger set on Chlorophyll-a red autofluorescence. The measurements for F_v/F_m were also performed on fresh samples using a fluorometer with Chlorophyll red detector (Waltz Water-PAM), whereby triplicate readings were taken after 30 min dark equilibration at culturing temperature. Samples for bacterial and virus abundances were fixed with glutaraldehyde to a final concentration of 0.5 % (EM grade, 25% stock, Merck) and subsequently flash frozen in liquid N_2 (Brussaard, 2004b). Samples were stored at -80°C until analysis using a FACSCalibur flow cytometer (Becton Dickinson, equipped with a 15 mW 488nm argon-ion laser). Prior to analysis the samples were diluted in TE-buffer and stained with nucleic acid specific dye SYBR Green I (Thermo Fisher) according to Brussaard et al. (2010). The algal viruses were differentiated on a green fluorescence versus side scatter cytogram. All flow cytometric data were analysed in detail using Cytowin (Vaulot, 1989).

Samples for the determination of DFe and ligand characteristics were taken at 0, 24, 50, 76 and 96 h p.i. Trace metal speciation samples were selected based on contamination and/or difficulties with electrochemical measurements in culture filtrates. Only samples with a DFe within 1nM of the LT medium's target of 3nM and for which a fit to the Langmuir model was possible were retained. All samples that remained were taken between 50 and 96 h p.i., ultimately representing all treatment end-states. Samples for siderophore analysis were taken at 96 h p.i. Following these samplings, the cultures were left in the dark for approximately 4 weeks (30 days) to study the effect of bacterial degradation of organic matter on additional samples for siderophore analysis. Samples taken after the 30 d senescence period could not be analysed for Fe-binding organic ligands due to electrochemical interference. Successful senescense of the phytoplankton cultures was verified with flow cytometery. All samples for DFe, ligand characteristics and siderophore analysis were filtered using a PC overpressure filtration system with a 0.2 µm polyethersulfone (PES) filter (Vivacell 250, Sartorius). This system, using a vertically oriented filter cup with minimal deadspace, was placed on an orbital shaker at mild velocity to minimize filter clogging. Pressure over the unfiltered sample (no vacuum) was kept to ~2 bar, minimalizing the potential for mechanical cell lysis.

8.2.3. Trace metal analyses

DFe samples were concentrated on a chelating column (NOBIAS chelate-PA1) using an automated sample preconcentration system (seaFAST, Elemental Scientific). 10 mL acidified seawater (0.024 M HCl; BASELINE, Seastar) was concentrated and eluted in 1 mL 1.5 M 2x SBD HNO_3, and subsequently

measured by high resolution inductively coupled plasma mass spectrometry (HR ICP-MS; Element2, Thermo Scientific). Calibration was performed by standard addition using diluted 1000-ppm stock solutions (TraceCERT for ICP, Fluka).

Ligand concentration ([L_t] in equivalent nM of Fe (Eq. nM Fe)) and conditional binding strengths relative to Fe' ($logK'_{Fe'L,}$ in mol^{-1}) were measured using competitive ligand exchange adsorptive cathodic stripping voltammetry (CLE-AdCSV). The competitive ligand salicydiaxomine (SA) was used in a concentration of 25 µM after Buck et al. (2007, 2015).

Siderophore analyses were performed after Mawji et al. (2008). Samples for siderophore analysis were preconcentrated onto hydroxylated polystyrene-divinyl benzene copolymer solid phase extraction columns (Isolute ENV+, Biotage) using a tubing pump (Ismatec). Tubing (Tygon®, Saint-Gobain) was first flushed with ~500 mL 1 M HCl (Normapur, VWR) followed by ~500 mL MQ at 10 mL min^{-1}. Columns were preconditioned with ~10 mL SBD methanol, followed by ~100 mL MQ at 3 mL min^{-1}. An average 923±48 mL sample was passed over the cartridges with exact volumes per sample registered for calculation of preconcentration factors. Cartridges were then stored at -18 °C prior to liquid chromatography. Before analysis the cartridges were washed with 5 mL 10 mM $(NH_4)_2CO_3$ and siderophores eluted with 84:14:5:0.1 (v:v:v:v) acetonitrile: propan-2-ol: MQ: NH_4formate. 2 mL eluant was reduced to ~100 µL by vacuum centrifuge at room temperature (SpeedVac, Thermo Scientific). Finally, 500 µL 5 mM NH_4formate was added to the reduced eluant, bringing the final volume to ~600 µL. Samples were divided into 5 aliquots. Aliquot 1 was analysed directly, aliquots 2, 3 and 4 were spiked with 0.5 mM $FeCl_3$ (made fresh from $FeCl_3.6H_2O$, Carl Roth) and aliquots 3 and 4 with ferrioxamines B, E (Sigma) and ferrioxamine G (EMC microcollections) to create a standard addition curve for the quantification of the respective ferrioxamine siderophores. Detection limits for ferrioxamine B, G and E were 0.4, 15.3 and 0.6 nmol L^{-1} respectively in the analysed solutions. Aliquot 5 was spiked with 10000 ppm Ga solution (final concentration 5mM Ga, VWR) and left overnight at room temperature before analysis.

Separation of siderophore-like substances was performed using a biocompatible UltiMate 3000 high-performace liquid chromatography (HPLC) system (Thermo Scientific), equipped with a poly styrene-divinylbenzene column (PRP H1, Hamilton; 5 µm 2.1 x 100 mm). Solvent A was 5% methanol and 5 mM ammonium formate (both Optima LC-MS, Fisher) in MQ (pH 5.8); solvent B was 100% methanol. The gradient spanned 15 minutes from 0 to 100% of solvent B, followed by 5 more minutes of solvent B. The column was then re-equilibrated to starting conditions. The flow rate was 400 µL min^{-1}. Separated samples were

passed to a hybrid quadrupole-orbitrap mass spectrometer (Q Exactive, Thermo Scientific) in +ve ion mode with a scan range of m/z 300-1500.

Chromatography data was was mined for the Ga isotopic ratio using Chelomex (Baars et al., 2014) after conversion to mzXML format using MSconvert (ProteoWizard; Kessner et al., 2008). A master list of potential Ga complexes was compiled, and monoisotopic masses for the uncharged metal free form of the molecule calculated (M), assuming the detected Ga isotopes were ionized as the $(M\text{-}2H+Ga)^+$ ion. Masses for $(M\text{-}2H+Fe)^+$, $(M\text{-}2H+^{69}Ga)^+$, $(M+H)^+$ and $(M+Na)^+$ were then calculated and chromatograms obtained from analysing aliquot 1 were mined for the corresponding masses in MZmine using an m/z tolerance of 10 ppm and a retention time tolerance of ±2 min with respect to the retention time of the $(M\text{-}2H+Ga)^+$ peak (Pluskal et al., 2010). The mined masses were filtered to remove duplicates and peaks with areas $<5\times10^5$ ion counts[2]. Finally, mass spectra for each putatively identified peak were examined for isotopic consistency and a list of peak m/z, retention times and peak areas produced. Graphics were produced in R (R Development Core Team, 2008).

8.3. Results

8.3.1. Growth characteristics

While the non-infected control cultures of *M. pusilla* and *P. globosa* showed expected growth during the experimental period (96 h), the infected cultures displayed a steady decline in abundances after about 1 day p.i. (Figure 1A, B). The duplicate infected *M. pusilla* cultures showed some discrepancies the second day of the experiment, whereby one of the replicates still mimicked the control abundances while the other already showed halted growth. The F_v/F_m values showed for *M. pusilla* a similar temporal dynamics as the algal abundances, whereas for *P. globosa* the decline in F_v/F_m occurred quickly upon infection (Figure 1C, D). Full lysis of the infected algal cultures was obtained after 72 h for *M. pusilla* and 60h for *P. globosa*. The latent period of the algal viruses, i.e. the time the abundance of extracellular viruses started to increase, was between 12-16 h and 8-12 h for MpV-08T an PgV-07T, respectively (Figure 1E, F).

Usable samples for Fe speciation characteristics represented the time cell lysis of the infected *M. pusilla* was halfway and almost complete for the infected *P. globosa* (50 h p.i.), and cell lysis was complete (76 h, 96 h p.i.).

8.3.2. Fe speciation characteristics

Ligand concentrations ($[L_t]$, Table 1, Fig. 2A) were not dissimilar for *M. pusilla* treatments with the exception of one high outlier in one replicate of the infected cultures (M3, 22.98 Eq. nM Fe at 76 h p.i.). The L_t concentrations in the *P.*

globosa control cultures were similar to the *M. pusilla* cultures, overall 11.78±1.49 Eq. nM Fe minus the outlier in infected *M. pusilla* above (N=10, see table 1). In the infected *P. globosa* cultures [L_t] was much higher at 17.75±0.60 Eq. nM Fe (N=3). This difference was reflected similarly in the free ligand concentration (L'), which represents the fraction of [L_t] that is available to bind additional Fe beyond the dissolved Fe concentration (DFe). If we normalize [L_t] to cytosol volume, assuming a cell radius of 1.5 µm for *M. pusilla* and 2 µm for *P. globosa*, the differences between host species are no longer present, with standard deviations between all treatments overlapping for an average 612.23±123.52 Eq. nM Fe μm^{-3}. Here again M3 at 76 h p.i. is an outlier (1185.84 Eq. nM Fe μm^{-3}) omitted from the average.

The conditional binding constant of *M. pusilla* cultures was also not significantly different between treatments (Fig. 2B). The $\log K'_{Fe'L}$ values for *P. globosa* controls were higher than for *M. pusilla*, but less so for the infected cultures of *P. globosa*. This was again similarly reflected in the reactivity value ($\log\alpha_{Fe'L}$), which is defined as the product of K' and L'. We find mean $\log\alpha_{Fe'L}$ values of 4.11±0.37 for *M. pusilla* and 4.81±0.34 for *P. globosa* (Fig. 2C).

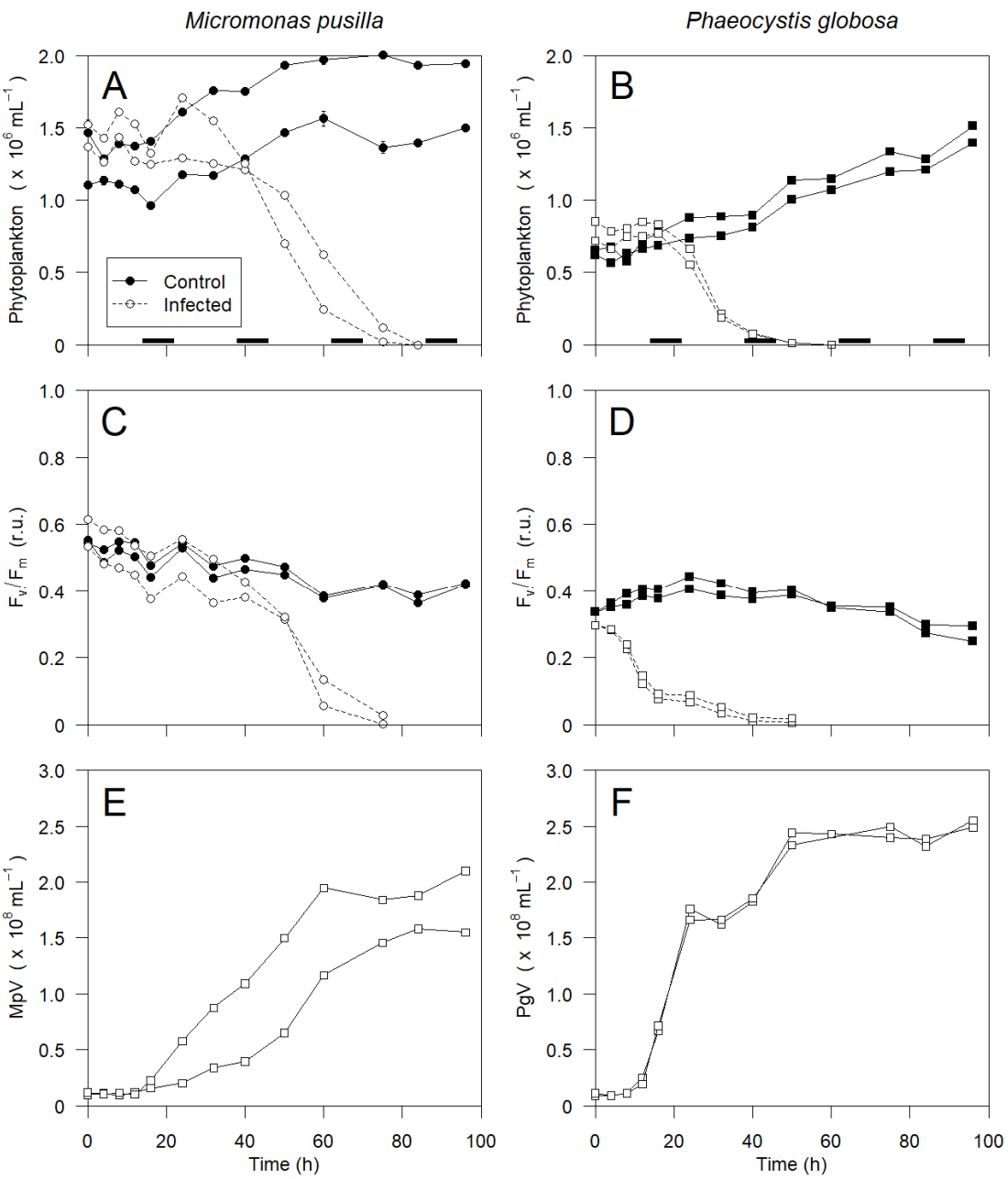

Figure 1 Temporal dynamics of *P. globosa* (A) and *M. pusilla* (B), F_v/F_m (C, D), MpV (E) and PgV (F). Black bars indicate dark periods. Duplicate cultures are shows separately in each graph. Error bars represent standard error of the mean of duplicate measurements (A, B, E-H) or triplicate measurements (C-D); where not visible these fall behind the symbols.

Table 1 Dissolved Fe (DFe) and Fe speciation characteristics for those samples that could successfully be analysed electrochemically. Reported here are the conditional binding strength of the ligands ($logK'_{Fe'L}$) with standard error, the total ligand concentration [L_t] with standard error, the excess ligand concentration [L'] and the reactivity of the ligands ($log\alpha_{Fe'}$).

	Code	T	DFe	$logK'_{FeL,Fe'}$	$logK'_{FeL,Fe'}$ SE	$[L_t]$	$[L_t]$ SE	[L']	$log\alpha_{Fe'}$
		h p.i.	*nM*	mol^{-1}	mol^{-1}	*Eq. nM Fe*	*Eq. nM Fe*	*Eq. nM Fe*	
M. pusilla	M2	50	1.99	12.47	0.34	10.05	0.36	8.06	4.38
control	M1	76	2.65	12.33	0.33	13.10	0.66	10.45	4.35
	M1	96	2.97	11.69	0.12	10.95	0.38	7.98	3.59
	M2	96	2.27	12.43	0.24	13.07	0.22	10.80	4.46
M. pusilla	M3	50	2.92	11.75	0.42	13.20	1.01	10.28	3.76
infected	M4	50	2.29	12.44	0.54	10.71	0.90	8.42	4.36
	M3	76	3.24	12.16	0.39	22.98	1.01	19.74	4.45
	M4	76	1.34	11.60	0.23	11.25	0.70	9.91	3.59
	M4	96	2.39	12.14	0.39	9.92	0.34	7.53	4.02
P. globosa	P1	50	3.72	13.31	0.54	13.02	0.30	9.30	5.28
control	P2	50	1.66	12.88	0.51	9.49	0.35	7.83	4.77
P. globosa	P3	50	3.34	12.44	0.34	17.50	0.42	14.16	4.59
infected	P4	50	1.43	12.79	0.66	17.32	0.66	15.89	4.99
	P4	76	1.43	12.19	0.19	18.43	0.28	17.00	4.42

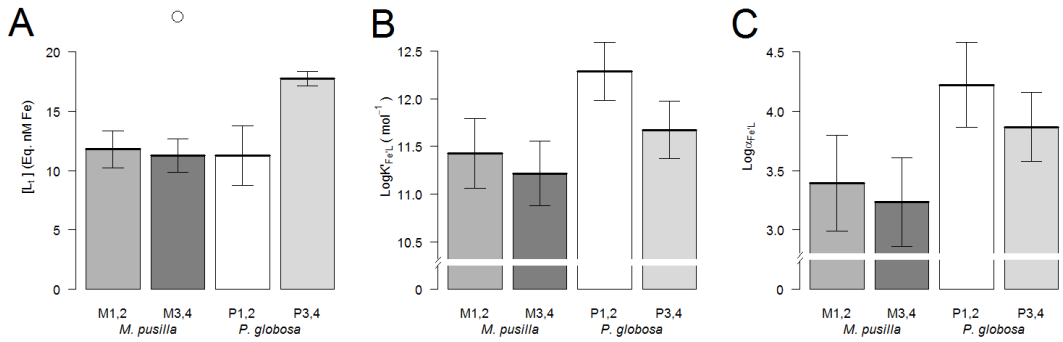

Figure 2 Fe speciation characteristics for selected samples as shown in Table 1: *M. pusilla* controls (M1,2) and infected (M3,4), *P. globosa* controls (P1,2) and infected (P3,4). A) Ligand concentration [L_t], B) conditional binding constant ($LogK'_{Fe'L}$) and C) reactivity ($Log\alpha_{Fe'L}$).

Ferrioxamine B, G and E concentrations were quantified at the end of the experiment (96 h p.i.) and after the 30-day senescence period (Table 2). Very few ferrioxamines could be resolved in *M. pusilla* cultures at 96 h p.i. However, concentrations in the senesced controls had increased just above the detection limit. Contrastingly, ferrioxamines in *P. globosa* cultures occurred in the highest concentrations at 96 h p.i., particularly FOG. FOG was largely undetectable after 30 days.

A further 21 ions with distinctive Ga isotopes were identified in the samples. For one of these ions (m/z ^{69}Ga isotope = 769.327, retention time = 6.92), the corresponding ^{56}Fe mass was detected after Fe addition (m/z = 756.335, retention time = 6.85, see Figure S1, page 174). The highest number of compounds was observed in the *P. globosa* controls (24 in P1 control and 21 in the P2 control). The three Ga ions observed in P1 but not in any other treatments included Ferrioxamine E, m/z(^{69}Ga) 769.327 and m/z(^{69}Ga) 727.279. Three ions (m/z ^{69}Ga isotope = 386.109, 414.104 and 521.020) were common to all treatments. Viral infection resulted in a reduction of ions exhibiting Ga isotopic signatures for *P. globosa* samples, but not for *M. pusilla* samples. Allowing the cultures to senesce for 30 days resulted in a reduction of the number of ions exhibiting Ga isotopic signatures for all treatments and species (Figure 3).

Table 2 Ferrioxamine B (FOB), G (FOG) and E (FOE) concentrations in pM in samples at the end of the infected cultures' lytic cycle (T = 96 h p.i.) and after a 30-day senescence period (T = 30 d p.i.). Measurements under the detection limit are denoted "<dl" in grey.

	T = 96 h				T = 30 d			
	Controls		*Infected*		*Controls*		*Infected*	
M. pusilla	**M1**	**M2**	**M3**	**M4**	**M1**	**M2**	**M3**	**M4**
FOB *(pM)*	<dl	<dl	<dl	2.6	2.3	13.5	<dl	1.6
FOG *(pM)*	<dl	<dl	<dl	<dl	<dl	9.2	<dl	<dl
FOE *(pM)*	2.7	<dl	<dl	<dl	4.7	<dl	<dl	<dl
P. globosa	**P1**	**P2**	**P3**	**P4**	**P1**	**P2**	**P3**	**P4**
FOB *(pM)*	<dl	0.8	0.7	<dl	<dl	<dl	0.8	<dl
FOG *(pM)*	747	35	33	20	<dl	<dl	10	<dl
FOE *(pM)*	9.5	<dl	<dl	<dl	1.5	<dl	<dl	<dl

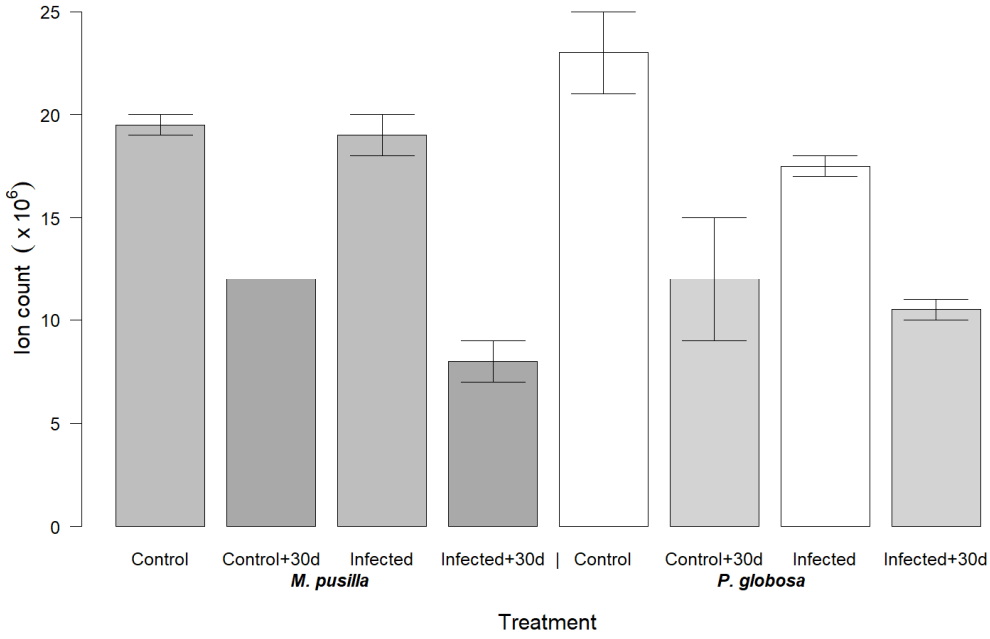

Figure 3 Peak surfaces pooled for 21 detected mass ratios (m/z) for Ga isotopic signatures detected in *M. pusilla* and *P. globosa* treatments at 96 h p.i., and after 30 days senescence (+30d).

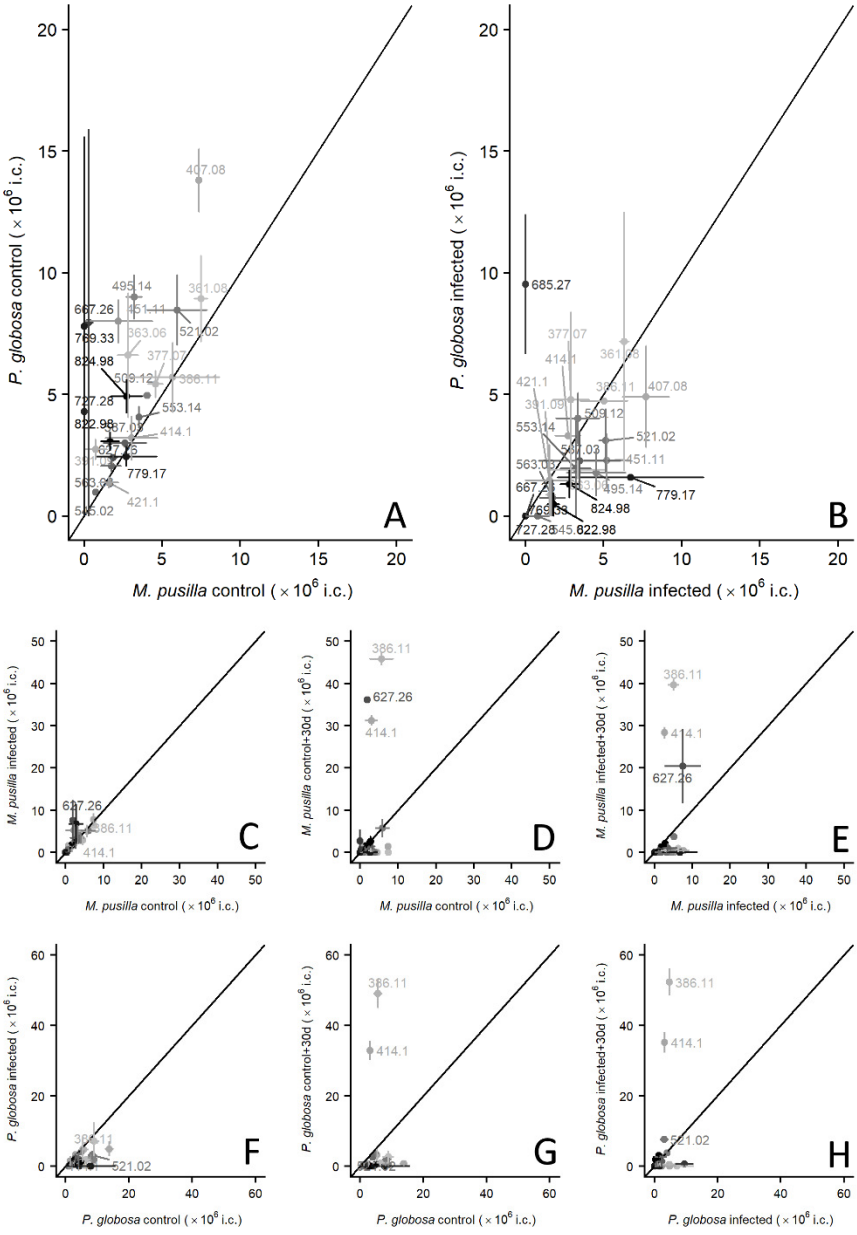

Figure 4 Comparison of peak surfaces for discrete mass ratios (m/z, values with points) for Ga isotopic signatures for A) all *P. globosa* controls against all *M. Pusilla* controls, B) all *P. globosa* infected against all *M. Pusilla* infected. Then for *M. pusilla*: C) infected vs. controls, D) controls after senescence vs. controls at 96 h p.i., E) infected after senescence vs. infected at 96 h p.i.; followed by the same 3 plots for *P. globosa* (F-H). Datapoints are greyed from high (black) to low (light grey) for contrast. Axes represent ion count (i.c.).

Comparison of the ion count registered with Ga isotopic signatures between species (Figure 4A) showed that the concentration of identified ions was higher in *P. globosa* controls than in *M. pusilla* control cultures, although there was considerable variability in ion count between the replicates. This difference between the algal species was not preserved in infected cultures (Figure 4B). The abundance of the putative Ga ions was similar or decreased slightly in infected samples. However, two ions (m/z 386.11 and 414.10) consistently increased in abundance by an order of magnitude in the samples allowed to senesce (Figure 4D-H). In *M. pusilla* cultures, ion counts of these two ions were within an order of magnitude of those observed for the ^{69}Ga complex of desferrioxamine B (m/z 627.267, Figure 4D, E).

8.4. Discussion

In absolute terms, the virally-infected *P. globosa* cultures showed the highest ligand concentrations, which would indicate that viral lysis of phytoplankton can enhance the concentration of ligands, to our knowledge not shown before the present study. However, when normalizing [L_t] to the cytosol volume, the errors again overlap. Lysates of *M. pusilla* did not seem to show a net effect of lysis in mean [L_t] values; however, one of the *M. pusilla* lysate replicates did show high [L_t] which remained significantly high after normalisation to cytosol volume.

The mean ligand binding strengths (log$K'_{Fe'L}$) were lower for the *P. globosa* lysates than for the controls, which implies that different types of ligands are released by virally lysed cells and senesced cultures. However, log$K'_{Fe'L}$ varies with host species and it cannot be excluded that the difference was due to differences in the bacterial activity and community composition between the control and infected cultures. Earlier studies have shown a rapid increase in bacterial production to viral lysis of *P. globosa*, which major shifts in the community composition (Brussaard et al., 2005; Sheik et al., 2014). log$K'_{Fe'L}$ values fall in the ranges associated with siderophore presence, at a mean 12.07±0.34 mol^{-1} for *M. pusilla* and 12.72±0.43 mol^{-1} for *P. globosa*.

Prior reported measurements of viral lysates of bacteria (Poorvin et al., 2011), LogK'_{Fe3+} of 20.08±0.58 mol^{-1} were found using CLE-AdCSV with 2-(2-thiazolylazo)-p-cresol (TAC), which would equate to a log$K'_{Fe'L}$ of 10.08 mol^{-1} assuming an inorganic side reaction coefficient of 10^{10}. In that same study, the log$K'_{Fe'L}$ found for purified siderophores was 12.12±0.16 mol^{-1}, putting the viral lysates in a different ligand class than siderophores. In a related study in natural waters, Velasquez and colleagues (2011) found log$K'_{Fe'L}$ values of 11.4 to 12.4 mol^{-1} (converted from their reported logK'_{Fe3+} values of 21.4 to 22.4 mol^{-1}) in conjunction with a strong siderophore presence. A similar study in which

bioassays were conducted on natural samples reported $\log K'_{Fe'L}$ values of 10.89 to 11.11 mol^{-1} in bacterial presence (converted from their reported $\log K'_{Fe3+}$ values of 20.89 to 21.11 mol^{-1}), with siderophore presence confirmed using LC-ESI-MS (Velasquez et al., 2016). While Hassler et al. (2011b) describe EPS as weak ligands of higher relative concentration, quoting $\log K'_{Fe'L}$ values as low as 8.7 mol^{-1} (Rue and Bruland, 2001); higher $\log K'_{Fe'L}$ values up to ranges similar to siderophores have also been attributed to EPS (Norman et al., 2015). Hassler et al. (2017) expend some effort tying K' to different functional groups and regions but concluded that such metrics lack the detail required to properly designate groups by themselves. In the present study

Taking into account both ligand concentration and binding strength, the reactivity of the ligands ($\alpha_{Fe'L}$) may better reflect the differences in ligand types found in the different cultures (Gledhill and Gerringa, 2017)., $\log\alpha_{Fe'L}$ showed near-complete separation between the host species. The relatively high concentrations of Fe-binding organic ligands present in the cultures most likely explains why $\log\alpha_{Fe'L}$ values in the present study are considerably higher than those found under natural conditions in the open ocean (Caprara et al., 2016). Alternatively, analytical issues may have played a role. CLE-AdCSV could not be successfully performed in senesced samples as electrochemical consistency could not be reached in the titrations. Changes in speciation must then be inferred from LC-ESI-MS. Ultimately, only a combination of more specific measurements and correlative relationships may yield enough information to elucidate relative contributors to the organic Fe-binding ligand pool (Gledhill and Gerringa, 2017; Hassler et al., 2017; Slagter et al., 2017).

The Ferrioxamine G concentration was well beyond the detection limit in *P. globosa* cultures at 96 h p.i. A contaminantly high concentration of Ferrioxamine G in one of the *P. globosa* controls corresponds to the highest $\log K'_{Fe'L}$ value found in those cultures. Given the high K' typically associated with siderophores(Hassler et al., 2017), the high K' may reflect the presence of Ferrioxamine G. Absence of these high concentrations after senescence indicates that Ferrioxamine G is lost or broken down over time. In contrast to *P. Globosa*, Ferrioxamine G was not found in *M. pusilla* cultures at 96 h p.i., and was detected in one post-senescence control of that host. Similarly, Ferrioxamine B was mostly detected in post-senescence *M. pusilla* cultures. This would indicate that the phytoplankton culture, or the community of heterotrophic bacteria endemic to these particular cultures, is determinant in the formation of these ferrioxamines. In *P. globosa*, Ferrioxamine B was only detected at concentrations near the detection limit without a clear disposition between samples. Ferrioxamine E was only found in one *M. pusilla* control, and in higher concentration after senescence. In contrast, Ferrioxamine E was

highest in one *P. globosa* control, and diminished after senescence. Overall, we can identify both production and breakdown processes, which are most strongly tied to the phytoplankton host species.

Ferrioxamine G was found in concentrations an order of magnitude higher than the ranges reported for the open ocean (e.g. Mawji et al., 2008; Boiteau et al., 2016), but only with one phytoplankton host species and only in the (recent) presence of the phytoplankton cells. Additionally, the picomolar concentrations of Ferrioxamines found in our analyses are 1-3 orders of magnitude below [L_t] found electrochemically, and therefore presumably only a small part of the Fe-binding organic ligand pool in these cultures.

Beyond the Ferrioxamines we report on a multitude of siderophore-like substances, i.e. substances in which Fe can be displaced by Gallium (Ga) and bound substances may be detected through the Ga isotope ratio (McCormack et al., 2003). It must be noted that the Ga complexes indicate possible siderophore-like substances, and not all types are detectable (Mawji et al., 2011). Siderophore-like substances were observed with different responses to experiment treatment and the senescence period. Many substances seem to a have a somewhat random presence, occurring in single replicates of the different treatments, sometimes with very large peaks. Overall, the Ga complexes detected were similar at 96 h p.i., and in all treatments diminished after 30 d senescence. This would indicate a loss of siderophore-like substances over time through breakdown or modification, either removing these from the Fe-binding organic ligand pool or possibly changed into other siderophore-like substances (Mawji et al., 2008).

Two substances with lower mass ratios (m/z 386.11 and 414.10) stood out in that these were uniformly present to meaningful levels across treatments and host species but only after dark senescence. This would suggest these substances were produced by the bacteria present. As the bacterial communities were presumably specific to the cultures, these may be very general Fe-binding substances produced by heterotrophic bacteria. A more recalcitrant substance was also observed (m/z 721) in most samples. Senesced *M. pusilla* also reflected the high concentration of Ferrioxamine B (m/z 627.26) reported earlier only in the 96 h p.i. samples, suggesting that it may not have been entirely eliminated as the standard additions would seem to indicate. However, ion counts do not necessarily equate (pico)molar concentrations above the detection level.

Loss factors of Fe-binding organic ligands thus far posited are photochemical degradation (Barbeau et al., 2003; Powell and Wilson-Finelli, 2003b) and topdown control by protists or viral lysis, in turn potentially releasing ligands (Hutchins et al., 1995; Poorvin et al., 2011) as well as modification and

breakdown by protists. However, it is unclear if these processes lead to a removal of the ligands or a modification into ligands of another class or group. For instance, it stands to reason that less than completely recalcitrant substances such as fulvic acids are broken down, the diverse Fe binding sites present in these substances are not necessarily removed from the system. Similarly, modification of siderophores may not necessarily remove their Fe binding properties, but modify them to a point these are shifted into a weaker ligand class. Electrochemistry cannot give insight in such processes due to its inherent "black-box" approach to ligand characterization. Broad spectrum analysis techniques such as the Ga-replacement LC-ESI-MS as used indiscriminately in the present study will be invaluable tools to enhance knowledge gained from electrochemical methods to a point where a complete picture of both specific ligand characterization and strength and kinetics of the redox interactions belying the Fe-binding organic ligand pool.

8.5. Conclusions

In all, an increased total ligand concentration in viral lysates of *P.globosa* shows that the viral shunt not only releases bioavailable Fe to the surrounding seawater (e.g. Poorvin et al., 2004), but also contributes to the Fe-binding organic ligand pool. The comparative lack of such influence from *M. pusilla* may be explained by the small cell size. Ligand classes differ between the two phytoplankton host species in the present study. While a differential in the presence of known siderophores and siderophore-like substances is also observed between host species and treatment in some cases, the relative abundance in comparison to the relatively high [L_t] found in our cultures cannot serve to tie these ligand classes to specific substances. What is evident is that the ligand pool is modified by bacterial both as a loss factor as well as a source of Fe-binding organic ligands, indicating that the viral shunt and bacterial remineralisation work in tandem.

Occurrence of siderophores produced by bacteria present in the different culture treatments are more dependent on the phytoplankton host species than the treatment. Ferrioxamine type siderophores seem to be produced mainly after senescence in *M. pusilla*, whereas they are dominant in the (recent) presence of the living *P. globosa* host. The highest Ferrioxamine G concentrations are reflected in ligand binding strength in one occurrence.

Ga complexes as representatives of potential siderophore-like substances show a uniform loss of these substances after the senescence period, identifying a loss factor of Fe-binding organic ligands. The timescale to study the effect of bacterial modification of Fe-binding organic ligands was chosen to guarantee

sufficient contrast, but it is too long to study specific processes. Further study of siderophore lability and evolution with smaller timescales would be advisable, preferably with larger volumes to increase detection limits and sample interval. Ideally, axenic phytoplankton host cultures with the addition of specific bacteria are used, although this will be very challenging in trace metal clean methodology. Many Ga complex isotopic signatures of siderophore-like substances here detected are thus far unknown. While this opens up a world of complexity to study in detail, this is not unwelcome given the "black box" extent of insight in specific substances thus far derived from established techniques. A combination of techniques shall be the avenue providing most insight going forward, as the new substance-specific techniques cannot convey information on the kinetics of these substances, and electrochemical techniques lack the specificity to characterize the Fe-binding organic ligand pool.

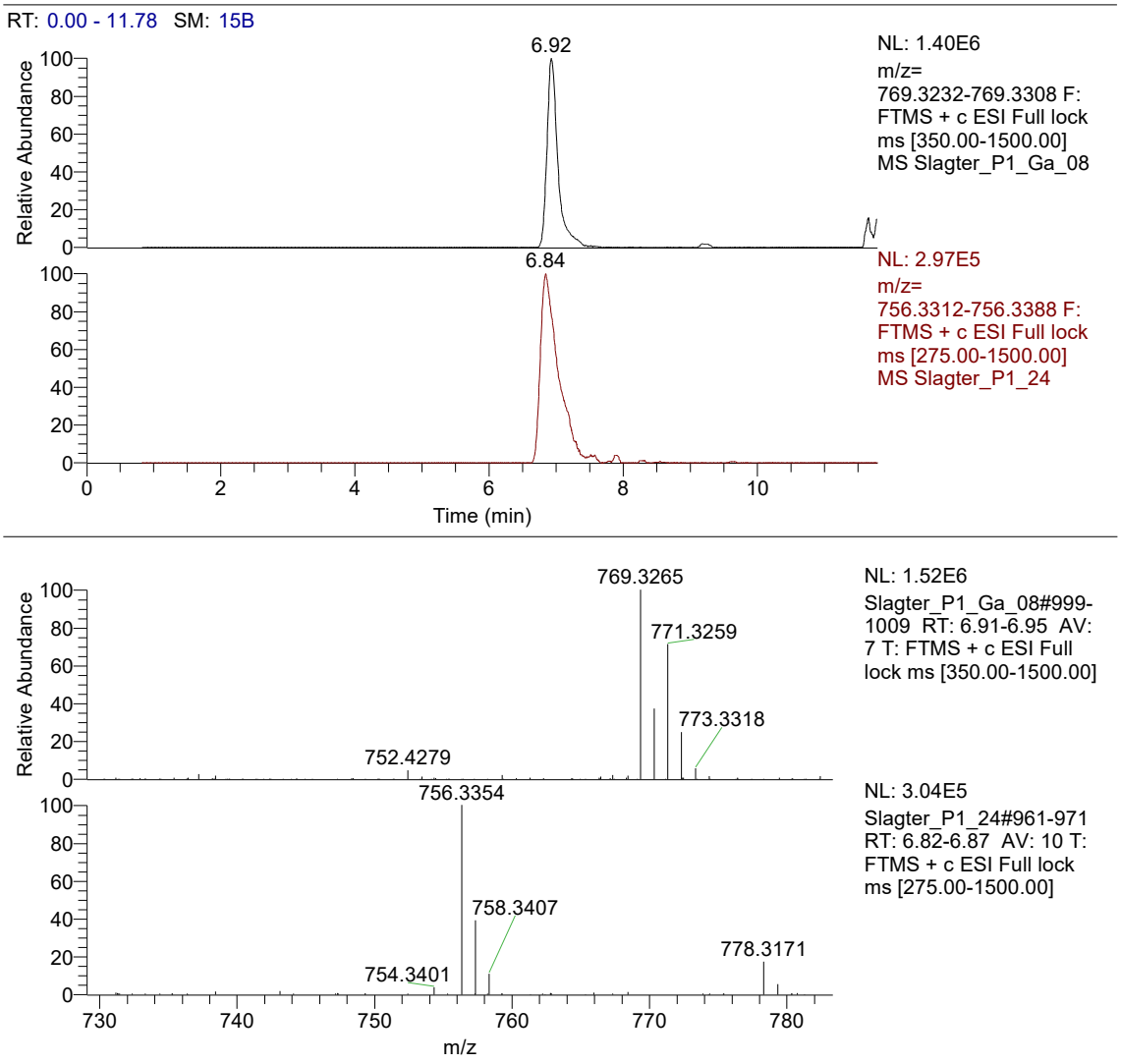

Figure S1 LC-ESI-MS data for a putative siderophore in one *P. globosa* control culture showing (A) the extracted mass chromatogram for the ^{69}Ga complex and (B) the ^{56}Fe complex after addition of the respective metal ions to separate aliquots of the sample. Average mass chromatograms obtained at the peak apex for (C) the Ga complex (N=7) showing the distinctive Ga isotopic signature and (D) the Fe complex (N=10) showing the presence of the ^{54}Fe isotope at 754.3401 (Δ1.995).

Chapter 9
Synthesis

9.1. Summary of conclusions

9.1.1. Mediterranean Fe and Fe-speciation

Sources and sinks of Fe and Fe-binding organic ligand in the Mediterranean Sea are diverse and do not necessarily share their origin. DFe was high at the surface, explained by atmospheric dust input primarily from North Africa. As the dust alone does not sufficiently contribute to the Fe-binding organic ligand pool to support DFe concentrations, ligands must have other origins, such as local microbial production or fluvial sources. Fe-binding organic ligands were near saturation and elevated in concentration. As our understanding evolved as detailed in Chapters 5 and 6, we now know that part of the humic Fe-binding organic ligand pool is not reflected by our measurements. As primary production was limited by nitrogen rather than Fe as found by a parallel study (van de Poll et al., 2015), microbial sources of Fe-binding organic ligands were expected to be only processes not specifically triggered by Fe-limitation such as grazing and lysis. The input of dust is in turn found to cause low DFe deeper in the water column due to scavenging and ballasting, which both act as a potential sink for Fe-bound ligands as well as emptying binding sites due to the removal of and downward transport of Fe.

DFe in the deeper Mediterranean Sea was not uniformly low, localized patches of high DFe occurred. These were found to relate to known locations of seamounts and mud volcanoes. Fe-binding organic ligands were present uniformly at relatively constant concentrations at depths >100 m and were completely saturated at these deep high-DFe patches. Given that DFe beyond the solubility provided by Fe-binding organic ligands will precipitate, $[L_t]$ limits deep DFe in these areas. A steady state between ligand-facilitated solubility and scavenging is expected for the deep Mediterranean water column, where outside of the high-DFe patches $[L_t]$/DFe ratios increase, making Fe-binding ligands an important determining factor for physical and chemical speciation of Fe throughout the Mediterranean Sea (Chapter 3).

9.1.2. The Arctic Ocean

The Arctic Ocean is another mediterranean system with a comparatively large shelf-to-basin ratio. This results in a strong terrestrial influence, especially at the surface Arctic Ocean by means of the Transpolar Drift. This surface current is known to carry terrestrial water originating from the large rivers surrounding the Arctic Ocean from the shelf seas across to the North Atlantic. These rivers have their catchments inside the Arctic Circle, where the negative feedback system of permafrost loss due to climate change is expected to rapidly increase riverine output of DOM to the shelf seas.

High DFe is carried by the TPD, causing a localized surface enrichment in the Arctic Ocean along the TPD flow path. Outside of the TPD, under-ice phytoplankton over the Nansen basin was Fe limited, and elsewhere in the Arctic Ocean nutrient ratios indicated that surface Fe is expected to be the next-limiting factor after light with the exception of the strongly enriched TPD. With the rapid changes in the Arctic Circle, alleviation of light limitation due to loss of sea ice cover may soon be reality (Chapter 4).

Given that DFe cannot be present in high concentrations without Fe-binding organic ligands, these must be present in sufficient concentrations to support the Fe enrichment found in the Arctic Ocean. Indeed, the surface enrichment of DFe in the TPD was supported by high ligand concentrations. The Fe-binding organic ligands in the Arctic Ocean, in contrast to the Mediterranean Sea, have their origin in common with DFe, as both are primarily introduced via the TPD. The TPD is known to carry 'Gelbstoffe' after the earliest mentions (e.g. Kalle, 1937, 1949), as HS are known for their effect on ocean colour. These may be detected as Chromophoric Dissolved Organic Matter (CDOM), which can be measured at specific wavelengths of absorbance or fluorescence spectra as well as direct voltammetric measurements of HS. Among the parameters thus describing the TPD flow path, a practical measure was chosen to constrain the border of the TPD in the form of a CDOM fluorescence sensor used to target the TPD for sampling. With the high data density this offered, a value of 0.5 a.u. was used to constrain the TPD in this work. Finally, while the Fe-binding organic ligand measurements correlated well with the CDOM and humic substance parameters, there were occurrences of ligand (over)saturation, which is thermodynamically improbable. Hence, our methodology employed on-board was missing part of the, very probably humic dominated, Fe-binding organic ligand pool (Chapter 5).

Expanding on the on-board measurements that were suspected not to reflect the Fe-binding organic ligand pool in the Arctic Ocean surface entirely, a subset of the data was reanalysed from stored samples using a variation of the CLE-AdCSV method with another competitive ligand. Hence, two established CLE-AdCSV methods are compared, as well as direct voltammetric measurements of humic substances using a fulvic acid (FA) as a standard. The latter data was augmented and confirmed with measurements in our colleagues' lab at the university of the Balearic Islands (UIB), where additional samples had arrived, using an evolution of the technique employed on board (Sukekava et al., 2018). Both datasets had excellent agreement and have been merged in Chapter 6. Ligand concentrations differ strongly between CLE-AdCSV methods but both show similar linear relations with HS though one reflects 60% of the other, detailed further in §9.2. With remarkable similarity in $\log K'_{Fe'L}$ determined by

either CLE-AdCSV method despite a large diversity of sample origin (inside and outside of the TPD), characterization of the Fe-binding ligand pool beyond the humic fraction remains veiled by methodological non-specifity. Additionally, we must question if the specific FA standard commonly used for these analyses is sufficiently representative of the HS that are to be determined. However, valuable insight is gained in the Fe-binding organic ligand pool in the Arctic Ocean. We can conclude that in the Arctic Ocean surface, Fe is primarily kept in solution by humic substances. This was not limited to the TPD alone, in the surface outside the TPD boundary humic substances also play a major role. In a similar set of measurements in the Mediterranean Sea, Dulaquais et al. (2018) found that local production was the major source of humic substances. As we cannot distinguish terrestrial humic substances from marine humics, no conclusions about the exact sources of HS can be made based on direct voltammetric measurement of HS. Although the complete ice cover of our stations does not make it likely that a local biological source offers a dominant contribution to the Fe-binding organic ligand pool, it cannot be excluded. However, given that ligand classes derived from analysis using a 2-ligand Langmuir model partly differed between CLE-AdCSV methods, the Arctic Ocean ligand pool is not limited to either a single class of humic substances, or humics alone. Furthermore, it is possible that stronger ligands such as siderophores are present but saturated and veiled by high concentrations of humic substances dominating the Fe-binding organic ligand pool. Ultimately, neither voltammetric method is able to give a complete picture, as CLE-AdCSV using TAC underestimates the contribution of humic substances but CLE-AdCSV using SA may well overestimate [L_t] (Chapter 6).

9.1.3. Fe speciation in phytoplankton cultures

Microbiota have been shown to contribute to the Fe-binding organic ligand pool. Specifically, production of siderophores by heterotrophic bacteria is a long-recognized process and it has been shown that viral lysis of phytoplankton cells contributes to Fe bioavailability, and is presumed to release ligands. However, before we could investigate the possible contribution of viral lysis to the Fe-binding organic ligand pool, we had to investigate the effect Fe limitation has on viral lysis. While the effect of major nutrient limitation on viral lysis of a phytoplankton host has been studied in some detail, the effect of Fe-limitation in this regard was thus far unknown.

Monocultures of the cosmopolitan phytoplankton species *Micromonas pusilla* and *Phaeocystis globosa* were cultured in a specially developed low-trace-metal medium, as well as their specific viral lysates. Fe-limited and Fe-replete cultures were infected with their respective lysates to study differences in the infection

process. These were also cross-inoculated to ascertain the effect of Fe limitation on the quality of the virus progeny and the effect of Fe added to limitation-adapted hosts at the time of infection. It was found that burst sizes were strongly reduced under Fe stress, as well as infectivity of the *M. pusilla* virus progeny. Introduction of Fe during the lytic cycle only partly alleviated the lowered production of virus progeny, indicating that host condition plays an important role as well. Overall the effects of Fe limitation were very similar to major nutrient limitation, though without affecting the latent period of the lytic cycle. The lowered burst size and infectivity of the progeny viruses under Fe limitation diminish viral control of phytoplankton. The viral shunt mobilizing nutrients (Wilhelm and Suttle, 2000) and increasing bioavailable Fe (Poorvin et al., 2011) may therefore be less important in low-Fe regions (Chapter 7). This stresses the importance of the viral shunt for Fe speciation, as there is a negative feedback on Fe cycling and release of Fe-binding organic ligands if these are indeed part of phytoplankton lysates.

In order to elucidate the role of viral lysis on Fe speciation, Fe-binding organic ligands were studied in Fe-limited cultures of *P. globosa* and *M. pusilla* during viral infection. The cultures and lysates were then left for a 4 week senescence period to allow for possible modification by heterotrophic bacteria present in the cultures. Both at the end of the experiment and the senescence period, samples were collected for ESI-MS analysis of siderophores and siderophore-like substances. As of yet unknown siderophore-like substances were found both after growth, lysis and senescence, with a number of unique substances after senescence though in lower abundance suggesting a changing Fe-binding organic ligand pool with a loss factor in bacterial breakdown of ligands.

An increase in $[L_t]$ was found upon lysis of *P. globosa*, indicating that viral lysis of phytoplankton releases Fe-binding organic ligands in the surrounding seawater. As no increase in $[L_t]$ was found upon lysis of *M. pusilla*, ligand release may be highly dependent on phytoplankton host species. Conditional binding strength also differed between phytoplankton host species, with no significant change in binding strength in lysed cultures compared to controls. The $\log\alpha_{Fe'L}$ showed similar relations to $\log K'_{Fe'L}$ between cultures and treatments. The $\log\alpha_{Fe'L}$ was considerably higher than oceanic samples (4.36, SD = 0.49, N = 14 for experimental samples; 2.85, SD = 0.33, N = 47 in Chapter 6 SA data). The $\alpha_{Fe'L}$ is dependent on both K' and L_t. The $[L_t]$ observed in the cultures was higher than typical open ocean values by an order of magnitude, which results in high $\log\alpha_{Fe'L}$. However, culture cell density will also be considerably higher than oceanic conditions.

9.2. Implications and recommendations

9.2.1. Surface waters and microbial activity

Both the Mediterranean Sea and the Arctic Ocean are examples of shelf-surrounded oceans with a strong terrestrial influence. In both, and in contrast to other world oceans, surface DFe is high and therefore the ligands to support it are present in relatively high concentrations. In the Arctic Ocean, humic substances are of particular importance for the Fe-binding organic ligand pool. We now also know from colleagues' efforts that this is also the case for the Mediterranean Sea (Dulaquais et al., 2018). They found, similarly to our first findings in the Arctic Ocean in Chapter 5, a clear relation between our $[L_t]_{TAC}$ measurements (Chapter 3) and HS. Their HS measurements explained L_t in the surface of the Mediterranean Sea in part, though with lower HS concentrations (ranging roughly 10-80 µg SRFA L^{-1}, compared to ~10-300 µg $SRFA^{-1}$ in the surface Arctic Ocean from Sukekava et al., 2018). Therefore, a revisit of Fe-speciation in the entire Mediterranean Sea using methods more representative of humic substances is called for. In the Arctic Ocean, CDOM and FDOM have good agreement with L_t from CLE-AdCSV. An improved method for direct voltammetric determination of humic substances also correlates well with ligand and DOM measurements, as confirmed by Sukekava et al. (2018). Together these properties and methods should be used to investigate the influence of HS in the Mediterranean Sea in more detail, as well as in other regions.

To constrain the flow path of the TPD, the choice was made to use an uncalibrated CDOM fluorescence sensor for its practicality and high sample density, which worked very well. However, for purposes of intercomparison and reproducibility it is recommended to use a metric that is less arbitrary. A common calibration scheme or another widely published spectral metric of terrestrial substance is recommended. Possible means to refine spectral data is the use of a specific absorbance wavelength (e.g. Coble, 2007), or if more precise equipment is available the use of spectral slopes (Helms et al., 2008). However, the use of a fast-response sensor system will still be vital to target sampling on-board.

Future analyses should focus on further elucidating the role of humic substances both inside and outside the TPD, as well as beyond the Arctic Ocean, e.g. in the North Atlantic where the TPD ultimately leads. Now that we know the extent of the TPD's influence on Fe speciation by crossing it, changes in the Fe-binding ligand pool along the length of the TPD flow path are important to describe. Gerringa et al. (2015) found that $[L_t]$ decreases along the flow of NADW which is directly influenced by Arctic outflow, illustrating the far reach of the TPD.

Climate change has a strong influence on the composition of DOM. Both conditions in the central Arctic Ocean (Bhatt et al., 2014), and the catchments of the source areas of the TPD (Peterson et al., 2002; Schuur et al., 2015) are already changing rapidly. As we found that Fe is potentially growth limiting once light limitation gives way in a future Arctic Ocean surface outside of the continuous supply of Fe inside the TPD, a time series of DFe, nutrients and Fe speciation measurements is warranted. It is imperative to not only elucidate these processes for predictive purposes, but also to track change as it happens.

Additionally, to pry apart the relative contribution of remotely produced terrestrial humics, their modification and local production of humic-like substances, these studies must be combined with detailed microbial surveys. For instance, while Gerringa et al. (2015) described the course of L_t in the west Atlantic, Achterberg et al. (2018) did not find an influx of DFe in Arctic water in the high latitude north Atlantic. This may very well be due to immediate utilization for primary production. The nutrient utilisation ratios used in Rijkenberg et al., 2018 (Chapter 4) to predict future Arctic Ocean supplies are highly dependent on the phytoplankton community. Thus, future studies must disparage chemical oceanography with microbiology in regard to Fe speciation.

In our efforts to identify microbiological interactions with the Fe-binding organic ligand pool, we found that viral lysis of phytoplankton and bacterial presence modify and contribute to the Fe-binding organic ligands pool. To this end we employed a novel culture medium without interfering chelates. This medium is ideally suited for future study of Fe-speciation in phytoplankton cultures. The contribution of siderophore-like Fe-binding organic ligands as well as the loss factor posed by heterotrophic bacteria may be strongly dependent on the bacterial community. In our study, we were limited to the natural bacterial community present in our non-axenic cultures. The composition of this bacterial community was unknown and future studies need to include genotyping of the bacterial phyla present. In order to gain a more conclusive insight in the effect of bacterial community composition it would be beneficial to control that community more precisely. Apart from study of bacterial monocultures (e.g. *Vibrio* sp., Gauglitz et al., 2012), it would be of great interest to further study natural bacterial communities and their interactions with phytoplankton (such as done by Sheik et al., 2014) in Fe-limited cultures. Such control of the bacterial communities would be a prime avenue of future study, as at present it is prohibitively difficult to maintain axenic cultures under a low trace metal regime for long enough. If this were attained, addition of specific bacterial phyla may elucidate the role of bacteria for the Fe-binding organic ligand pool further. Such studies should include the role of heterotrophic bacteria in breakdown as

a loss factor of Fe-binding organic ligands or conversion into substances of a possibly lower binding strength.

Furthermore, our results from culture experiments in Chapter 8 suggest a strong host species dependence of conditional binding strengths and of the occurrence of ligand increase in viral lysates. Studies with a more diverse set of phytoplankton species will help us understand this phytoplankton host species dependence. For one, cell size may be an important factor. Additionally, it will be of great interest to involve a diatom representative, given diatom importance in marine phytoplankton community succession as well as their divergent genetic background from secondary endosymbiosis. The latter may have led to siderophore-related pathways being present in diatoms.

9.2.2. Deep waters

Lateral transport is expected to play a major role in distributing DFe in the deep Mediterranean Sea, transporting Fe and possibly Fe-binding organic ligands from their sources. We suggest a link between mud volcanoes and Fe-speciation, as these were present in the area of the deep high-DFe patches found. Further study is required to confirm these possible sources. Similarly, hydrothermal sources are important point sources along the ridges separating the deep basins of the arctic. The importance of hydrothermal sources is well known for DFe (a.o. Tagliabue et al., 2010; Klunder et al., 2012). Fe-binding organic ligands near hydrothermal sources are typically at saturation (Bennett et al., 2008; Hawkes et al., 2013; Gerringa et al., 2015). Our measurements of Fe-binding organic ligands in Chapter 5 did not have the required resolution to reflect the hydrothermal DFe source described in Chapter 4. In order to better describe deep Fe-speciation, deep sampling resolution should be increased, for instance by pairing sampling density with source distance. The importance of scavenging for Fe-speciation was visible in our measurements in the Mediterranean Sea and deep Makarov Basin of the Arctic Ocean, reflected by an increased ratio $[L_t]$/DFe.

Furthermore, while we did not take HS samples beyond 200 m depth, HS profiles seemed to settle at values between 10-30 µg SRFA L^{-1}. Similar values were reported in the deep Atlantic near the Strait of Gibraltar by Dulaquais et al. (2018), indicating that the recalcitrant HS play a role in deep Fe speciation. To what extent HS are contributing to the ligand pool at depth is a lingering question, in the Arctic Ocean as well as elsewhere. With more detailed studies of deep Fe-speciation in shelf-surrounded systems, both in resolution and diversity of measurements, we may start to unravel the interactions between point sources of DFe and possibly Fe-binding organic ligands, scavenging and ballasting, and the reach of humic substances at depth.

9.2.3. Methodological considerations

A number of voltammetric methods using different competitive ligands are employed in studies of Fe-binding organic ligands. Earlier intercomparisons show that open ocean studies have been found to give similar results within acceptable tolerances (Buck et al., 2012, 2016). However, in our study of Fe speciation in the Arctic Ocean where there is a strong influence of HS, a clear discrepancy in results between different CLE-AdCSV methods was found. The competitive ligand TAC has been previously reported to suffer from interference when measuring HS (Laglera et al., 2011), particularly the commonly used SRFA standard, as we have also concluded (Chapter 5). However, we find that measurements using TAC in fact do respond to changes in a HS-dominated system, and reflects terrestrial influences at least in part. Assuming measurements using SA measure the humic influence in entirety, measurements using TAC only reflect 61% (Chapter 6).

CLE-AdCSV using SA evidently reflects humic substances in a more complete manner. However, we found a large offset with an HS-derived measure of $[L_t]$ in a HS-dominated system (0.88 nM). In the application of CLE-AdCSV using SA, only the FeSA complex is measured voltammetrically. The formation of the non-electroactive $FeSA_2$ (Abualhaija and van den Berg, 2014) is subtracted from the signal in the Langmuir model: the sum of both K'_{FeSA}, and $\beta'_{Fe(SA)2}$ are taken into account together with α_i to calculate [Fe']. Our choice was to follow Buck and used an equilibration time of 15 minutes, assuming a plateau in $FeSA_2$ formation, to minimize the effect on sensitivity. Overnight equilibration would ensure the kinetics of SA to run their course as they do with the TAC method (Croot and Johansson, 2000; Gerringa et al., 2007). However, the existence of an equilibrium state is essential to use the Langmuir equation (Langmuir, 1916; Gerringa et al., 2014; Laglera and Filella, 2015). The assumption of a plateau in $FeSA_2$ formation may be matrix-dependent, and use of SA may lead to an overestimation of $[L_t]$. The intricacies of SA kinetics are subject to ongoing research and these questions need to be resolved in order to gain confidence in the method. In all, it may be required to rely on multiple added ligands in CLE-AdCSV to come to a complete picture of Fe speciation. To what extent different CLE-AdCSV methods represent the Fe-binding organic ligand pool in a dissimilar manner must also be extended beyond our comparisons of TAC and SA as added ligands. To this end a revisit of methods employing 2,3-dihydroxynaphthalene (DHN; van den Berg, 2006) or 1-nitroso-2-napthol (NN; Gledhill and van den Berg, 1994) would increase our insight and allow for comparison against earlier studies.

In order to confidently compare methods, their implementation in different labs as well as identify matrix dependence, intercalibration standards such as those available for DFe (Johnson et al., 2007) are direly needed. Adoption of multiple methods in different labs will also assist in increasing confidence in their application. In order to readily adopt these methods, it is imperative to pay very close attention to detail in the descriptions of method application, with special attention to preparatory steps and material handling, which is often highly lab-dependent and in our experience has a profound influence on results.

In the studies here described, we found a remarkable lack of variation in $\log K'_{Fe'L}$ both in *in-situ* samples and in cultures of diverse treatment. Attempts are being made to translate specific ranges of $\log K'_{Fe'L}$ to relatively specific ligand classes and locales (e.g. Hassler et al., 2017). However, the extent to which these may be applied to *in-situ* sampling given the mixed character of Fe-binding organic ligands in the oceans is questionable. In the studies combined in this dissertation, we could not identify such specific locales based on $\log K'_{Fe'L}$. Characterisation of the ligand pool may depend more on the identification of specific substances through other means (E Mawji et al., 2008; Helms et al., 2008; Stedmon et al., 2011; Boiteau et al., 2013; Sukekava et al., 2018). When such analyses yield insight into the relative importance of those substances, CLE-AdCSV methods may in turn provide measures of binding capacity and strength of a ligand pool as a whole, or specific isolates where available.

9.3. Concluding remarks

This dissertation has set out to generate more insight in the sources and sinks of Fe-binding organic ligands with the twofold approach of *in-situ* study and experiments in culture. By correlating measurements of possible contributors with traditional measurements of Fe-binding organic ligands, we have found that humic substances make a particularly important contribution to the Fe-binding organic ligands pool in the surface waters of the Arctic Ocean, both inside and outside of the avenue of terrestrial substances formed by the TPD. In deeper waters no strong correlations with DOM could be identified, but a smaller concentration of recalcitrant humics may play a role here.

Concentrations of Fe-binding ligands increase upon viral lysis of phytoplankton, dependent on phytoplankton species. Additionally, senescence of cultures in the presence of heterotrophic bacteria indicated that these can be both contributors and a loss factor for specific substances. To what extent the Fe-binding ligand pool can be diminished requires further study. Identification of loss factors due to the activity of heterotrophic bacteria via ligand concentration and conditional binding strength in cultures is severely complicated by the lack of sensitivity in

electrochemical methods in the 'organic soup' resultant from these processes. More substance-specific methods such as LC-ESI-MS as used in Chapter 8 may assist in these efforts. However, more control over bacterial communities is required.

We have identified that methodologically, the study of Fe-binding organic ligands will strongly benefit from diversity in methods, as none are capable of elucidating the Fe-binding organic ligand pool in its entirety alone. Profiling of ligands into specific regimes based on electrochemical parameters is at odds with their dependence on method, application and inconsistent reflection of different contributors to the ligand pool.

Nederlandse samenvatting *(Dutch summary)*

10.1. IJzer en liganden

De basis voor leven in de wereldzeeën wordt, net als voor leven op land, gevormd door organismen die anorganisch koolstof omzetten in organisch materiaal; kortom, planten. Hierbij wordt gebruik gemaakt van energie uit zonlicht, en daarom heet dit proces fotosynthese. In essentie zet fotosynthese koolstofdioxide (CO_2) uit de lucht om in organisch materiaal en zuurstof. Dit eerst gevormde organisch materiaal in de voedselketen, ook primaire productie genoemd, wordt in de oceanen gevormd door micro-organismen. Eéncellige algen en fotosynthetiserende bacteriën vormen zodanig de basis van de voedselketen in de wereldzeeën, welke 70% van de Aarde bedekken. Al met al zijn de micro-organismen in zee verantwoordelijk voor grofweg de helft van de zuurstofproductie uit fotosynthese op Aarde.

In een uitgebreidere kijk op primaire productie zoals in het Engelstalige introductiehoofdstuk wordt gedaan moet benadrukt worden dat dit proces niet beperkt kan worden tot opname van alleen CO_2. Om te groeien hebben planten, en zo ook de micro-algen, meer nutriënten nodig. De belangrijkste nutriënten zijn fosfaat en nitraat, en ook ijzer is een essentieel sporenelement. Bij mensen en andere dieren komt ijzer voor in het bloed als cofactor in de enzymen die noodzakelijk zijn om zuurstof door het lichaam te kunnen transporteren. Zo hebben fotosynthetiserende organismen ijzer nodig om lichtenergie om te zetten in chemische energie. Nu zijn wij op land gewend dat ijzer alom aanwezig is, echter in de oceanen is dit een andere zaak. Om beschikbaar te zijn voor micro-organismen dient het ijzer opgelost te zijn in het zeewater, iets dat echter niet vanzelf gaat gezien zeewater iets basischer is dan pH-neutraal (de pH van zeewater is ongeveer 8). Dit is een probleem daar ijzer alleen oplost in water met een grotere zuurtegraad, en daarmede een lager pH. Indien ijzer niet in oplossing gehouden wordt in zeewater zal dit deeltjes vormen en uitzinken naar de zeebodem.

Om ijzer in opgeloste toestand te houden bij een pH-waarde van 8, moet dit gebonden zijn aan een stof die wel oplosbaar is in deze omstandigheden. Deze ijzerbindende stoffen worden liganden genoemd. IJzerbindende liganden maken onderdeel uit van het opgelost organisch materiaal dat alom aanwezig is in de

oceanen en een grote diversiteit kennen in oorsprong en complexiteit. Sommige stoffen worden specifiek door organismen aangemaakt om ijzer beschikbaar te maken en/of te houden in de directe omgeving van de cel. Andere stoffen zijn een divers mengsel van bijvoorbeeld afbraakproducten en uitscheidingen welke vele associaties met metalen aangaan. Deze diverse stoffen hebben dan ook een diverse oorsprong, en deze oorsprong probeer ik in dit proefschrift beter in kaart te brengen.

10.2. Bronnen van liganden in zee

Hoofdstukken 3 tot en met 6 behandelen verschillende bronnen en bijdragende processen voor ijzer en ijzerbindende liganden zoals onderzocht in het veld; in de Middellandse Zee (hoofdstuk 3), ijzer in de Noordelijke IJszee (hoofdstuk 4) en ijzerbindende liganden in de Noordelijke IJszee (hoofdstukken 5 en 6).

In de Middellandse Zee tonen wij aan dat ijzer en ijzerbindende liganden zeer diverse oorsprongen hebben. Er bevindt zich een hoge concentratie opgelost ijzer in het oppervlaktewater van de Middellandse Zee, welk haar oorsprong heeft in atmosferisch stof uit Noord-Afrika. Het stof kan echter niet voldoende oplosbaarheid van ijzer garanderen, en voor de ijzerbindende liganden zullen andere bronnen verantwoordelijk zijn, zoals lokale productie door micro-organismen of inbreng van rivieren. Voortschrijdend inzicht over humuszuren, bacteriële afbraakproducten uit de bodem die ijzer binden (uiteengezet vanaf hoofdstuk 5), leert ons dat deze ook een grote rol kunnen spelen in de Middellandse Zee. In de diepe Middellandse Zee komen – zeer lokaal – ook verhogingen van de concentratie opgelost ijzer voor. Hier waren de ijzerbindende liganden algemeen aanwezig maar niet in verhoogde concentratie, wat leidt tot verzadiging van de aanwezige liganden met ijzer in deze lokale verhogingen.

De Noordelijke IJszee kan ook omschreven worden als een mediterrane oceaan, daar deze omgeven is door land, en beperkte uitwisseling heeft met de andere oceanen. Een belangrijk component van deze uitwisseling is de TransPolar Drift (TPD), reeds bekend sinds de wereldberoemde expeditie van Fridtjof Nansen en zijn schip de *Fram*. Zij raakten, volgens plan, tijdens een expeditie naar de Noordpool ingevroren in het pakijs in de Noordelijke IJszee, en dreven met dit ijs van de randzeeën boven Siberië naar Spitsbergen. Het pad van de TPD varieert per jaar met de arctische oscillatie, een meteorologisch begrip, en kan soms meer langs de randzeeën, en soms zelfs over de Noordpool voeren. Uiteindelijk loopt de TPD tot wat nu de Fram Straat heet, tussen Groenland en Spitsbergen, waar de Noordelijke IJszee overgaat in de Atlantische Oceaan. Nansen had pech, in het jaar van de expeditie werd de ingevroren *Fram* langs

de randzeeën gevoerd, en ook een expeditie met hondensleeën deed hen de pool niet bereiken. Desalniettemin was de expeditie een enorm succes voor de oceanografie, en vormt nog altijd de basis voor wat wij nu weten over de TPD.

In het algemeen voert het pad van de TPD van de randzeeën naar de Fram straat. De randzeeën staan onder invloed van grote rivieren, voor het voedingsgebied van de TPD vooral die in noord-Siberië. Deze rivieren voeren veel organisch materiaal en nutriënten mee uit hun stroomgebied. Er is reeds aangetoond dat dit onder invloed staat van klimaatverandering. Door verlies van permafrost, permanent bevroren bodem, kan in korte tijd een enorme hoeveelheid organisch materiaal vrijkomen. Dit materiaal wordt door de rivieren meegevoerd en in de randzeeën gebracht, een fenomeen dat reeds aangetoond is door andere onderzoekers. De TPD voert het organisch materiaal van de randzeeën, over de Noordelijke IJszee, uiteindelijk naar de Atlantische Oceaan. Gezien de herkomst van het organisch materiaal bevat dit ook veel humuszuren. Deze humuszuren zijn ook goed meetbaar, en zijn zo duidelijk zichtbaar dat zij het stroomgebied van de TPD duidelijk kunnen aangeven. Wij zien ook dat het voorkomen van humuszuren sterk overeenkomt met verhoogde concentraties van ijzer en ijzerbindende stoffen. Echter tonen we ook aan dat verschillende methoden om ijzerbindende stoffen te meten deze humuszuren verschillend weerspiegelen, uitgelegd in meer detail in 10.4.

10.3. Bronnen van liganden in experiment

Micro-organismen zijn ook bekende producenten van organische ijzerbindende liganden. Bacteriën zijn al lang bekend als doelbewuste producenten van liganden, sideroforen genoemd, welke bedoeld zijn om de oplosbaarheid van ijzer in de directe nabijheid van de cel te vergroten. Ook is reeds aangetoond dat het openbreken van cellen door virusinfectie, virale lyse genoemd, de beschikbaarheid van ijzer verhoogt – vermoedelijk door het vrijkomen van liganden uit het binnenste van de gastheercel.

Hoofdstukken 7 en 8 behandelen experimenten met mariene algen, virussen en bacteriën in het laboratorium. Twee algensoorten zijn in cultuur gebracht bij lage concentraties ijzer, evenals twee soorten specifieke virussen die deze infecteren. In eerste instantie omschrijven wij hoe laag-ijzer kweken verschillen van ijzerrijke omstandigheden en hoe het infectieproces reageert op ijzertekort (hoofdstuk 7). Wij tonen aan dat ijzertekort een behoorlijke negatieve invloed heeft op het virusinfectieproces.

Voorts zijn ijzerbindende liganden bestudeerd in bovengenoemde cultures van micro-algen, zowel met als zonder infectie door virussen (hoofdstuk 8). Hieruit blijkt dat ligandconcentraties verhoogd kunnen worden door virale lyse en dat

dit een effect heeft op de bindingssterkte van liganden. Dit geeft aan dat, afhankelijk van de algensoort, virale lyse verschillende liganden vrij maakt, een proces dat sturend kan zijn voor de beschikbaarheid van ijzer in natuurlijk zeewater.

Tenslotte is de rol van bacteriën bestudeerd. Bovenstaande experimenten zijn bemonsterd na verloop van het infectieproces, en ook na 30 dagen 'rust', een periode waarin de in de cultures aanwezige bacteriën aanwezige stoffen kunnen metaboliseren en hun eigen bijdrage kunnen leveren. Hieraan zien wij dat er inderdaad siderofoor-achtige stoffen na groei en lyse aanwezig waren, en dat hierin een modificatie optrad na de rustperiode. Dat hier bepaalde siderofoor-achtige stoffen verdwenen geeft ook aan dat de omzetting die plaats vindt een mogelijke verliesfactor voor organische ijzerbindende liganden kan zijn.

10.4. Metingen van liganden

Met name in hoofdstuk 6 gaan we dieper in op het belang van de manier waarop we liganden meten. In het kort, we kunnen liganden niet rechtstreeks meten, we kunnen slechts de eigenschappen meten van alle liganden bij elkaar in een zeewatermonster. Dit gebeurt door gebruik te maken van de elektrische geleidingseigenschappen van de binding van ijzer en liganden. Verschillende soorten ijzerbindende liganden zijn aanwezig in verschillende concentraties, en ijzerionen en het ijzerbindende deel van een ligand gaan een binding aan van verschillende sterkte. We nemen aan dat deze binding omkeerbaar is, en hieruit volgt dat de binding van ijzer in zeewater met uiteenlopende ijzerbindende liganden in een evenwicht verkeert. Daar wij de verschillende natuurlijke ijzerbindende liganden niet rechtstreeks kunnen duiden in termen van bindingssterkte en relatieve concentratie doen wij onze metingen door een bekend ligand toe te voegen aan het evenwicht. De associatie van ijzer met dit toegevoegde ligand weten we rechtstreeks te typeren doormiddel van elektrochemie. Doordat wij de kinetiek van dit toegevoegde ligand weten, kunnen we uitspraken doen over de kinetiek van de natuurlijke liganden in het monster. Hieruit volgt, wellicht vanzelfsprekend, dat de eigenschappen van dit toegevoegde ligand bepalend zijn voor welke natuurlijke liganden wij kunnen typeren. In hoofdstuk 6 wordt dit duidelijk voor de bepaling van het belang van humuszuren in de wateren van de Noordelijke IJszee, waarbij het gebruik van verschillende toegevoegde liganden de nodige verschillen oplevert.

10.5. Relevantie

Met dit proefschrift wordt meer inzicht gegeven in de bronnen en eventuele verliesfactoren van organische ijzerbindende stoffen in de oceanen. Door bemonstering op zee en van specifieke algencultures en door correlaties te

zoeken met mogelijke bijdragende processen vinden we een grote rol voor humuszuren in land-omringde gebieden, welke vervolgens ook verder naar de oceanen getransporteerd worden. In een veranderend klimaat, herhaaldelijk vastgesteld door vele wetenschappers, kunnen deze processen grote veranderingen ondergaan. Met name de toevoer van organisch materiaal in de Noordelijke IJszee zal toenemen bij verlies van permafrost in de stroomgebieden van de grote rivieren rond de arctische randzeeën. Daar ook vermindering van zee-ijs een voortdurend proces is, zou deze toename van nutrienten kunnen leiden tot verhoging van primaire productie in het oppervlak van de Noordelijke Ijszee. Dit is een potentieel veranderproces dat gezien haar invloed op primaire productie en opname van CO_2, en dus ons voorspellend vermogen omtrent klimaatverandering, de aanhoudende aandacht van de wetenschappelijke gemeenschap vereist. Daarnaast tonen wij aan dat de interactie tussen micro-algen, bacteriën en virussen in zee de nodige veranderingen teweegbrengt in de uitwisseling van organische ijzerbindende liganden. Dit is slechts een start van de opheldering van deze processen, en ook hier valt meer onderzoek aan te bevelen. Meer controle over de bacteriële gemeenschap in cultures zou inzicht kunnen geven in de rol van deze groep micro-organismen, en een bredere selectie micro-algen kan meer inzicht geven in het verloop van deze processen in verschillende gebieden.

Tenslotte identificeren wij een aantal methodische overwegingen die essentieel zijn voor de correcte meting van met name de rol van humuszuren als onderdelen van de totale groep organische ijzerbindende stoffen. Het determineren van verschillende groepen liganden op basis van elektrochemische analyses wordt hierdoor bemoeilijkt, en in toekomstige analyse van deze stoffen moet een zorgvuldige afweging gemaakt worden met betrekking tot de toegepaste methodiek.

Acknowledgements

First of all, I would like to thank my primary supervisor Loes Gerringa for the opportunity she gave me, and who has with her expertise, advice, supportive impetus and above all patience taught me so much about her subject, and perhaps re-taught me many of the things I thought I knew. In addition, my co-promotor Corina Brussaard has both added a great deal to my knowledge of the microbiological side of things, while her zeal for science has been a tremendous inspiration. Both have also expended a great deal of effort as co-authors of these chapters. Furthermore, I would like to recognize my promotor Hein de Baar, who has not only been a great inspiration going back to my first lectures in oceanography at the University of Groningen, but whose excellent comments and suggestions have contributed considerably to this thesis.

I would also like to thank the other co-authors that have both contributed and taught me many details about the subject of this thesis – Martha Gledhill, Luis Laglera, Michiel Rutgers van der Loeff, Heather Reader and Micha Rijkenberg. Also co-authors Jan van Ooijen and Camila Sukekava are recognized for their analytical contributions, as well as the advice and support of colleagues Patrick Laan, Rob Middag, Anna Noordeloos, Kirsten Kooijman, Klaas Timmermans, Douwe Maat, Josje Snoek, Tanja Moerdijk, Karel Bakker, Swier Oosterhuis, Harry Witte, Judith van Bleijswijk, Bas van der Wagt, Sven Ober and Gert-Jan Reichaart at NIOZ; as well as Willem van de Poll and Anita Buma at the University of Groningen for their insightful discussions.

This work has also benefited tremendously from the excellent efforts of our students, Niels Muntjewerf, Robert Sluijter, Ismaël Salazar, David Amptmeijer, Maikel Breederland, and in memoriam, Oscar Dijkstra, who left us so much too soon.

For their excellent support during work at sea I would like to thank captain Pieter Kuijt and the crew of RV Pelagia from NIOZ; captain Stefan Schwarze, principle scientist Ursula Schauer and the crew of FS Polarstern from the Alfred Wegener Institute, Ultraclean Sampling team Aridane, Lars-Eric, Michael and Micha; as well as those I met on board for wonderful and productive cruises.

For their support and camaraderie, I thank my fellow phd's and staff and students residing at the Potvis – Uli, David, Simone, Eveline, Esmee, Laura, Sabine, Linda, Sofia, Alice, Michelle, Indah, Siham, Mathijs, Stanley, Roos, Inge, Marc, Julie, Marten, Robin, Ryan, Milou, Ella, Cees, and whosever's name I have forgotten over the years, the good times were not.

For their mental support as well as an unending string of silliness to take my mind of the hard work and blow off steam, I thank my close friends, in no particular order – Vincent, Rudy, Gijs, Jasper, Bas, Iwe, Hendrik, Remco, Sander, Mark, Hidde, Henk-Jaap and Wietze. I am happy my friends Uli and Vincent will stand with me during the ceremony as paranimphs, for which my thanks.

Finally, I would like to thank my parents. While my father could not experience the conclusion of my studies, I know he would be proud. His endless practicality, natural skill and curiosity have clearly rubbed off on me, and allowed me to be what I am today. My mother, the one constant in my life, the pillar I can always lean on, you make me intensely proud.

Biography

Hans Slagter was born on August 29th, 1983 in Drachten, the Netherlands. He grew up in south-east Frisia and finished high school in Harlingen before moving to Groningen to study Biology at the Rijksuniversiteit Groningen. Here he found his passion for marine biology, which led him to internships at the Royal Netherlands Institute for Sea Research on Texel, studying CO_2 fluxes with Dr. Henk Zemmelink; North Sea microbiology with Dr. Corina Brussaard, now professor at the UvA; going on various cruises, and getting more and more interested in pursuing oceanography as a career. Under supervision of his mentor Prof. Dr. Ir. Hein de Baar he finished his masters degree finally in 2012, and in 2013 was offered the opportunity to do the PhD by Dr. Loes Gerringa, culminating in the dissertation before you. Hans is currently looking to find a next challenge in oceanography.

References

Aagaard, K., Swift, J.H., Carmack, E.C., 1985. Thermohaline circulation in the Arctic Mediterranean Seas. J. Geophys. Res. 90, 4833–4846.

Abualhaija, M.M., van den Berg, C.M.G., 2014. Chemical speciation of iron in seawater using catalytic cathodic stripping voltammetry with ligand competition against salicylaldoxime. Mar. Chem. 164, 60–74.

Abualhaija, M.M., Whitby, H., van den Berg, C.M.G., 2015. Competition between copper and iron for humic ligands in estuarine waters. Mar. Chem. 172, 46–56.

Achterberg, E.P., Steigenberger, S., Marsay, C.M., Lemoigne, F.A.C., Painter, S.C., Baker, A.R., Connelly, D.P., Moore, C.M., Tagliabue, A., Tanhua, T., 2018. Iron Biogeochemistry in the High Latitude North Atlantic Ocean. Sci. Rep. 8, 1–15.

Aguilar-Islas, A.M., Rember, R.D., Mordy, C.W., Wu, J., 2008. Sea ice-derived dissolved iron and its potential influence on the spring algal bloom in the Bering Sea. Geophys. Res. Lett. 35, L24601.

Aguilar-Islas, A.M., Séguret, M.J.M., Rember, R., Buck, K.N., Proctor, P., Mordy, C.W., Kachel, N.B., 2016. Temporal variability of reactive iron over the Gulf of Alaska shelf. Deep. Res. Part II Top. Stud. Oceanogr. 132, 90–106.

Aguilar-islas, A.M., Wu, J., Rember, R., Johansen, A.M., Shank, L.M., 2010. Dissolution of aerosol-derived iron in seawater: Leach solution chemistry, aerosol type, and colloidal iron fraction. Mar. Chem. 120, 25–33.

Ambar, I., Serra, N., Neves, F., Ferreira, T., 2008. Observations of the Mediterranean Undercurrent and eddies in the Gulf of Cadiz during 2001. J. Mar. Syst. 71, 195–220.

Amon, R.M.W., Gereon, B., Benedikt, M., 2003. Dissolved organic carbon distribution and origin in the Nordic Seas: Exchanges with the Arctic Ocean and the North Atlantic. J. Geophys. Res. 108, 3221.

Apte, S.C., Gardner, M.J., Ravenscroft, J.E., 1988. An evaluation of voltammetric titration procedures for the determination of trace metal complexation in natural waters by use of computer simulation. Anal. Chim. Acta 212, 1–21.

Arrigo, K.R., van Dijken, G., Pabi, S., 2008. Impact of a shrinking Arctic ice cover on marine primary production. Geophys. Res. Lett. 35, 1–6.

Arrigo, K.R., Van Dijken, G.L., 2011. Secular trends in Arctic Ocean net primary production. J. Geophys. Res. Ocean. 116, 1–15.

Baars, O., Morel, F.M.M., Perlman, D.H., 2014. ChelomEx: Isotope-assisted discovery of metal chelates in complex media using high-resolution LC-MS. Anal. Chem. 86, 11298–11305.

Baker, A.R., Croot, P.L., 2010. Atmospheric and marine controls on aerosol iron solubility in seawater. Mar. Chem. 120, 4–13.

Baker, A.R., Jickells, T.D., 2006. Mineral particle size as a control on aerosol iron solubility. Geophys. Res. Lett. 33, 1–4.

Baker, E.T., Edmonds, H.N., Michael, P.J., Bach, W., Dick, H.J.B., Snow, J.E., Walker, S.L., Banerjee, N.R., Langmuir, C.H., 2004. Hydrothermal venting in magma deserts: The ultraslow-spreading Gakkel and Southwest Indian Ridges. Geochemistry, Geophys. Geosystems 5, 1–29.

Barbeau, K., Rue, E.L., Bruland, K.W., Butler, a, 2001. Photochemical cycling of iron in the surface ocean mediated by microbial iron(III)-binding ligands. Nature 413, 409–413.

Barbeau, K., Rue, E.L., Trick, C.G., Bruland, K.W., Butler, A., 2003. Photochemical reactivity of siderophores produced by marine heterotrophic bacteria and

cyanobacteria, based on characteristic Fe(III) binding groups. Limnol. Oceanogr. 48, 1069–1078.
Bartual, S.G., Otero, J.M., Garcia-Doval, C., Llamas-Saiz, A.L., Kahn, R., Fox, G.C., van Raaij, M.J., 2010. Structure of the bacteriophage T4 long tail fiber receptor-binding tip. Proc. Natl. Acad. Sci. U. S. A. 107, 20287–92.
Batchelli, S., Muller, F.L.L., Chang, K.C., Lee, C.L., 2010. Evidence for strong but dynamic iron-humic colloidal associations in humic-rich coastal waters. Environ. Sci. Technol. 44, 8485–8490.
Bauch, D., Cherniavskaia, E., Timokhov, L., 2016. Shelf basin exchange along the Siberian continental margin: Modification of Atlantic Water and Lower Halocline Water. Deep Sea Res. Part I 115, 188–198.
Bauch, D., van der Loeff, M.R., Andersen, N., Torres-Valdes, S., Bakker, K., Abrahamsen, E.P., 2011. Origin of freshwater and polynya water in the Arctic Ocean halocline in summer 2007. Prog. Oceanogr. 91, 482–495.
Baudoux, A.-C., Brussaard, C.P.D., 2005. Characterization of different viruses infecting the marine harmful algal bloom species Phaeocystis globosa. Virology 341, 80–90.
Baudoux, A.C., Brussaard, C.P.D., 2005. Characterization of different viruses infecting the marine harmful algal bloom species Phaeocystis globosa. Virology 341, 80–90.
Baudoux, A.C., Noordeloos, A.A.M., Veldhuis, M.J.W., Brussaard, C.P.D., 2006. Virally induced mortality of Phaeocystis globosa during two spring blooms in temperate coastal waters. Aquat. Microb. Ecol. 44, 207–217.
Baudoux, A.C., Veldhuis, M.J.W., Witte, H.J., Brussaard, C.P.D., 2007. Viruses as mortality agents of picophytoplankton in the deep chlorophyll maximum layer during IRONAGES III. Limnol. Oceanogr. 52, 2519–2529.
Beaulieu, S.E., Baker, E.T., German, C.R., 2015. Where are the undiscovered hydrothermal vents on oceanic spreading ridges? Deep. Res. Part II Top. Stud. Oceanogr. 121, 202–212.
Behrenfeld, M.J., Bale, A.J., Kolber, Z.S., Aiken, J., Falkowski, P.G., 1996. Confirmation of iron limitation of phytoplankton photosynthesis in the equatorial Pacific Ocean. Nature.
Behrenfeld, M.J., Worthington, K., Sherrell, R.M., Chavez, F.P., Strutton, P., McPhaden, M., Shea, D.M., 2006. Controls on tropical Pacific Ocean productivity revealed through nutrient stress diagnostics. Nature 442, 1025–8.
Bennett, S.A., Achterberg, E.P., Connelly, D.P., Statham, P.J., Fones, G.R., German, C.R., 2008. The distribution and stabilisation of dissolved Fe in deep-sea hydrothermal plumes. Earth Planet. Sci. Lett. 270, 157–167.
Bergeron, M., Tremblay, J.-É., 2014. Shifts in biological productivity inferred from nutrient drawdown in the southern Beaufort Sea (2003-2011) and northern Baffin Bay (1997-2011), Canadian Arctic. Geophys. Res. Lett. 41, 3979–3987.
Beşiktepe, Ş.T., Sur, H.İ., Özsoy, E., Latif, M.A., Oğuz, T., Ünlüata, Ü., 1994. The circulation and hydrography of the Marmara Sea. Prog. Oceanogr. 34, 285–334.
Bhatt, U.S., Walker, D.A., Walsh, J.E., Carmack, E.C., Frey, K.E., Meier, W.N., Moore, S.E., Parmentier, F.-J.W., Post, E., Romanovsky, V.E., Simpson, W.R., 2014. Implications of Arctic Sea Ice Decline for the Earth System. Annu. Rev. Environ. Resour. 39, 57–89.
Birchill, A.J., Milne, A., Woodward, E.M.S., Harris, C., Annett, A., Rusiecka, D., Achterberg, E.P., Gledhill, M., Ussher, S.J., Worsfold, P.J., Geibert, W., Lohan, M.C., 2017. Seasonal iron depletion in temperate shelf seas. Geophys. Res. Lett. 44, 8987–8996.
Blain, S., Bonnet, S., Guieu, C., 2008. Dissolved iron distribution in the tropical and sub tropical South Eastern Pacific. Biogeosciences 5, 269–280.

Bluhm, B.A., Kosobokova, K.N., Carmack, E.C., 2015. A tale of two basins: An integrated physical and biological perspective of the deep Arctic Ocean. Prog. Oceanogr. 139, 89–121.

Boiteau, R.M., Fitzsimmons, J.N., Repeta, D.J., Boyle, E.A., 2013. Detection of iron ligands in seawater and marine cyanobacteria cultures by high-performance liquid chromatography-inductively coupled plasma-mass spectrometry. Anal Chem 85, 4357–4362.

Boiteau, R.M., Mende, D.R., Hawco, N.J., McIlvin, M.R., Fitzsimmons, J.N., Saito, M.A., Sedwick, P.N., DeLong, E.F., Repeta, D.J., 2016. Siderophore-based microbial adaptations to iron scarcity across the eastern Pacific Ocean. Proc. Natl. Acad. Sci. 113, 14237–14242.

Bonini, M., Mazzarini, F., 2010. Mud volcanoes as potential indicators of regional stress and pressurized layer depth. Tectonophysics 494, 32–47.

Bonnain, C., Breitbart, M., Buck, K.N., 2016. The Ferrojan Horse Hypothesis: Iron-Virus Interactions in the Ocean. Front. Mar. Sci. 3, 1–11.

Bonnet, S., Guieu, C., 2006. Atmospheric forcing on the annual iron cycle in the western Mediterranean Sea: A 1-year survey. J. Geophys. Res. 111.

Boyd, P.W., Arrigo, K.R., Strzepek, R., Dijken, G.L. Van, van Dijken, G.L., 2012. Mapping phytoplankton iron utilization: Insights into Southern Ocean supply mechanisms. J. Geophys. Res. 117, 1–18.

Boyd, P.W., Ibisanmi, E., Sander, S.G., Hunter, K.A., Jackson, G.A., 2010. Remineralization of upper ocean particles: Implications for iron biogeochemistry. Limnol. Oceanogr. 55, 1271–1288.

Boyd, P.W., Jickells, T., Law, C.S., Blain, S., Boyle, E. a, Buesseler, K.O., Coale, K.H., Cullen, J.J., de Baar, H.J.W., Follows, M., Harvey, M., Lancelot, C., Levasseur, M., Owens, N.P.J., Pollard, R., Rivkin, R.B., Sarmiento, J., Schoemann, V., Smetacek, V., Takeda, S., Tsuda, A., Turner, S., Watson, A.J., 2007. Mesoscale iron enrichment experiments 1993-2005: synthesis and future directions. Science 315, 612–617.

Boyle, E.A., Edmond, J.M., Sholkovitz, E.R., 1977. The mechanism of iron removal in estuaries. Geochim. Cosmochim. Acta 41, 1313–1324.

Brand, L.E., 1991. Minimum iron requirements of marine phytoplankton and the implications for the biogeochemical control of new production. Limnol. Oceanogr. 36, 1756–1771.

Brand, L.E., 1991. Minimum iron requirements of marine phytoplankton and the implications for the biogeochemical control of new production. Limnol. Oceanogr. 36, 1756–1771.

Bratbak, G., Jacobsen, A., Heldal, M., Nagasaki, K., Thingstad, F., 1998. Virus production in Phaeocystis pouchetii and its relation to host cell growth and nutrition. Aquat. Microb. Ecol. 16, 1–9.

Breitbarth, E., Achterberg, E., Ardelan, M. V., Baker, A.R., Bucciarelli, E., Chever, F., Croot, P.L., Duggen, S., Gledhill, M., Hassellöv, M., Hassler, C., Hoffmann, L.J., Hunter, K.A., Hutchins, D.A., Ingri, J., Jickells, T., Lohan, M.C., Nielsdóttir, M.C., Sarthou, G., Schoemann, V., Trapp, J.M., Turner, D.R., Ye, Y., 2010. Iron biogeochemistry across marine systems–progress from the past decade. Biogeosciences 7, 1075–1097.

Bronk, D.A., 2002. Dynamics of DON. In: Hansell, D.A., Carlson, C.A. (Eds.), Biogeochemistry of Marine Dissolved Organic Matter. Academic Press, London, pp. 153–247.

Brown, M.T., Lippiatt, S.M., Lohan, M.C., Bruland, K.W., 2012. Trace metal distributions within a Sitka eddy in the northern Gulf of Alaska. Limnol. Oceanogr. 57, 503–518.

Browning, T.J., Achterberg, E.P., Rapp, I., Engel, A., Bertrand, E.M., Tagliabue, A., Moore, C.M., 2017. Nutrient co-limitation at the boundary of an oceanic gyre. Nature 551, 242–246.
Bruland, K.W., Middag, R., Lohan, M.C., 2014. Controls of Trace Metals in Seawater. In: Treatise on Geochemistry. Elsevier, pp. 19–51.
Brussaard, C.P.D., 2004a. Viral control of phytoplankton populations - a review. J. Eukaryot. Microbiol. 51, 125–138.
Brussaard, C.P.D., 2004b. Optimization of Procedures for Counting Viruses by Flow Cytometry. Appl. Environ. Microbiol. 70, 1506–1513.
Brussaard, C.P.D., Mari, X., Van Bleijswijk, J.D.L., Veldhuis, M.J.W., 2005. A mesocosm study of Phaeocystis globosa (Prymnesiophyceae) population dynamics: II. Significance for the microbial community. Harmful Algae 4, 875–893.
Brussaard, C.P.D., Martínez, J.M., 2008. Algal Bloom Viruses. Plant Viruses 2, 1–10.
Brussaard, C.P.D., Payet, J.P., Winter, C., Weinbauer, M.G., Wilhelm, D.W., Suttle, C.A., 2010. Quantification of aquatic viruses by flow cytometry. In: Manual of Aquatic Viral Ecology. ASLO, pp. 102–109.
Brussaard, C.P.D., Thyrhaug, R., Marie, D., Bratbak, G., 1999. Flow Cytometric Analyses of Viral Infection in Two Marine Phytoplankton Species, Micromonas Pusilla (Prasinophyceae) and Phaeocystis Pouchetii (Prymnesiophyceae). J. Phycol. 35, 941–948.
Brussaard, C.P.D., Wilhelm, S.W., Thingstad, T.F., Weinbauer, M.G., Bratbak, G., Heldal, M., Kimmance, S.A., Middelboe, M., Nagasaki, K., Paul, J.H., Schroeder, D.C., Suttle, C.A., Vaqué, D., Wommack, K.E., 2008. Global-scale processes with a nanoscale drive: the role of marine viruses. Isme J. 0, 1–4.
Buck, C.S., Landing, W.M., Resing, J.A., Measures, C.I., 2010. The solubility and deposition of aerosol Fe and other trace elements in the North Atlantic Ocean: Observations from the A16N CLIVAR/CO2 repeat hydrography section. Mar. Chem. 120, 57–70.
Buck, K.N., Gerringa, L.J.A., Rijkenberg, M.J.A., 2016. An Intercomparison of Dissolved Iron Speciation at the Bermuda Atlantic Time-series Study (BATS) Site: Results from GEOTRACES Crossover Station A. Front. Mar. Sci. 3, 262.
Buck, K.N., Lohan, M.C., Berger, C.J.M., Bruland, K.W., 2007. Dissolved iron speciation in two distinct river plumes and an estuary: Implications for riverine iron supply. Limnol. Oceanogr. 52, 843–855.
Buck, K.N., Moffett, J., Barbeau, K.A., Bundy, R.M., Kondo, Y., Wu, J., 2012. The organic complexation of iron and copper : an intercomparison of competitive ligand exchange – adsorptive cathodic stripping voltammetry (CLE-ACSV) techniques. Limnol. Oceanogr. Methods 10, 496–515.
Buck, K.N., Sohst, B., Sedwick, P.N., 2015. The organic complexation of dissolved iron along the U.S. GEOTRACES (GA03) North Atlantic Section. Deep. Res. Part II Top. Stud. Oceanogr. 116, 152–165.
Buffle, J., 1988. Complexation Reactions in Aquatic Systems; An Analytical Approach, 1st ed. Ellis Horwood, Chichester, UK.
Buffle, J., 1990. The analytical challenge posed by fulvic and humic compounds. Anal. Chim. Acta 232, 1–2.
Bullard, J.E., 2017. The distribution and biogeochemical importance of high-latitude dust in the Arctic and Southern Ocean-Antarctic regions. J. Geophys. Res. Atmos. 122, 3098–3103.
Bundy, R.M., Abdulla, H.A.N., Hatcher, P.G., Biller, D. V., Buck, K.N., Barbeau, K.A., 2015. Iron-binding ligands and humic substances in the San Francisco Bay estuary and estuarine-influenced shelf regions of coastal California. Mar. Chem. 173, 183–

194.
Bundy, R.M., Boiteau, R.M., McLean, C., Turk-Kubo, K.A., McIlvin, M.R., Saito, M.A., Van Mooy, B.A.S., Repeta, D.J., Mooy, B.A. Van, Repeta, D.J., Van Mooy, B.A.S., Repeta, D.J., 2018. Distinct Siderophores Contribute to Iron Cycling in the Mesopelagic at Station ALOHA. Front. Mar. Sci. 5, 1–15.
Bundy, R.M., Jiang, M., Carter, M., Barbeau, K.A., 2016. Iron-Binding Ligands in the Southern California Current System: Mechanistic Studies. Front. Mar. Sci. 3, 1–17.
Butler, A., 2005. Marine siderophores and microbial iron mobilization. Biometals 18, 369–374.
Calbet, A., Landry, M.R., 2004. Phytoplankton growth, microzooplankton grazing, and carbon cycling in marine systems. Limnol. Oceanogr. 49, 51–57.
Caprara, S., Buck, K.N., Gerringa, L., Rijkenberg, M., Monticelli, D., 2016. A compilation of iron speciation data for open oceanic waters. Front. Mar. Sci. 3, 221.
Carlson, C.A., 2002. Production and Removal Processes. In: Hansell, D.A., Carlson, C.A. (Eds.), Biogeochemistry of Marine Dissolved Organic Matter. Academic Press, London, pp. 91–151.
Carmack, E.C., Yamamoto-Kawai, M., Haine, T.W.N., Bacon, S., Bluhm, B.A., Lique, C., Melling, H., Polyakov, I. V., Straneo, F., Timmermans, M.L., Williams, W.J., 2016. Freshwater and its role in the Arctic Marine System: Sources, disposition, storage, export, and physical and biogeochemical consequences in the Arctic and global oceans. J. Geophys. Res. G Biogeosciences 121, 675–717.
Coble, P.G., 2007. Marine optical biogeochemistry: The chemistry of ocean color. Chem. Rev. 107, 402–418.
Coble, P.G., Del Castillo, C.E., Avril, B., 1998. Distribution and optical properties of CDOM in the Arabian Sea during the 1995 Southwest Monsoon. Deep Sea Res. Part II 45, 2195–2223.
Codispoti, L.A., Kelly, V., Thessen, A., Matrai, P., Suttles, S., Hill, V., Steele, M., Light, B., 2013. Synthesis of primary production in the Arctic Ocean: III. Nitrate and phosphate based estimates of net community production. Prog. Oceanogr. 110, 126–150.
Cooper, L.W., Whitledge, T.E., Grebmeier, J.M., Weingartner, T., 1997. The nutrient, salinity, and stable oxygen isotope composition of Bering and Chukchi Sea waters. J. Geophys. Res. 102, 12563–12573.
Cottrell, M.T., Suttle, C. a., Aransas, P., 1995. Dynamics of lytic virus infecting the photosynthetic marine picoflagellate Micromonas pusilla. Limnol. Oceanogr. 40, 730–739.
Croot, P.L., Johansson, M., 2000. Determination of iron speciation by cathodic stripping voltammetry in seawater using the competing ligand 2-(2- thiazolylazo)-p-cresol (TAC). Electroanalysis 12, 565–576.
Croot, P.L., Streu, P., Baker, A.R., 2004. Short residence time for iron in surface seawater impacted by atmospheric dry deposition from Saharan dust events. Geophys. Res. Lett. 31.
Cuttler, G., Andersson, P.S., Codispoti, L.A., Croot, P.L., Francois, R., Lohan, M.C., Obata, H., Rutgers van der Loeff, M., 2010. Sampling and sample-handling protocols for GEOTRACES cruises 1–238.
Dai, M., Martin, J.M., Cauwet, G., 1995. The Significant Role of Colloids in the Transport and Transformation of Organic-Carbon and Associated Trace-Metals (Cd, Cu and Ni) in the Rhone Delta (France). Mar. Chem. 51, 159–175.
de Baar, H.J.W., Boyd, P.W., Coale, K.H., Landry, M.R., Tsuda, A., Assmy, P., Bakker, D.C.E., Bozec, Y., Barber, R.T., Brzezinski, M.A., Buesseler, K.O., Boye, M., Croot, P.L., Gervais, F., Gorbunov, M.Y., Harrison, P.J., Hiscock, W.T., Laan, P., Lancelot,

C., Law, C.S., Nojiri, Y., Oijen, T. Van, Riebesell, U., Rijkenberg, M.J.A., Waite, A.M., Wong, C., de Baar, H.J.W., 2005. Synthesis of iron fertilization experiments: From the Iron Age in the Age of Enlightenment. J. Geophys. Res. 110, 1–24.

de Baar, H.J.W., Buma, A.G.J., Nolting, R.F., Cadee, G.C., Jacques, G., Treguer, P.J., 1990. On iron limitation of the Southern Ocean : experimental observations in the Weddell and Scotia Seas. Mar. Ecol. Prog. Ser. 65, 105–122.

de Baar, H.J.W., de Jong, J.T.M., Bakker, D.C.E., Löscher, B.M., Veth, C., Bathmann, U., Smetacek, V., 1995. Importance of iron for plankton blooms and carbon dioxide drawdown in the Southern Ocean. Nature 373, 412–415.

de Baar, H.J.W., La Roche, J., 2003. Trace Metals in the Oceans: Evolution, Biology and Global Change. In: Wefer, G., Lamy, F., Mantoura, F. (Eds.), Marine Science Frontiers for Europe. Springer Berlin Heidelberg, Berlin, Heidelberg, pp. 79–105.

de Baar, H.J.W., Timmermans, K.R., Laan, P., De Porto, H.H., Ober, S., Blom, J.J., Bakker, M.C., Schilling, J., Sarthou, G., Smit, M.G., Klunder, M., Baar, H.J.W. De, Timmermans, K.R., Laan, P., Porto, H.H. De, Ober, S., 2008. Titan: A new facility for ultraclean sampling of trace elements and isotopes in the deep oceans in the international Geotraces program. Mar. Chem. 111, 4–21.

de Baar, H.J.W., van Heuven, S.M.A.C., Middag, R., 2017. Ocean Biochemical Cycling and Trace Elements. In: White, W.M. (Ed.), Encyclopedia of Geochemistry: A Comprehensive Reference Source on the Chemistry of the Earth. Springer International Publishing, Cham, pp. 1–21.

de Jong, J., Schoemann, V., Lannuzel, D., Croot, P., de Baar, H., Tison, J., Jong, J. De, Schoemann, V., Lannuzel, D., Croot, P., Baar, H. De, Tison, J., 2012. Natural iron fertilization of the Atlantic sector of the Southern Ocean by continental shelf sources of the Antarctic Peninsula. J. Geophys. Res. 117.

Dulaquais, G., Waeles, M., Gerringa, L.J.A., Middag, R., Rijkenberg, M.J.A., Riso, R., 2018. The biogeochemistry of electroactive humic substances and its connection to iron chemistry in the North East Atlantic and the Western Mediterranean Sea. J. Geophys. Res. Ocean.

Edmonds, H.N., Michael, P.J., Baker, E.T., Connelly, D.P., Snow, J.E., Langmuir, C.H., Dick, H.J.B., Mühe, R., German, C.R., Graham, D.W., 2003. Discovery of abundant hydrothermal venting on the ultraslow-spreading Gakkel ridge in the Arctic Ocean. Nature 421, 252–256.

Fernández-Méndez, M., Katlein, C., Rabe, B., Nicolaus, M., Peeken, I., Bakker, K., Flores, H., Boetius, A., 2015. Photosynthetic production in the central Arctic Ocean during the record sea-ice minimum in 2012. Biogeosciences 12, 3525–3549.

Field, C.B., Behrenfeld, M.J., Randerson, J.T., Falkowski, P.G., 1998. Primary Production of the Biosphere : Integrating Terrestrial and Oceanic Components. Science (80-.). 281, 237–240.

Fishwick, M.P., Sedwick, P.N., Lohan, M.C., Worsfold, P.J., Buck, K.N., Church, T.M., Ussher, S.J., 2014. Global Biogeochemical Cycles on the dissolution of aerosol iron.

Fitzsimmons, J.N., Boyle, E.A., Jenkins, W.J., 2014. Distal transport of dissolved hydrothermal iron in the deep South Pacific Ocean. Proc. Natl. Acad. Sci. 111, 16654–16661.

Fitzsimmons, J.N., Bundy, R.M., Al-Subiai, S.N., Barbeau, K.A., Boyle, E.A., 2015. The composition of dissolved iron in the dusty surface ocean: An exploration using size-fractionated iron-binding ligands. Mar. Chem. 173, 125–135.

Fitzsimmons, J.N., John, S.G., Marsay, C.M., Hoffman, C.L., Nicholas, S.L., Toner, B.M., German, C.R., Sherrell, R.M., 2017. Iron persistence in a distal hydrothermal plume supported by dissolved–particulate exchange. Nat. Geosci. 10, 195–201.

Fortier, M., Fortier, L., Michel, C., Legendre, L., 2002. Climatic and biological forcing of

the vertical flux of biogenic particles under seasonal Arctic sea ice. Mar. Ecol. Prog. Ser. 225, 1–16.
Francis, J., Madinaveitia, J., Macturk, H.M., Snow, G.A., 1949. Isolation from Acid-Fast Bacteria of a Growth-Factor for Mycobacterium johnei and of a Precursor of Phthiocol. Nature 163, 365–366.
Frey, K.E., McClelland, J.W., 2009. Impacts of permafrost degradation on arctic river biogeochemistry. Hydrol. Process. 23, 169–182.
Garg, S., Rose, A.L., Waite, T.D., 2007. Superoxide-mediated reduction of organically complexed iron(III): Impact of pH and competing cations (Ca2+). Geochim. Cosmochim. Acta 71, 5620–5634.
Gascard, J.-C., 1973. Vertical motions in a region of deep water formation. In: Deep Sea Research and Oceanographic Abstracts. Elsevier, pp. 1011–1027.
Gauglitz, J.M., Zhou, H., Butler, A., 2012. A suite of citrate-derived siderophores from a marine Vibrio species isolated following the Deepwater Horizon oil spill. J. Inorg. Biochem. 107, 90–95.
Geider, R.J., La Roche, J., 1994. The role of iron in phytoplankton photosynthesis, and the potential for iron-limitation of primary productivity in the sea. Photosynth. Res. 39, 275–301.
Geider, R.J., La Roche, J., Greene, R.M., Olaizola, M., 1993. Response of the photosynthetic apparatus of Phaeodactylum Tricornutum (Bacillariophyceae) to nitrate, phosphate, or iron starvation. J. Phycol. 29, 755–766.
Genty, B., Briantais, J.-M., Baker, N.R., 1989. The relationship between the quantum yield of photosynthetic electron transport and quenching of chlorophyll fluorescence. Biochim. Biophys. Acta 990, 87–92.
Gerringa, L.J.A., Rijkenberg, M.J.A., Bown, J., Margolin, A.R., Laan, P., de Baar, H.J.W., 2016. Fe-Binding Dissolved Organic Ligands in the Oxic and Suboxic Waters of the Black Sea. Front. Mar. Sci. 3, 1–16.
Gerringa, L.J.A., Rijkenberg, M.J.A., Schoemann, V., Laan, P., de Baar, H.J.W., 2015. Organic complexation of iron in the West Atlantic Ocean. Mar. Chem. 177, 434–446.
Gerringa, L.J.A., Rijkenberg, M.J.A., Thuróczy, C.E., Maas, L.R.M., 2014. A critical look at the calculation of the binding characteristics and concentration of iron complexing ligands in seawater with suggested improvements. Environ. Chem. 11, 114–136.
Gerringa, L.J.A., Rijkenberg, M.J.A., Wolterbeek, H.T., Verburg, T.G., Boye, M., de Baar, H.J.W., 2007. Kinetic study reveals weak Fe-binding ligand, which affects the solubility of Fe in the Scheldt estuary. Mar. Chem. 103, 30–45.
Gerringa, L.J.A., Slagter, H.A., Bown, J., van Haren, H., Laan, P., de Baar, H.J.W., Rijkenberg, M.J.A., 2017. Dissolved Fe and Fe-binding organic ligands in the Mediterranean Sea - GEOTRACES G04. Mar. Chem. 194, 100–113.
Gerringa, L.J.A., Veldhuis, M.J.W., Timmermans, K.R., Sarthou, G., de Baar, H.J.W., 2006. Co-variance of dissolved Fe-binding ligands with phytoplankton characteristics in the Canary Basin. Mar. Chem. 102, 276–290.
Gledhill, M., Buck, K.N., 2012. The organic complexation of iron in the marine environment: a review. Front. Microbiol. 3, 69.
Gledhill, M., Gerringa, L.J.A., 2017. The Effect of Metal Concentration on the Parameters Derived from Complexometric Titrations of Trace Elements in Seawater—A Model Study. Front. Mar. Sci. 4, 254.
Gledhill, M., McCormack, P., Ussher, S., Achterberg, E.P., Mantoura, R.F.C., Worsfold, P.J., 2004. Production of siderophore type chelates by mixed bacterioplankton populations in nutrient enriched seawater incubations. Mar. Chem. 88, 75–83.
Gledhill, M., van den Berg, C.M.G., 1994. Determination of complexation of iron(III) with

natural organic complexing ligands in seawater using cathodic stripping voltammetry. Mar. Chem. 47, 41–54.
Gobler, C.J., Hutchins, D.A., Fisher, N.S., 1997. Release and bioavailability of C, N, P, Se, and Fe following viral lysis of a marine chrysophyte. Limnol. Oceanogr. 42, 1492–1504.
González, A.G., Santana-Casiano, J.M., González-Dávila, M., Pérez-Almeida, N., Suárez De Tangil, M., 2014. Effect of Dunaliella tertiolecta organic exudates on the Fe(II) oxidation kinetics in seawater. Environ. Sci. Technol. 48, 7933–7941.
Gordienko, P.A., Laktionov, A.F., 1969. Circulation and physics of the Arctic basin waters. In: Gordon, A.L., Baker, F.W.G. (Eds.), Oceanography: Annals of The International Geophysical Year, Volume 46. Pergamon Press, London, pp. 94–112.
Grasshoff, K., 1983. Determination of nitrate. In: Grasshoff, K., Erhardt, M., Kremling, K. (Eds.), Methods of Seawater Analysis. Verlag Chemie, pp. 143–187.
Gregor, D.J., Loeng, H., Barrie, L., 1998. The Influence of Physical and Chemical Processes on Contaminant Transport into and within the Arctic, Arctic Monitoring and Assessment Report: Arctic Pollution Issues.
Guieu, C., Chester, R., Nimmo, M., Martin, J.M., Guerzoni, S., Nicolas, E., Mateu, J., Keyse, S., 1997. Atmospheric input of dissolved and particulate metals to the northwestern Mediterranean. Deep. Res. Part II Top. Stud. Oceanogr. 44, 655–674.
Guieu, C., Dulac, F., Desboeufs, K., Wagener, T., Pulido-Villena, E., Grisoni, J.M., Louis, F., Ridame, C., Blain, S., Brunet, C., Bon Nguyen, E., Tran, S., Labiadh, M., Dominici, J.M., 2010a. Large clean mesocosms and simulated dust deposition: a new methodology to investigate responses of marine oligotrophic ecosystems to atmospheric inputs. Biogeosciences 7, 2765–2784.
Guieu, C., Loÿe-Pilot, M.D., Benyahya, L., Dufour, A., 2010b. Spatial variability of atmospheric fluxes of metals (Al, Fe, Cd, Zn and Pb) and phosphorus over the whole Mediterranean from a one-year monitoring experiment: Biogeochemical implications. Mar. Chem. 120, 164–178.
Guieu, C., Martin, J.M., Thomas, A.J., Elbaz-Poulichet, F., 1991. Atmospheric versus river inputs of metals to the Gulf of Lions. Total concentrations, partitioning and fluxes. Mar. Pollut. Bull. 22, 176–183.
Haas, C., Pfaffling, A., Hendricks, S., Rabenstein, L., Etienne, J.L., Rigor, I., 2008. Reduced ice thickness in Arctic Transpolar Drift favors rapid ice retreat. Geophys. Res. Lett. 35, 1–5.
Hassler, C.S., Alasonati, E., Mancuso Nichols, C.A., Slaveykova, V.I., 2011a. Exopolysaccharides produced by bacteria isolated from the pelagic Southern Ocean — Role in Fe binding, chemical reactivity, and bioavailability. Mar. Chem. 123, 88–98.
Hassler, C.S., Schoemann, V., Nichols, C.M., Butler, E.C. V, Boyd, P.W., 2011b. Saccharides enhance iron bioavailability to Southern Ocean phytoplankton. Proc. Natl. Acad. Sci. U. S. A. 108, 1076–81.
Hassler, C.S., van den Berg, C.M.G., Boyd, P.W., 2017. Toward a Regional Classification to Provide a More Inclusive Examination of the Ocean Biogeochemistry of Iron-Binding Ligands. Front. Mar. Sci. 4, 19.
Hatta, M., Measures, C.I., Wu, J., Roshan, S., Fitzsimmons, J.N., Sedwick, P., Morton, P., 2015. An overview of dissolved Fe and Mn distributions during the 2010-2011 U.S. GEOTRACES north Atlantic cruises: GEOTRACES GA03. Deep. Res. Part II Top. Stud. Oceanogr. 116, 117–129.
Hawkes, J.A., Connelly, D.P., Gledhill, M., Achterberg, E.P., 2013. The stabilisation and transportation of dissolved iron from high temperature hydrothermal vent systems. Earth Planet. Sci. Lett. 375, 280–290.

Heimbürger, L.E., Migon, C., Losno, R., Miquel, J.C., Thibodeau, B., Stabholz, M., Dufour, A., Leblond, N., 2014. Vertical export flux of metals in the Mediterranean Sea. Deep. Res. Part I Oceanogr. Res. Pap. 87, 14–23.

Helms, J.R., Stubbins, A., Ritchie, J.D., Minor, E.C., Kieber, D.J., Mopper, K., 2008. Absorption spectral slopes and slope ratios as indicators of molecular weight, source, and photobleaching of chromophoric dissolved organic matter. Limonology Oceanogr. 53, 955–969.

Hirst, C., Andersson, P.S., Shaw, S., Burke, I.T., Kutscher, L., Murphy, M.J., Maximov, T., Pokrovsky, O.S., Mörth, C.M., Porcelli, D., 2017. Characterisation of Fe-bearing particles and colloids in the Lena River basin, NE Russia. Geochim. Cosmochim. Acta 213, 553–573.

Hofmann, T., Hanlon, A.R.M., Taylor, J.D., Ball, A.S., Osborn, A.M., Underwood, G.J.C., 2009. Dynamics and compositional changes in extracellular carbohydrates in estuarine sediments during degradation. Mar. Ecol. Prog. Ser. 379, 45–58.

Hogle, S.L., Barbeau, K.A., Gledhill, M., 2014. Heme in the marine environment: from cells to the iron cycle. Metallomics 6, 1107–1120.

Hölemann, J.A., Schirmacher, M., Kassens, H., Prange, A., 1999. Geochemistry of surficial and ice-rafted sediments from the Laptev Sea (Siberia). Estuar. Coast. Shelf Sci. 49, 45–59.

Hopkinson, B.M., Barbeau, K.A., 2007. Organic and redox speciation of iron in the eastern tropical North Pacific suboxic zone. Mar. Chem. 106, 2–17.

Hopkinson, B.M., Morel, F.M., Franc, B.M.H.Æ., Morel, M.M., 2009. The role of siderophores in iron acquisition by photosynthetic marine microorganisms. Biometals 22, 659–669.

Hudson, R.J.M., Rue, E.L., Bruland, K.W., 2003. Modeling complexometric titrations of natural water samples. Environ. Sci. Technol. 37, 1553–1562.

Hutchins, D.A., Wang, W.-X., Fisher, N.S., 1995. Copepod Grazing and the Biogeochemical Fate of Diatom Iron. Limnol. Oceanogr. 40, 989–994.

Ibisanmi, E., Sander, S.G., Boyd, P.W., Bowie, A.R., Hunter, K.A., 2011. Vertical distributions of iron-(III) complexing ligands in the Southern Ocean. Deep Sea Res. Part II Top. Stud. Oceanogr. 58, 2113–2125.

IOC, S., 2010. The international thermodynamic equation of seawater—2010: calculation and use of thermodynamic properties. Intergovernmental Oceanographic Commission, Manuals and Guides No. 56. In: Manual and Guides. UNESCO.

IPCC, 2013. Summary for Policymakers. In: Stocker, T.F., Qin, D., Plattner, G.-K., Tignor, M., Allen, S.K., Boschung, J., Nauels, A., Xia, Y., Bex, V., Midgley, P.M. (Eds.), Climate Change 2013: The Physical Science Basis. Contribution of Working Group I to the Fifth Assessment Report of the Intergovernmental Panel on Climate Change. Cambridge University Press, Cambridge, United Kingdom and New York, NY, USA, pp. 1–30.

IPCC, 2014. Climate Change 2014: Synthesis Report. Contribution of Working Groups I, II and III to the Fifth Assessment Report of the Intergovernmental Panel on Climate Change. IPCC, Geneva, Switzerland.

Jiao, N., Herndl, G.J., Hansell, D.A., Benner, R., Kattner, G., Wilhelm, S.W., Kirchman, D.L., Weinbauer, M.G., Luo, T., Chen, F., Azam, F., 2010. Microbial production of recalcitrant dissolved organic matter: Long-term carbon storage in the global ocean. Nat. Rev. Microbiol. 8, 593–599.

Johansen, A.M., Siefert, R.L., Hoffmann, M.R., 2000. Chemical composition of aerosols collected over the tropical North Atlantic Ocean. J. Geophys. Res. 105, 15277–15312.

Johnson, K.S., Boyle, E., Bruland, K., Coale, K., Measures, C., Moffett, J., Aguilar-Islas,

A., Barbeau, K., Bergquist, B., Bowie, A., Buck, K., Cai, Y., Chase, Z., Cullen, J., Doi, T., Elrod, V., Fitzwater, S., Gordon, M., King, A., Laan, P., Laglera-Baquer, L., Landing, W., Lohan, M., Mendez, J., Milne, A., Obata, H., Ossiander, L., Plant, J., Sarthou, G., Sedwick, P., Smith, G.J., Sohst, B., Tanner, S., Van den Berg, S., Wu, J., 2007. Developing standards for dissolved iron in seawater. Eos (Washington. DC). 88, 131–132.

Jones, M.E., Beckler, J.S., Taillefert, M., 2011. The flux of soluble organic-iron(III) complexes from sediments represents a source of stable iron(III) to estuarine waters and to the continental shelf. Limnol. Oceanogr. 56, 1811–1823.

Journet, E., Desboeufs, K. V, Caquineau, S., Colin, J.-L., 2008. Mineralogy as a critical factor of dust iron solubility. Geophys. Res. Lett. 35, n/a-n/a.

Kalle, K., 1937. Meereskundliche chemische Untersuchungen mit Hilfe des Zeisschen Pulfrich Photometers. Ann. Hydrogr., Berl. 65, 276.

Kalle, K., 1949. Fluoreszenz und Gelbstoff im Bottnischen und Finnischen Meerbusen. Dtsch. Hydrogr. Zeitschrift 2, 117–124.

Kessner, D., Chambers, M., Burke, R., Agus, D., Mallick, P., 2008. ProteoWizard: Open source software for rapid proteomics tools development. Bioinformatics 24, 2534–2536.

King, A.L., Buck, K.N., Barbeau, K.A., 2012. Quasi-Lagrangian drifter studies of iron speciation and cycling off Point Conception, California. Mar. Chem. 128–129, 1–12.

Kleint, C., Hawkes, J.A., Sander, S.G., Koschinsky, A., 2016. Voltammetric Investigation of Hydrothermal Iron Speciation. Front. Mar. Sci. 3, 1–11.

Klunder, M.B., Bauch, D., Laan, P., de Baar, H.J.W., van Heuven, S., Ober, S., 2012a. Dissolved iron in the Arctic shelf seas and surface waters of the central Arctic Ocean: Impact of Arctic river water and ice-melt. J. Geophys. Res. 117.

Klunder, M.B., Laan, P., Middag, R., de Baar, H.J.W., Bakker, K., 2012b. Dissolved iron in the Arctic Ocean: Important role of hydrothermal sources, shelf input and scavenging removal. J. Geophys. Res. 117, C04014.

Klunder, M.B., Laan, P., Middag, R., De Baar, H.J.W., van Ooijen, J.C., Baar, H.J.W. De, Ooijen, J.C. Van, 2011. Dissolved iron in the Southern Ocean (Atlantic sector). Deep Sea Res. Part II 58, 2678–2694.

Koron, N., Ogrinc, N., Metzger, E., Riedel, B., Faganeli, J., 2015. The impact of induced redox transitions on nutrient diagenesis in coastal marine sediments (Gulf of Trieste, northern Adriatic Sea). J. Soils Sediments 15, 2443–2452.

Korte, L.F., Brummer, G.J.A., Van Der Does, M., Guerreiro, C. V., Hennekam, R., Van Hateren, J.A., Jong, Di., Munday, C.I., Schouten, S., Stuut, J.B.W., 2017. Downward particle fluxes of biogenic matter and Saharan dust across the equatorial North Atlantic. Atmos. Chem. Phys. 17, 6023–6040.

Kustka, A.B., Shaked, Y., Milligan, A.J., King, D.W., Morel, F.M.M., 2005. Extracellular production of superoxide by marine diatoms: Contrasting effects on iron redox chemistry and bioavailability. Limnol. Oceanogr. 50, 1172–1180.

Kwok, R., Cunningham, G.F., Wensnahan, M., Rigor, I., Zwally, H.J., Yi, D., 2009. Thinning and volume loss of the Arctic Ocean sea ice cover: 2003-2008. J. Geophys. Res. Ocean. 114, 2003–2008.

Laglera, L.M., Battaglia, G., van den Berg, C.M.G., 2007. Determination of humic substances in natural waters by cathodic stripping voltammetry of their complexes with iron. Anal. Chim. Acta 599, 58–66.

Laglera, L.M., Battaglia, G., van den Berg, C.M.G., 2011. Effect of humic substances on the iron speciation in natural waters by CLE/CSV. Mar. Chem. 127, 134–143.

Laglera, L.M., Downes, J., Santos-Echeandia, J., Santos-Echeandía, J., 2013. Comparison and combined use of linear and non-linear fitting for the estimation of complexing

parameters from metal titrations of estuarine samples by CLE/AdCSV. Mar. Chem. 155, 102–112.
Laglera, L.M., Filella, M., 2015. The relevance of ligand exchange kinetics in the measurement of iron speciation by CLE–AdCSV in seawater. Mar. Chem. 173, 100–113.
Laglera, L.M., Santos-Echeandía, J., Caprara, S., Monticelli, D., Santos-Echeandia, J., Caprara, S., Monticelli, D., Santos-Echeandía, J., Caprara, S., Monticelli, D., 2013. Quantification of iron in seawater at the low picomolar range based on optimization of bromate/ammonia/dihydroxynaphtalene system by catalytic adsorptive cathodic stripping voltammetry. Anal. Chem. 85, 2486–2492.
Laglera, L.M., Tovar-Sánchez, A., Iversen, M.H., González, H.E., Naik, H., Mangesh, G., Assmy, P., Klaas, C., Mazzocchi, M.G., Montresor, M., Naqvi, S.W.A., Smetacek, V., Wolf-Gladrow, D.A., 2017. Iron partitioning during LOHAFEX: Copepod grazing as a major driver for iron recycling in the Southern Ocean. Mar. Chem.
Laglera, L.M., van den Berg, C.M.G., 2009. Evidence for geochemical control of iron by humic substances in seawater. Limnol. Oceanogr. 54, 610–619.
Lam, P.J., Bishop, J.K.B., Henning, C.C., Marcus, M.A., Waychunas, G.A., Fung, I.Y., 2006. Wintertime phytoplankton bloom in the subarctic Pacific supported by continental margin iron. Global Biogeochem. Cycles 20, n/a-n/a.
Langmuir, I., 1916. The Constitution and Fundamental Properties of Solids and Liquids. Part I. Solids. J. Am. Chem. Soc. 252, 2221–2295.
Lannuzel, D., Bowie, A.R., Remenyi, T., Lam, P., Townsend, A., Ibisanmi, E., Butler, E., Wagener, T., Schoemann, V., 2011. Distributions of dissolved and particulate iron in the sub-Antarctic and Polar Frontal Southern Ocean (Australian sector). Deep Sea Res. Part II Top. Stud. Oceanogr. 58, 2094–2112.
Laukert, G., Frank, M., Bauch, D., Hathorne, E.C., Rabe, B., von Appen, W.-J., Wegner, C., Zieringer, M., Kassens, H., 2017. Ocean circulation and freshwater pathways in the Arctic Mediterranean based on a combined Nd isotope, REE and oxygen isotope section across Fram Strait. Geochim. Cosmochim. Acta 202, 285–309.
Lazar, C.S., John Parkes, R., Cragg, B.A., L'Haridon, S., Toffin, L., 2012. Methanogenic activity and diversity in the centre of the Amsterdam Mud Volcano, Eastern Mediterranean Sea. FEMS Microbiol. Ecol. 81, 243–254.
Liu, X., Millero, F.J., 2002. The solubility of iron in seawater. Mar. Chem. 77, 43–54.
Lønborg, C., Middelboe, M., Brussaard, C.P.D., 2013. Viral lysis of Micromonas pusilla: Impacts on dissolved organic matter production and composition. Biogeochemistry 116, 231–240.
Lupton, J., Ronde, C. de, Sprovieri, M., Baker, E.T., Bruno, P.P., Italiano, F., Walker, S., Faure, K., Leybourne, M., Britten, K., Greene, R., 2011. Active hydrothermal discharge on the submarine Aeolian Arc. J. Geophys. Res. Solid Earth 116.
Maat, D.S., Brussaard, C.P.D., 2016. Both phosphorus and nitrogen limitation constrain viral proliferation in marine phytoplankton. Aquat. Microb. Ecol.
Maat, D.S., Crawfurd, K.J., Timmermans, K.R., Brussaard, C.P.D., 2014. Elevated CO2 and phosphate limitation favor Micromonas pusilla through stimulated growth and reduced viral impact. Appl. Environ. Microbiol. 80, 3119–27.
Maat, D.S., Van Bleijswijk, J.D.L., Witte, H.J., Brussaard, C.P.D., 2016. Virus production in phosphorus limited Micromonas pusilla stimulated by a supply of naturally low concentrations of different phosphorus sources, far into the lytic cycle. FEMS Microbiol. Ecol. fiw136.
Macdonald, R.W., Harner, T., Fyfe, J., 2005. Recent climate change in the Arctic and its impact on contaminant pathways and interpretation of temporal trend data. Sci. Total Environ. 342, 5–86.

Mahmood, A., Abualhaija, M.M., van den Berg, C.M.G., Sander, S.G., 2015. Organic speciation of dissolved iron in estuarine and coastal waters at multiple analytical windows. Mar. Chem. 177, 706–719.
Maldonado, M.T., Strzepek, R.F., Sander, S., Boyd, P.W., 2005. Acquisition of iron bound to strong organic complexes, with different Fe binding groups and photochemical reactivities, by plankton communities in Fe-limited subantarctic waters. Global Biogeochem. Cycles 19, n/a-n/a.
Mari, X., Rassoulzadegan, F., Brussaard, C.P.D., Wassmann, P., 2005. Dynamics of transparent exopolymeric particles (TEP) production by Phaeocystis globosa under N- or P-limitation: A controlling factor of the retention/export balance. Harmful Algae 4, 895–914.
Martin, J.H., Fitzwater, S.E., 1988. Iron deficiency limits phytoplankton growth in the north-east Pacific subarctic. Nature 331, 341–343.
Martin, J.H., Fitzwater, S.E., Gordon, R.M., 1990. Iron deficiency limits phytoplankton growth in Antarctic waters. Global Biogeochem. Cycles 4, 5–12.
Martínez Martínez, J., Boere, A., Gilg, I., van Lent, J.W.M., Witte, H.J., van Bleijswijk, J.D.L., Brussaard, C.P.D., 2015. New lipid envelope-containing dsDNA virus isolates infecting Micromonas pusilla reveal a separate phylogenetic group. Aquat. Microb. Ecol. 74, 17–28.
Martínez Martínez, J., Swan, B.K., Wilson, W.H., 2014. Marine viruses, a genetic reservoir revealed by targeted viromics. ISME J. 8, 1079–1088.
Mascle, J., Mary, F., Praeg, D., Brosolo, L., Camera, L., Ceramicola, S., Dupré, S., 2014. Distribution and geological control of mud volcanoes and other fluid/free gas features in the Mediterranean Sea and nearby Gulf of Cadiz. Geo-Marine Lett. 34, 89–110.
Maslanik, J., Stroeve, J., Fowler, C., Emery, W., 2011. Distribution and trends in Arctic sea ice age through spring 2011. Geophys. Res. Lett. 38, 2–7.
Mawji, E., Gledhill, M., Milton, J.A., Tarran, G.A., Ussher, S., Thompson, A., Wolff, G.A., Worsfold, P.J., Achterberg, E.P., 2008. Hydroxamate siderophores: occurrence and importance in the Atlantic Ocean. Environ. Sci. Technol. 42, 8675–8680.
Mawji, E., Gledhill, M., Milton, J.A., Zubkov, M. V, Thompson, A., Wolff, G.A., Achterberg, E.P., 2011. Production of siderophore type chelates in Atlantic Ocean waters enriched with different carbon and nitrogen sources. Mar. Chem. 124, 90–99.
Mawji, E., Gledhill, M., Worsfold, P.J., Achterberg, E.P., 2008. Collision-induced dissociation of three groups of hydroxamate siderophores: ferrioxamines, ferrichromes and coprogens/fusigens. Rapid Commun. Mass Spectrom. 22, 2195–2202.
McCormack, P., Worsfold, P.J., Gledhill, M., 2003. Separation and Detection of Siderophores Produced by Marine Bacterioplankton Using High-Performance Liquid Chromatography with Electrospray Ionization Mass Spectrometry. Anal Chem 75, 2647–2652.
Mengel, K., 1994. Iron availability in plant tissues - iron chlorosis on calcareous soils. Plant Soil 165, 275–283.
Menzel Barraqueta, J., Klar, J.K., Gledhill, M., Schlosser, C., Shelley, R., Wenzel, B., Sarthou, G., Achterberg, E.P., 2018. Atmospheric aerosol deposition fluxes over the Atlantic Ocean : A GEOTRACES case study. Biogeosciences Discuss. 1–25.
Middag, R., de Baar, H.J.W., Laan, P., Klunder, M.B., 2011. Fluvial and hydrothermal input of manganese into the Arctic Ocean. Geochim. Cosmochim. Acta 75, 2393–2408.
Middag, R., Séférian, R., Conway, T.M., John, S.G., Bruland, K.W., de Baar, H.J.W., 2015. Intercomparison of dissolved trace elements at the Bermuda Atlantic Time Series

station. Mar. Chem. 177, 476–489.
Millero, F.J., 1998. Solubility of Fe (III) in seawater. Earth Planet. Sci. Lett. 154, 323–329.
Millot, C., 1999. Circulation in the Western Mediterranean Sea. J. Mar. Syst. 20, 423–442.
Millot, C., Taupier-Letage, I., 2005. Circulation in the Mediterranean Sea. pp. 29–66.
Mills, M.M., Brown, Z.W., Lowry, K.E., van Dijken, G.L., Becker, S., Pal, S., Benitez-Nelson, C.R., Downer, M.M., Strong, A.L., Swift, J.H., Pickart, R.S., Arrigo, K.R., 2015. Impacts of low phytoplankton NO3-: PO43- utilization ratios over the Chukchi Shelf, Arctic Ocean. Deep. Res. Part II Top. Stud. Oceanogr. 118, 105–121.
Mioni, C.E., Poorvin, L., Wilhelm, S.W., 2005. Virus and siderophore-mediated transfer of available Fe between heterotrophic bacteria: characterization using an Fe-specific bioreporter. Aquat. Microb. Ecol. 41, 233–245.
Mojica, K.D.A., Brussaard, C.P.D., 2014. Factors affecting virus dynamics and microbial host-virus interactions in marine environments. FEMS Microbiol. Ecol. 89, 495–515.
Mojica, K.D.A., Huisman, J., Wilhelm, S.W., Brussaard, C.P.D., 2016. Latitudinal variation in virus-induced mortality of phytoplankton across the North Atlantic Ocean. ISME J. 10, 500–513.
Moore, J.K., Braucher, O., 2008. Sedimentary and mineral dust sources of dissolved iron to the World Ocean. Biogeosciences 5, 631–656.
Mopper, K., Schultz, C.A., 1993. Fluorescence as a possible tool for studying the nature and water column distribution of DOC components. Mar. Chem. 41, 229–238.
Mundy, C.J., Gosselin, M., Ehn, J., Gratton, Y., Rossnagel, A., Barber, D.G., Martin, J., Tremblay, J.É., Palmer, M., Arrigo, K.R., Darnis, G., Fortier, L., Else, B., Papakyriakou, T., 2009. Contribution of under-ice primary production to an ice-edge upwelling phytoplankton bloom in the Canadian Beaufort Sea. Geophys. Res. Lett. 36, 1–5.
Murphy, J., Riley, J.P., 1962. A modified single solution method for the determination of phosphate in natural waters. Anal. Chim. Acta 27, 31–36.
Nakayama, Y., Fujita, S., Kuma, K., Shimada, K., 2011. Iron and humic-type fluorescent dissolved organic matter in the Chukchi Sea and Canada Basin of the western Arctic Ocean. J. Geophys. Res. Ocean. 116, 1–16.
National Snow and Ice Data Center, 2012. Arctic sea ice extent settles at record seasonal minimum [WWW Document]. Natl. Snow Ice Data Cent. URL http://nsidc.org/arcticseaicenews/2012/09/arctic-sea-ice-extent-settles-at-record-seasonal-minimum/ (accessed 10.20.17).
National Snow and Ice Data Center, 2015. Arctic sea ice reaches fourth lowest minimum [WWW Document]. Natl. Snow Ice Data Cent. URL http://nsidc.org/arcticseaicenews/2015/09/2015_arctic-minimum/ (accessed 10.20.17).
Netz, D.J.A., Stith, C.M., Stümpfig, M., Köpf, G., Vogel, D., Genau, H.M., Stodola, J.L., Lill, R., Burgers, P.M.J., Pierik, A.J., 2012. Eukaryotic DNA polymerases require an iron-sulfur cluster for the formation of active complexes. Nat. Chem. Biol. 8, 125–132.
Nishino, S., Kikuchi, T., Yamamoto-Kawai, M., Kawaguchi, Y., Hirawake, T., Itoh, M., 2011. Enhancement/reduction of biological pump depends on ocean circulation in the sea-ice reduction regions of the Arctic Ocean. J. Oceanogr. 67, 305–314.
Nomikou, P., Papanikolaou, D., Alexandri, M., Sakellariou, D., Rousakis, G., 2013. Submarine volcanoes along the aegean volcanic arc. Tectonophysics 597–598, 123–146.
Norman, L., Worms, I.A.M., Angles, E., Bowie, A.R., Nichols, C.M., Ninh Pham, A.,

Slaveykova, V.I., Townsend, A.T., David Waite, T., Hassler, C.S., 2015. The role of bacterial and algal exopolymeric substances in iron chemistry. Mar. Chem. 173, 148–161.

Not, F., Latasa, M., Marie, D., Cariou, T., Vaulot, D., Simon, N., 2004. A single species, Micromonas pusilla (Prasinophyceae), dominates the eukaryotic picoplankton in the Western English Channel. Appl. Environ. Microbiol. 70, 4064–4072.

Not, F., Massana, R., Latasa, M., Marie, D., Colson, C., Eikrem, W., Pedrós-Alió, C., Vaulot, D., Simon, N., 2005. Late summer community composition and abundance of photosynthetic picoeukaryotes in Norwegian and Barents seas. Limnol. Oceanogr. 50, 1677–1686.

Obata, H., Karatani, H., Nakayama, E., 1993. Automated Determination of Iron in Seawater by Chelating Resin Concentration and Chemiluminescence Detection. Anal. Chem. 65, 1524–1528.

Obernosterer, I., Herndl, G.J., 2000. Differences in the optical and biological reactivity of the humic and nonhumic dissolved organic carbon component in two contrasting coastal marine environments 45, 1120–1129.

Olli, K., Wassmann, P., Reigstad, M., Ratkova, T.N., Arashkevich, E., Pasternak, A., Matrai, P.A., Knulst, J., Tranvik, L., Klais, R., Jacobsen, A., 2007. The fate of production in the central Arctic Ocean - top-down regulation by zooplankton expatriates? Prog. Oceanogr. 72, 84–113.

Omoregie, E.O., Mastalerz, V., De Lange, G., Straub, K.L., Kappler, A., Røy, H., Stadnitskaia, A., Foucher, J.P., Boetius, A., 2008. Biogeochemistry and community composition of iron- and sulfur-precipitating microbial mats at the Chefren mud volcano (Nile deep sea fan, eastern Mediterranean). Appl. Environ. Microbiol. 74, 3198–3215.

Parekh, P., Follows, M.J., Boyle, E.A., 2005. Decoupling of iron and phosphate in the global ocean. Global Biogeochem. Cycles 19, 1–16.

Paris, R., Desboeufs, K. V, Journet, E., 2011. Variability of dust iron solubility in atmospheric waters: Investigation of the role of oxalate organic complexation. Atmos. Environ. 45, 6510–6517.

Passmore, R., Hsu, J., Liu, R.X., Tam, E., Cai, Y., Su, W., Frasca, J., Brigden, S.M., Comeau, A.M., Ortmann, A.C., Lavergne, A., Suttle, C.A., 2000. MPN Assay Analyzer.

Passow, U., 2002. Transparent exopolymer particles (TEP) in aquatic environments. Prog. Oceanogr. 55, 287–333.

Paucot, H., Wollast, R., 1997. Transport and transformation of trace metals in the Scheldt estuary. Mar. Chem. 58, 229–244.

Pekey, H., 2006. The distribution and sources of heavy metals in Izmit Bay surface sediments affected by a polluted stream. Mar. Pollut. Bull. 52, 1197–1208.

Pernet-Coudrier, B., Waeles, M., Filella, M., Quentel, F., Riso, R.D., 2013. Simple and simultaneous determination of glutathione, thioacetamide and refractory organic matter in natural waters by DP-CSV. Sci. Total Environ. 463–464, 997–1005.

Peterson, B.J., Holmes, R.M., McClelland, J.W., Vörösmarty, C.J., Lammers, R.B., Shiklomanov, A.I., Shiklomanov, I.A., Rahmstorf, S., 2002. Increasing river discharge to the Arctic Ocean. Science 298, 2171–3.

Peterson, B.J., McClelland, J.W., Curry, R., Holmes, R.M., Walsh, J.E., Aagaard, K., 2006. Trajectory Shifts in the Arctic and Subarctic Freshwater Cycle. Science (80-.). 313, 1061–1066.

Pižeta, I., Sander, S.G., Hudson, R.J.M., Omanović, D., Baars, O., Barbeau, K.A., Buck, K.N., Bundy, R.M., Carrasco, G., Croot, P.L., Garnier, C., Gerringa, L.J.A., Gledhill, M., Hirose, K., Kondo, Y., Laglera, L.M., Nuester, J., Rijkenberg, M.J.A., Takeda, S.,

Twining, B.S., Wells, M., 2015. Interpretation of complexometric titration data: An intercomparison of methods for estimating models of trace metal complexation by natural organic ligands. Mar. Chem. 173, 3–24.
Pluskal, T., Castillo, S., Villar-Briones, A., Orešič, M., 2010. MZmine 2: Modular framework for processing, visualizing, and analyzing mass spectrometry-based molecular profile data. BMC Bioinformatics 11, 395.
Pollak, M.J., 1951. The sources of the deep water of the eastern Mediterranean Sea. J. Mar. Res. 10, 128–152.
Poorvin, L., Rinta-Kanto, J.M., Hutchins, D.A., Wilhelm, S.W., 2004. Viral release of iron and its bioavailability to marine plankton. Limnol. Oceanogr. 49, 1734–1741.
Poorvin, L., Sander, S.G., Velasquez, I., Ibisanmi, E., LeCleir, G.R., Wilhelm, S.W., 2011. A comparison of Fe bioavailability and binding of a catecholate siderophore with virus-mediated lysates from the marine bacterium Vibrio alginolyticus PWH3a. J. Exp. Mar. Bio. Ecol. 399, 43–47.
Powell, R.T., Wilson-Finelli, A., 2003a. Importance of organic Fe complexing ligands in the Mississippi River plume. Estuar. Coast. Shelf Sci. 58, 757–763.
Powell, R.T., Wilson-Finelli, A., 2003b. Photochemical degradation of organic iron complexing ligands in seawater. Aquat. Sci. - Res. Across Boundaries 65, 367–374.
Press, W.H., Teukolsky, S.A., Vetterling, W.T., Flannery, B.P., 2007. Numerical Recipes: The Art of Scientific Computing, 3rd ed. Cambridge University Press, Cambridge, United Kingdom.
Price, N.M., Ahner, B.A., Morel, F.M.M., 1994. The equatorial Pacific Ocean: grazer controlled phytoplankton populations in an iron-limited ecosystem. Limnol. Oceanogr. 39, 520–534.
Puig, P., Madron, X.D. de, Salat, J., Schroeder, K., Martín, J., Karageorgis, A.P., Palanques, A., Roullier, F., Lopez-Jurado, J.L., Emelianov, M., Moutin, T., Houpert, L., 2013. Thick bottom nepheloid layers in the western Mediterranean generated by deep dense shelf water cascading. Prog. Oceanogr. 111, 1–23.
Quentel, F., Filella, M., 2008. Quantification of refractory organic substances in freshwaters: Further insight into the response of the voltammetric method. Anal. Bioanal. Chem. 392, 1225–1230.
R Development Core Team, 2008. R: A language and environment for statistical computing. R Foundation for Statistical Computing, Vienna, Austria.
Rabe, B., Karcher, M., Kauker, F., Schauer, U., Toole, J.M., Krishfield, R.A., Pisarev, S., Kikuchi, T., Su, J., 2014. Arctic Ocean basin liquid freshwater storage trend 1992-2012. Geophys. Res. Lett. 41, 961–968.
Rabe, B., Schauer, U., Ober, S., Horn, M., Hoppmann, M., Korhonen, M., Pisarev, S., Hampe, H., Villacieros, N., Savy, J.P., Wisotzki, A., 2016. Physical oceanography during POLARSTERN cruise PS94 (ARK-XXIX/3). Bremerhaven.
Raiswell, R., Anderson, T.F., 2005. Reactive iron enrichment in sediments deposited beneath euxinic bottom waters: constraints on supply by shelf recycling. Geol. Soc. London, Spec. Publ. 248, 179–194.
Rank, D., Özsoy, E., Salihoğlu, I., 1999. Oxygen-18, deuterium and tritium in the Black Sea and the Sea of Marmara. J. Environ. Radioact. 43, 231–245.
Reader, H.E., Stedmon, C.A., Nielsen, N.J., Kritzberg, E.S., 2015. Mass and UV-visible spectral fingerprints of dissolved organic matter: sources and reactivity. Front. Mar. Sci. 2, 1–10.
Redfield, A., Ketchum, B., Richards, F., 1963. The influence of organisms on the composition of sea water. In: Hill, M. (Ed.), The Sea. Interscience, New York, pp. 26–77.
Redfield, A.C., 1958. The biological control of chemical factors in the environment. Am.

Sci. 46, 230A–221.
Reinthaler, T., Sintes, E., Herndl, G.J., 2008. Dissolved organic matter and bacterial production and respiration in the sea-surface microlayer of the open Atlantic and the western Mediterranean Sea. Limnol. Oceanogr. 53, 122–136.
Rijkenberg, M.J.A., de Baar, H.J.W., Bakker, K., Gerringa, L.J.A., Keijzer, E., Laan, M., Laan, P., Middag, R., Ober, S., van Ooijen, J., Ossebaar, S., van Weerlee, E.M., Smit, M.G., 2015. "PRISTINE", a new high volume sampler for ultraclean sampling of trace metals and isotopes. Mar. Chem. 177, 501–509.
Rijkenberg, M.J.A., Gerringa, L.J. a, Timmermans, K.R., Fischer, A.C., Kroon, K.J., Buma, A.G.J., Wolterbeek, B.T., de Baar, H.J.W., 2008a. Enhancement of the reactive iron pool by marine diatoms. Mar. Chem. 109, 29–44.
Rijkenberg, M.J.A., Middag, R., Laan, P., Gerringa, L.J.A., Van Aken, H.M., Schoemann, V., De Jong, J.T.M., De Baar, H.J.W., 2014. The distribution of dissolved iron in the West Atlantic Ocean. PLoS One 9.
Rijkenberg, M.J.A., Powell, C.F., Dall'Osto, M., Nielsdottir, M.C., Patey, M.D., Hill, P.G., Baker, A.R., Jickells, T.D., Harrison, R.M., Achterberg, E.P., 2008b. Changes in iron speciation following a Saharan dust event in the tropical North Atlantic Ocean. Mar. Chem. 110, 56–67.
Rijkenberg, M.J.A., Slagter, H.A., Rutgers van der Loeff, M., van Ooijen, J., Gerringa, L.J.A., 2018a. Dissolved Fe in the Deep and Upper Arctic Ocean With a Focus on Fe Limitation in the Nansen Basin. Front. Mar. Sci. 5, 1–14.
Rijkenberg, M.J.A., Slagter, H.A., Rutgers van der Loeff, M., Van Ooijen, J., Gerringa, L.J.A., 2018b. Dissolved Fe in the Arctic Ocean shows Fe limitation in the Nansen Basin. Front. Mar. Sci. 1–14.
Rijkenberg, M.J.A., Steigenberger, S., Powell, C.F., van Haren, H., Patey, M.D., Baker, A.R., Achterberg, E.P., 2012. Fluxes and distribution of dissolved iron in the eastern (sub-) tropical North Atlantic Ocean. Global Biogeochem. Cycles 26, GB3004.
Ringbom, A., Still, E., 1972. The calculation and use of a coefficients. Anal. Chim. Acta 59, 143–146.
Rodellas, V., Garcia-Orellana, J., Masqué, P., Feldman, M., Weinstein, Y., 2015. Submarine groundwater discharge as a major source of nutrients to the Mediterranean Sea. Proc. Natl. Acad. Sci. 112, 3926–3930.
Roeske, T., Loeff, M.R. vd, Middag, R., Bakker, K., 2012. Deep water circulation and composition in the Arctic Ocean by dissolved barium, aluminium and silicate. Mar. Chem. 132–133, 56–67.
Roether, W., Klein, B., Manca, B.B., Theocharis, A., Kioroglou, S., 2007. Transient Eastern Mediterranean deep waters in response to the massive dense-water output of the Aegean Sea in the 1990s. Prog. Oceanogr. 74, 540–571.
Rolison, J.M., Middag, R., Stirling, C.H., Rijkenberg, M.J.A., de Baar, H.J.W., 2015. Zonal distribution of dissolved aluminium in the Mediterranean Sea. Mar. Chem. 177, 1–14.
Romeo, A.M., Christen, L., Niles, E.G., Kosman, D.J., 2001. Intracellular chelation of iron by bipyridyl inhibits DNA virus replication: Ribonucleotide reductase maturation as a probe of intracellular iron pools. J. Biol. Chem. 276, 24301–24308.
Rudels, B., 2008. Arctic Ocean Circulation. In: Steele, J., Turekian, K., Thorpe, S. (Eds.), Encyclopedia of Ocean Sciences. Academic Press, pp. 211–225.
Rudels, B., 2012. Arctic Ocean circulation and variability - Advection and external forcing encounter constraints and local processes. Ocean Sci. 8, 261–286.
Rudels, B., 2015. Arctic Ocean circulation, processes and water masses: A description of observations and ideas with focus on the period prior to the International Polar Year 2007-2009. Prog. Oceanogr. 132, 22–67.

Rue, E., Bruland, K., 2001. Domoic acid binds iron and copper: A possible role for the toxin produced by the marine diatom Pseudo-nitzschia. Mar. Chem. 76, 127–134.
Rue, E.L., Bruland, K.W., 1995. Complexation of iron(III) by natural organic ligands in the Central North Pacific as determined by a new competitive ligand equilibration/adsorptive cathodic stripping voltammetric method. Mar. Chem. 50, 117–138.
Rutgers van der Loeff, M., Cai, P., Stimac, I., Bauch, D., Hanfland, C., Roeske, T., Moran, S.B., 2012. Shelf-basin exchange times of Arctic surface waters estimated from228Th/228Ra disequilibrium. J. Geophys. Res. Ocean. 117.
Rutgers van der Loeff, M.M., Key, R.M., Scholten, J., Bauch, D., Michel, A., 1995. 228Ra as a tracer for shelf water in the arctic ocean. Deep Sea Res. Part II 42, 1533–1553.
Sander, S.G., Koschinsky, A., 2011. Metal flux from hydrothermal vents increased by organic complexation. Nat. Geosci. 4, 145–150.
Sarthou, G., Baker, A.R., Kramer, J., Laan, P., Laës, A., Ussher, S., Achterberg, E.P., de Baar, H.J.W., Timmermans, K.R., Blain, S., 2007. Influence of atmospheric inputs on the iron distribution in the subtropical North-East Atlantic Ocean. Mar. Chem. 104, 186–202.
Sarthou, G., Jeandel, C., 2001. Seasonal variations of iron concentrations in the Ligurian Sea and iron budget in the Western Mediterranean Sea. Mar. Chem. 74, 115–129.
Sarthou, G., Vincent, D., Christaki, U., Obernosterer, I., Timmermans, K.R., Brussaard, C.P.D., 2008. The fate of biogenic iron during a phytoplankton bloom induced by natural fertilisation: Impact of copepod grazing. Deep Sea Res. Part II Top. Stud. Oceanogr. 55, 734–751.
Saydam, A.C., Senyuva, H.Z., 2002. Deserts: Can they be the potential suppliers of bioavailable iron? Geophys. Res. Lett. 29, 19-1-19–3.
Schauer, U., 2016. The expedition PS94 of the Research Vessel POLARSTERN to the central Arctic Ocean in 2015. Berichte zur Polar- und Meeresforsch. - Reports Polar Mar. Res. 703, 170.
Schlitzer, R., 2016. Ocean Data View.
Schoemann, V., Becquevort, S., Stefels, J., Rousseau, V., Lancelot, C., 2005. Phaeocystis blooms in the global ocean and their controlling mechanisms: a review. J. Sea Res. 53, 43–66.
Scholten, J.C., Rutgers van der Loeff, M.M., Michel, A., 1995. Distribution of 230Th and 231Pa in the water column in relation to the ventilation of the deep Arctic basins. Deep. Res. Part II 42, 1519–1531.
Schroeder, K., Taillandier, V., Vetrano, A., Gasparini, G.P., 2008. The circulation of the western Mediterranean Sea in spring 2005 as inferred from observations and from model outputs. Deep Sea Res. Part I Oceanogr. Res. Pap. 55, 947–965.
Schuur, E.A.G., Abbott, B.W., Bowden, W.B., Brovkin, V., Camill, P., Canadell, J.G., Chanton, J.P., Chapin, F.S., Christensen, T.R., Ciais, P., Crosby, B.T., Czimczik, C.I., Grosse, G., Harden, J., Hayes, D.J., Hugelius, G., Jastrow, J.D., Jones, J.B., Kleinen, T., Koven, C.D., Krinner, G., Kuhry, P., Lawrence, D.M., McGuire, A.D., Natali, S.M., O'Donnell, J.A., Ping, C.L., Riley, W.J., Rinke, A., Romanovsky, V.E., Sannel, A.B.K., Schädel, C., Schaefer, K., Sky, J., Subin, Z.M., Tarnocai, C., Turetsky, M.R., Waldrop, M.P., Walter Anthony, K.M., Wickland, K.P., Wilson, C.J., Zimov, S.A., 2013. Expert assessment of vulnerability of permafrost carbon to climate change. Clim. Change 119, 359–374.
Schuur, E.A.G., McGuire, A.D., Grosse, G., Harden, J.W., Hayes, D.J., Hugelius, G., Koven, C.D., Kuhry, P., 2015. Climate change and the permafrost carbon feedback. Nature 520, 171–179.

Sedwick, P.N., Church, T.M., Bowie, A.R., Marsay, C.M., Ussher, S.J., Achilles, K.M., Lethaby, P.J., Johnson, R.J., Sarin, M.M., McGillicuddy, D.J., 2005. Iron in the Sargasso Sea (Bermuda Atlantic Time-series Study region) during summer: Eolian imprint, spatiotemporal variability, and ecological implications. Global Biogeochem. Cycles 19, n/a-n/a.

Sedwick, P.N., Sholkovitz, E.R., Church, T.M., 2007. Impact of anthropogenic combustion emissions on the fractional solubility of aerosol iron: Evidence from the Sargasso Sea. Geochemistry, Geophys. Geosystems 8, n/a-n/a.

Sedwick, P.N., Sohst, B.M., Ussher, S.J., Bowie, A.R., 2015. A zonal picture of the water column distribution of dissolved iron(II) during the U.S. GEOTRACES North Atlantic transect cruise (GEOTRACES GA03). Deep. Res. Part II Top. Stud. Oceanogr. 116, 166–175.

Serreze, M.C., Stroeve, J., 2015. Arctic sea ice trends, variability and implications for seasonal ice forecasting. Philos. Trans. R. Soc. A Math. Phys. Eng. Sci. 373, 20140159.

Serreze, M.C., Stroeve, J., Barrett, A.P., Boisvert, L.N., 2016. Summer atmospheric circulation anomalies over the Arctic Ocean and their influences on September sea ice extent: A cautionary tale. J. Geophys. Res. Atmos. 121, 11,463-11,485.

Shaked, Y., Lis, H., 2012. Disassembling Iron Availability to Phytoplankton. Front. Microbiol. 3, 1–26.

Sheik, A.R., Brussaard, C.P.D., Lavik, G., Lam, P., Musat, N., Krupke, A., Littmann, S., Strous, M., Kuypers, M.M.M., 2014. Responses of the coastal bacterial community to viral infection of the algae Phaeocystis globosa. ISME J. 8, 212–225.

Sholkovitz, E.R., 1976. Flocculation of dissolved organic and inorganic matter during the mixing of river water and seawater. Geochim. Cosmochim. Acta 40, 831–845.

Sholkovitz, E.R., 1993. The geochemistry of rare earth elements in the Amazon River estuary. Geochim. Cosmochim. Acta 57, 2181–2190.

Slagter, H.A., Gerringa, L.J.A., Brussaard, C.P.D., 2016. Phytoplankton Virus Production Negatively Affected by Iron Limitation. Front. Mar. Sci. 3, 1–11.

Slagter, H.A., Reader, H.E., Rijkenberg, M.J.A., Rutgers van der Loeff, M., de Baar, H.J.W., Gerringa, L.J.A., 2017. Organic Fe speciation in the Eurasian Basins of the Arctic Ocean and its relation to terrestrial DOM. Mar. Chem. 197, 11–25.

Soria-Dengg, S., Reissbrodt, R., Horstmann, U., 2001. Siderophores in marine coastal waters and their relevance for iron uptake by phytoplankton: experiments with the diatom Phaeodactylum tricornutum. Mar Ecol Prog Ser 220, 73–82.

Spokes, L.J., Jickells, T.D., 1995. Factors controlling the solubility of aerosol trace metals in the atmosphere and on mixing into seawater. Aquat. Geochemistry 1, 355–374.

Stedmon, C.A., Amon, R.M.W., Rinehart, A.J., Walker, S.A., 2011. The supply and characteristics of colored dissolved organic matter (CDOM) in the Arctic Ocean: Pan Arctic trends and differences. Mar. Chem. 124, 108–118.

Stedmon, C.A., Markager, S., Kaas, H., 2000. Optical Properties and Signatures of Chromophoric Dissolved Organic Matter (CDOM) in Danish Coastal Waters. Estuar. Coast. Shelf Sci. 51, 267–278.

Stoderegger, K., Herndl, G.J., 1998. Stoderegger y Herndl, 1998 - Production and release of bacterial capsular material and its subsequent utilization by marine bacterioplankton. Limnol. Oceanogr. 43, 877–884.

Strass, V.H., Nöthig, E.M., 1996. Seasonal shifts in ice edge phytoplankton blooms in the Barents Sea related to the water column stability. Polar Biol. 16, 409–422.

Strickland, J., Parsons, T., 1972. A practical handbook of seawater analysis.

Stroeve, J.C., Serreze, M.C., Holland, M.M., Kay, J.E., Malanik, J., Barrett, A.P., 2012. The Arctic's rapidly shrinking sea ice cover: A research synthesis. Clim. Change

110, 1005–1027.
Strzepek, R.F., Maldonado, M.T., Hunter, K.A., Frew, R.D., Boyd, P.W., 2011. Adaptive strategies by Southern Ocean phytoplankton to lessen iron limitation: Uptake of organically complexed iron and reduced cellular iron requirements. Limnol. Oceanogr. 56, 1983–2002.
Sukekava, C., Downes, J., Slagter, H.A., Gerringa, L.J.A., Laglera, L.M., 2018. Determination of the contribution of humic substances to iron complexation in seawater by catalytic cathodic stripping voltammetry. Talanta.
Sunda, W.G., 1997. Control of dissolved iron concentrations in the world ocean, A comment. Mar. Chem. 57, 169–172.
Sunda, W.G., Huntsman, S. a, 1997. Interrelated influence of iron, light and cell size on marine phytoplankton growth. Nature 390, 389–392.
Suttle, C.A., 1993. Enumeration and isolation of viruses. In: Kemp, P.F., Sherr, B.F., Sherr, E.B., Cole, J.J. (Eds.), Handbook of Methods in Aquatic Microbial Ecology. CRC Press, pp. 121–134.
Suttle, C.A., 2005. Viruses in the sea. Nature 437, 356–361.
Tachikawa, K., Roy-Barman, M., Michard, A., Thouron, D., Yeghicheyan, D., Jeandel, C., 2004. Neodymium isotopes in the Mediterranean Sea: comparison between seawater and sediment signals. Geochim. Cosmochim. Acta 68, 3095–3106.
Tagliabue, A., Aumont, O., DeAth, R., Dunne, J.P., Dutkiewicz, S., Galbraith, E., Misumi, K., Moore, J.K., Ridgwell, A., Sherman, E., Stock, C., Vichi, M., Völker, C., Yool, A., 2016. How well do global ocean biogeochemistry models simulate dissolved iron distributions? Global Biogeochem. Cycles 30, 149–174.
Tagliabue, A., Bopp, L., Dutay, J.-C., Bowie, A.R., Chever, F., Jean-Baptiste, P., Bucciarelli, E., Lannuzel, D., Remenyi, T., Sarthou, G., Aumont, O., Gehlen, M., Jeandel, C., 2010. Hydrothermal contribution to the oceanic dissolved iron inventory. Nat. Geosci. 3, 252–256.
Tagliabue, A., Bowie, A.R., Boyd, P.W., Buck, K.N., Johnson, K.S., Saito, M.A., 2017. The integral role of iron in ocean biogeochemistry. Nature 543, 51–59.
Tanhua, T., Jones, E.P., Jeansson, E., Jutterström, S., Smethie, W.M., Wallace, D.W.R., Anderson, L.G., 2009. Ventilation of the arctic ocean: Mean ages and inventories of anthropogenic CO2 and CFC-11. J. Geophys. Res. Ocean. 114, 1–11.
Taylor, R.L., Semeniuk, D.M., Payne, C.D., Zhou, J., Tremblay, J.-É., Cullen, J.T., Maldonado, M.T., 2013. Colimitation by light, nitrate, and iron in the Beaufort Sea in late summer. J. Geophys. Res. Ocean. 118, 3260–3277.
Testor, P., Gascard, J.C., 2003. Large-scale spreading of deep waters in the Western Mediterranean Sea by submesoscale coherent eddies. J. Phys. Oceanogr. 33, 75–87.
Thuróczy, C.-E., Gerringa, L.J.A., Klunder, M., Laan, P., Le Guitton, M., de Baar, H.J.W., 2011. Distinct trends in the speciation of iron between the shallow shelf seas and the deep basins of the Arctic Ocean. J. Geophys. Res. 116, C10009.
Thuróczy, C.-E., Gerringa, L.J.A., Klunder, M.B., Middag, R., Laan, P., Timmermans, K.R., de Baar, H.J.W., 2010. Speciation of Fe in the Eastern North Atlantic Ocean. Deep Sea Res. Part I 57, 1444–1453.
Timmermans, K.R., Davey, M.S., van der Wagt, B., Snoek, J., Geider, R.J., Veldhuis, M.J.W., Gerringa, L.J.A., De Baar, H.J.W., 2001a. Co-limitation by iron and light of Chaetoceros brevis, C. dichaeta and C. calcitrans (Bacillariophyceae). Mar. Ecol. Prog. Ser. 217, 287–297.
Timmermans, K.R., Gerringa, L.J.A., de Baar, H.J.W., van der Wagt, B., Veldhuis, M.J.W., de Jong, J.T.M., Croot, P.L., Boye, M., 2001b. Growth rates of large and small Southern Ocean diatoms in relation to availability of iron in natural seawater.

Limnol. Oceanogr. 46, 260–266.
Timmermans, K.R., Gledhill, M., Nolting, R.F., Veldhuis, M.J.W., de Baar, H.J.W., van den Berg, C.M.G., 1998. Responses of marine phytoplankton in iron enrichment experiments in the northern North Sea and northeast Atlantic Ocean. Mar. Chem. 61, 229–242.
Timmermans, K.R., van der Wagt, B., de Baar, H.J.W., 2004. Growth rates, half saturation constants, and silicate, nitrate, and phosphate depletion in relation to iron availability of four large open-ocean diatoms from the Southern Ocean. Limnol. Oceanogr. 49, 2141–2151.
Timmermans, K.R., van der Wagt, B., Veldhuis, M.J.W., Maatman, A., de Baar, H.J.W., 2005. Physiological responses of three species of marine pico-phytoplankton to ammonium, phosphate, iron and light limitation. J. Sea Res. 53, 109–120.
Town, R.M., Filella, M., 2000. Dispelling the myths: Is the existence of L1 and L2 ligands necessary to explain metal ion speciation in natural waters? Limnol. Oceanogr. 45, 1341–1357.
Tremblay, J.-É., Gagnon, J., 2009. The effects of irradiance and nutrient supply on the productivity of Arctic waters: a perspective on climate change. In: Nihoul, J.C.J., Kostianoy, A.G. (Eds.), Influence of Climate Change on the Changing Arctic and Sub-Arctic Conditions. Springer, Dordrecht, pp. 73–93.
Tremblay, J.É., Anderson, L.G., Matrai, P., Coupel, P., Bélanger, S., Michel, C., Reigstad, M., 2015. Global and regional drivers of nutrient supply, primary production and CO2 drawdown in the changing Arctic Ocean. Prog. Oceanogr. 139, 171–196.
Tremblay, J.É., Simpson, K., Martin, J., Miller, L., Gratton, Y., Barber, D., Price, N.M., 2008. Vertical stability and the annual dynamics of nutrients and chlorophyll fluorescence in the coastal, southeast Beaufort Sea. J. Geophys. Res. Ocean. 113, 1–14.
Trezzi, G., Garcia-Orellana, J., Rodellas, V., Santos-Echeandia, J., Tovar-Sánchez, A., Garcia-Solsona, E., Masqué, P., 2016. Submarine groundwater discharge: A significant source of dissolved trace metals to the North Western Mediterranean Sea. Mar. Chem. 186, 90–100.
Twining, B.S., Baines, S.B., 2013. The trace metal composition of marine phytoplankton. Ann. Rev. Mar. Sci. 5.
Twining, B.S., Rauschenberg, S., Morton, P.L., Vogt, S., 2015. Metal contents of phytoplankton and labile particulate material in the North Atlantic Ocean. Prog. Oceanogr. 137, 261–283.
Ulfsbo, A., Cassar, N., Korhonen, M., Heuven, S. Van, Hoppema, M., Kattner, G., Anderson, L.G., 2014. Late summer net community production in the central Arctic Ocean using multiple approaches. Global Biogeochem. Cycles 28, 1129–1148.
Ünlülata, Ü., Oğuz, T., Latif, M.A., Özsoy, E., 1990. On the physical oceanography of the Turkish Straits. In: The Physical Oceanography of Sea Straits. Springer, pp. 25–60.
van de Poll, W.H., Janknegt, P.J., van Leeuwe, M.A., Visser, R.J.W., Buma, A.G.J., 2009. Excessive irradiance and antioxidant responses of an Antarctic marine diatom exposed to iron limitation and to dynamic irradiance. J. Photochem. Photobiol. B Biol. 94, 32–37.
van de Poll, W.H.H., Boute, P.G.G., Rozema, P.D.D., Buma, A.G.J.G.J., Kulk, G., Rijkenberg, M.J.A.J.A., 2015. Sea surface temperature control of taxon specific phytoplankton production along an oligotrophic gradient in the Mediterranean Sea. Mar. Chem. 177, 536–544.
van den Berg, C.M.G., 1995. Evidence for organic complexation of iron in seawater. Mar. Chem. 50, 139–157.
van den Berg, C.M.G., 2006. Chemical speciation of iron in seawater by cathodic stripping

voltammetry with dihydroxynaphthalene. Anal. Chem. 78, 156–163.
van den Berg, C.M.G., Kramer, J.R., 1979. Determination of complexing capacities of ligands in natural waters and conditional stability constants of the copper complexes by means of manganese dioxide. Anal. Chim. Acta 106, 113–120.
van den Berg, C.M.G., Nimmo, M., Daly, P., Turner, D.R., 1990. Effects of the detection window on the determination of organic copper speciation in estuarine waters. Anal. Chim. Acta 232, 149–159.
van Haren, H., Millot, C., 2009. Slantwise convection: A candidate for homogenization of deep newly formed dense waters. Geophys. Res. Lett. 36.
van Haren, H., Millot, C., Taupier-Letage, I., 2006. Fast deep sinking in Mediterranean eddies. Geophys. Res. Lett. 33, L04606.
van Haren, H., The ANTARES Collaboration, 2014. High-frequency internal wave motions at the ANTARES site in the deep Western Mediterranean. Ocean Dyn. 64, 507–517.
van Leeuwe, M.A., Stefels, J., 1998. Effects of iron and light stress on the biochemical composition of Antarctic Phaeocystis sp. (Prymnesiophyceae). II. Pigment composition. J. Phycol. 34, 496–503.
van Leeuwe, M.A., Stefels, J., 2007. Photosynthetic responses in Phaeocystis antarctica towards varying light and iron conditions. Phaeocystis, Major Link Biogeochem. Cycl. Clim. Elem. 61–70.
Vancoppenolle, M., Bopp, L., Madec, G., Dunne, J., Ilyina, T., Halloran, P.R., Steiner, N., 2013. Future arctic ocean primary productivity from CMIP5 simulations: Uncertain outcome, but consistent mechanisms. Global Biogeochem. Cycles 27, 605–619.
Vaulot, D., 1989. CYTOPC: Processing software for flow cytometric data. Signal and Noise 2:8.
Vaulot, D., Birrien, J.-L., Marie, D., Casotti, R., Veldhuis, M.J.W., Kraay, G.W., Chrétiennot-Dinet, M.-J., 1994. Morphology, ploidy, pigment composition, and genome size of cultured strains of Phaeocystis (Prymnesiophyceae). J. Phycol. 30, 1022–1035.
Vaulot, D., Eikrem, W., Viprey, M., Moreau, H., 2008. The diversity of small eukaryotic phytoplankton (≤3 µm) in marine ecosystems. FEMS Microbiol. Rev. 32, 795–820.
Velasquez, I., Nunn, B.L., Ibisanmi, E., Goodlett, D.R., Hunter, K.A., Sander, S.G., 2011. Detection of hydroxamate siderophores in coastal and Sub-Antarctic waters off the South Eastern Coast of New Zealand. Mar. Chem. 126, 97–107.
Velasquez, I.B., Ibisanmi, E., Maas, E.W., Boyd, P.W., Nodder, S., Sander, S.G., 2016. Ferrioxamine Siderophores Detected amongst Iron Binding Ligands Produced during the Remineralization of Marine Particles. Front. Mar. Sci. 3, 1–14.
Veldhuis, M.J.W., Timmermans, K.R., Croot, P., van der Wagt, B., 2005. Picophytoplankton; a comparative study of their biochemical composition and photosynthetic properties. J. Sea Res. 53, 7–24.
Visser, F., Gerringa, L.J.A., Gaast, S.J. Van Der, Baar, H.J.W. De, Timmermans, K.R., Van Der Gaast, S.J., De Baar, H.J.W., Timmermans, K.R., 2003. The role of the reactivity and content of iron of aerosol dust on growth rates of two Antarctic diatom species. J. Phycol. 39, 1085–1094.
von der Heyden, B.P., Roychoudhury, A.N., Mtshali, T.N., Tyliszczak, T., Myneni, S.C.B., 2012. Chemically and Geographically Distinct Solid-Phase Iron Pools in the Southern Ocean. Science (80-.). 338, 1199–1201.
Vonk, J.E., Mann, P.J., Davydov, S., Davydova, A., Spencer, R.G.M., Schade, J., Sobczak, W. V., Zimov, N., Zimov, S., Bulygina, E., Eglinton, T.I., Holmes, R.M., 2013. High biolability of ancient permafrost carbon upon thaw. Geophys. Res. Lett. 40, 2689–2693.
Vonk, J.E., Sánchez-García, L., van Dongen, B.E., Alling, V., Kosmach, D., Charkin, A.,

Semiletov, I.P., Dudarev, O. V., Shakhova, N., Roos, P., Eglinton, T.I., Andersson, A., Gustafsson, Ö., 2012. Activation of old carbon by erosion of coastal and subsea permafrost in Arctic Siberia. Nature 489, 137–140.

Voorhis, A.D., Webb, D.C., 1970. Large vertical currents observed in a winter sinking region of the northwestern Mediterranean. Woods Hole Oceanographic Institution.

Wagener, T., Guieu, C., Leblond, N., 2010. Effects of dust deposition on iron cycle in the surface Mediterranean Sea: results from a mesocosm seeding experiment. Biogeosciences 7, 3769–3781.

Wagener, T., Pulido-Villena, E., Guieu, C., 2008. Dust iron dissolution in seawater: Results from a one-year time-series in the Mediterranean Sea. Geophys. Res. Lett. 35.

Walker, S.A., Amon, R.M.W., Stedmon, C., Duan, S., Louchouarn, P., 2009. The use of PARAFAC modeling to trace terrestrial dissolved organic matter and fingerprint water masses in coastal Canadian Arctic surface waters. J. Geophys. Res. 114, 1–12.

Weitz, J.S., Wilhelm, S.W., 2012. Ocean viruses and their effects on microbial communities and biogeochemical cycles. F1000 Biol. Rep. 8, 2–9.

Wilhelm, C., Büchel, C., Fisahn, J., Goss, R., Jakob, T., LaRoche, J., Lavaud, J., Lohr, M., Riebesell, U., Stehfest, K., Valentin, K., Kroth, P.G., 2006. The Regulation of Carbon and Nutrient Assimilation in Diatoms is Significantly Different from Green Algae. Protist 157, 91–124.

Wilhelm, S.W., King, A.L., Twining, B.S., LeCleir, G.R., DeBruyn, J.M., Strzepek, R.F., Breene, C.L., Pickmere, S., Ellwood, M.J., Boyd, P.W., Hutchins, D.A., 2013. Elemental quotas and physiology of a southwestern Pacific Ocean plankton community as a function of iron availability. Aquat. Microb. Ecol. 68, 185–194.

Wilhelm, S.W., MacAuley, K., Trick, C.G., Nielsen, I., 1998. Evidence for the importance of catechol-type siderophores in the iron-limited growth of a cyanobacterium. Limnol. Oceanogr. 43, 992–997.

Wilhelm, S.W., Suttle, C.A., 1999. Viruses and Nutrient Cycles in the Sea. Bioscience 49, 781.

Wilhelm, S.W., Suttle, C.A., 2000. Viruses as regulators of nutrient cycles in aquatic environments. In: Microbial Biosystems: New Frontiers. Proceedings of the VIII International Symposium on Microbial Ecology. Atlantic Canada Society for Microbial Ecology, Halifax, Nova Scotia. pp. 551–556.

Wilhelm, S.W., Trick, C.G., 1994. Iron-limited growth of cyanobacteria: Multiple siderophore production is a common response. Limnol. Oceanogr. 39, 1979–1984.

Wozniak, A.S., Shelley, R.U., McElhenie, S.D., Landing, W.M., Hatcher, P.G., 2015. Aerosol water soluble organic matter characteristics over the North Atlantic Ocean: Implications for iron-binding ligands and iron solubility. Mar. Chem. 173, 162–172.

Wu, J., Boyle, E., Sunda, W., Wen, L.S., 2001. Soluble and colloidal iron in the oligotrophic North Atlantic and North Pacific. Science 293, 847–849.

Zapata, M., Rodríguez, F., Garrido, J.L., 2000. Separation of chlorophylls and carotenoids from marine phytoplankton: A new HPLC method using a reversed phase C8 column and pyridine-containing mobile phases. Mar. Ecol. Prog. Ser. 195, 29–45.

Zhang, C., 2014. Essential functions of iron-requiring proteins in DNA replication, repair and cell cycle control. Protein Cell 5, 750–60.

Zitter, T.A.C., 2004. Mud volcanism and fluid emissions in eastern Mediterranean neotectonic zones. Applied geology.